Novel Gates with Superconducting Fluxonium Qubits

by

Leon Ding

B.S., California Institute of Technology, 2017

Submitted to the Department of Physics
in partial fulfillment of the requirements for the degree of

Doctor of Philosophy in Physics

at the

MASSACHUSETTS INSTITUTE OF TECHNOLOGY

June 2023

Author .....
Department of Physics
May 19, 2023

Certified by .....
William D. Oliver
Professor of Electrical Engineering and Computer Science
Professor of Physics
Thesis Supervisor

Accepted by .....
Lindley Winslow
Associate Department Head of Physics

Novel Gates with Superconducting Fluxonium Qubits

by

Leon Ding

Submitted to the Department of Physics
on May 19, 2023, in partial fulfillment of the
requirements for the degree of
Doctor of Philosophy in Physics

Abstract

Over the past two decades, superconducting qubits have emerged as a leading platform for gate-based quantum computation. Despite tremendous technological advancements, errors accumulating during gate operations are still a major bottleneck toward building a robust quantum computer. In general, these errors may be reduced by both increasing qubit coherences and improving gate design.

In this thesis, we develop the fluxonium qubit for superconducting quantum computing, a relatively newer qubit with advantages in qubit coherence. We first outline the design and simulation of these and other qubits, including a procedure to minimize flux noise in flux-tunable qubits. We then introduce a new fluxonium architecture containing fluxonium qubits coupled via a transmon coupler (FTF for fluxonium-transmon-fluxonium) and demonstrate high-fidelity novel gates, achieving up to 99.99% fidelity single-qubit gates and 99.9% two-qubit gates on the same device. We show that this coupling scheme has advantages for scalability, ZZ reduction, and performance. These results mark a technological milestone for fluxonium qubits and contribute to the ultimate goal of error-corrected universal quantum computing with superconducting qubits.

Thesis Supervisor: William D. Oliver
Title: Professor of Electrical Engineering and Computer Science
Professor of Physics

Acknowledgments

I would first like to thank my advisor, Professor William D. Oliver for accepting me into the group, advising me, and setting the standard for quality work in the group. He has set a standard in lab to do things properly instead of quickly, to take care of your setup, and to perform research both thoroughly and boldly. Without a doubt, this expectation has had a large positive influence on my personal research habits starting from my first day in lab until my last. This thanks extends to the rest of the EQuS leadership. Notably, Terry P. Orlando, Jeffrey Grover, Joel Wang, and Simon Gustavsson have all been incredibly positive and supportive figures throughout my career. They are smart, attentive, patient, and seemingly incapable of being unkind. Finally, Kyle Serniak deserves a special acknowledgement for helping out with anything and everything ranging from nitty gritty research details, logistics, career advice, emotional support, and diligently editing this thesis.

I next thank my direct research mentors during the initial years of my PhD, Jochen Braumüller, Youngkyu Sung, and Bharath Kannan. Jochen Braumüller took me under his wing at the start of my PhD, taught me the basics of qubit measurement as well as instilling the importance of doing research thoughtfully and cleanly. I thank Youngkyu Sung for teaching me about gates during our tunable coupler experiment and giving me an opportunity to join such an exciting project and showing me immense patience and support in any form I asked for throughout my entire graduate career. I credit a lot of my success in my PhD to him. I thank Bharath Kannan for being a great friend and aggressively providing assistance with any political situations, career decisions, and infrastructural support. He is to credit solely for my having a functional measurement setup for the fluxonium projects.

I am also greatly appreciative of Max Hays and David Rower for being such pleasant people to work with as well as great friends outside of lab. Max Hays joined the fluxonium gate project near the end while I was in dire need of assistance and simply made magic happen. He was supportive, sharp, and developed the final bit of calibrations to end the project in an absolutely ideal fashion. I had the privilege

of working with David Rower during the final stretch of my PhD, giving me an opportunity to mentor and hand off my fluxonium setup in practiced hands. His positivity is noticed by all and is a great influence on the entire lab.

With the growing size of the group, there is unfortunately more than could possibly be said, but I appreciate each individual member of the group that I have interacted with for contributing to my graduate journey: Antti Vepsäläinen, Agustin Di Paolo, Daniel Campbell, Morten Kjaergaard, Roni Winik, Aranya Goswami, Daniel Rodan Legrain, Réouven Assouly, Patrick Harrington, Ilan Rosen, Miuko Tanaka, Mirabella Pulido, Chihiro Watanabe, Margaret McCroby, Alex Greene, Tim Menke, Benjamin Lienhard, Jack Qiu, Gabriel Samach, Aziza Almanakly, Junyoung An, Lamia Ateshian, William Banner, Shoumik Chowdhury, Qi Ding, Shantanu Jha, Hanlim Kang, Amir Karamlou, Junghyun Kim, Chris McNally, Miguel Moreira, Sarah Muschinske, David Pahl, Lukas Pahl, Beatriz Yankelevich, and Sameia Zaman. I especially enjoyed sharing two fridges and two offices with Amir Karamlou throughout the years, and I grateful to Junyoung An for joining me in developing protected qubits on campus and for taking over the liquid nitrogen czar duties. Due to a fruitful collaboration between EQuS and Lincoln Laboratory, I have also had the pleasure to collaborate with David K. Kim, Jonilyn Yoder, Bethany M. Niedzielski, Alexander Melville, Tom Hazard, Mollie E. Schwartz, and Kate Azar. The thanks they deserve is beyond what I can offer, as the success of nearly every project in EQuS is made possible by their team.

Outside of the group, I learned almost everything I know about atomic physics through classes taught by Wolfgang Ketterle and Misha Lukin. The thought and effort they put into their classes is a true service to the entire physics community. The combination of their classes completely transformed me as a scientist and I owe a significant part of my education to them. Through Misha, I learned to be mathematically proficient, to connect superconducting qubits to atomic physics, and to never overrate clarity. Through Wolfgang, I learned to be intuitively proficient and the importance of being able to explain the same concept using different approaches. To understand deeply is to know something simple but in many different ways. On a

related note, I found myself in a position to be the first and only person taking the atomic physics oral qualifying exam in my group. Fortunately, I had the privilege of studying daily with Alyssa Rudelis and Eugene Knyazev over a period of months near the end of my second year. Without this group, studying for the oral exam would have certainly been much more daunting and directionless.

Last but not least, I am extremely grateful to Devin Underwood for his support throughout my entire fluxonium journey. I was put into contact with Devin as part of the IBM PhD Fellowship, during the 2nd year of my PhD, and we met every two weeks as I slowly learned to perform simulations, design devices, setup an experiment, and benchmark gates. Unbeknownst to many, Devin was almost the only person I talked to about research during the majority of the lockdown period. Even after the conclusion of the fellowship, Devin has remained an invaluable friend and supportive figure.

Contents

1 Introduction **29**

1.1 Quantum Information Science 30

1.1.1 Single-Qubit Gates 31

1.1.2 Two-Qubit Gates 33

1.2 Quantum Mechanics 34

1.2.1 State vectors 34

1.2.2 Observables as Operators 35

1.2.3 Quantum Measurement 36

1.2.4 Time Evolution 36

1.2.5 Non-Unitary Dynamics 38

1.3 The Rabi Oscillation 39

1.4 Thesis Outline 43

2 Circuit QED: Building Towards a Quantum Processor **45**

2.1 The Circuit QED Hamiltonian 45

2.1.1 Classical to Quantum LC Oscillator 46

2.1.2 Forming a Qubit with the Josephson Junction 49

2.1.3 More General Circuit Quantization 51

2.2 Numerical Diagonalization: From Pen and Paper to Code 57

2.2.1 Charge Basis 58

2.2.2 Phase Basis 60

2.2.3 Fock Basis 62

2.3 Quantization of Different Qubits 62

2.3.1 Cooper Pair Box . . . 63
2.3.2 Transmon . . . 64
2.3.3 C-Shunt Flux-Qubit . . . 66
2.3.4 Fluxonium . . . 68
2.3.5 Grounded vs. Differential Qubits . . . 73
2.4 Building upon a Qubit . . . 75
2.4.1 Qubit - Resonator Coupling . . . 75
2.4.2 Qubit - Qubit Coupling . . . 80
2.4.3 Qubit - Charge Line . . . 81
2.4.4 Qubit - Flux Line . . . 83
2.5 A Time Limit for Qubits . . . 83

3 Minimizing Flux Noise in Tunable Qubits 87
3.1 Flux Noise Model . . . 88
3.1.1 Analytic Approximation . . . 89
3.1.2 Numerical computation of the current distribution in a superconducting strip of finite thickness . . . 91
3.2 Experimental Setup . . . 94
3.3 Experimental Protocol . . . 96
3.4 Geometric Trends . . . 99
3.5 Discussion . . . 106

4 Getting Started with Fluxonium 107
4.1 Readout and Initialization . . . 107
4.1.1 Dispersive Readout . . . 107
4.1.2 Measurements at Low Qubit Frequency . . . 109
4.1.3 Readout Heralding . . . 110
4.1.4 Microwave Cooling . . . 115
4.1.5 Overview of Initialization Options . . . 117
4.2 Time-domain Measurements . . . 118
4.2.1 Rabi . . . 118

4.2.2 Lifetime T_1 . . . 118
4.2.3 Ramsey . . . 120
4.2.4 Spin-Echo . . . 120
4.3 Single-Qubit Gate Calibration . . . 121
4.3.1 Single-Qubit Clifford Benchmarking . . . 121
4.3.2 Calibration Algorithm . . . 123
4.3.3 Error Analysis . . . 126

5 FTF Architecture for Quantum Computing 131
5.1 The FTF Architecture . . . 132
5.1.1 Gate Operation . . . 133
5.1.2 ZZ Reduction . . . 135
5.1.3 Grounded vs. Differential Qubits . . . 140
5.2 Experimental Setup . . . 143
5.2.1 Wiring . . . 143
5.2.2 Readout and Initialization . . . 146
5.2.3 DC Biasing . . . 146
5.3 Gates . . . 147
5.3.1 Single-Qubit Gates . . . 147
5.3.2 Two-Qubit Gate Calibration . . . 149
5.3.3 CZ Gate vs. Flux . . . 153
5.3.4 Reinforcement Learning for CZ Gates . . . 157
5.3.5 Relative Drive Amplitude and Phase Calibration . . . 160
5.4 Error Analysis . . . 163
5.4.1 Relaxation of Higher Energy Levels . . . 164
5.4.2 CZ Phase Error . . . 166
5.4.3 Amplitude Error . . . 167
5.5 Secondary Device . . . 168
5.6 Discussion . . . 169

6 Conclusions 171

A Designing the FTF Device **173**

A.1 Junction Parameters . . . 173

A.1.1 Josephson Energy . . . 173

A.1.2 Inductive Energy . . . 174

A.1.3 Capacitance Across Junction . . . 174

A.1.4 Junction Chain Capacitance . . . 175

A.2 DC Electromagnetic Simulations . . . 178

A.2.1 Qubit Parameters . . . 180

A.2.2 Qubit - Resonator Couplings . . . 180

A.2.3 Qubit - Charge Line Couplings . . . 181

A.2.4 Capacitive Quantum Crosstalk . . . 182

A.3 RF Electromagnetic Simulations . . . 183

A.3.1 Resonator Simulations . . . 183

A.3.2 Purcell Filter Simulation . . . 184

A.3.3 Flux Lines . . . 185

A.3.4 Decay Rate into Control Lines . . . 185

A.3.5 Qubit Capacitance . . . 187

A.3.6 Qubit - Qubit Coupling . . . 188

A.3.7 Qubit - Resonator Coupling . . . 190

List of Figures

1-1 **Illustration of the Bloch sphere.** The surface of the Bloch sphere represents all possible superpositions of $|0\rangle$ and $|1\rangle$. 32

1-2 **Off-resonant Rabi oscillations. (a)** Bloch sphere trajectories for three different detunings (different shades of blue, dashed lines) and an initial state of $|0\rangle$. Solid blue arrows show the rotation axis. **(b)** Population as a function of time for the three trajectories shown in (a). 42

2-1 ***LC* oscillator. (a)** Circuit representation of a LC oscillator. **(b)** Plot of parabolic potential energy of an LC oscillator along with associated energy levels. 48

2-2 **Diagram of a Josephson junction. (a)** Illustration of Josephson junction. **(b)** Circuit diagram representation of a Josephson junction. 50

2-3 **Cooper Pair Box. (a)** Circuit representation of Cooper Pair Box, with a Josephson junction and capacitor in parallel. **(b)** Illustration of the cosine potential energy, leading to unevenly spaced energy levels. 52

2-4 **Generic superconducting circuit composed of capacitors, inductors, and Josephson junctions.** 53

2-5 **Circuit schematic of a tunable transmon capacitively coupled to a resonator to illustrate general circuit QED techniques.** . 54

2-6 **Energy spectra of the Cooper Pair Box vs. offset charge.** As the ratio E_J/E_C is increased, charge dispersion exponentially decreases. The regime $E_J/E_C \approx 50$ defines the typical transmon qubit regime. 64

2-7 **Asymmetric tunable-transmon. (a)** Circuit diagram of a tunable-transmon. **(b)** Energy spectrum of Transmon with parameters $E_C/h = 0.2\,\text{GHz}$, $E_{J1}/h = 13\,\text{GHz}$, and $E_{J2}/h = 5\,\text{GHz}$. 66

2-8 **Capacitively-shunted flux qubit (a)** Circuit diagram of a C-shunt flux qubit. **(b)** Energy spectrum of qubit with parameters $C_{\text{sh}} = 51\,\text{fF}$, $C = 5\,\text{fF}$, $E_J/h = 84.2\,\text{GHz}$, $\alpha = 0.43$. 67

2-9 **Circuit representation of a fluxonium qubit using a Josephson junction array.** 69

2-10 **Fluxonium qubit. (a)** Circuit diagram of fluxonium. **(b)** Energy spectrum of a fluxonium with parameters $E_C/h = 1.3\,\text{GHz}$, $E_L/h = 1\,\text{GHz}$, $E_J/h = 5.7\,\text{GHz}$. **(c)** Phase-space wavefunctions of the fluxonium at 0 flux, showing the first four energy states of the qubit. **(d)** Wavefunctions of the fluxonium at a half-flux quantum. 71

2-11 **Light and heavy variants of fluxonium. (a)** Energy spectrum of a light fluxonium, with parameters $E_C/h = 7.07\,\text{GHz}$, $E_L/h = 66.5\,\text{MHz}$, $E_J/h = 4.7\,\text{GHz}$ [58]. **(b)** Wavefunctions of the corresponding light fluxonium. **(c)** Energy spectrum of a heavy fluxonium, with parameters $E_C/h = 0.479\,\text{GHz}$, $E_L/h = 0.132\,\text{MHz}$, $E_J/h = 3.395\,\text{GHz}$ [109]. **(d)** Wavefunctions of the corresponding heavy fluxonium. 72

2-12 **Differential variant of a qubit. (a)** Circuit diagram of a differential fluxonium qubit. **(b)** Image of a differential fluxonium qubit in a .gds file. 74

2-13 **Qubit coupled to resonator (a)** Circuit diagram of a generic single-node qubit capacitively coupled to a readout resonator. **(b)** Image of a qubit capatively coupled to a quarter-wavelength resonator, which is in turn coupled to a transmission line. 76

2-14 **Two capacitively coupled qubits. (a)** Circuit diagram of two capacitively coupled arbitrary single-node qubits. **(b)** Image of a two capacitively coupled qubits, each in turn capacitively coupled to a resonator. 80

2-15 **Charge and flux lines. (a)** Circuit diagram of a charge line capacitively coupled to a qubit. **(b)** Circuit diagram of a flux line inductively coupled to a qubit. 81

3-1 **3D illustration of the Josephson junction loop of a C-shunt flux qubit.** 90

3-2 **Schematic drawing of a section of the junction loop in our experiment.** Current is flowing along the z-direction and we plot the numerically simulated current distribution J_z/I_0 at its cross-section, normalized to a reference current I_0. Simulation parameters are a standard design with wire width $W = 1\,\mu\text{m}$ and film thickness $b = 190\,\text{nm}$. In order to compute the magnetic field on the surface of the strip (blue) that enters in the flux noise model Eq. (3.9), we use Biot-Savart's law. 91

3-3 **Numerical simulation results for various film thicknesses b.** We plot the numerical value $\mu_0^{-2} \int B^2(x)/I^2\, dx$ which enters the model for magnetic flux noise in Eq. (3.9), replacing the analytic approximation. The purple lines and circles show the results for only considering the top surface of the loop and the red lines with triangles show the result for both the top surface and the side faces summed. The analytic approximation is given as a black line. **(a)** Results for a very thin aluminum thickness $b = 20\,\text{nm}$, where the numerical simulation agrees with the analytic formula for $W \gg b, \lambda$. **(b)** Results for the thickness $b = 190\,\text{nm}$ as used in our experiment. **(c)** The analytic expression breaks down entirely for a thick film with $b = 800\,\text{nm}$, while the numerical result indicates a reduced noise sensitivity as compared to smaller wire thicknesses. 93

3-4 **Noise spectroscopy device. (a)** Each chip holds ten uncoupled capacitively shunted flux qubits with individual readout resonators, featuring five different junction loop geometries at a two-fold redundancy. **(b)** Optical micrograph of one of the qubits and part of its readout resonator. The capacitive shunt is colored in blue. **(c)** Electron microscope image of a fabricated C-shunt junction loop. **(d)** Schematic representation of the loop parameters varied across different designs. The loop dimensions X, Y are measured along the inner edge of the SQUID, W is the width of the superconducting leads, and b is the film thickness. **(e)** Effective schematic for one qubit-resonator pair coupled to the common transmission line (TL). 96

3-5 **Experimental technique used for noise spectroscopy. (a)** Qubit spectrum around its flux sweet spot at $\Phi = \Phi_0/2$. A hyperbolic fit enables us to numerically extract the slope $(2\pi)^{-1}\partial\omega/\partial\Phi$ of the spectrum. **(b)** Spin echo dephasing traces at three illustrative locations of the spectrum (indicated by the arrows). **(c)** By plotting the extracted pure dephasing rates Γ_ϕ^{E} as a function of the spectrum slope, we can extract the $1/f$ flux noise amplitude $\sqrt{A_\Phi}$ from a linear fit. 98

3-6 **1D plots of flux noise against perimeter and width.** Flux noise amplitudes $\sqrt{A_\Phi}$ as a function of SQUID geometry parameters for **(a)** constant wire width W and **(b)** constant inner perimeter $2X + 2Y$. Each line corresponds to an independent fit in this two-dimensional parameter space to the analytic approximation (black) and numeric variations (purple and red) of the model (see inset). 100

3-7 **2D plots of flux noise against perimeter and width. (a)** $\sqrt{A_\Phi}$ as a function of the effective width $\langle W \rangle$ and perimeter P based on a fit to the numeric model taking into account all relevant interfaces (red lines in Fig. 3-6). **(b)** Data points show experimentally investigated parameter combinations with relative deviations from the same numerical model color-coded. 103

4-1 **Resonator shift from a fluxonium.** **(a)** Simulation of the resonator frequency with the fluxonium in $|0\rangle$ (blue) and $|1\rangle$ (gray). **(b)** Experimental spectroscopy of the resonator capacitively coupled to a fluxonium. Colors indicate the magnitude of transmission through the resonator. 109

4-2 **Resonator shift dependent on qubit state.** **(a)** Illustration of the magnitude response of a resonator dependent on the qubit state. **(b)** Illustration of the phase response of a resonator dependent on the qubit state. We note that these illustrations are specific to a hanging resonator geometry. 110

4-3 **Two-tone spectroscopy of a fluxonium qubit.** **(a)** Two-tone spectroscopy of fluxonium qubit as a function of the external flux. **(b)** Same data with fits overlaid. Qubit has extracted Hamiltonian parameters $E_C = 1.51\,\text{GHz}$, $E_L = 1.05\,\text{GHz}$, $E_J = 6.09\,\text{GHz}$. Legend indicates transitions between the correspond qubit states. The notation "/2" indicates a two-photon transition, and the text "res" indicates that a photon is additionally added to the resonator. 111

4-4 **Pulse diagram for different readout configurations.** **(a)** Standard measurement and readout sequence. Pulses are played on a repeated trigger so that the time between the trigger's start and the readout's start is kept constant. **(b)** Single-readout post-selection sequence, also known as heralding. Each readout pulse simultaneously sets the initial state for the subsequent qubit pulses and records the measurement outcome of the previous qubit pulses. To herald the fluxonium ground (excited) state $|0\rangle$ ($|1\rangle$), we only accept measurement results for which the previous readout result was $|0\rangle$ ($|1\rangle$). **(c)** Two-pulse post-selection (heralding) technique. The first readout is used to initialize the qubit state, and the second is used to measure the result of the qubit pulses. This extra readout pulse allows for an additional buffer time τ_3 without impacting the fidelity of the state preparation. 113

4-5 **Repeated single-shot readouts at the fluxonium sweet spot.** **(a)** Histogram of 30,000 digitized single-shot readouts. **(b)** Time series of the in-phase component (I), showing the first 2,000 single-shot readouts. The plot resembles a telegraph signal associated with the qubit switching states. 114

4-6 **Microwave Cooling.** **(a)** Level diagram of the microwave cooling protocol. Two simultaneous drives transfer population from the qubit $|1\rangle$ and $|2\rangle$ states into $|0\rangle$ by using the resonator decay. **(b)** Experimental scan of each of the two drives frequencies. The diagonally sloped resonance corresponds to the two-photon transition $|1\rangle_{\text{qb}}|0\rangle_{\text{res}} \rightarrow |0\rangle_{\text{qb}}|1\rangle_{\text{res}}$, and the horizontal resonance corresponds to the one-photon transition $|1\rangle_{\text{qb}}|0\rangle_{\text{res}} \leftrightarrow |2\rangle_{\text{qb}}|0\rangle_{\text{res}}$. Red correlates with larger population in the qubit ground state after application of the microwave drives. 116

4-7 **Fluxonium single-shot readout histograms with and without microwave cooling.** **(a)** Single-shots without microwave cooling. There is a large distribution of both $|0\rangle$ and $|1\rangle$ states due to the thermal population. **(b)** Single-shots with microwave cooling prior to each readout, which transfers population into ground state. 117

4-8 **Illustration of time-domain measurements.** Prior to each pulse sequence, the qubit is initialized in $|0\rangle$. **(a)** Rabi oscillations measured as a function of amplitude. Alternatively, these oscillations can be measured as a function of pulse duration. **(b)** T_1 measurement by initializing the state into $|1\rangle$ with a pi-pulse. Since low-frequency fluxonium qubits have considerable thermal population, a T_1 measurement can also be performed without a pi-pulse. In that case, there will be a decay from $|0\rangle$ to the thermal equilibrium state. **(c)** Ramsey oscillations as a function of time to measure T_2^R. **(d)** Spin-echo decay measured as a function of time. 119

4-9 **Illustrative diagrams for randomized benchmarking (a)** Block diagram for standard randomized benchmarking. **(b)** Block diagram for interleaved randomized benchmarking, with the interleaved gate denoted 'Gate'. 123

4-10 **Single-qubit X_π calibration procedure. (a-c, g-i)** Measurement pulse sequences for panels **(d-f, j-l)** respectively. **(d)** Ramsey vs. bias voltage measurement in order to precisely determine the voltage corresponding to $\Phi_{\text{ext}} = 0.5\,\Phi_0$ (termed the "sweet spot"). **(e)** Calibrating the readout I and Q coordinates for the fluxonium $|0\rangle$ and $|1\rangle$ states. **(f)** Low-power spectroscopy of the qubit to precisely determine the qubit frequency. **(j)** DRAG calibration of the qubit. We play a varying even number of X_π pulses with alternating amplitude while also varying the DRAG scaling. **(k)** A more precise DRAG calibration. **(l)** A pulse train consisting of an odd number of X_π pulses to precisely calibrate the amplitude of the pulse. **(m)** Calibration flowchart for single-qubit gates. Panels are shown for all calibrations starting from the precise sweet spot calibration. 125

5-1 **Device overview and gate principle. (a)** Simplified circuit schematic of two fluxonium qubits (red) capacitively coupled to a tunable-transmon coupler (blue). **(b)** False-colored optical micrograph of the two fluxonium qubits and the transmon along with their readout resonators, charge lines, and local flux lines. Arrays of 102 Josephson junctions in series form the fluxonium inductances. **(c)** Energy level diagram illustrating the principle of the CZ gate. In practice, levels $|201\rangle$, $|102\rangle$, and $|111\rangle$ are highly hybridized, and selectively driving any of these transitions results in a CZ gate. 134

5-2 ***ZZ*-reduction in the FTF architecture. (a)** A perturbative treatment of the couplings J_{ij} shows energy shifts in FTF to be dominated by virtual transitions (dashed arrows) of second (dark purple), third (light purple), and fourth (pink) order between the fluxonium qubits (maroon circles) and the coupler (blue circle). **(b)** Numerical simulation of ζ as a function of $J_c = J_{1c} = J_{2c}$ and J_{12} with the experimentally extracted qubit parameters. With the coupler, a ratio of coupling strengths always exists that minimizes ζ (dark gray). **(c)** Plot of ζ along the "Minimum ZZ" parabola in (a), as a function of J_{12}. The black curve shows a numerical diagonalization of the Hamiltonian, which is accurately described by 4th order perturbation theory (red). Without the coupler (gray), $|\zeta|$ is roughly an order of magnitude larger for this range of coupling strengths. 137

5-3 **Numerical simulations of ζ in the FTF system. (a)** Measured and simulated ζ as a function of the coupler flux for the experimental device parameters. The ZZ rate remains nearly constant between -1.5 and $-2.7\,\mathrm{kHz}$. **(b)** Numerical simulation of ζ as a function of the coupler frequency. The Device A parameters from Table 5.1 are used, except the effective transmon E_J is changed to vary the transmon frequency. As this frequency increases, $|\zeta|$ decreases asymptotically to below $10\,\mathrm{Hz}$ for this set of device parameters. 139

5-4 **Simplified circuit model of FTF circuits. (a)** FTF circuit with a grounded transmon. The capacitance network is simplified for the purpose of a theoretical analysis, with no direct fluxonium-fluxonium capacitance. **(b)** Same circuit except with a differential transmon coupler. 141

5-5 **A detailed wiring schematic of the experimental setup.** 144

5-6 **Single-qubit benchmarking on our multi-qubit device. (a)** Average single-qubit gate fidelities obtained by individual and simultaneous Clifford randomized benchmarking as a function of pulse width. **(b-c)** Individual (I) and simultaneous (S) RB traces of a 18 ns gate (purple box in (a)) for qubit 1 and qubit 2, respectively. Individual and simultaneous average gate fidelities have a standard error of about 3×10^{-6} for qubit 1 and 4×10^{-6} for qubit 2. The larger error bars in the qubit 2 data arise from coherent errors, which begin to overtake the incoherent errors for gates shorter than 18 ns (red points in (a)). . 148

5-7 **Two-tone spectroscopy of the higher energy levels of the FTF system.** Panels **(a-d)** consist of the same spectroscopy run post-selecting for $|000\rangle$, $|100\rangle$, $|001\rangle$, or $|101\rangle$ respectively. **(d)** Shows the relevant transitions for driving the CZ gate in our experiment. 150

5-8 **Driven dynamics of CZ gate (a)** Illustration of how gates were driven in this experiment. Simultaneous frequency-locked pulses were applied to the charge lines of each fluxonium. **(b)** Time-domain Rabi oscillations of the $|101\rangle \leftrightarrow |102\rangle$ transition as a function of the drive frequency. The faint chevron pattern at 4.52 GHz arises from the $|001\rangle \leftrightarrow |002\rangle$ transition and is visible due to imperfect state initialization. . . 151

5-9 **CZ Gate calibration procedure.** **(a-c)** Pulse sequences for **(d-f)** respectively. The double arrow in (c) indicates that the same pulse sequence was performed twice, with qubits 1 and 2 exchanged. **(d)** Calibrating the global amplitude of the CZ drive by minimizing the leakage. **(e)** Calibrating the frequency of the CZ drive by measuring a conditional phase accumulation via Ramsey-like measurements. Each gate should contribute a 180° conditional phase shift. **(f)** Measuring the single-qubit phase accumulations per CZ gate using the same Ramsey-like measurements. **(g)** Graphical illustration of the full two-qubit calibration routine. When recalibrating the system for small flux drifts or periodic check-ins, we found it unnecessary to recalibrate the relative drive amplitude or phase. 152

5-10 **CZ gate fidelities versus operation frequency.** All gate fidelities were obtained from interleaved randomized benchmarking, averaging over 20 random seeds. CZ gates used a fixed 100 ns cosine pulse envelope, driving each transition in Fig. 5-7(d) across the entire $0.5 - 1\,\Phi_0$ range, linearly sampled over 21 points. A secondary device (Device B) with slightly different Hamiltonian parameters shows the reliability of our architecture. Points with fidelity below 98.9% correspond to failures in the automated calibration and are therefore excluded from the plot. All gate fidelities were obtained from interleaved randomized benchmarking averaged over different 20 randomizations, with error bars corresponding to the standard error. 153

5-11 **Alternate plotting of RB vs. Flux data.** Gate fidelities with a fixed 100 ns pulse width as a function of the coupler flux for Device A **(a)** and **(b)**. The drive frequency is plotted in gray, represented on the right axis. All points missing from the full set of 21 correspond to more severe calibration failures. 154

5-12 **Qubit coherences in Device A with both qubits biased at half-flux-quantum**. Panels **(a)**, **(b)**, **(c)** show the T_1, Ramsey, and echo decay times respectively as a function of the coupler flux. All decays were fit to an exponential and measurements were performed over a 12 hour period. 156

5-13 **CZ gate optimization. (a)** Gate fidelities as a function of the width of the cosine pulse envelope. The $|101\rangle \leftrightarrow |102\rangle$ transition was used at $\Phi_{\text{ext,c}} = 0.575\,\Phi_0$. Benchmarking traces are averaged over 20 randomizations. **(b)** Standard and interleaved randomized benchmarking trace corresponding to the 85 ns data point. 157

5-14 **Reinforcement learning process.** Fidelity of an interleaved randomized benchmarking sequence with 28 Cliffords using trial CZ gates sampled from the policy of a model-free reinforcement learning agent. After each epoch, the measurement results were used to update the agent's policy according to the PPO algorithm. 158

5-15 **Reinforcement training and testing run.** In a full training run, the agent was first seeded with a 50 ns cosine pulse, with an amplitude determined by a physics-calibrated 60 ns gate (black diamond) but scaled by 60/50. Then, the agent was trained to optimize the sequence fidelity of the 50 ns pulse. The learned gate was then repeatedly evaluated using interleaved randomized benchmarking averaged over 10 randomizations. The next round of training was seeded with the optimized pulse from the previous round. Horizontal bars indicate the averaged fidelity after each round of training. All uncertainties correspond to the standard error of the mean. 159

5-16 **Optimized gate results. (a)** Optimized pulse shape as learned by the agent. The agent was given control over six evenly-spaced $I(t)$ and $Q(t)$ voltage points (colored circles), with the pulse in between points determined by a cubic interpolation. Inset shows the Fourier transform of $I(t) + iQ(t)$. **(b)** Reference and interleaved randomized benchmarking curves averaged over all 70 randomizations after the second round of training (orange points in Fig. 5-15). 160

5-17 **Relative drive amplitude and phase calibration. (a, b)** Pulse sequences for (d-f) respectively. π-pulses before measurement are purely for increasing signal contrast. **(c)** Rabi oscillation of the unwanted transition with a frequency-locked drive on each charge line. The phase difference was scanned to show destructive (white dashed line) and constructive interference. **(d)** With $\phi_2 - \phi_1$ specified to give destructive interference, the relative amplitudes of the two drives were scanned for *complete* destructive interference (white dashed line). **(e)** The value of $\phi_2 - \phi_1$ that gave destructive interference was extracted as a function of drive frequency. The linear fit is motivated by a cable length difference. **(f)** Calibration flowchart for the illustrated procedure. . . 163

5-18 **Selected data from Device B. (a)** Repeated T_1 measurements of fluxonium 2 over a roughly nine-hour time span. The dashed blue line indicates the median T_1 of 1.26 ms, and the blue shaded region encompasses ± 1 standard deviations. **(b)** Individual (I) and simultaneous (S) randomized benchmarking for both qubits, varying the width of a cosine pulse envelope. **(c)** Measured ZZ-interaction strength as a function of the coupler flux. **(d)** Spectroscopy of the non-computational states which activate the two-qubit gate. **(e)** CZ fidelities with varying pulse width, driving the $|101\rangle \leftrightarrow |111\rangle$ transition at $\Phi_{\text{ext,c}} = 0.063$. **(f)** Reference and interleaved randomized benchmarking trace averaged over 20 random seeds for a pulse width of 60 ns. 169

A-1 **Capacitance network model of a junction array. (a)** Model of a junction array with capacitance C_J between junctions and C_g between each junction to ground **(b)** Capacitance network after application of the delta-star transformation to the circuit subsections circled in red. The new capacitance network has the exact same form except with different capacitance values C'_J, C'_g and an accumulating capacitance to ground at the end nodes of the junction chain. 175

A-2 **Numerical computational of ground capacitance.** The exact recurrence relation is numerically evaluated as a function of N_JJ for three different values of $C_\mathrm{J}/C_\mathrm{g}$. The gray dashed line corresponds to the small junction limit, and the colored dashed lines represent to the corresponding infinite junction limit. 177

A-3 **Maxwell DC electromagnetic simulation of FTF device. (a)** Imported .gds file corresponding to the capacitance network of the FTF design. **(b)** Simulated capacitance matrix in units of fF. Diagonal entries are total summed capacitances touching the node, and off-diagonal entries are the negative of the capacitance between the two corresponding nodes. 179

A-4 **Sonnet resonator simulations. (a)** Sonnet screenshot setting up scattering matrix simulations of the resonator probed at the input of the feed line. **(b)** The normalized derivative of the phase of $S_{11}(\omega)$ fitted to a Lorentzian. 184

A-5 **Sonnet Purcell filter simulations. (a)** Screen shot of simulation setup for one resonator. **(b)** Fitting to $\angle S_{11}(\omega)$ to extract all relevant parameters. 185

A-6 **Sonnet mutual inductance simulations.** Screenshot of simulation setup for one flux line - qubit pair. 186

A-7 **Sonnet simulation for loss into local lines (a)** Simulation setup for the loss into the qubit 1 charge line by qubit 1. The qubit is modeled as a harmonic oscillator with the correct capacitance and resonance frequency. **(b)** Lorentzian fit to the derivative of the phase of $S_{11}(\omega)$. 186

A-8 **Sonnet simulation to extract the qubit capacitances.** Simulation setup probing the resonance of qubit 1 by placing a lumped element inductor between the qubit 1 capacitor pads and measuring the reflection at the qubit 1 resonator port. 188

A-9 **Sonnet simulation to extract qubit-qubit coupling strengths.** **(a)** Simulation setup with qubits 1 and 2 modeled as harmonic oscillators using lumped element inductors. The microwave reflection coefficient can be measured through either port 2 or port 3. **(b)** Avoided crossing between the two qubits as one of the qubit inductances is scanned. **(c)** The difference between the two dressed harmonic oscillator frequencies as the inductance of one of them is scanned. The points are fit to a hyperbola to extract the avoided crossing size. **(d)** The mean frequency as a function of the inductance to extract the bare frequency on resonance. 190

A-10 **Sonnet simulation to extract qubit-resonator coupling strengths.** **(a)** Simulation setup with resonator 1 coupled to qubit 1. The qubit 1 inductance is scanned until qubit 1 goes through resonance with resonator 1. **(b)** Avoided crossing between the qubit and resonator as the inductance is scanned. **(c)** The difference between the two dressed frequencies as the inductance is scanned. **(d)** The mean frequency of the two resonances as the inductance is scanned to extract the bare frequency on resonance. 191

List of Tables

2.1 **Table of formulas used in this section.** 57

3.1 **Complete dataset for all qubits measured in this experiment.** For each qubit, we list the junction loop geometry parameters X, Y, and W, the qubit transition frequency $\omega/2\pi$ at the optimal bias point, the average relaxation time $\bar{T}_1$ in the measured region of the spectrum, and the extracted noise amplitudes $\sqrt{A_\Phi}$ left and right of the optimal bias point. Missing values are due to a faulty qubit, electric two-level system modes cutting through the qubit spectrum, or have not been measured. 105

3.2 **Measured data of six qubits on one sample with either a floating or grounded shunt capacitor.** All other parameters were otherwise kept identical. The data show no trend in the noise amplitudes extracted for the different layouts, indicating that the noise amplitude values are not dependent on qubit architecture but only on the junction loop geometry. For each measured qubit, we list the loop geometry parameters X, Y, and W, the qubit transition frequency $\omega/2\pi$ at the optimal bias point, the average relaxation time $\bar{T}_1$ in the measured region of the spectrum, and the extracted noise amplitudes $\sqrt{A_\Phi}$ left and right of the optimal bias point. Missing values have not been measured. 106

5.1 **Characterization of FTF devices.** Hamiltonian parameters for both Device **A** and Device **B** were obtained by fitting two-tone spectroscopy data and the static ZZ rate vs. coupler flux. Coherence times were measured by biasing each fluxonium at $\Phi_{\text{ext}} = 0.5\,\Phi_0$ using only the global flux bias. Unless otherwise stated, all data corresponds to Device A. 133

5.2 **Summary of control equipment.** The manufacturers and model numbers of the control equipment used for this experiment. 145

Chapter 1

Introduction

With the rapidly growing prevalence of quantum computing and outburst of quantum funding programs, the first question one asks is why quantum computing is so important in the first place. Simply put, nature solves some complex problems more efficiently than a modern computer, which performs various tasks by shuttling electrons back and forth across billions of transistors. An ocean wave knows how it will ripple, a tree knows how it will grow, and a snowflake knows how it will crystallize faster and more accurately than our laptops can predict. In this regard, quantum computing is not so dissimilar to controlling and observing other complex natural processes.

Unfortunately, the above examples lack a more practical benefit that would compel them to be developed into a mature technology. A more concrete and controllable natural phenomenon is the behavior of light as it passes through a lens. The light at the back focal plane of a lens is directly related to the light at the front focal plane by the Fourier transform [11]. The Fourier transform happens to be one of the most important algorithms in all of computing, and shining light through a lens provides a way to compute the Fourier transform at literally the speed of light. Despite the practical benefits and obvious computational advantage, Fourier transforms are still typically calculated on everyday computers, rather than lenses. In large part, this is because the Fourier transform has a polynomial time complexity (the total computation time scales as a polynomial function of the size of the input) and therefore, any

alternative mode of its computation offers only a polynomial time speedup. The price to pay for reinventing precise computations on a different platform is typically not worth the benefit of a slightly improved computational complexity. It is for this reason that quantum computing is fundamentally different and so sought after. By taking advantage of the properties of quantum mechanical two-level systems (quantum bits, known as qubits), quantum computing offers an *exponential* speedup over the best known classical algorithms for certain classes of problems. Most famously, Shor's algorithm [90] provides a polynomial time algorithm to factor an integer into a product of primes using a theoretically functional quantum computer. Implementation of such an algorithm would have immediate and drastic implications for cryptography and security. Quantum computing can also be used to simulate and study the exact physics of molecules — typically a prohibitively hard task which would aid in drug discovery and medicine.

In this Chapter, we introduce the theoretical foundation of quantum mechanics and how it applies to quantum information science — the study of the properties and consequences of quantum computing assuming perfectly functional qubits. We then pay tribute to the field of atomic physics and use its machinery to understand how these qubits are controlled, creating quantum gates. In this thesis work, we develop the relatively less established fluxonium superconducting qubit [56] for use in quantum computation and demonstrate world-class qubit and gate performance at a two qubit scale.

1.1 Quantum Information Science

The theoretical study of quantum computing, known as quantum information science, involves representing a **qubit**, or a equivalently a **two-level system**, as a column vector

$$|\psi\rangle = c_0 |0\rangle + c_1 |1\rangle \equiv \begin{bmatrix} c_0 \\ c_1 \end{bmatrix}, \tag{1.1}$$

where $|c_0|^2 + |c_1|^2 = 1$ is the normalization condition, with $c_0, c_1 \in \mathbb{C}$. Likewise, the representation of two qubits is the matrix tensor product of the individual column vectors

$$|\psi_1\rangle \otimes |\psi_0\rangle = (a_0 |0\rangle + a_1 |1\rangle) \otimes (b_0 |0\rangle + b_1 |1\rangle) = \begin{bmatrix} c_{00} \\ c_{01} \\ c_{10} \\ c_{11} \end{bmatrix}. \tag{1.2}$$

Classically, each "bit" can only take on a value of 0 or 1, but a qubit can take on any normalized complex linear combination of 0 and 1. This continuum of possible states if often represented on a **Bloch sphere** [Fig. 1-1], where $|0\rangle$ is located on top, $|1\rangle$ at the bottom, and all other points on the surface of the sphere represent coherent combinations, known as **superpositions**, of these two states. For example, the intersection of the Bloch sphere with the $+\hat{x}$ axis represents the $\frac{1}{\sqrt{2}}(|0\rangle + |1\rangle)$ state, and the intersection of the Bloch sphere with the $+\hat{y}$ axis represents the $\frac{1}{\sqrt{2}}(|0\rangle + i\,|1\rangle)$ state. This property of superposition is a primary reason why computing with qubits allows for an exponential speedup over classical binary bits. For a more thorough introduction to qubits and specific algorithms that offer a quantum speedup, I point the interested reader to the bible of quantum information by Nielsen and Chuang [69].

1.1.1 Single-Qubit Gates

We can also consider operations on qubits using this same Bloch sphere picture. By rotating an initial state by some angle along some axis through the origin, we arrive at another state on the Bloch sphere. In fact, there exists a one-to-one mapping between all unitary qubit operations and Bloch sphere rotations about an axis through the origin. Explicitly, a rotation about axis $\hat{r} \in \mathbb{R}^3$ of angle θ is given by the unitary

$$R_{\hat{r}}(\theta) = e^{-i(\theta/2)\sigma_{\hat{r}}} = \cos(\theta/2)I - i\sin(\theta/2)\sigma_{\hat{r}} \tag{1.3}$$

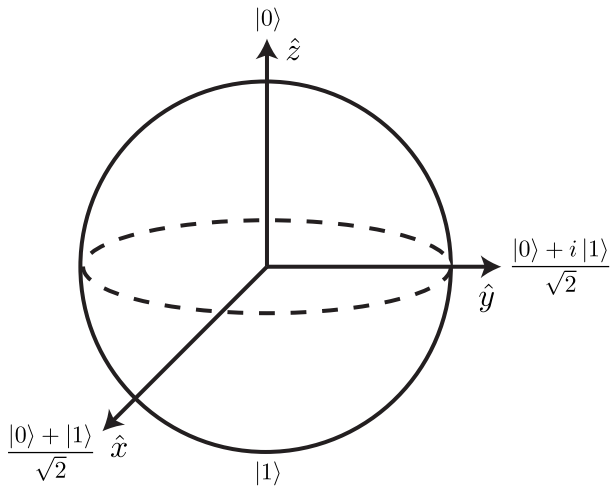

Figure 1-1: **Illustration of the Bloch sphere.** The surface of the Bloch sphere represents all possible superpositions of $|0\rangle$ and $|1\rangle$.

where $\sigma_{\hat{r}} \equiv \hat{r} \cdot (\sigma_x, \sigma_y, \sigma_x)$. These σ matrices are known as the **Pauli matrices**, defined as

$$\sigma_x = \begin{bmatrix} 0 & 1 \\ 1 & 0 \end{bmatrix}, \qquad \sigma_y = \begin{bmatrix} 0 & -i \\ i & 0 \end{bmatrix}, \qquad \sigma_z = \begin{bmatrix} 1 & 0 \\ 0 & -1 \end{bmatrix}. \tag{1.4}$$

Some examples of common single-qubit gates are the X_π gate (rotation about the $+\hat{x}$-axis by π radians), Y_π gate (rotation about $+\hat{y}$ by π radians), Z_θ gate (rotation about $+\hat{z}$ by θ radians), and the **Hadamard (H)** gate (rotation about $\frac{1}{\sqrt{2}}(\hat{x} + \hat{z})$ by π radians):

$$X_\pi = \begin{bmatrix} 0 & -i \\ -i & 0 \end{bmatrix} \tag{1.5}$$

$$Y_\pi = \begin{bmatrix} 0 & -1 \\ 1 & 0 \end{bmatrix} \tag{1.6}$$

$$Z_\theta = \begin{bmatrix} e^{-i\theta/2} & 0 \\ 0 & e^{i\theta/2} \end{bmatrix} \tag{1.7}$$

$$H = \frac{1}{\sqrt{2}} \begin{bmatrix} 1 & 1 \\ 1 & -1 \end{bmatrix}. \tag{1.8}$$

Colloquially, rotations about the $+\hat{x}$-axis or $+\hat{y}$-axis by π radians are known as **pi-pulses**, and rotations by $\pi/2$ radians are likewise known as **pi-half pulses**.

1.1.2 Two-Qubit Gates

When moving beyond a single-qubit, the Bloch sphere representation can no longer be so conveniently used, and one must rely more heavily on mathematical formalisms or other intuition. Two-qubit gates are loosely defined as a reversible gate operation (matrix multiplication) on two-qubits which cannot be factored into a tensor product of single-qubit gates on each respective qubit. These gates are said to be **entangling**, as the effect of the gate on one qubit will depend on the state of the other qubit. The resultant two-qubit state will therefore be an entangled state, in which the measured state of each qubit influences the state of the other. For superconducting qubits, three of the most most commonly implemented two-qubit gates are the CNOT, iSWAP, and CZ gates:

$$\text{CNOT} = \begin{bmatrix} 1 & 0 & 0 & 0 \\ 0 & 1 & 0 & 0 \\ 0 & 0 & 0 & 1 \\ 0 & 0 & 1 & 0 \end{bmatrix}, \quad \text{iSWAP} = \begin{bmatrix} 1 & 0 & 0 & 0 \\ 0 & 0 & i & 0 \\ 0 & i & 0 & 0 \\ 0 & 0 & 0 & 1 \end{bmatrix}, \quad \text{CZ} = \begin{bmatrix} 1 & 0 & 0 & 0 \\ 0 & 1 & 0 & 0 \\ 0 & 0 & 1 & 0 \\ 0 & 0 & 0 & -1 \end{bmatrix}, \tag{1.9}$$

where the matrix indices represent, in order, the basis states $\{|00\rangle, |01\rangle, |10\rangle, |11\rangle\}$. The CNOT gate inverts the population of the second qubit depending on the state of the first qubit and is natively implemented using the cross-resonance gate scheme [81]. The iSWAP gate swaps the populations between the two qubits and introduces an additional i phase between the swapped states and can be implemented by either tuning two qubits onto resonance for a period of time [54] or by parametrically driving at the frequency difference between the two qubits [78]. Finally, the CZ gate introduces a selective phase shift on the $|11\rangle$ state of the system, traditionally implemented by tuning the $|11\rangle$ state into a non-computational state of the system [8], or by driving it to a non-computational state of the system [18]; in each case, a single-period popu-

lation oscillation is used. Conveniently, any two-qubit gate can be converted into any other two-qubit gate by application of arbitrary single-qubit gates [69]. For example, the CZ gate can be converted into the CNOT gate by applying Hadamard gates on the second qubit, before and after the CZ gate. It additionally follows that arbitrary unitary operations in a multi-qubit Hilbert space can be performed by composing any one type of two-qubit gate with arbitrary single-qubit rotations [69]. This then outlines the goal of quantum control very clearly: the need for high-fidelity single-qubits gates and any one high-fidelity two-qubit gate.

1.2 Quantum Mechanics

Quantum mechanics is the study of nature at the scale of atoms or subatomic particles. It is at this small scale that the traditional laws of classical mechanics break down and no longer apply. The physical realization of our qubits and its properties will be rooted in the foundations of quantum mechanics and thus an understanding of it is essential in working with qubits of any kind. In this Section, we give a brief overview of quantum mechanics, going over the important postulates of quantum mechanics and their consequences. For a more in-depth study of quantum mechanics, I point to a few of my favorite introductory textbooks [87, 33].

1.2.1 State vectors

The state of a system can be described by a wavefunction $|\psi\rangle$ living in some Hilbert space.

In quantum mechanics, we can describe our system using the basis of energy eigenstates, with integer labels corresponding to a monotonically increasing ordering of eigenvalues

$$|\psi\rangle = c_0 |0\rangle + c_1 |1\rangle + c_2 |2\rangle + \cdots \tag{1.10}$$

These states $|\psi\rangle$ are represented as **kets** $|\psi\rangle$, which each come with a corresponding

adjoint represented as a **bra** $\langle\psi|$, and is mathematically computed as the complex conjugate of $|\psi\rangle$

$$\langle\psi| = c_0^* \langle 0| + c_1^* \langle 1| + c_2^* \langle 2| + \cdots \tag{1.11}$$

These basis states, by definition, are also **orthonormal**, meaning that they satisfy the condition

$$\langle i|\, j\rangle = \delta_{ij}. \tag{1.12}$$

Inherent in this postulate of quantum mechanics is that (properly normalized) linear combinations of two states

$$\alpha\,|\psi_1\rangle + \beta\,|\psi_1\rangle \tag{1.13}$$

are guaranteed to yield another state which lives in the same Hilbert space. This linear combination represents a **superposition** of states, one of the standout features of quantum mechanics.

1.2.2 Observables as Operators

Every observable of a state $|\psi\rangle$ is described by an operator which acts on it.

This statement provides the link between the mathematical formalism of quantum mechanics and physical properties that are observed or measured in the real world. An **operator** $\hat{O}$ maps one state $|\psi\rangle$ onto another state $|\psi'\rangle$ within the Hilbert space, and its action on the state is represented by left multiplication

$$\hat{O}\,|\psi\rangle = |\psi'\rangle\,. \tag{1.14}$$

The most common type of operator we will encounter in quantum mechanics is a **linear operator**, which for two states $|\psi_1\rangle$ and $|\psi_2\rangle$ satisfies the condition:

$$\hat{O}(a_1\,|\psi_1\rangle + a_2\,|\psi_2\rangle) = a_1(\hat{O}\,|\psi_1\rangle) + a_2(\hat{O}\,|\psi_2\rangle). \tag{1.15}$$

Associated with each operator is a set of **eigenstates** $\{|O_k\rangle\}$, which are unchanged

up to a multiplicative factor after being acted on by the operator

$$\hat{O}\,|O_k\rangle = O_k\,|O_k\rangle\,. \tag{1.16}$$

This prefactor is known as the **eigenvalue** corresponding to the eigenstate $|O_k\rangle$ for operator $\hat{O}$.

1.2.3 Quantum Measurement

A measurement in state $|\psi\rangle$ of an observable $\hat{O}$ with eigenvalues $\{O_k\}$ and eigenstates $\{|O_k\rangle\}$ results in O_k with probability $|\,\langle O_k|\psi\rangle\,|^2$. Afterward $|\psi\rangle$, is changed into $|O_k\rangle$.

The measurement of a quantum state is perhaps the most mysterious property of quantum mechanics. Contrary to classical physics, the measurement of a quantum state yields only discrete possibilities, governed by the eigenvalues of the operator $\hat{O}$. While a classical voltage can read any value between 0 V and 1 V, a qubit $|\psi\rangle = c_0\,|0\rangle + c_1\,|1\rangle$ can only be measured be in state $|0\rangle$ or $|1\rangle$. Furthermore, a quantum measurement changes the state of the system upon measurement. The state is said to be projected onto the measured state, and further measurements of the same operator will deterministically yield the same value over and over, despite this value initially being stochastically determined.

1.2.4 Time Evolution

The time evolution of a state $|\psi(t)\rangle$ obeys the Schrödinger equation

$$i\hbar\frac{d}{dt}\,|\psi(t)\rangle = \hat{H}\,|\psi(t)\rangle\,, \tag{1.17}$$

*where $\hat{H}$ is the **Hamiltonian** of the system.*

In a closed quantum system, this equation successfully predicts the time evolution of $|\psi(t)\rangle$, for all time. If $|\psi(0)\rangle$ and $\hat{H}$ are known, then all quantities of interest can be

predicted by solving integrating the Schrödinger equation and even controlled by altering $\hat{H}$. Unfortunately, it is never the case that $|\psi(0)\rangle$ and $\hat{H}$ are known to arbitrary precision, and numerical simulation of the time evolution of larger systems becomes intractable on classical computers. Nevertheless, any simplifications to the Hamiltonian, or truncations to approximately isolated smaller systems provides immense value to the engineer or physicist in predicting dynamics and building intuition. After all, the entirety of quantum computation relies on controlling the time evolution of states via the Schrödinger equation precisely and to our desire.

An extremely useful simplification can be made when $\hat{H}$ is time independent. In that case, the time evolution of the state simply involves application of a unitary operator $\hat{U}(t)$

$$|\psi(t)\rangle = \hat{U}(t)\,|\psi(0)\rangle\,, \tag{1.18}$$

where $\hat{U}$ is given by an exponentiation of the Hamiltonian

$$\hat{U}(t) = e^{-i\hat{H}t/\hbar}. \tag{1.19}$$

One can verify by substitution that this $|\psi(t)\rangle$ satisfies the time-dependent Schrödinger equation. If one can **diagonalize** the Hamiltonian by finding all its eigenvectors $\{|E_k\rangle\}$ and corresponding eigenvalues $\{E_k\}$ (alternatively termed **eigenenergies** for the operator $\hat{H}$), the computation of this matrix exponentiation may be simplified to

$$\hat{U}(t) = \sum_k |E_k\rangle\,\langle E_k|\,e^{-iE_kt/\hbar}. \tag{1.20}$$

This equation yields a very intuitive interpretation of the time dynamics of a closed quantum system: with the state decomposed into eigenvectors of the Hamiltonian, each eigenvector undergoes a phase accrual according to its eigenenergy

$$|E_k\rangle \to e^{-iE_kt/\hbar}\,|E_k\rangle\,. \tag{1.21}$$

1.2.5 Non-Unitary Dynamics

We conclude this Section with two examples of non-unitary time evolution applied to a qubit wavefunction $|\psi\rangle = c_0 |0\rangle + c_1 |1\rangle$. This state vector will preferentially decay into its minimum energy eigenstate (more generally to its thermal equilibrium state, which we approximate to be $|0\rangle$ in the limit of no thermal energy excitations) with an exponential time decay constant called $T_\mathbf{1}$. This process is termed **relaxation**. For this qubit system, the $|1\rangle$ state decays as

$$|1\rangle \rightarrow e^{-t/T_1} |1\rangle , \tag{1.22}$$

with the missing population returning to the ground state $|0\rangle$. Since all states $|\psi\rangle$ decay into $|0\rangle$ after a sufficiently long time, this process is necessarily non-unitary (cannot be reversed). In realistic quantum systems, the T_1 of a state places a time limit for which useful operations or unitary evolution must be done.

Our second example of non-unitary time evolution is **dephasing**. As mentioned previously, the phase of the $|1\rangle$ state evolves as

$$|1\rangle \rightarrow e^{-iE_1 t/\hbar} |1\rangle , \tag{1.23}$$

where this phase is referenced relative to the phase of the $|0\rangle$ state. If the energy of this eigenstate E_1 fluctuates unpredictably in time, then the phase of $|1\rangle$ relative to $|0\rangle$ gradually becomes lost in time to these fluctuations. If one imagines a statistical ensemble of these states under this energy fluctuation ΔE_1, then the time evolution of the $|1\rangle$ state can be averaged over all ensembles. Assuming a zero-mean Markovian noise processes, the time-integral of this phase factor results in an exponentially decaying phase coherence between $|0\rangle$ and $|1\rangle$ with the time constant defined as $T_\mathbf{2}$

$$\int e^{-i\Delta E_1 t/\hbar} \, dt \rightarrow e^{-t/T_2}. \tag{1.24}$$

1.3 The Rabi Oscillation

With a physical understanding of the qubit through quantum mechanics, what remains is to understand how to implement gates with these qubits in order to implement gate-based quantum computation. Generally, gates are realized by altering the Hamiltonian of a system in a precise manner and for a precise amount of time such that the total unitary operation becomes our desired gate. Controlling two-level systems in this way was originally studied in the field of atomic physics [31, 19], the study of how atoms behave when interacting with light or other atoms. While there are many ways to engineer the Hamiltonian to perform gates, I choose here to derive the **Rabi oscillation**, the simplest and most widespread method to arbitrarily control the state of a qubit. In this derivation, we will use the shared language of atomic physics and introduce many other indispensable concepts, such as the rotating frame transformation, the rotating wave approximation, and the generalized Rabi frequency.

Consider a semi-classical treatment in which the lowest two levels on an atom (the ground state $|0\rangle$ being the zero energy reference)

$$\hat{H}_0 = \hbar\omega \, |1\rangle \langle 1| \tag{1.25}$$

are driven by a classical oscillating electric field

$$E(t) = \mathcal{E} e^{-i\omega_d t} + \mathcal{E}^* e^{i\omega_d t}. \tag{1.26}$$

This electric field interacts with the atomic dipole of the two-level system,

$$\hat{d} = |1\rangle \langle 0| \, \mu + |0\rangle \langle 1| \, \mu^*, \tag{1.27}$$

where μ is the dipole matrix element $\langle 1| \, \hat{d} \, |0\rangle$. The full classically driven Hamiltonian is then

$$\hat{H} = \hbar\omega \, |1\rangle \langle 1| - (|1\rangle \langle 0| \, \mu + |0\rangle \langle 1| \, \mu^*)(\mathcal{E} e^{-i\omega_d t} + \mathcal{E}^* e^{i\omega_d t}). \tag{1.28}$$

To more easily understand the dynamics of the system, it is customary perform

a **rotating frame transformation** to move into a frame where the Hamiltonian becomes time independent. Mathematically, this involves applying the transformation

$$\tilde{H} = \hat{U}\hat{H}\hat{U}^{-1} - i\hbar\hat{U}\frac{\partial\hat{U}^{-1}}{\partial t} \tag{1.29}$$

where in this specific case, we choose

$$\hat{U} = e^{i\omega_d t|1\rangle\langle 1|}. \tag{1.30}$$

The excited state is transformed into a frame rotating at the same frequency as the drive, so that the drive is largely time independent.

$$\tilde{H} = \hbar(\omega - \omega_d)\,|1\rangle\langle 1| - (\mathcal{E}\mu\,|1\rangle\langle 0| + \mathcal{E}^*\mu e^{2i\omega_d t}\,|1\rangle\langle 0| + \mathcal{E}\mu^* e^{-2i\omega_d t}\,|0\rangle\langle 1| + \mathcal{E}^*\mu^*\,|0\rangle\langle 1|) \tag{1.31}$$

After applying this transformation, we drop terms with factors $e^{\pm 2i\omega_d t}$ according to the **rotating wave approximation**, provided these oscillations are "fast" relative to the driven dynamics of the system. When this condition is satisfied, one can replace the $e^{\pm 2i\omega_d t}$ terms with their time average, which is conveniently zero. This approximation allows a final simplification of the Hamiltonian

$$\tilde{H} = \hbar\delta\,|1\rangle\langle 1| - \hbar\left(\frac{\Omega}{2}\,|1\rangle\langle 0| + \frac{\Omega^*}{2}\,|0\rangle\langle 1|\right) \tag{1.32}$$

where $\delta \equiv \omega - \omega_d$ is the **detuning** between the drive frequency and the qubit frequency, and we've introduced the very important quantity

$$\Omega = \frac{2\mathcal{E}\mu}{\hbar} \tag{1.33}$$

called the **Rabi frequency**. The condition for the rotation wave approximation can now be stated $\omega_q \gg \Omega$ in the most common case where the drive is resonant with the qubit ($\delta = 0$). To understand the physical interpretation of Ω, we solve the time dependent Schrödinger equation with the Hamiltonian Eq. (1.31) for resonant driving

($\delta = 0$) and $\Omega > 0$ (for simplicity). By inserting the ansatz

$$|\psi\rangle = c_0(t)\,|0\rangle + c_1(t)\,|1\rangle\,, \tag{1.34}$$

and assuming the initial conditions $c_0(0) = 1$ and $c_1(0) = 0$, these amplitude coefficients can be solved to obtain

$$c_0(t) = \cos\left(\frac{\Omega}{2}t\right) \tag{1.35}$$

$$c_1(t) = i\sin\left(\frac{\Omega}{2}t\right). \tag{1.36}$$

The populations themselves, $p_i(t) = |c_i(t)|^2$, are

$$p_0(t) = \frac{1}{2} + \frac{1}{2}\cos(\Omega t) \tag{1.37}$$

$$p_1(t) = \frac{1}{2} - \frac{1}{2}\cos(\Omega t). \tag{1.38}$$

As a result of this resonant drive, the population oscillates back and forth between the ground and excited states with frequency Ω. These dynamics can be visualized on the Bloch sphere as the state (initially $|0\rangle$) precessing about an axis pointing from the center of the sphere to a point on the equator. This axis is conventionally then defined as the $+\hat{x}$ axis; an alternative way of thinking about this is that this first transformation sets the phase reference for all other drives, and corresponds the $\hat{x}$-axis with a relative phase of 0. The Hamiltonian Eq. (1.31) can also be solved in the case $\delta \neq 0$, though we omit the derivation from this thesis and state the result for the population of the excited state

$$p_1(t) = \frac{\Omega^2}{\tilde{\Omega}^2}\left(\frac{1}{2} - \frac{1}{2}\cos(\tilde{\Omega}t)\right). \tag{1.39}$$

The new quantity introduced here is the **generalized Rabi frequency**

$$\tilde{\Omega} = \sqrt{\Omega^2 + \delta^2}. \tag{1.40}$$

When a two-level system is driven off-resonantly, the new rotation axis becomes the unit vector (again, defining the drive as along the $\hat{x}$-axis without loss of generality)

$$\frac{\delta\hat{z} + \Omega\hat{x}}{\sqrt{\delta^2 + \Omega^2}}. \tag{1.41}$$

As a result, the amplitude of the population oscillations decreases, but frequency of oscillations increases. This apparent increase in frequency comes about from the fact that the total traversal distance on the Bloch sphere is less when traversing a smaller circle. See Fig. 1-2 for a Bloch sphere illustration of the state trajectory with varying amounts of drive detuning.

With this, we conclude the our brief derivation of the Rabi oscillation in the traditional language of atomic physics. When we turn to superconducting qubits, the two-level system will then be the lowest two energy states of a superconducting circuit, and the driving electric field will be either a charge or flux fluctuation.

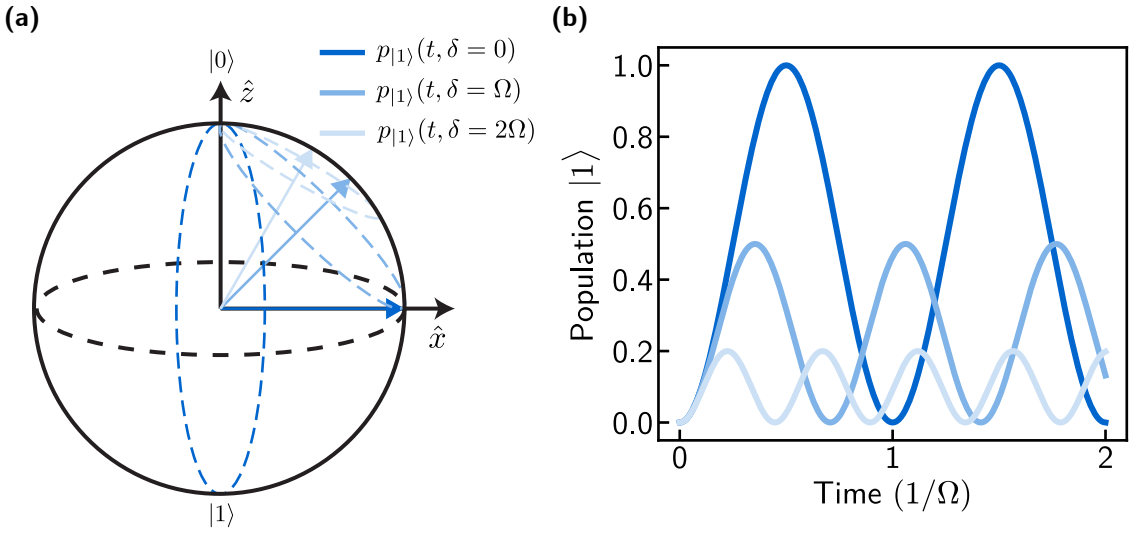

Figure 1-2: **Off-resonant Rabi oscillations. (a)** Bloch sphere trajectories for three different detunings (different shades of blue, dashed lines) and an initial state of $|0\rangle$. Solid blue arrows show the rotation axis. **(b)** Population as a function of time for the three trajectories shown in (a).

1.4 Thesis Outline

We begin the journey into the field of superconducting quantum computing in Chapter 2 by introducing the basic building blocks of circuit quantum electrodynamics. Starting from the LC oscillator, the Josephson junction is introduced to provide the critical non-linearity to convert a harmonic oscillator into a qubit. From there, general circuit quantization tools are introduced to construct the Hamiltonians of nearly arbitrary circuits, with numerical techniques to compute their eigenvalues and eigenvectors. Using these techniques, the properties of a variety of qubits are derived, in preparation for their use in later Chapters. Moving beyond a single qubit, we give a circuit QED treatment of how to model qubits coupled to other circuit elements. Together, Chapter 2 and Appendix A provide all the necessary information for simulating and designing multi-qubit circuits and serves as the theoretical foundation for much of the thesis. Chapter 2 concludes with a discussion of why qubits are not perfect in practice, with an overview of common relaxation and dephasing mechanisms ailing superconducting qubits.

In Chapter 3, we undertake a deep dive into one particular mechanism for dephasing in superconducting qubits — $1/f$ flux noise. Magnetic two-level system defects residing in the physical materials forming the circuits are observed to fluctuate and cause flux noise dephasing in any flux-tunable qubit. Despite the widespread nature of this problem, the microscopic mechanism of this $1/f$ flux noise has proven difficult to pinpoint, and treatments to completely remedy superconducting qubits of this noise source are lacking. We show that the geometric construction of the superconducting qubit loops impacts the magnitude of the flux noise, in agreement with a microscopic model of $1/f$ flux noise. Furthermore, we provide guidelines for superconducting qubit design to minimize the total amount of flux noise.

Chapter 4 begins to introduce the heart of this dissertation, by outlining basic measurements techniques for fluxonium qubits, which were all newly developed as part of this work. Section 4.1 is devoted to the readout and initialization of fluxonium qubits, made difficult by the low qubit frequency, which results in significant

population in the excited state in thermal equilibrium with even the coldest stages of our experimental setup. Without strategies to initialize the qubit in the ground or excited state, this thermal population can obstruct any and all measurements of the qubit. We then follow up with basic coherence characterization measurements of the fluxonium qubit and outline a calibration procedure for high-fidelity single-qubit gates.

The first experiment requiring these new fluxonium qubits was the FTF two-qubit gate work [24] detailed in Chapter 5. Two fluxonium qubits are coupled together via a large capacitive coupling to a tunable transmon coupler. This strong coupling and combination of qubits brings about a rich system with interesting and counterintuitive behavior. Section 5.1 introduces the theory of the FTF architecture and explores some interesting facets of the system. For example, the transmon provides a means to cancel out the static controlled-phase entangling rate (ZZ) even in the limit where the transmon-fluxonium detuning approaches infinity. Chapter 5.3 contains the results for high-fidelity single- and two-qubit fluxonium gates using the FTF system. As of the writing of this thesis, both the two-qubit fluxonium gate and the simultaneous single-qubit gates demonstrated have the highest published fidelities out of any superconducting qubit demonstration. Furthermore, we demonstrate the robustness of this gate by performing the gate across a 2 GHz range of drive frequencies and across multiple devices.

Finally, we summarize the main results of this thesis work and discuss the future prospects of the fluxonium qubit for superconducting quantum computing.

Chapter 2

Circuit QED: Building Towards a Quantum Processor

This Chapter reviews the basic elements comprising most superconducting circuits: the capacitor, the inductor, and the Josephson junction. From these, we will introduce the circuit quantum electrodynamics (circuit QED) framework to model collections of these elements as qubits (Section 2.1), and numerically obtain their eigenenergies and eigenstates (Section 2.2). Section 2.3 will derive from scratch all qubits that will be used in this thesis (the transmon, the c-shunt flux qubit, and the fluxonium) and investigate notable features of each. These qubits can then be integrated with other circuits forming resonators, control lines, and other qubits in order to build up complex quantum processors (Section 2.4). We conclude with Section 2.5, where we begin to move away from our models of idealized qubits and discuss common mechanisms that limit qubit coherence. As the details in this chapter serve as the foundation for designing and understanding any experiment, we aim to derive circuit properties as fundamentally and as exhaustively as possible.

2.1 The Circuit QED Hamiltonian

In this Section, we first introduce the tools of circuit quantization to derive the quantum harmonic oscillator from the classical LC-oscillator. From there, the Josephson

junction is introduced as the non-linear element needed to create superconducting qubits, which by itself forms the Cooper-pair-box circuit [10, 64]. We wrap up this Section by outlining procedures to write down more generic circuit Hamiltonians without needing to rely on any intuition or hindsight.

2.1.1 Classical to Quantum LC Oscillator

The starting point of our exploration are the classical quantities describing the energy stored in the capacitor and the inductor. Familiar to students taking their first E&M class, the energy stored in a capacitor is $\frac{1}{2}CV^2$ (C is the capacitance and V is the voltage across the capacitor), and the energy stored in an inductor is $\frac{1}{2}LI^2$, which we will conveniently re-write as $\frac{1}{2}\Phi^2/L$ using the classical definition of inductance, $L = \Phi/I$ (L is the inductance, I is the current through the inductor, and Φ is the magnetic flux produced by the current). By ascribing capacitive energy as kinetic energy and inductive energy as potential energy (a widespread convention that we will adopt throughout), we can then define the circuit **Lagrangian**,

$$\mathcal{L} \equiv T - V. \tag{2.1}$$

The simplest circuit with any resonant features is the LC oscillator, a capacitor and inductor in parallel. The Lagrangian for this circuit is

$$\mathcal{L} = \frac{1}{2}CV^2 - \frac{1}{2}\frac{\Phi^2}{L} \tag{2.2}$$

which we write down by using the previously defined energies. Using Φ as our generalized position coordinate, we rewrite the Lagrangian in terms of it and its time derivative as

$$\mathcal{L}(\Phi, \dot{\Phi}) = \frac{1}{2}C\dot{\Phi}^2 - \frac{1}{2L}\Phi^2, \tag{2.3}$$

where we've used Faraday's Law to relate the voltage to the time derivative of the flux. From the Lagrangian, the corresponding canonical momentum to Φ is defined

as

$$\frac{\partial \mathcal{L}}{\partial \dot{\Phi}} = C\dot{\Phi} \equiv q. \tag{2.4}$$

Conveniently, this quantity physically represents the charge stored in the capacitor. We emphasize that it is the quantity $\partial\mathcal{L}/\partial\dot{\Phi}$ which defines conjugate momentum, and not the charge itself. By performing a Legendre transformation, we arrive at the classical circuit Hamiltonian and express it in terms of the generalized position and momentum variables

$$H \equiv \dot{\Phi}q - \mathcal{L} \tag{2.5}$$

$$= \frac{1}{2}C\dot{\Phi}^2 + \frac{1}{2}L\Phi^2 \tag{2.6}$$

$$= \frac{1}{2}\frac{q^2}{C} + \frac{1}{2}\frac{\Phi^2}{L} \tag{2.7}$$

At this point, we are ready to promote our classical Hamiltonian into a quantum one. This works as follows: we promote the Hamiltonian, charge coordinate, and flux coordinate into operators $H \to \hat{H}$, $q \to \hat{q}$, $\Phi \to \hat{\Phi}$, then establish a commutation relation between $\hat{q}$ and $\hat{\Phi}$. Following [25], the quantum commutation relation between two operators $\hat{A}$, $\hat{B}$ is related to the classical Poisson bracket

$$[\hat{A}, \hat{B}] \equiv i\hbar\{A, B\}. \tag{2.8}$$

Using the fact that the classical Poisson bracket between two canonically conjugate variables is invariant under canonical transformations and is equal to 1, we obtain our commutation relation

$$[\hat{\Phi}, \hat{q}] = \hat{\Phi}\hat{q} - \hat{q}\hat{\Phi} = i\hbar. \tag{2.9}$$

From this point forward, the standard procedure to analytically diagonalize the quantum harmonic oscillator is to introduce two new operators, $\hat{a}$ and $\hat{a}^\dagger$, defined as

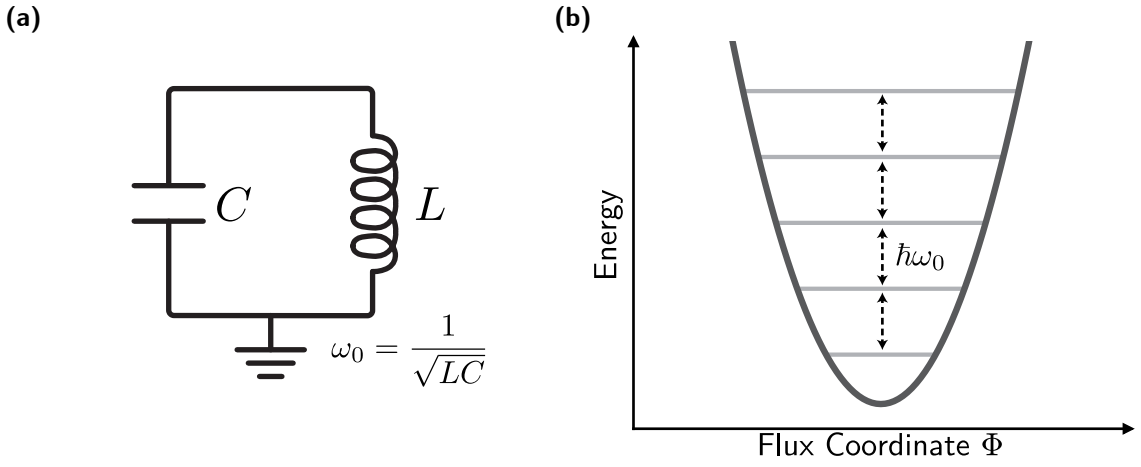

Figure 2-1: ***LC* oscillator. (a)** Circuit representation of a LC oscillator. **(b)** Plot of parabolic potential energy of an LC oscillator along with associated energy levels.

linear combinations of the original operators

$$\hat{q} = -i\sqrt{\frac{\hbar}{2Z_0}}(a - a^\dagger) \tag{2.10}$$

$$\hat{\Phi} = \sqrt{\frac{\hbar Z_0}{2}}(a + a^\dagger), \tag{2.11}$$

where $Z_0 = \sqrt{L/C}$ is the characteristic impedance of the circuit. Substitution into the original Hamiltonian conveniently results in

$$\hat{H} = \hbar\omega_0 \left(a^\dagger a + \frac{1}{2}\right), \tag{2.12}$$

where $\omega_0 = 1/\sqrt{LC}$ represents the resonant frequency of the system. Some algebraic manipulations with the commutation relation reveal that eigenstates of $\hat{H}$, denoted $|N\rangle$, must obey the relations $\hat{a}\,|N\rangle = \sqrt{N}\,|N-1\rangle$, $\hat{a}^\dagger\,|N\rangle = \sqrt{N+1}\,|N+1\rangle$, and $\hat{a}^\dagger\hat{a}\,|N\rangle = N\,|N\rangle$, for $N \in \mathbb{Z}^{\geq 0}$. These eigenstates are typically referred to as Fock states (or simply harmonic oscillator states), with the eigenenergy of $|N\rangle$ being $E_N = \hbar\omega_0(n+\frac{1}{2})$. The quantum harmonic oscillator is one of few systems in which techniques exist to analytically determine the eigenenergies and eigenstates. Typically, we will not be so lucky, and will have to resort to other methods.

The most notable feature of the harmonic oscillator is that the energy difference

between adjacent eigenstates $(E_n - E_{n-1})$ is equal to $\hbar\omega_0$ for all n. Exciting one transition in this system excites all transitions, which makes it unfeasible to define a qubit subspace in which population will remain. If the goal in forming a qubit is to procure true two-level system, the quantum harmonic oscillator is in fact the least suitable quantum system that exists. We must look elsewhere for superconducting qubits.

2.1.2 Forming a Qubit with the Josephson Junction

The circuit element which enables the construction of most superconducting qubits is the **Josephson junction**, which consists of two superconductors separated by a thin insulating material [Fig. 2-2(a)]. We will show that the energy stored in the Josephson junction behaves as that of a nonlinear inductor, breaking the harmonic nature of the previous LC oscillators. The first of two fundamental equations surrounding Josephson junctions is the current-phase relation, which gives the current due to Cooper-pairs tunneling across the insulating barrier

$$I = I_c \sin(\phi(t)). \tag{2.13}$$

The critical current of the junction is denoted by I_c and $\phi(t)$ is the superconducting phase difference across the insulation region. The second relation is the voltage-phase relation, which gives the voltage across the insulator as a function of the same phase difference

$$V = \frac{\hbar}{2e}\frac{d\phi}{dt}. \tag{2.14}$$

By comparing these equations to the voltage-current relationship for a classical inductor, $V = L\frac{dI}{dt}$, we can attribute an effective inductance to the Josephson junction

$$L_{\text{eff}} = \frac{\Phi_0}{2\pi I_c \cos(\phi)}, \tag{2.15}$$

rewriting some constants to instead use the **superconducting magnetic flux quantum**, $\Phi_0 = h/2e$. Due to the presence of the $\cos(\phi)$ term in this expression, the

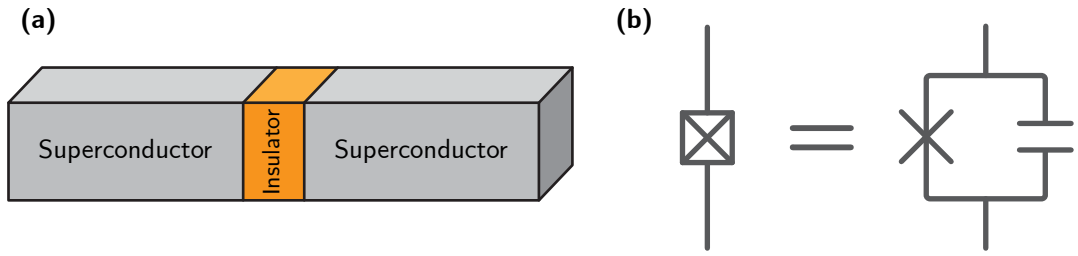

Figure 2-2: **Diagram of a Josephson junction.** **(a)** Illustration of Josephson junction. **(b)** Circuit diagram representation of a Josephson junction.

Josephson junction does not behave as a typical linear inductor. The energy stored in this non-linear inductor can be obtained by performing a time-integral of the voltage times the current

$$U(t) = \int_{-\infty}^{t} V(t')I(t')\,dt' = E_J(1 - \cos(\phi(t)) = -E_J\cos(\phi) + \text{const.}, \tag{2.16}$$

where we've introduced the **Josephson energy** $E_J \equiv I_c\Phi_0/2\pi$. Written as a circuit element, the Josephson junction is represented with an "X". A box is typically included around the "X" to represent a junction in parallel with the intrinsic junction capacitance, which is formed by the two superconducting leads across the insulator [Fig. 2-2(b)].

By replacing the inductor in the LC oscillator with this Josephson junction, we form the **Cooper-pair box** Hamiltonian [64]

$$\hat{H} = \frac{2e^2}{C}\hat{n}^2 - E_J\cos(\hat{\phi}). \tag{2.17}$$

In writing this Hamiltonian, we've introduced the **charge operator**

$$\hat{n} = \frac{\hat{q}}{2e}, \tag{2.18}$$

and promoted the superconducting phase difference across the Josephson junction into the **phase operator**, which relates to the flux operator as

$$\hat{\phi} = 2\pi\frac{\hat{\Phi}}{\Phi_0}. \tag{2.19}$$

This new pair of operators can be viewed as a dimensionless rescaling of the old operators, but for the Cooper-pair box, $\hat{n}$ physically represents the number of Cooper pairs that have tunneled across the junction and $\hat{\phi}$ represents phase difference of the superconducting condensate across the junction. We now further define the **charging energy**, which equals the energy of a single-electron charge stored in a capacitance C,

$$E_C \equiv \frac{e^2}{2C}. \tag{2.20}$$

Finally, after accounting for a continuous charge offset $n_g = V_g C_g$ induced by an external gate voltage V_g coupled with a capacitance C_g, the Hamiltonian as it typically appears in literature is

$$\hat{H} = 4E_C(\hat{n} - n_g)^2 - E_J \cos(\hat{\phi}). \tag{2.21}$$

A convenient way to illustrate how this Hamiltonian is different from that of the harmonic oscillator is to perform a Taylor expansion of the classical potential energy (Josephson junction term)

$$V(\phi) = -E_J \cos(\phi) \approx E_J \left(\frac{1}{2}\phi^2 - \frac{1}{24}\phi^4 \right) + \text{const.} \tag{2.22}$$

This expression takes the form of the quadratic potential associated with a linear inductance but with a quartic correction. As we will learn to compute precisely in the following Sections, this additional curvature breaks the equal spacing of the energy levels, allowing one to define a functional qubit using the lowest two energy levels of the system.

2.1.3 More General Circuit Quantization

Up until now, we've only explained how to write down Hamiltonians for circuits containing only two connected circuit elements. The goal for the remainder of this Section is to detail the construction of the circuit Hamiltonian for an arbitrary combination of inductors, capacitors, and Josephson junctions. We define a **node** of the circuit

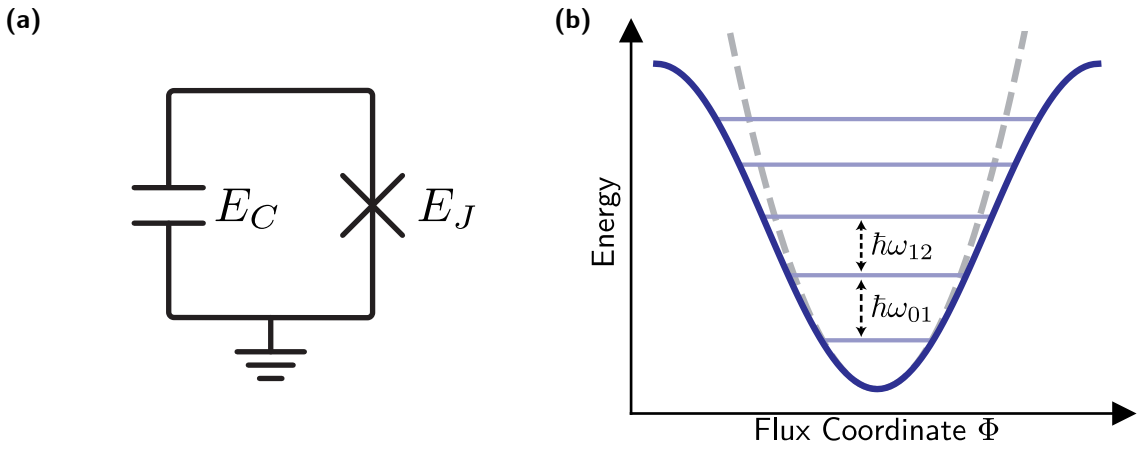

Figure 2-3: **Cooper Pair Box. (a)** Circuit representation of Cooper Pair Box, with a Josephson junction and capacitor in parallel. **(b)** Illustration of the cosine potential energy, leading to unevenly spaced energy levels.

as any continuous piece of metal, unseparated by junctions or capacitors. Typically the ground metal is discounted from being classified as a nontrivial node, as we treat it as the zero-voltage reference. We once again use Φ as our generalized position coordinate, but now formally define it as the time integral of the voltage at the node (referenced to ground).

$$\Phi(t) = \int_{-\infty}^{t} V(t')dt' \tag{2.23}$$

The expressions for the kinetic and potential energy of the circuit can generally be expressed in matrix notation as

$$T = \frac{1}{2}\dot{\vec{\Phi}}^T \mathbf{C} \dot{\vec{\Phi}} \tag{2.24}$$

$$V = \frac{1}{2}\vec{\Phi}^T \mathbf{L_{inv}} \vec{\Phi} + V_{\mathrm{JJ}}, \tag{2.25}$$

where $\vec{\Phi}$ is a vector of fluxes defined such that Φ_i is the flux at node i, $\mathbf{C}$ is the circuit capacitance matrix, $\mathbf{L_{inv}}$ is another circuit matrix with units of inverse inductance, and V_{JJ} is the sum of all potential energies from Josephson junctions. For each junction between node i and j (this can include the ground), its potential energy is $-E_{J_{ij}} \cos(\phi_i - \phi_j)$, where $\phi_i = 2\pi\Phi_i/\Phi_0$ is the phase at each node, and the ground phase is 0.

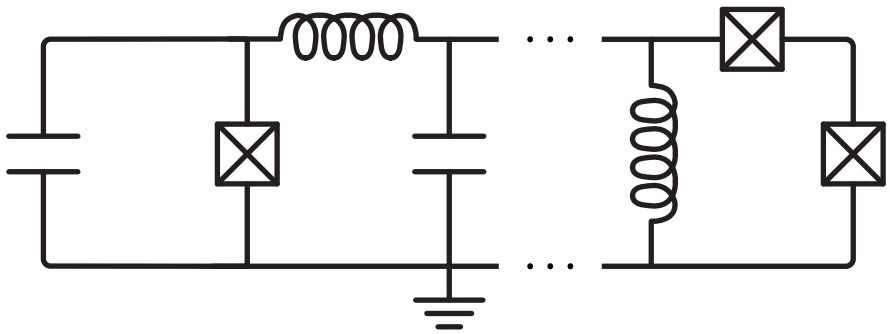

Figure 2-4: **Generic superconducting circuit composed of capacitors, inductors, and Josephson junctions.**

Following the previously outlined procedure, the circuit Lagrangian is

$$\mathcal{L} = \frac{1}{2}\dot{\vec{\Phi}}^T \mathbf{C}\dot{\vec{\Phi}} - \frac{1}{2}\vec{\Phi}^T \mathbf{L_{inv}}\vec{\Phi} - V_{\mathrm{JJ}}, \tag{2.26}$$

with the vector of conjugate momenta defined as

$$\frac{\partial \mathcal{L}}{\partial \dot{\vec{\Phi}}} = \mathbf{C}\dot{\vec{\Phi}} \equiv \vec{q}, \tag{2.27}$$

resulting in the Hamiltonian

$$\hat{H} = \dot{\vec{\Phi}} \cdot \vec{q} - \mathcal{L} \tag{2.28}$$

$$= \frac{1}{2}\hat{\vec{q}}^T \mathbf{C}^{-1}\hat{\vec{q}} + \frac{1}{2}\hat{\vec{\Phi}}^T \mathbf{L_{inv}}\hat{\vec{\Phi}} + V_{\mathrm{JJ}}(\hat{\vec{\Phi}}) \tag{2.29}$$

$$= 2e^2 \hat{\vec{n}}^T \mathbf{C}^{-1}\hat{\vec{n}} + \frac{1}{2}\left(\frac{\Phi_0}{2\pi}\right)^2 \hat{\vec{\phi}}^T \mathbf{L_{inv}}\hat{\vec{\phi}} + V_{\mathrm{JJ}}(\hat{\vec{\phi}}). \tag{2.30}$$

For full clarity we show two equivalent Hamiltonians (Eq. (2.29), Eq. (2.33)) expressed using different pairs of conjugate variables

$$[\hat{\Phi}_j, \hat{q}_k] = i\hbar\delta_{jk} \tag{2.31}$$

$$[\hat{\phi}_j, \hat{n}_k] = i\delta_{jk}. \tag{2.32}$$

As a final modification, each node is susceptible to a continuous charge offset n_g

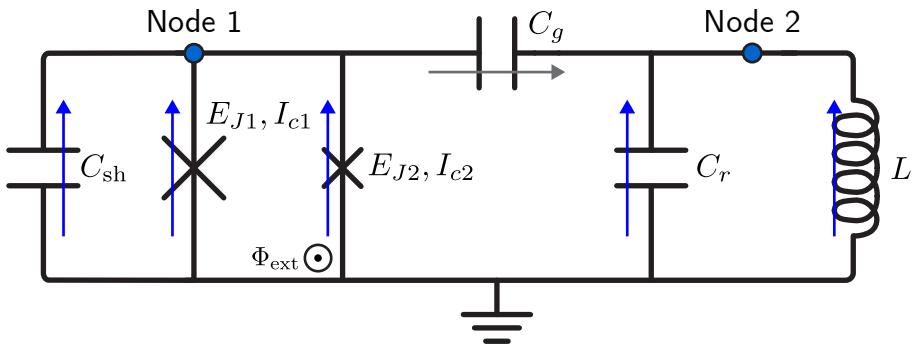

Figure 2-5: **Circuit schematic of a tunable transmon capacitively coupled to a resonator to illustrate general circuit QED techniques.**

as described previously, and for each closed loop (junctions and inductors form closed loops, capacitors break loops), we must account for the possibility of an external flux being threaded through that loop. While the proper treatment is a complex problem for fast changing fluxes [15, 108], for quasi-static flux changes (flux does not change fast enough to cause qubit transitions), one simply needs to modify any of the phase terms in each closed loop with an external phase, which is related to the external flux by $\phi_{\text{ext}} = 2\pi\Phi_{\text{ext}}/\Phi_0$. In full generality, the circuit Hamiltonian with any assortment of capacitors, inductors, and Josephson junctions is now

$$\hat{H} = 2e^2(\hat{\vec{n}} - \vec{n}_g)^T\mathbf{C}^{-1}(\hat{\vec{n}} - \vec{n}_g) + \frac{1}{2}\left(\frac{\Phi_0}{2\pi}\right)^2(\hat{\vec{\phi}} - \vec{\phi}_{\text{ext}})^T\mathbf{L_{inv}}(\hat{\vec{\phi}} - \vec{\phi}_{\text{ext}}) + V_{\text{JJ}}(\hat{\vec{\phi}} - \vec{\phi}_{\text{ext}}). \tag{2.33}$$

As we will see in future Sections, charge is extremely damaging to qubit coherence. Most qubits are therefore designed to be insensitive to charge offsets.

The biggest question remaining before we can construct a circuit Hamiltonian in practice is how to determine the capacitance and inductance matrices $\mathbf{C}$ and $\mathbf{L_{inv}}$. In this thesis, we will motivate an approach based on Kirchoff's laws, but point out that the theory of circuit quantization is much deeper for the interested reader [22, 98]. Using the circuit in Fig. 2-5 as an example, we illustrate a procedure for obtaining the circuit Hamiltonian as follows

1. **Identify the nontrivial nodes of the circuit.** Here there is node 1 and node

2.

2. **Draw arrows to form a directed spanning tree across the nodes such that all nodes are connected to ground through only one path (blue).** GND $\rightarrow$ 1, and GND $\rightarrow$ 2.

3. **Draw remaining arrows in either direction to complete arrows between each node (gray).** $1 \rightarrow 2$.

4. **Apply Kirchhoff's current law at each node, expressing the equations in terms of Φ_i.** We will assign a "+" sign to currents going into a node and a "-" sign to currents going out of a node.

$$C_{\text{sh}}\ddot{\Phi}_1 - C_g(\ddot{\Phi}_2 - \ddot{\Phi}_1) + I_{c1}\sin\left(2\pi\frac{\Phi_1}{\Phi_0}\right) + I_{c2}\sin\left(2\pi\frac{\Phi_1}{\Phi_0}\right) = 0 \tag{2.34}$$

$$C_r\ddot{\Phi}_2 + C_g(\ddot{\Phi}_2 - \ddot{\Phi}_1) + \frac{\Phi_2}{L} = 0 \tag{2.35}$$

5. **Invert the above equations using the Euler-Lagrange equations to obtain the Lagrangian**

$$\frac{\partial\mathcal{L}}{\partial\Phi_i} = \frac{d}{dt}\frac{\partial\mathcal{L}}{\partial\dot{\Phi}_i}. \tag{2.36}$$

In practice, this can be done either by guessing and checking or assuming a form of the Lagrangian $\mathcal{L} = f_1(\Phi_1, \Phi_2) + f_2(\dot{\Phi}_1, \dot{\Phi}_2)$, substituting into the Euler-Lagrange equations, equating to corresponding terms in the current law equations, and integrating to find a $\mathcal{L}$ which satisfies all equations. In either case, the below Lagrangian can easily be verified, and we convert it into a matrix

expression in Eq. (2.38).

$$\mathcal{L} = \underbrace{\frac{1}{2}C_{\text{sh}}\dot{\Phi}_1^2 + \frac{1}{2}C_r\dot{\Phi}_2^2 + \frac{1}{2}C_g(\dot{\Phi}_1 - \dot{\Phi}_2)^2}_{T} - \underbrace{\left(\frac{\Phi_2^2}{2L} - E_{J1}\cos\left(2\pi\frac{\Phi_1}{\Phi_0}\right) - E_{J2}\cos\left(2\pi\frac{\Phi_1}{\Phi_0}\right)\right)}_{V} \tag{2.37}$$

$$\mathcal{L} = \frac{1}{2}\dot{\vec{\Phi}}^T\begin{pmatrix} C_{\text{sh}}+C_g & -C_g \\ -C_g & C_r+C_g \end{pmatrix}\dot{\vec{\Phi}} - \frac{1}{2}\vec{\Phi}^T\begin{pmatrix} 0 & 0 \\ 0 & \frac{1}{L} \end{pmatrix}\vec{\Phi} + E_{J1}\cos\left(2\pi\frac{\Phi_1}{\Phi_0}\right) + E_{J2}\cos\left(2\pi\frac{\Phi_1}{\Phi_0}\right) \tag{2.38}$$

6. **The quantities C, $\mathbf{L_{inv}}$ and $V_{\mathbf{JJ}}$ can now be easily identified and we can write down the Hamiltonian**

$$\hat{H} = 2e^2\hat{\vec{n}}^T\mathbf{C}^{-1}\hat{\vec{n}} + \frac{\Phi_0^2}{8\pi^2}\hat{\vec{\phi}}^T\mathbf{L_{inv}}\hat{\vec{\phi}} + E_{J1}\cos(\hat{\phi}_1) + E_{J2}\cos(\hat{\phi}_1) \tag{2.39}$$

$$= 2e^2\hat{\vec{n}}^T\mathbf{C}^{-1}\hat{\vec{n}} + \frac{1}{2}E_L\hat{\phi}_2^2 + E_{J1}\cos(\hat{\phi}_1) + E_{J2}\cos(\hat{\phi}_1), \tag{2.40}$$

$$\tag{2.41}$$

where we've introduced E_L, the **inductive energy** defined as

$$E_L \equiv \left(\frac{\Phi_0}{2\pi}\right)^2\frac{1}{L}. \tag{2.42}$$

With the capacitance and inductance matrices sorted out, we complete the Hamiltonian by adding in continuous charge and flux offsets. In this case, there is only one closed loop, and we choose to add the external flux to the junction

$$\hat{H} = 2e^2(\hat{\vec{n}} - \vec{n}_g)^T\mathbf{C}^{-1}(\hat{\vec{n}} - \vec{n}_g) + \frac{1}{2}E_L\hat{\phi}_2^2 + E_{J1}\cos(\hat{\phi}_1) + E_{J2}\cos(\hat{\phi}_1 - \phi_{\text{ext}}) \tag{2.43}$$

.

Thankfully, the above procedure was only presented for pedagogy and is not necessary to obtain the circuit Lagrangian (or Hamiltonian). By considering how each

Variable	Formula	Variable	Formula
$\hat{q}$	$-i\sqrt{\frac{\hbar}{2Z_0}}(a-a^\dagger)$	$\hat{\Phi}$	$\sqrt{\frac{\hbar Z_0}{2}}(a+a^\dagger)$
$\hat{n}$	$-\frac{i}{\sqrt{2}}\left(\frac{E_L}{8E_C}\right)^{1/4}(a-a^\dagger)$	$\hat{\phi}$	$\frac{1}{\sqrt{2}}\left(\frac{8E_C}{E_L}\right)^{1/4}(a+a^\dagger)$
Z_0	$\sqrt{L/C}$	ω_0	$1/\sqrt{LC}$
$\hat{n}$	$\hat{q}/2e$	$\hat{\phi}$	$2\pi\hat{\Phi}/\Phi_0$
$[\hat{\Phi}_j, \hat{q}_k]$	$i\hbar\delta_{jk}$	$[\hat{\phi}_j, \hat{n}_k]$	$i\delta_{jk}$
E_C	$e^2/2C$	E_J	$I_c\Phi_0/2\pi$
E_L	$(\Phi_0/2\pi)^2/L$	α	$(E_2-E_1)-(E_1-E_0)$
H	$2e^2\hat{\vec{n}}\mathbf{C}^{-1}\hat{\vec{n}}+\frac{\Phi_0^2}{8\pi^2}\hat{\vec{\phi}}^T\mathbf{L_{inv}}\hat{\vec{\phi}}+V_{JJ}(\hat{\vec{\phi}})$		

Table 2.1: **Table of formulas used in this section.**

capacitor (or inductor) between two nodes would contribute to this matrix through Kirchhoff's laws and the Euler Lagrange equations, the following observation can be made:

Each diagonal element $\mathbf{C}_{ii}$ *is equal to the sum of all capacitances connected to node* i *and each off-diagonal element* $\mathbf{C}_{ij}$ *is equal to the negative of the direct capacitance between node* i *and node* j. Analogously, *Each diagonal element* $\mathbf{L_{inv}}_{,ii}$ *is equal to* $\sum_{L'} 1/L'$ *where the sum is taken over each inductor connected to node* i*, and each off-diagonal element* $\mathbf{L_{inv}}_{,ij}$ *is equal to -1 times the reciprocal of the direct inductance between node* i *and node* j.

2.2 Numerical Diagonalization: From Pen and Paper to Code

As warned previously, there is no hope for us to analytically solve the Hamiltonian Eq. (2.33) for arbitrary circuits. In this Section, we develop tools to numerical diagonalize these Hamiltonians to obtain their eigenenergies and eigenvalues. The first step in numerical diagonalization is choosing a basis for which all others states will be expressed with. In order to make a good choice of basis, we borrow from the concept of a "good quantum number". If the eigenstates of a qubit can be expressed com-

pactly using a given basis set, then it is a desirable basis. On the other hand, if the eigenstates are very delocalized or converge slowly (or even not at all) with increasing basis size, then it is a bad basis. This is especially important as the techniques in this Section are inherently discretized, and the true infinite number of the basis states are only well approximated by a finite set of states if one makes a good choice of basis. Three common choices of bases that will be covered in this Section are the **charge basis**, **phase basis**, and **Fock basis**. In general, different Hamiltonians will be more efficiently diagonalized using different bases, and it is up to the engineer to develop the intuition and expertise to choose the most efficient basis. For all of these potential bases, the goal will be to express both $\hat{n}$ and $\hat{\phi}$ in terms of basis vectors.

2.2.1 Charge Basis

Assuming a quantization of charge, the charge basis consists of the set of states which are the eigenstates of the charge operator $\hat{n}$ with integer eigenvalue. The phase operator, related to the charge basis through the Fourier transform, will be the trickier operator to represent. Due to the dual nature of this operator, it will be most convenient to obtain expressions for $\cos(k\hat{\phi}), k \in \mathbb{Z}$, and express any other functions of $\hat{\phi}$ through a Fourier cosine series. We can formally define the phase basis through the discrete Fourier transform

$$|\phi\rangle = \sum_{n=-\infty}^{\infty} e^{in\phi} |n\rangle \tag{2.44}$$

and additionally introduce the operator

$$e^{i\hat{\phi}} \equiv \frac{1}{2\pi} \int_0^{2\pi} e^{i\phi} |\phi\rangle \langle\phi| \, d\phi. \tag{2.45}$$

Using the above the equations, we can undertake some algebraic manipulations to obtain an expression for $\cos(k\hat{\phi})$.

$$\cos(k\hat{\phi}) = \frac{1}{2}\left(e^{ik\hat{\phi}} + e^{-ik\hat{\phi}}\right) \tag{2.46}$$

$$= \frac{1}{4\pi}\int_0^{2\pi}\left(e^{ik\phi} + e^{-ik\phi}\right)|\phi\rangle\langle\phi|\, d\phi \tag{2.47}$$

$$= \frac{1}{4\pi}\int_0^{2\pi}\sum_{n,m}\left(e^{ik\phi} + e^{-ik\phi}\right)e^{in\phi}e^{-im\phi}|n\rangle\langle m|\, d\phi \tag{2.48}$$

$$= \frac{1}{4\pi}\int_0^{2\pi}\sum_{n,m}\left(e^{i(k+n-m)\phi} + e^{i(-k+n-m)}\right)|n\rangle\langle m|\, d\phi \tag{2.49}$$

$$= \frac{1}{2}\sum_n |n\rangle\langle n+k| + |n\rangle\langle n-k| \tag{2.50}$$

$$= \frac{1}{2}\sum_n |n\rangle\langle n+k| + |n+k\rangle\langle n| \tag{2.51}$$

Similar derivations show that the phase difference between two nodes is

$$\cos(\hat{\phi}_1 - \hat{\phi}_2) = \frac{1}{2}\left(e^{i\hat{\phi}_1}e^{-i\hat{\phi}_2} + e^{-i\hat{\phi}_1}e^{i\hat{\phi}_2}\right) \tag{2.52}$$

$$= \frac{1}{2}\left(\left[\sum_n |n\rangle\langle n+1|\right]_1 \otimes \left[\sum_n |n+1\rangle\langle n|\right]_2\right) \tag{2.53}$$

$$+ \frac{1}{2}\left(\left[\sum_n |n+1\rangle\langle n|\right]_1 \otimes \left[\sum_n |n\rangle\langle n+1|\right]_2\right), \tag{2.54}$$

and the phase difference between a node and an external flux (represented as a phase) is

$$\cos(\hat{\phi} - \phi_{\text{ext}}) = \frac{1}{2}\left(e^{-i\phi_{\text{ext}}}e^{i\hat{\phi}} + e^{i\phi_{\text{ext}}}e^{-i\hat{\phi}}\right) \tag{2.55}$$

$$= \frac{1}{2}\left(\sum_n e^{-i\phi_{\text{ext}}}|n\rangle\langle n+1| + e^{i\phi_{\text{ext}}}|n+1\rangle\langle n|\right). \tag{2.56}$$

While theoretically all summations in the above formulas are infinite, we must choose a truncated Hilbert space size of $2n_{\max}+1$ in practice. The optimal value of $n_{\max}$ needs to be determined through trial and error, by considering the trade-off between accuracy and convergence speed. Explicitly, charge states would be represented by

arrays such as

$$|n=-1\rangle = \begin{pmatrix} 0 \\ \vdots \\ 1 \\ 0 \\ 0 \\ \vdots \\ 0 \end{pmatrix} \qquad |n=0\rangle = \begin{pmatrix} 0 \\ \vdots \\ 0 \\ 1 \\ 0 \\ \vdots \\ 0 \end{pmatrix} \qquad |n=1\rangle = \begin{pmatrix} 0 \\ \vdots \\ 0 \\ 0 \\ 1 \\ \vdots \\ 0 \end{pmatrix}, \tag{2.57}$$

and the important operators $\hat{n}$ and $\cos(\hat{\phi})$ are represented as the following matrices

$$\hat{n} = \begin{pmatrix} -n_{\max} & & & \\ & -n_{\max}+1 & & \\ & & \ddots & \\ & & & n_{\max} \end{pmatrix} \qquad \cos(\hat{\phi}) = \begin{pmatrix} & 1 & & \\ 1 & & \ddots & \\ & \ddots & & 1 \\ & & 1 & \end{pmatrix}. \tag{2.58}$$

These equations should cover all common Hamiltonians that may arise in circuit QED and allow for numerical diagonalization by expressing operators as matrices and states as vectors using the charge eigenstates as the basis.

2.2.2 Phase Basis

In the phase basis, basis states are now eigenstates of the phase operator $\hat{\phi}\,|\phi\rangle = \phi\,|\phi\rangle$, and the charge operator is expressed using its definition as a phase derivative

$$\hat{n} \equiv -i\frac{d}{d\phi}. \tag{2.59}$$

Similar to before, we choose a minimum and maximum phase $\phi_{\max}$ in addition to a step size Δ to numerically represent our phase states. The phasis basis states are

analogously written in array as

$$|\phi = -\Delta\rangle = \begin{pmatrix} 0 \\ \vdots \\ 1 \\ 0 \\ 0 \\ \vdots \\ 0 \end{pmatrix} \qquad |\phi = 0\rangle = \begin{pmatrix} 0 \\ \vdots \\ 0 \\ 1 \\ 0 \\ \vdots \\ 0 \end{pmatrix} \qquad |\phi = \Delta\rangle = \begin{pmatrix} 0 \\ \vdots \\ 0 \\ 0 \\ 1 \\ \vdots \\ 0 \end{pmatrix}. \tag{2.60}$$

This basis then allows us to numerically represent the derivative operator as a symmetric derivative, with subscripts indexing the phase states

$$\hat{n} = -i \sum_i \frac{|\phi\rangle_{i+1} - |\phi\rangle_{i-1}}{2\Delta} \langle\phi|_i \,. \tag{2.61}$$

One word of caution is that many Hamiltonians contain just an $\hat{n}^2$ term, and in those cases it's correct to use the following for $\hat{n}^2$, as opposed to the square of the $\hat{n}$ matrix.

$$\hat{n}^2 = -\sum_i \frac{|\phi\rangle_{i+1} - 2\,|\phi\rangle_i + |\phi\rangle_{i-1}}{\Delta^2} \langle\phi|_i \tag{2.62}$$

This avoids numerical artifacts related to the discretization of the basis states

If we remember that Φ was the canonical position and q was the canonical momentum, then expressing eigenstates in the phase basis is analogous to solving for position state wavefunctions $\psi(x)$ in introductory quantum classes. Likewise, the previous diagonalization techniques in the charge basis were analogous to solving for wavefunctions in momentum space. This analogy is reinforced by Eq. (2.59), which exactly resembles the equation for the momentum operator (up to an $\hbar$ factor) in terms of the position.

2.2.3 Fock Basis

The final basis we will consider is spanned by the Fock states, eigenstates of the harmonic oscillator Hamiltonian. While neither the charge nor the phase operator is diagonal in this basis, it is a well motivated choice of basis for systems that closely resemble harmonic oscillators. In this basis, the charge and phase operators are expressed in terms of the familiar creation and annihilation operators

$$\hat{n} = -\frac{i}{\sqrt{2}} \left(\frac{E_L}{8E_C} \right)^{1/4} (a - a^\dagger) \tag{2.63}$$

$$\hat{\phi} = \frac{1}{\sqrt{2}} \left(\frac{8E_C}{E_L} \right)^{1/4} (a + a^\dagger). \tag{2.64}$$

These equations can be derived from the previous relations [Eq. (2.10) and Eq. (2.11)] by making the usual substitutions $E_L = (\Phi_0/2\pi)^2/L$ and $E_C = e^2/2C$. In circuits without a pure inductance, the E_L can often be substituted by the Josephson energy E_J by grouping the quadratic term from the cosine expansion with the kinetic energy. Represented in matrix form, these creation and annihilation operators are

$$a^\dagger = \begin{pmatrix} \sqrt{1} & & & \\ & \sqrt{2} & & \\ & & \ddots & \\ & & & \sqrt{N} \end{pmatrix} \qquad a = \begin{pmatrix} \sqrt{1} & & & \\ & \sqrt{2} & & \\ & & \ddots & \\ & & & \sqrt{N} \end{pmatrix}. \tag{2.65}$$

2.3 Quantization of Different Qubits

With the ability to write down any circuit Hamiltonian and compute its eigenenergies and eigenstates, we return back to superconducting qubits, ready to investigate their properties. This Section is also a good opportunity for those needing practice with circuit QED to use the tools from previous two Sections of this Chapter and follow along by reproducing all Hamiltonians and energy spectra.

2.3.1 Cooper Pair Box

When last examined, the Cooper pair box Hamiltonian [Eq. (2.21)] was claimed to yield uneven energy levels due to the cosine potential energy differing from a parabolic potential energy. This unevenness in the first three energy levels is precisely defined as the **anharmonicity** of the qubit

$$\hbar\alpha \equiv (E_2 - E_1) - (E_1 - E_0), \tag{2.66}$$

which we can now calculate explicitly by diagonalizing Eq. (2.21) using the charge basis [see Fig. 2-6]. In addition to uneven energy levels, we can also explicitly see the dependence of the qubit energies as a function of the offset charge n_g. Due to the capricious nature of the offset charge, this was ultimately seen as an unacceptable feature of the qubit, as charge fluctuations are both uncontrollable and cause considerable qubit dephasing. Although flux noise factors in identically, individual charge defects can cause jumps on the order of e, whereas individual magnetic defects typically change the flux by much less than Φ_0. This qubit can be conceptualized as a superconducting island storing a number of cooper pairs. The quantum state is then impacted by cooper pairs tunneling across the junction to change the number on the island as well as by any other charge noise coupled in from the environment. We can increase the ease in which cooper pairs tunnel across the junction by increasing E_J/E_C, so that in the eigenstates of the qubit, charge is continually tunneling across the junction. Naturally, this reduces the sensitivity to offset charge; however, increasing E_J/E_C infinitely causes the potential energy to once again become parabolic. This increase in E_J/E_C means an increase in current flowing through the junction, which when large enough causes the junction to behave as a linear inductor. Fortunately the regime of $E_J/E_C \approx 50$ exists to sufficiently suppress charge sensitivity while retaining a sufficiently anharmonic energy spectrum.

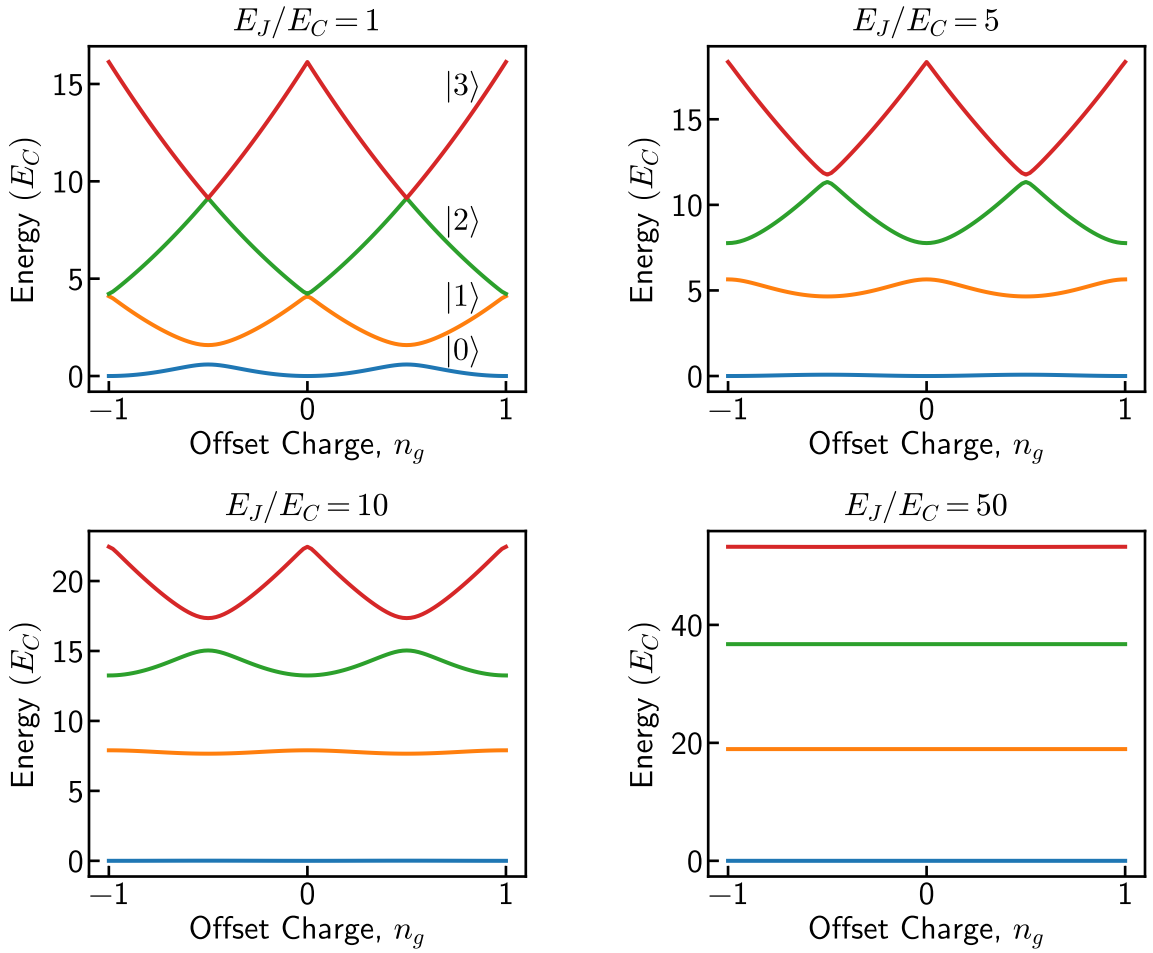

Figure 2-6: **Energy spectra of the Cooper Pair Box vs. offset charge.** As the ratio E_J/E_C is increased, charge dispersion exponentially decreases. The regime $E_J/E_C \approx 50$ defines the typical transmon qubit regime.

2.3.2 Transmon

The reduction in dephasing and insensitivity to offset charge proved to be such impactful changes that the original Cooper Pair Box in the regime $E_J/E_C \gg 1$ (and practically speaking, > 50) was termed a new qubit called the **transmon** [44] (although its circuit is identical to the Cooper Pair Box circuit). To this day, the transmon remains the de facto qubit, favored for its simplicity of circuit design, intuitive understanding as a perturbation on a harmonic oscillator, and impressive performance [4, 1].

Duffing Oscillator

The resemblance of the transmon to the harmonic oscillator enables a useful approximation by expanding the cosine potential and then inserting the Fock basis representation of the charge and phase operators [Eq. (2.63) and Eq. (2.64)]. Since $E_J/E_C \gg 1$, higher order terms of the cosine expansion fall off rapidly and the transmon can be approximately described as a harmonic oscillator with a quartic correction term to its potential energy

$$\hat{H} = 4E_C\hat{n}^2 - E_J\left(1 - \frac{1}{2}\hat{\phi}^2 + \frac{1}{24}\hat{\phi}^4\right) \tag{2.67}$$

$$= \sqrt{8E_JE_C}\left(a^\dagger a + \frac{1}{2}\right) - E_J - \frac{E_C}{12}\left(a^\dagger + a\right)^4 \tag{2.68}$$

$$= \left(\sqrt{8E_JE_C} - E_C\right)a^\dagger a - \frac{E_C}{2}a^\dagger a^\dagger aa + \text{const.} \tag{2.69}$$

$$= \hbar\omega a^\dagger a + \hbar\frac{\alpha}{2}a^\dagger a^\dagger aa + \text{const.} \tag{2.70}$$

This final equation gives precisely the mathematical form of an anharmonic oscillator with qubit frequency ω and anharmonicity α, allowing for a simplistic modeling of the qubit. Typical values of the qubit frequency are $3 \sim 6\,\text{GHz}$ with an anharmonicity of $-200 \sim -300\,\text{MHz}$.

Tunable Transmon

Transmons designed in this way have a fixed frequency depending on their E_C and E_J and cannot be changed after device fabrication. By increasing the complexity of the transmon circuit by one additional junction, we can form a tunable transmon; the effective critical current (or Josephson energy) can be tuned by adjusting the external flux through the closed loop [see Fig. 2-7]

$$\hat{H} = 4E_C\hat{n}^2 - E_{J1}\cos(\hat{\phi}) - E_{J2}\cos(\hat{\phi} - \phi_{\text{ext}}). \tag{2.71}$$

The straightforward approach is to numerical diagonalize the above Hamiltonian using the charge basis, but one can alternatively perform some trigonometric ma-

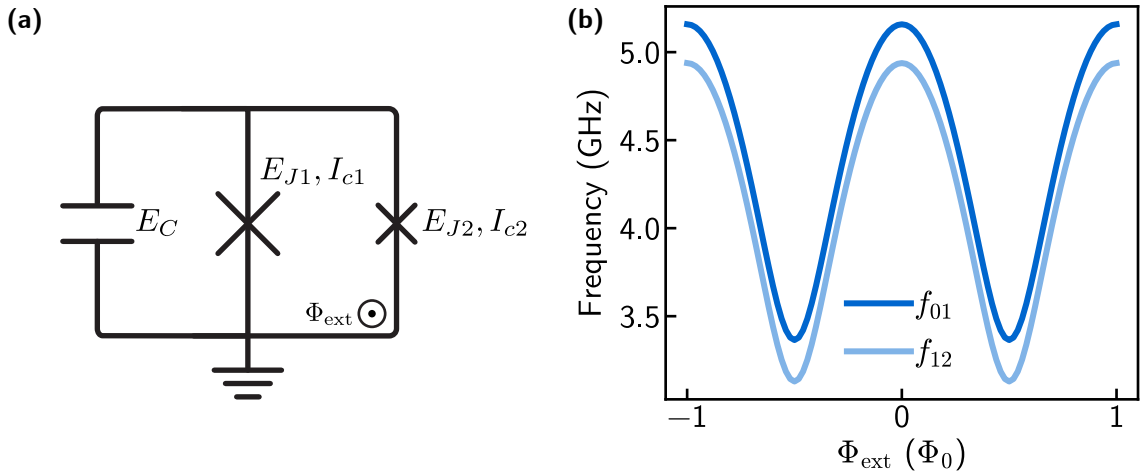

Figure 2-7: **Asymmetric tunable-transmon.** **(a)** Circuit diagram of a tunable-transmon. **(b)** Energy spectrum of Transmon with parameters $E_C/h = 0.2\,\text{GHz}$, $E_{J1}/h = 13\,\text{GHz}$, and $E_{J2}/h = 5\,\text{GHz}$.

nipulations to convert this Hamiltonian back into a single cosine potential with a flux dependent Josephson energy [44]. This results in the same Hamliltonian as the fixed-frequency transmon with the substitution

$$E_J \rightarrow E_{J\Sigma} \cos\left(\frac{\pi\Phi}{\Phi_0}\right) \sqrt{1 + d^2 \tan^2\left(\frac{\pi\Phi}{\Phi_0}\right)}, \tag{2.72}$$

where $E_{J\Sigma} \equiv E_{J1} + E_{J2}$ is the summed Josephson energy and $d \equiv (E_{J2} - E_{J1})/(E_{J1} + E_{J2})$ is the junction asymmetry parameter. This new value of E_J has a minimum value of $|E_{J1} - E_{J2}|$ and a maximum value of $E_{J1} + E_{J2}$, supporting the notion that the second junction can be tuned to constructively or destructively interfere with the first. Not only does this tunability help guard against fabrication variations, but it also enables new methods of qubit control [17, 94].

2.3.3 C-Shunt Flux-Qubit

The **C-shunt flux qubit** [105] has in series a large shunt capacitance, a small Josephson junction, and two large Josephson junctions all in parallel. This has historically developed from the original persistent-current flux qubit [60, 71] by adding an additional capacitive shunt in order to improve its reproducibility. The Hamiltonian of

the qubit is

$$\hat{H} = 2e^2\hat{\vec{n}}\mathbf{C}^{-1}\hat{\vec{n}} - \alpha E_J \cos(\hat{\phi}_2 - \phi_{\text{ext}}) - E_J \cos(\hat{\phi}_1) - E_J \cos(\hat{\phi}_2 - \hat{\phi}_1), \tag{2.73}$$

with capacitance matrix

$$\mathbf{C} = \begin{pmatrix} 2C & -C \\ -C & \alpha C + C + C_{\text{sh}} \end{pmatrix}. \tag{2.74}$$

Each circuit variable is defined according to the circuit diagram in Fig. 2-8(a). As our first two-node circuit, numerical diagonalization will take noticeably longer due to the exponentially increasing size of the Hilbert space with number of nodes. Nevertheless, sticking to the charge basis diagonalization allows us to uncover the following energy spectra plotted in Fig. 2-8(b).

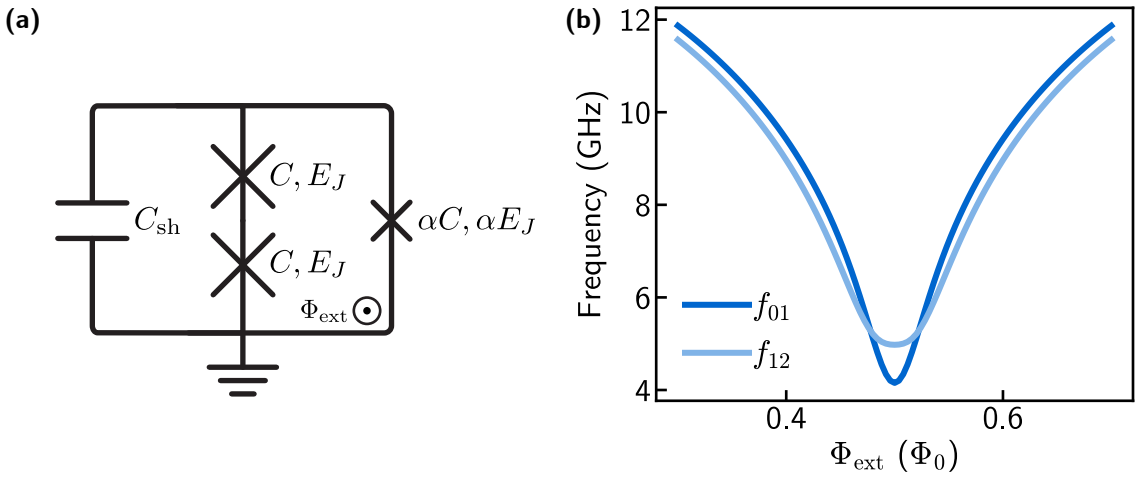

Figure 2-8: **Capacitively-shunted flux qubit (a)** Circuit diagram of a C-shunt flux qubit. **(b)** Energy spectrum of qubit with parameters $C_{\text{sh}} = 51\,\text{fF}$, $C = 5\,\text{fF}$, $E_J/h = 84.2\,\text{GHz}$, $\alpha = 0.43$.

The small junction is often called the "black-sheep" junction or the "alpha" junction and is shunted by two larger junctions which primarily act as an inductance. It is called this because its Josephson energy is αE_J, where E_J is the Josephson energy of one of the large junctions. Like the transmon, this qubit at its sweet spot ($\phi_{\text{ext}} = \pi$) behaves as an anharmonic oscillator, with a similar frequency but with a positive

(and typically larger) anharmonicity. This qubit was primarily used in this thesis work for its sensitivity to flux noise away from the sweet spot in order to characterize and minimize flux noise in superconducting qubits [see Chapter 3].

2.3.4 Fluxonium

The **fluxonium qubit** is the primary qubit of interest in this thesis work. In comparison to the flux qubit, the fluxonium has an increased inductive shunt which reduces the qubit sensitivity to flux noise. Moreover, the number of junctions in the shunt is increased to reach the linear regime of the junction array. This qubit has quickly gained traction in recent years, owing to its much larger anharmonicity and longer coherence times than transmon qubits [56, 29, 67], and is thus a promising candidate for gate-based quantum information processing [66]. In contrast with the transmon, fluxonium transition frequencies are typically less than 1 GHz at the half-flux sweet spot with coherence times upwards of 1 ms and anharmonicities of several GHz. These two characteristics bring fluxonium extremely close to the ideal long-lived, two-level system model of a qubit. The qubit circuit consists of a capacitor, a Josephson junction, and a series of larger junctions, all in parallel. The first priority is to simplify the circuit from an N node circuit (where N is the number of junctions) into a single-node circuit. Only then will it be feasible to numerically diagonalize the qubit Hamiltonian.

We first consider the kinetic energy (capacitive energies) of the circuit drawn in Fig. 2-9

$$T = \frac{C_{\text{ar}}}{2}\dot{\Phi}_1^2 + \frac{C_{\text{ar}}}{2}(\dot{\Phi}_2 - \dot{\Phi}_1)^2 + \cdots + \frac{C_{\text{ar}}}{2}(\dot{\Phi}_N - \dot{\Phi}_{N-1})^2 + \frac{C_{\text{sh}} + C_{\text{small}}}{2}\dot{\Phi}_N^2. \quad (2.75)$$

In the limit of a large number of junctions, we can assume the phase drop across successive junctions in the array is the same and equal to $1/N$ of the total phase drop

$$\Phi_i - \Phi_{i-1} = \Phi_1 = \Phi_N/N. \quad (2.76)$$

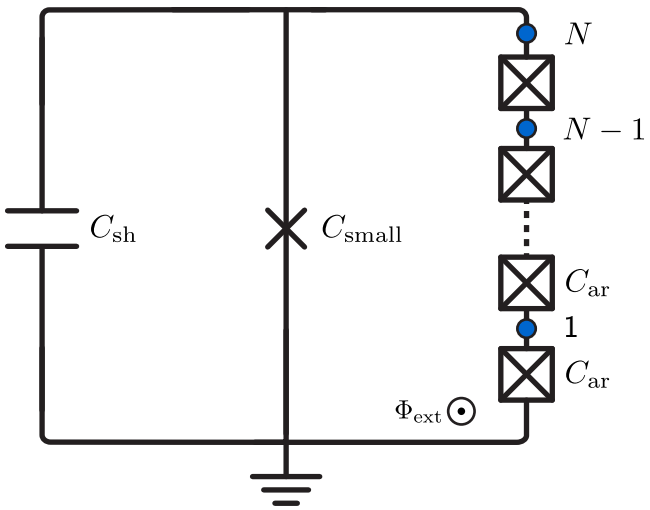

Figure 2-9: **Circuit representation of a fluxonium qubit using a Josephson junction array.**

The kinetic energy is thereby simplified as

$$T = \frac{C_{\text{ar}}/N + C_{\text{sh}} + C_{\text{small}}}{2}\dot{\Phi}_N^2 \tag{2.77}$$

The potential energy can be simplified using the same phase drop assumption and Taylor expanding the large junction cosine potentials (expansion is more accurate for larger N)

$$\begin{aligned} V &= -E_{J,\text{ar}}\cos(\phi_1) - \cdots - E_{J,\text{ar}}\cos(\phi_N - \phi_{N-1}) - E_J\cos(\phi_N - \phi_{\text{ext}}) && (2.78)\\ &= -NE_{J,\text{ar}}\cos\left(\frac{\phi_N}{N}\right) - E_J\cos(\phi_N - \phi_{\text{ext}}) && (2.79)\\ &\approx -NE_{J,\text{ar}}\left(1 - \frac{\phi_N^2}{2N^2}\right) - E_J\cos(\phi_N - \phi_{\text{ext}}) && (2.80)\\ &= \frac{1}{2}\frac{E_{J,\text{ar}}}{N}\phi_N^2 - E_J\cos(\phi_N - \phi_{\text{ext}}) + \text{const.} && (2.81) \end{aligned}$$

This simplification reveals that a large array of junctions behaves identically to a classical inductance. The reason junctions are favored over simply using a long stretch of wire is the superior areal compactness which junctions produce inductance. This is owed to the fact that the inductance from junctions comes from the kinetic inductance

of the superconducting condensate, rather than a geometric inductance. Alternatively, other high-kinetic-inductance materials may be used to form the inductance in place of a junction chain, but those works fall out of the scope of this thesis [35, 38, 43].

With expressions for the kinetic and potential energies that fluxonium Hamiltonian can be written as

$$\hat{H} = 4E_C\hat{n}^2 + \frac{1}{2}E_L\hat{\phi}^2 - E_J\cos(\hat{\phi} - \phi_{\text{ext}}), \tag{2.82}$$

where we've introduced $E_C = e^2/[2(C_{\text{ar}}/N + C_{\text{sh}} + C_{\text{small}})]$, $E_L = E_{J,\text{ar}}/N$, and $\hat{\phi} = \hat{\phi}_n$. We re-emphasize here that the quantization techniques in this Chapter assume quasi-static flux offsets. For the fluxonium Hamiltonian specifically, any component of the external flux that is not quasi-static must go inside the inductance term [15, 108]. Due to the presence of the non-periodic $\hat{\phi}^2$ term, the charge basis is an undesired choice to numerically diagonalize this Hamiltonian. Instead, a typical fluxonium is most conveniently diagonalized in the Fock or phase basis. An example energy spectrum and wavefunctions are plotted in Fig. 2-10.

In analogy to varying E_J/E_C in the Cooper pair box, one can increase E_C (or decrease E_L) relative to the other parameters to create "light" fluxonium, characterized by the qubit modes being delocalized across many of the cosine potential wells [see Figs. 2-11(a-b)], and one can decrease E_C (or increase E_L) relative to other parameters to create a "heavy" fluxonium, characterized by qubit modes being heavily localized inside the cosine wells [see Figs. 2-11(c-d)]. As the fluxonium becomes heavier, the Fock basis is found to converge more and more slowly. When the qubit wavefunctions becomes sufficiently localized, they begin to have a definitive value of phase, resulting in the phase basis becoming the more efficient basis to express the Hamiltonian.

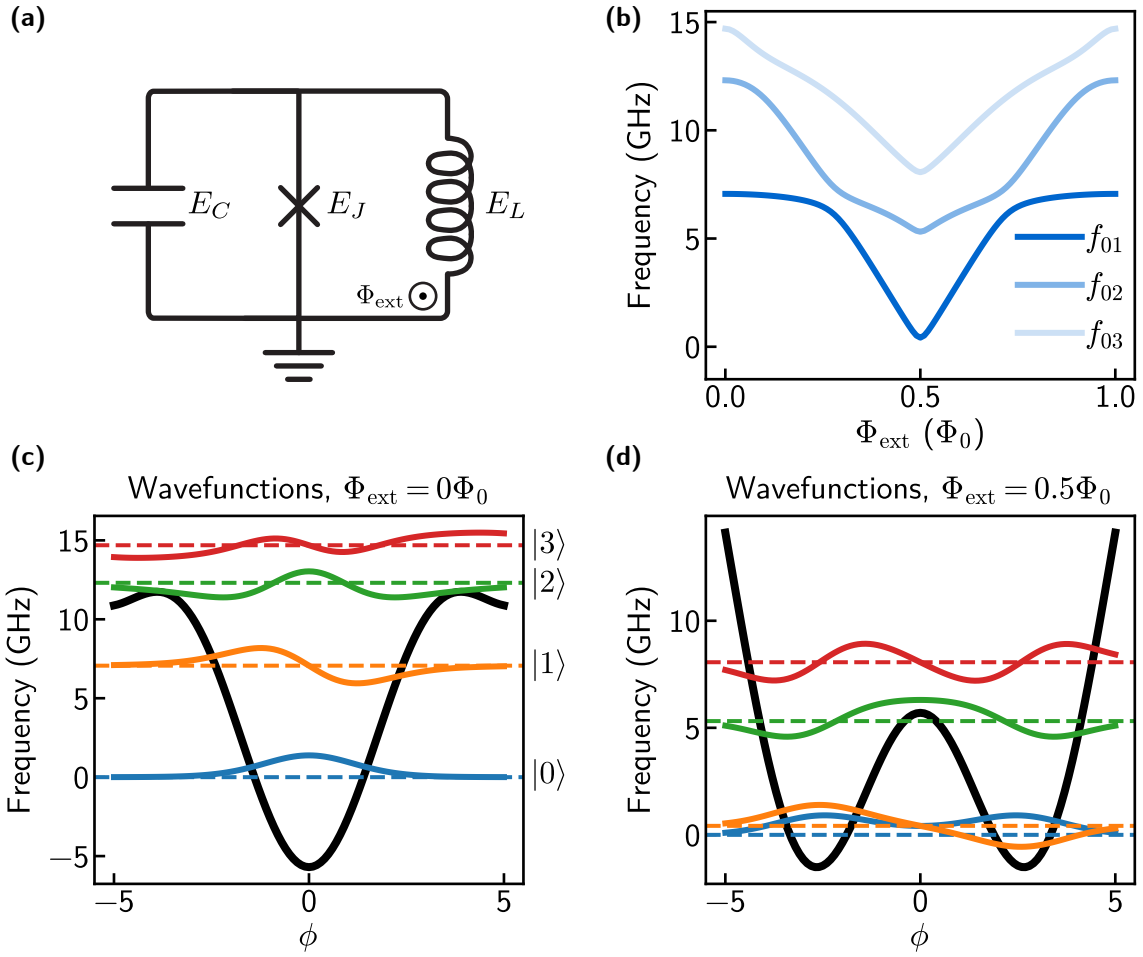

Figure 2-10: **Fluxonium qubit.** **(a)** Circuit diagram of fluxonium. **(b)** Energy spectrum of a fluxonium with parameters $E_C/h = 1.3\,\text{GHz}$, $E_L/h = 1\,\text{GHz}$, $E_J/h = 5.7\,\text{GHz}$. **(c)** Phase-space wavefunctions of the fluxonium at 0 flux, showing the first four energy states of the qubit. **(d)** Wavefunctions of the fluxonium at a half-flux quantum.

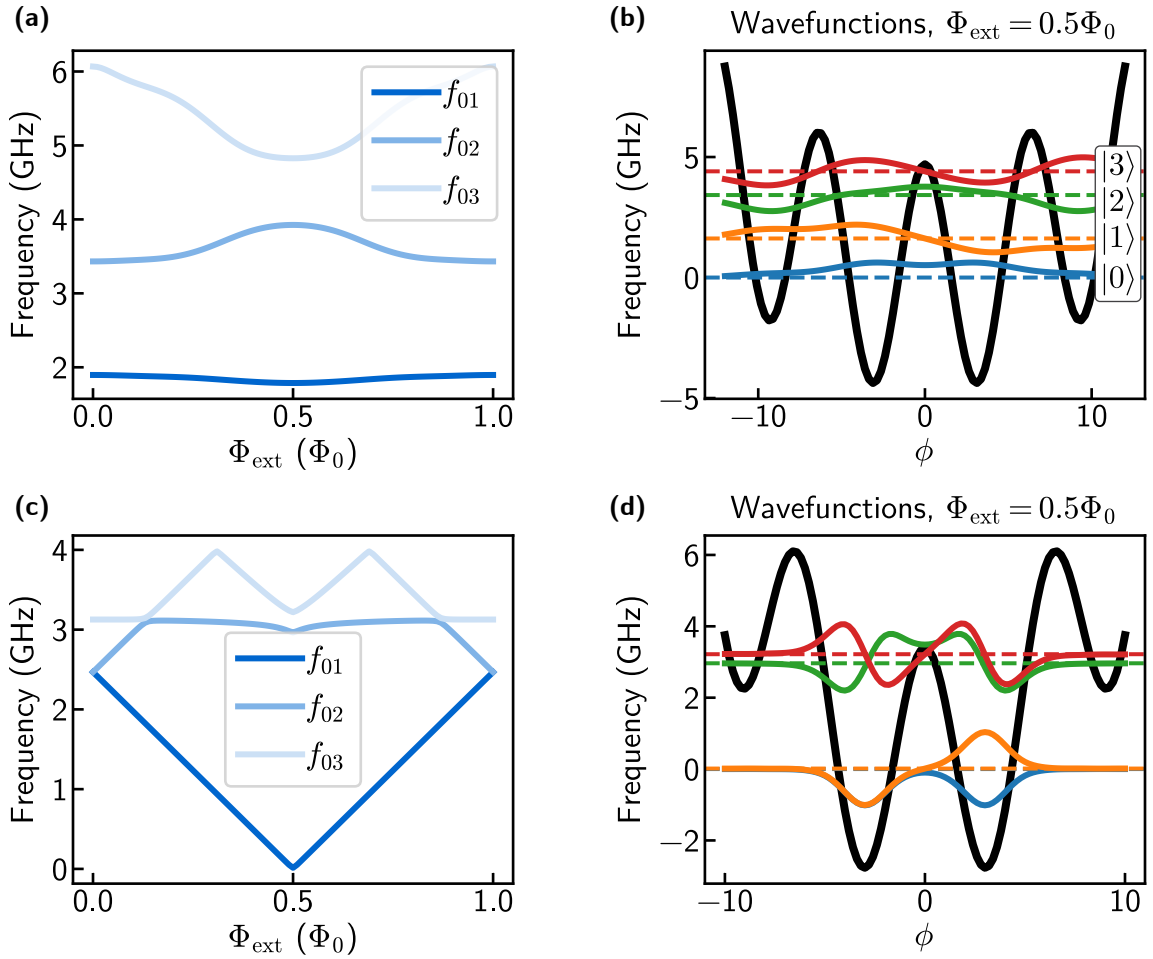

Figure 2-11: **Light and heavy variants of fluxonium.** **(a)** Energy spectrum of a light fluxonium, with parameters $E_C/h = 7.07\,\text{GHz}$, $E_L/h = 66.5\,\text{MHz}$, $E_J/h = 4.7\,\text{GHz}$ [58]. **(b)** Wavefunctions of the corresponding light fluxonium. **(c)** Energy spectrum of a heavy fluxonium, with parameters $E_C/h = 0.479\,\text{GHz}$, $E_L/h = 0.132\,\text{MHz}$, $E_J/h = 3.395\,\text{GHz}$ [109]. **(d)** Wavefunctions of the corresponding heavy fluxonium.

Selection Rules

At at external flux of $\Phi_{\text{ext}} = 0$ or $\Phi_{\text{ext}} = 0.5\Phi_0$, the fluxonium qubit has a symmetric potential energy ($V(\Phi) = V(-\Phi)$), meaning eigenstates of our Hamiltonian can be chosen to have definite parity; these properties are shared with the harmonic oscillator eigenstates. When viewed in the Fock basis, eigenstates then only have finite amplitude in odd-numbered photon states (odd parity) or even-numbered photon states (even parity). Under the dipole approximation, all single-photon operations involve either $\hat{a}$ or $\hat{a}^\dagger$ acting on the initial state. Therefore, a single photon can only transition odd-parity states into even-parity states and vice-versa. Transitions such as $|0\rangle \leftrightarrow |2\rangle$ are thereby **parity forbidden**. However, unlike the harmonic oscillator, single-photon transitions need not only change the fluxonium excitation number by one, and transitions such as $|0\rangle \leftrightarrow |3\rangle$ and $|1\rangle \leftrightarrow |4\rangle$ are allowed.

2.3.5 Grounded vs. Differential Qubits

Previously, we quantized our circuits assuming they were grounded at one end. What if instead no nodes were directly connected to ground? These qubits are termed **floating** or **differential** [see Fig. 2-12]. While conceptually it may be clear that a differential qubit should not behave wildly differently, an obstacle arises when performing the circuit quantization: there is now an additional node, leaving no possibility that the Hamiltonian can be exactly equal to its grounded variant.

To recover the original qubit mode, we must perform of change of variables into the sum and difference variables of the two nodes. Taking the cue from the potential energy only depending on the difference between the two nodes, we make our qubit mode the difference mode and the summed mode becomes a free kinetic mode which can be discarded freely.

$$\tilde{\vec{\Phi}} = \mathbf{M}\vec{\Phi} \tag{2.83}$$

$$\begin{pmatrix} \tilde{\Phi}_1 \\ \tilde{\Phi}_2 \end{pmatrix} = \begin{pmatrix} 1 & 1 \\ 1 & -1 \end{pmatrix} \begin{pmatrix} \Phi_1 \\ \Phi_2 \end{pmatrix} = \begin{pmatrix} \Phi_1 + \Phi_2 \\ \Phi_1 - \Phi_2 \end{pmatrix} \tag{2.84}$$

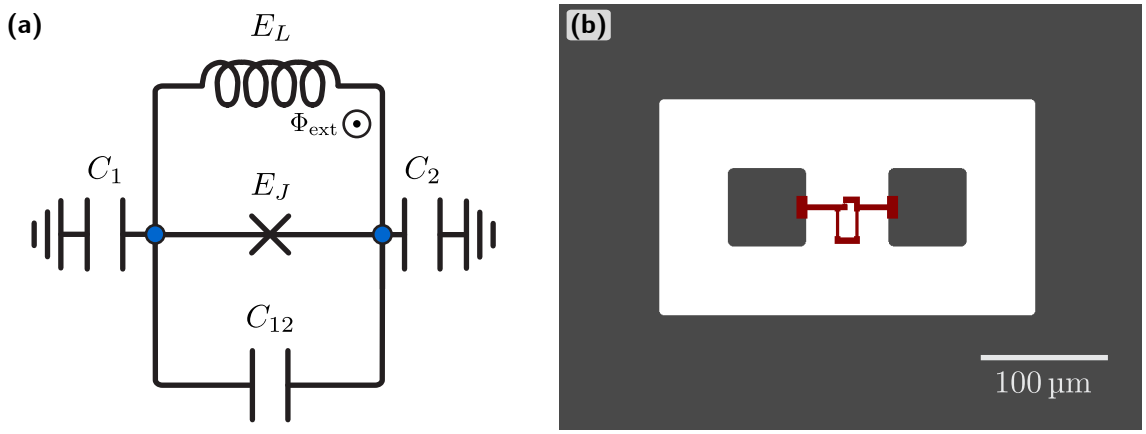

Figure 2-12: **Differential variant of a qubit. (a)** Circuit diagram of a differential fluxonium qubit. **(b)** Image of a differential fluxonium qubit in a .gds file.

It is important to make this variable substitution in the Lagrangian, before computing the Hamiltonian. After doing so, we arrive at a Hamiltonian with the exact same form with the original capacitance matrix $\mathbf{C}$ replaced with the new transformed matrix

$$\tilde{\mathbf{C}} = (\mathbf{M}^T)^{-1}\mathbf{C}\mathbf{M}^{-1} \tag{2.85}$$

In general, all variable transformations performing this sum and difference mode transformation can be written as a symmetric matrix, so a further simplification can be made in those cases by equating $M^T = M$. After the variable transformation, the qubit mode is well described by only the difference mode ($\tilde{\Phi}_2$ in the example), and terms involving the summed mode ($\tilde{\Phi}_1$ in the example) can be safely discarded. This procedure can be extended to larger systems with both differential and grounded qubits, and in these systems, the sum and difference transformation is only applied to the differential qubit nodes; $\mathbf{M}$ will be the identity when indexed across all other nodes. Examples of this transformation are shown in Section A.2 for a circuit with two differential fluxonium qubits and a grounded transmon.

2.4 Building upon a Qubit

The next step in understanding the physics of a superconducting quantum processor is to learn how additional circuit components interface with the qubits and how different qubits couple together. These additional coupled components give us the tools to readout the state of a qubit, to control qubits, and to perform gates in multi-qubit systems.

2.4.1 Qubit - Resonator Coupling

Superconducting resonators are typically long meandering stretches of a coplanar waveguide terminated at each end by either a short or an open. The most common use of resonators is to off-resonantly couple to the qubit, so that it's transmission or reflection properties are altered depending on the qubit state. By coupling our external control signals to the readout resonator instead of the qubit directly, we provide an additional layer of protection for the qubit against the outside world and improve qubit coherence.

To illustrate the circuit QED techniques with a specific example, we will consider a single-node qubit with capacitance C_1 capacitively coupled (C_g) to a resonator with capacitance C_r [see Fig. 2-13]. The Hamiltonian can be written in the form Eq. (2.33) with

$$\mathbf{C} = \begin{pmatrix} C_1 + C_g & -C_g \\ -C_g & C_r + C_g \end{pmatrix} \tag{2.86}$$

One can expand the kinetic portion of the Hamiltonian ($T = 2e^2 \hat{\vec{n}}^T \mathbf{C}^{-1} \hat{\vec{n}}$) to find that the term coupling the qubit and the resonator is

$$\hat{H}_{\text{coupling}} = 4e^2 \mathbf{C}^{-1}[0,1]\hat{n}_1\hat{n}_r \tag{2.87}$$

$$= 4e^2 \frac{C_g}{C_1C_g + C_1C_r + C_gC_r}\hat{n}_1\hat{n}_r \tag{2.88}$$

This by itself is completely sufficient to model the interaction between the qubit and the resonator, but this coupling term is typically re-expressed using a variable g which

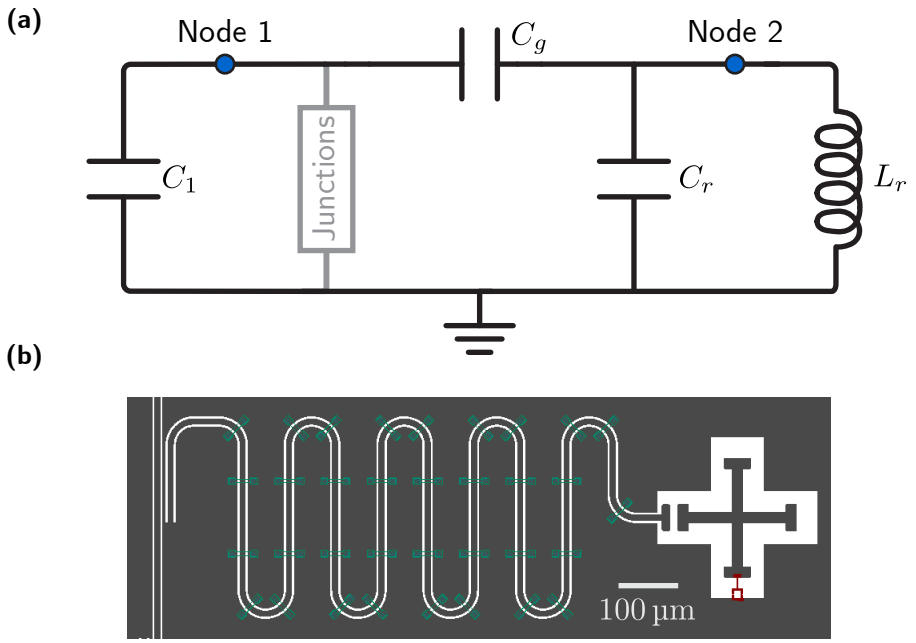

Figure 2-13: **Qubit coupled to resonator (a)** Circuit diagram of a generic single-node qubit capacitively coupled to a readout resonator. **(b)** Image of a qubit capatively coupled to a quarter-wavelength resonator, which is in turn coupled to a transmission line.

is unfortunately defined differently across the fluxonium community and transmon community [44, 47, 56].

Fluxonium - Resonator Coupling

For fluxonium qubits, the coupling g is typically defined as

$$\hat{H}_{\text{coupling}} = -i\hbar g \hat{n}_1 (\hat{a}_r - \hat{a}_r^\dagger), \tag{2.89}$$

where the resonator charge operator has been written out explicitly with its matrix elements absorbed into g. The coupling strength g notably does not include the qubit matrix elements, so that the coupling defined in this way is independent of the qubit and completely determined by the capacitance network and resonator. By equating

this with Eq. (2.88), we find

$$\hbar g = e\sqrt{2\hbar}\left(\frac{C_r}{L_r}\right)^{1/4}\frac{C_g}{C_1C_g + C_1C_r + C_gC_r} \tag{2.90}$$

This can be re-expressed in terms of the impedance of the resonator, $Z_0 = \frac{\pi}{4}\sqrt{\frac{L}{C}}$ for a $\lambda/4$-resonator, which is usually designed to be $50\,\Omega$

$$\hbar g = e\sqrt{\frac{\pi\hbar}{2Z_0}}\frac{C_g}{C_1C_g + C_1C_r + C_gC_r}. \tag{2.91}$$

Transmon - Resonator Coupling

For transmon qubits, the coupling g is often defined through the following coupling Hamiltonian

$$\hat{H}_{\text{coupling}} = -\hbar g(a_1 - a_1^\dagger)(a_r - a_r^\dagger). \tag{2.92}$$

Instead of being motivated as an intrinsic geometric quantity of the circuit, this g describes the size of the avoided level crossing ($2g$) between the resonator and the qubit when they are on resonance. By equating this with Eq. (2.88),

$$g = \frac{1}{2}\sqrt{\omega_1 C_1}\sqrt{\omega_r C_r}\frac{C_g}{C_1C_g + C_1C_r + C_gC_r}. \tag{2.93}$$

To create even more confusion with different conventions, we point out that this g is often expressed in the form

$$\hbar g = 2\beta V_{\text{rms}}\langle 1|\,\hat{n}_1\,|0\rangle \tag{2.94}$$

where V_{rms} is the root mean square voltage of the resonator $V_{\text{rms}} = \sqrt{\hbar\omega_r/2C_r}$ and β is defined as the ratio between the gate capacitance and the total qubit capacitance $\beta = C_g/(C_g + C_1)$. To obtain this formula from the more generic equation Eq. (2.93), one needs to make the approximation $C_r \gg C_1, C_g$

Dispersive Shift

In order to readout the qubit state, the resonators are **dispersively** coupled to the qubit – the coupling strength between the relevant qubit transition and the resonator is much smaller than their detuning. This is typically stated as $|g/\Delta| \ll 1$ using the transmon-resonator definition of g for states $|0\rangle$ and $|1\rangle$ of the qubit, but should be revised to be $|g \langle i| \hat{n} |j\rangle / \Delta| \ll 1$ for the transition $|i\rangle \leftrightarrow |j\rangle$ of a general qubit to be dispersively coupled to the resonator, where Δ is the detuning between that transition and the resonator frequency and g is the geometric coupling strength excluding matrix elements. It is in this dispersive limit in which a mostly longitudinal coupling exists between the dressed qubit states and the resonator, allowing for a **quantum nondemolition** (**QND**) readout. Otherwise, the readout of the resonator can cause state transitions in the qubit, resulting in a non-QND readout.

In this section we will derive the frequency shift of the resonator χ_j depending on the qubit being in $|j\rangle$ using second-order perturbation theory. Taking the fluxonium convention of g, we can write the complete coupled Hamiltonian as

$$H = \hbar \sum_j \omega_j |j\rangle \langle j| + \hbar\omega_r a^\dagger a - i\hbar g \hat{n}(a - a^\dagger). \tag{2.95}$$

Assuming a dispersive coupling, the frequency shift of some state $|j, N\rangle$ (representing the $|j\rangle$ excitation of the qubit and Nth excitation of the resonator) up to second-order perturbation theory is

$$\Delta\omega_{j,N} = \sum_{(k,M)\neq(j,N)} \frac{|\langle k, N| g\hat{n}(a - a^\dagger) |j, N\rangle|^2}{\omega_{j,N} - \omega_{k,M}} \tag{2.96}$$

$$= \sum_{k\neq j} \frac{|\langle k, N+1| g\hat{n}(a - a^\dagger) |j, N\rangle|^2}{\omega_{j,N} - \omega_{k,N+1}} + \frac{|\langle k, N-1| g\hat{n}(a - a^\dagger) |j, N\rangle|^2}{\omega_{j,N} - \omega_{k,N-1}} \tag{2.97}$$

$$= g^2 \sum_{k\neq j} \frac{2\omega_{j,k}N + (\omega_{j,k} + \omega_r)}{\omega_{j,k}^2 - \omega_r^2} |\langle k| \hat{n} |j\rangle|^2 \tag{2.98}$$

$$= g^2 \sum_{k\neq j} \frac{2\omega_{j,k}N}{\omega_{j,k}^2 - \omega_r^2} |\langle k| \hat{n} |j\rangle|^2 + g^2 \sum_{k\neq j} \frac{1}{\omega_{j,k} - \omega_r} |\langle k| \hat{n} |j\rangle|^2 \tag{2.99}$$

where the summation is taken over all states excluding the initial state $|j, N\rangle$.

The first term in Eq. (2.99), proportional to N, is termed the dispersive shift and causes a change in the resonator frequency dependent on the qubit state (and vice-versa).

$$\chi_j \equiv g^2 \sum_{k \neq j} \frac{2\omega_{j,k}}{\omega_{j,k}^2 - \omega_r^2} |\langle k| \hat{n} |j\rangle|^2 \tag{2.100}$$

A common re-writing of this formula involves converting the charge matrix elements into phase matrix elements. This can be done using the facts 1) $[\hat{\phi}, \hat{n}] = i$ and 2) $\hat{\phi}$ commutes with the entirity of $\hat{H}$ except for the $4E_C\hat{n}^2$ term

$$\langle j| [\hat{\phi}, \hat{H}] |k\rangle = (\omega_k - \omega_j) \langle j| \hat{\phi} |k\rangle \qquad \text{(fact 1)} \tag{2.101}$$

$$\langle j| [\hat{\phi}, \hat{H}] |k\rangle = 4E_C \langle j| [\hat{\phi}, \hat{n}^2] |k\rangle \qquad \text{(fact 2)} \tag{2.102}$$

$$= 8iE_c \langle j| \hat{n} |k\rangle \tag{2.103}$$

$$\implies \langle j| \hat{n} |k\rangle = \frac{\omega_{kj}}{8iE_C} \langle j| \hat{\phi} |k\rangle \tag{2.104}$$

The second term in Eq. (2.99) represents a global change in the energy of all resonator states, dependent on the qubit state. Energy changes of this nature are known as **Lamb shifts**. These types of energy changes cannot be directly measured in spectroscopy without uncoupling the qubit from the resonator. Most pertinently, we would like the resonator to have a different frequency depending on whether the qubit is in the ground or excited state. We will use this to define χ, the **dispersive shift**

$$2\chi \equiv (\omega_{1,N+1} - \omega_{1,N}) - (\omega_{0,N+1}, -\omega_{0,N}) \tag{2.105}$$

For the fluxonium qubit, due to the absence of nearest-neighbor selection rules (a single photon can change the qubit state by more than one excitation), an unwieldy sum must be kept in the final expression, as several different transitions may impact the dispersive shift, and these transitions will depend on the exact fluxonium parameters as well. In the regime of fluxonium used in this thesis work, the $|0\rangle \leftrightarrow |3\rangle$ transition was typically closest to the resonator and caused the largest level repulsion.

For transmon qubits, the presence of nearest-neighbor selection rules allows for great simplification for χ. In keeping with typical transmon conventions, we omit the qubit charge matrix element from the χ expression and assume it is accounted for within g

$$2\chi_{\text{transmon}} = \frac{2g^2}{\Delta} - \frac{2g^2}{\Delta + \alpha} \tag{2.106}$$

$$= \frac{2g^2\alpha}{\Delta(\Delta + \alpha)} \tag{2.107}$$

Where $\Delta = (\omega_1 - \omega_0) - \omega_r$ is the detuning and $\alpha = (\omega_1 - \omega_0) - (\omega_2 - \omega_1)$ is the anharmonicity of the transmon.

2.4.2 Qubit - Qubit Coupling

We perform a near identical circuit analysis for two single-node qubits capacitively coupled via capacitance C_c [Fig. 2-14] to find a coupling Hamiltonian described by the capacitance matrix

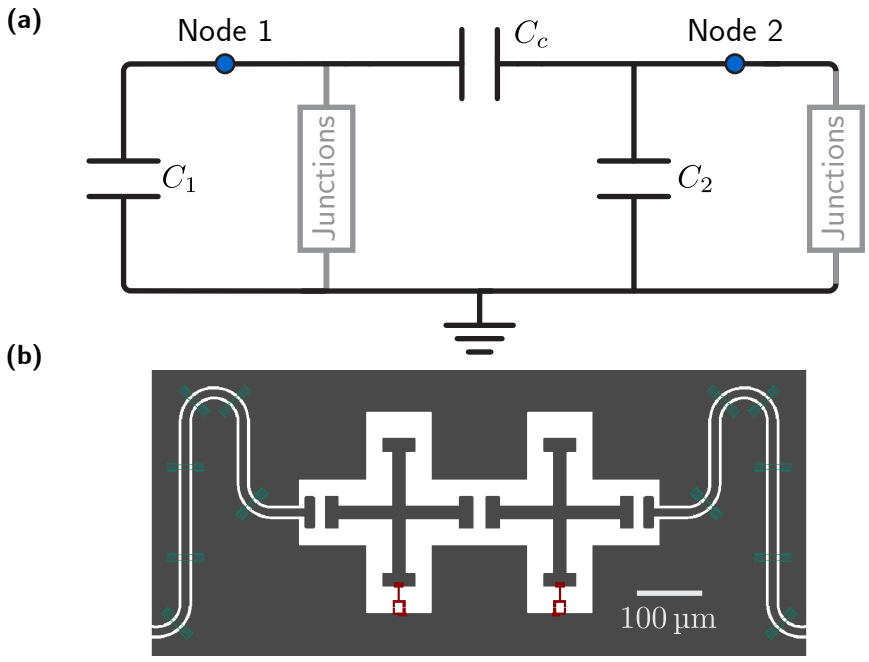

Figure 2-14: **Two capacitively coupled qubits. (a)** Circuit diagram of two capacitively coupled arbitrary single-node qubits. **(b)** Image of a two capacitively coupled qubits, each in turn capacitively coupled to a resonator.

$$\mathbf{C} = \begin{pmatrix} C_1 + C_c & -C_c \\ -C_c & C_2 + C_c \end{pmatrix} \tag{2.108}$$

While there is once again a question of conventions, we choose all qubit-qubit coupling strengths J to be defined as the coefficient of the charge operators in the coupling Hamiltonian

$$\hat{H}_{\text{qubit-qubit}}/\hbar = J\hat{n}_1\hat{n}_2. \tag{2.109}$$

Equating this with the kinetic energy of the circuit, we find

$$\hbar J = 4e^2\mathbf{C}^{-1}[0,1] \tag{2.110}$$

$$= 4e^2\frac{C_c}{C_1C_c + C_2C_c + C_1C_2}. \tag{2.111}$$

Once again, this quantity depends only on the capacitance network of the circuit, and not on the qubit states themselves.

2.4.3 Qubit - Charge Line

In order to charge drive our qubits, we capacitively couple sections of coplanar waveguides with an open terminal to our qubits [Fig. 2-15(a)]. These lines are then con-

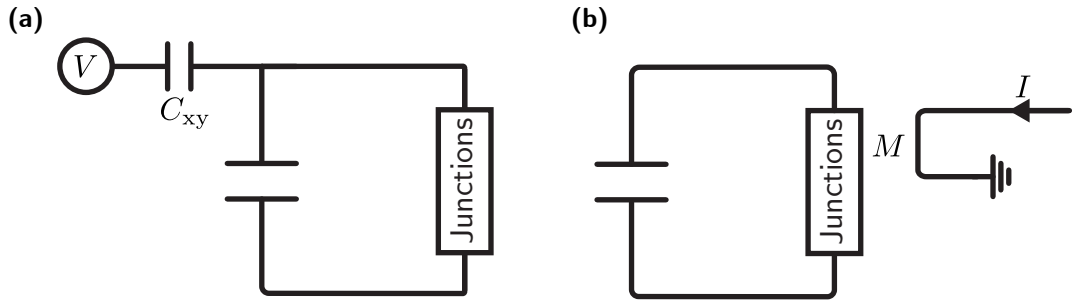

Figure 2-15: **Charge and flux lines. (a)** Circuit diagram of a charge line capacitively coupled to a qubit. **(b)** Circuit diagram of a flux line inductively coupled to a qubit.

nected through wirebonds to coaxial cables extending from the device up to room temperature. An RF voltage bias applied at the top of the fridge then propagates

downward to interact with the qubit. We model these lines carrying classical voltage by adding a term

$$\frac{1}{2}(\dot{\Phi}_j - V_i)^2 C_{\mathrm{xy},ij}, \tag{2.112}$$

where V_i is a classical voltage capacitively coupled via capacitance $C_{\mathrm{xy},ij}$ to circuit node j. The resulting Lagrangian (omitting the potential energy component and including only the kinetic portion for brevity of equations) is then

$$\mathcal{L} = \frac{1}{2}\dot{\vec{\Phi}}^T \mathbf{C} \dot{\vec{\Phi}} + \frac{1}{2}\sum_{ij}(\dot{\Phi}_j - V_i)^2 C_{\mathrm{xy},ij} + \cdots \tag{2.113}$$

$$= \frac{1}{2}\dot{\vec{\Phi}}^T \mathbf{C} \dot{\vec{\Phi}} + \frac{1}{2}(\dot{\vec{\Phi}}^T \mathbf{N}_{\mathrm{xy}} \dot{\vec{\Phi}} - 2\vec{V}^T \mathbf{C}_{\mathrm{xy}} \dot{\vec{\Phi}} + \vec{V}^T \mathbf{M}_{\mathrm{xy}} \vec{V}) + \cdots \tag{2.114}$$

$$= \frac{1}{2}\dot{\vec{\Phi}}^T \mathbf{C} \dot{\vec{\Phi}} + \frac{1}{2}\dot{\vec{\Phi}}^T \mathbf{N}_{\mathrm{xy}} \dot{\vec{\Phi}} - \vec{V}^T \mathbf{C}_{\mathrm{xy}} \dot{\vec{\Phi}} + \text{const.} + \cdots \tag{2.115}$$

$$\tag{2.116}$$

Where $\vec{V}$ is an $m \times 1$ vector of classical voltages, $\vec{\Phi}$ is the $n \times 1$ vector of node flux variables, $\mathbf{C}_{\mathrm{xy}}$ is an $m \times n$ matrix encapsulating the capacitive coupling of each voltage source to each node, $\mathbf{N}_{\mathrm{xy}}$ is an $n \times n$ diagonal matrix constructed from the summed rows of $\mathbf{C}_{\mathrm{xy}}$ ($\mathbf{N}_{\mathrm{xy},jj} = \sum_i \mathbf{C}_{\mathrm{xy},ij}$), and $\mathbf{M}_{\mathrm{xy}}$ is an $m \times m$ diagonal matrix constructed from the summed columns of $\mathbf{C}_{\mathrm{xy}}$ ($\mathbf{M}_{\mathrm{xy},ii} = \sum_j \mathbf{C}_{\mathrm{xy},ij}$).

Proceeding with the normal Legendre transformation,

$$\vec{q} \equiv \frac{\partial \mathcal{L}}{\partial \dot{\vec{\Phi}}} = (\mathbf{C} + \mathbf{N}_{\mathrm{xy}})\dot{\vec{\Phi}} - \mathbf{C}_{\mathrm{xy}}^T \vec{V} \tag{2.117}$$

$$\dot{\vec{\Phi}} = (\mathbf{C} + \mathbf{N}_{\mathrm{xy}})^{-1}(\vec{q} + \mathbf{C}_{\mathrm{xy}}^T \vec{V}) \tag{2.118}$$

we see that we now have a shifted charge coordinate, corresponding to the additional charge induced by the external voltage and the added node capacitances. After performing the transformation into the Hamiltonian and adding back in the junction potential energy terms, we arrive at the following Hamiltonian

$$H = \frac{1}{2}\vec{q}^T(\mathbf{C} + \mathbf{N}_{\mathrm{xy}})^{-1}\vec{q} + \vec{V}^T \mathbf{C}_{\mathrm{xy}} \mathbf{C}^{-1} \vec{q} + \frac{1}{2}\vec{\Phi}^T L_{\mathrm{inv}} \vec{\Phi} + V_{\mathrm{JJ}}(\vec{\Phi}). \tag{2.119}$$

Qualitatively the additional classical voltage sources produce two effects. The first smaller effect is add on to the capacitances of all the nodes. The second more significant effect is to introduce a classical linear driving term onto the system, proportional to the applied voltage $\vec{V}^T \mathbf{C}_{\text{xy}} \mathbf{C}^{-1} \vec{q}$. This linear drive is an essential feature, completing the analogy of voltage driven superconducting qubits with linearly driven two-level systems.

2.4.4 Qubit - Flux Line

The final component introduced in this Section will be the flux line, which is made of a ground-terminated section of coplanar waveguide [Fig. 2-15(b)]. Instead of a voltage antinode at the end of the line, there is a current antinode, which may induce currents in closed loops of the circuit. Multiple flux lines allow us to accurately adjust the external flux of different qubits simultaneously (after any crosstalk is compensated for). The induced flux Φ_{ext} into the qubit loop is characterized by the mutual inductance

$$\Phi_{\text{ext}} = MI, \tag{2.120}$$

where I is the current propagating down the flux line.

2.5 A Time Limit for Qubits

While the entirety of this Chapter has been devoted to understanding the Hamiltonian of different circuits and thus their unitary time evolution, various external loss channels limit the time for which useful computations can be performed. In this brief introduction, only a few of the most limiting loss mechanisms will be discussed, with more comprehensive treatments can be found in Nguyen et al. [67] and Koch et al. [44].

Most qubits' lifetimes are limited by electric field coupling to defects residing on the surfaces of the materials which form the physical qubit; this is known as **dielectric loss** [67]. Throughout the history of superconducting qubit design, much effort has

been made in reducing the amount of defects which reside in regions of high electric field density. Modeling the loss of the qubit energy into this continuum of defects via Fermi's golden rule, the decay rate of a qubit at frequency ω_{01} is given by

$$\Gamma_{01}(\omega_{01}) = \frac{1}{\hbar^2} |\langle 0| 2e\hat{n} |1\rangle|^2 S_{\text{diel}}(\omega_{01}) \tag{2.121}$$

with spectral density

$$S_{\text{diel}}(\omega_{01}) = \frac{\hbar}{CQ_{\text{diel}}(\omega_{01})} \left(1 + \coth \frac{\hbar\omega}{2k_B T}\right). \tag{2.122}$$

Here, C is the effective qubit capacitance, given by $E_C = e^2/2C$, and Q_{diel} is a frequency-dependent quality factor associated with the capacitance. This quality factor may also be expressed as a loss tangent via $\tan\delta^{-1} \equiv Q_{\text{diel}}$.

A more controllable source of qubit decay is the **Purcell effect**. Intuitively, it can be thought that the qubit inherits part of the resonator coupling to the environment, resulting in an increased decay rate of the qubit. In the dispersive (qubit-resonator coupling strength less than the qubit-resonator detuning, $g < \Delta$) strong (coupling strength larger than the resonator linewidth, $g > \kappa$) coupling regime, this contribution is

$$\Gamma_{\text{purcell}} = \kappa \frac{g^2}{\Delta^2}. \tag{2.123}$$

The quantity g in the above expression is defined to include the matrix element for the qubit transition. This naturally imposes a trade-off between fast measurement and qubit lifetimes. A higher κ gives fast measurement, but increased Purcell decay. A **Purcell filter** gives a way to introduce a frequency dependent κ by coupling two resonators in series, so that it is higher at the resonator frequency, and lower at the qubit frequency [84].

Coupling between the qubit and the resonator can additionally result in pure dephasing. Due to the dispersive coupling between the qubit and resonator, the qubit frequency also in turn depends on the state of the resonator. This is immaterial during readout, as readout projects the qubit state anyways, but any fluctuations in

the resonator state before the readout contributes to unwanted qubit dephasing. This dephasing source is termed **photon shot noise**, with resonator state fluctuations determined by residual photons from previous pulses or the thermal distribution of photons in the resonator at some effective resonator temperature T, typically around 55 mK in the setups at EQuS [104]

$$n_{\text{th}}(\omega) = \frac{1}{\exp(\hbar\omega/k_B T) - 1}. \tag{2.124}$$

In the limit of small $n_{\text{th}}(\omega)$, the dephasing contribution due to shot noise is

$$\Gamma_\phi^{\text{SN}} = \frac{4\chi_{01}^2\kappa}{\kappa^2 + 4\chi_{01}^2} n_{\text{th}}(\omega), \tag{2.125}$$

where χ_{01} is defined as half the resonator shift between the qubit being in the $|0\rangle$ and $|1\rangle$ state ($2\chi_{01} \equiv \chi_1 - \chi_0$) [34].

A more direct source of dephasing is **flux noise** in flux-tunable qubits. Since the qubit frequency depends on the external flux, any noise in flux directly translates into noise in the qubit frequency. Flux noise can either arise from noise in the control electronics or from magnetic defects located on the surfaces of the device. With proper line filtering and grounding, the dominant contribution to flux noise will come from material defects, which will be the primary subject of the next chapter.

Chapter 3

Minimizing Flux Noise in Tunable Qubits

Many promising superconducting qubit architectures rely on frequency-tunable qubits, where the qubit frequency can be varied by an applied magnetic flux. Away from first-order insensitive points, so called "sweet spots," the dominant source of dephasing in these qubits [7, 4] is low-frequency flux noise with a power spectral density (PSD) that is inversely proportional to frequency [72]. Such $1/f$ noise is ubiquitous in condensed matter systems [28] and was observed in the context of Josephson devices more than three decades ago [45]. This $1/f$ noise in superconducting quantum interference devices (SQUIDs) has been shown to cause qubit dephasing [107, 42, 46, 9, 36, 105, 16] as well as qubit relaxation [105, 77]. It was proposed that $1/f$ flux noise in qubits comprising SQUIDs originates from magnetic two-level system defects residing in the oxide layers in proximity to the SQUID loops [46]. The model assumes a temperature-activated flipping of independent electronic spins that are randomly oriented and have a random energy distribution [28], leading to a $1/f$ noise PSD. Oxygen adsorbates were determined to be candidate sources for such spin defects by density functional theory calculations [99] and x-ray spectroscopy [48].

An analytic approximation of this particular microscopic model has been derived by Bialczak *et al.* [9], yielding an expression for the noise PSD $S(\omega) \propto R/W$, where R is the radius of the SQUID loop and W is the width of the superconducting wire

forming the loop. Indications of such scaling with wire width have been reported [49], but experiments with superconducting phase qubits could not quantitatively confirm the noise amplitudes predicted by the microscopic model, mostly due to uncertainties in the surface spin density. Furthermore, the formation of spin clusters was proposed in order to reconcile the observed noise levels with the model [83, 3]. The origin and microscopic nature of $1/f$ noise in SQUIDs has remained an unsolved question.

In this Chapter, we study $1/f$ flux noise in more than 50 capacitively shunted flux qubits [105] with systematically varied parameters of their qubit loop geometry. Our data show quantitative agreement with the proposed microscopic model of independent magnetic defects that reside at the metal-surface and metal-substrate interfaces. In particular, we demonstrate that the extracted flux noise amplitudes follow the expected trends over a large range of loop parameters and for a noise bandwidth relevant to contemporary quantum circuits. We further validate this agreement by introducing a numerical extension to the model, overcoming the limited applicability and accuracy of the analytic approximation [9] for realistic circuit geometries.

3.1 Flux Noise Model

For our flux-noise model, we assume non-interacting magnetic two-level system (TLS) defects distributed uniformly across the interfaces surrounding the junction loop. We model these TLS's as spins with magnetic moment $\vec{m}$, each coupled to the junction loop through a flux-mediated mutual inductance [46, 9]. If a current I_{QB} in the junction loop would cause a magnetic field $\vec{B}$ at the location of the TLS, then the magnetic flux induced in the junction loop by this TLS can be derived as

$$\Phi_{\mathrm{TLS}} = \vec{B} \cdot \vec{A}_{\mathrm{TLS}} \tag{3.1}$$

$$\Phi_{\mathrm{TLS}} = \frac{\vec{B} \cdot \vec{m}}{I_{\mathrm{TLS}}} \tag{3.2}$$

$$\Phi_{\mathrm{TLS}} I_{\mathrm{TLS}} = \vec{B} \cdot \vec{m} = \Phi_{\mathrm{QB}} I_{\mathrm{QB}} \tag{3.3}$$

$$\Phi_{QB} = \frac{\vec{B} \cdot \vec{m}}{I_{\mathrm{QB}}}. \tag{3.4}$$

We compute the average variance of the flux induced by a single TLS by performing a spherical integral assuming a uniformly random distribution of TLS orientations (let θ be the angle between $\vec{B}$ and $\vec{m}$)

$$\Phi^2_{\text{single}} = \left\langle \left(\frac{\vec{B} \cdot \vec{m}}{I_{\text{QB}}} \right)^2 \right\rangle_{\text{angles}} \tag{3.5}$$

$$= \frac{Bm}{I_{\text{QB}}} \frac{\int_0^\pi \cos^2\theta \sin\theta d\theta}{\int_0^\pi \sin\theta d\theta} \tag{3.6}$$

$$= \frac{1}{3}\left(\frac{Bm}{I_{\text{QB}}} \right)^2. \tag{3.7}$$

From here, we can calculate the total flux variance by integrating over the entire areal surface of the junction loop

$$\langle \Phi^2 \rangle = \frac{1}{3}\sigma m^2 \int \left(\frac{B}{I_{\text{QB}}} \right)^2 dA \tag{3.8}$$

where σ is the areal density of defects.

The geometries for a toroidal loop and a circular junction loop with rectangular cross-section have been treated by Ref. [9]. For the geometry in our experiment – a rectangular loop with rectangular cross-section – we find

$$\langle \Phi^2 \rangle = \frac{1}{3} m^2 \sigma P \int \left(\frac{B(x)}{I_{\text{QB}}} \right)^2 dx, \tag{3.9}$$

where $P = 2X + 2Y + 4W$ is the perimeter of the loop with X, Y, and W (width) being the loop dimensions as shown in Fig. 3-1. In this calculation, we only integrate over the top surface of the metal-air interface. The remaining integral, parameterized by x, is taken over the lengths of the considered interfaces perpendicular to the extension of the loop arms (across the width of the arms).

3.1.1 Analytic Approximation

The analytic approximation of the model only considers the top surface of the junction loop as a host for magnetic defects, assuming an effectively two-dimensional film with

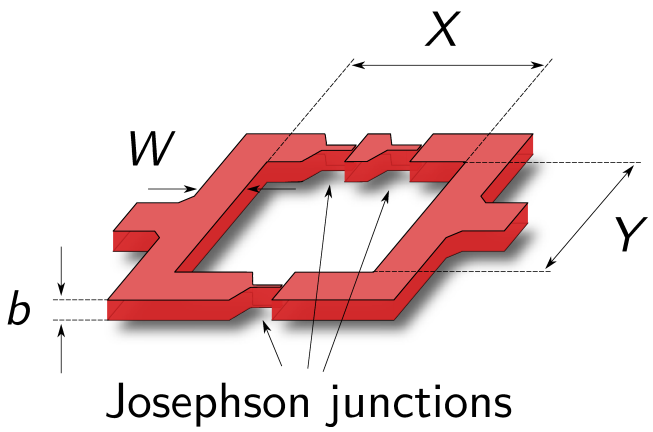

Figure 3-1: **3D illustration of the Josephson junction loop of a C-shunt flux qubit.**

$W \gg b$. In the integrals involved in this calculation, $x = 0$ is treated as the center of the loop wire and $x = \pm W/2$ corresponds to its two edges. Assuming that the superconducting current flows only at the loop surface, the magnetic field at the surface is given by $B(x) = \mu_0 K(x)/2$ where $K(x)$ is the surface current density (this can be derived in a textbook use case of Ampere's law). We use a surface current density proportional to $1/\sqrt{1-(2x/W)^2}$ [80] away from the edges, joined by an exponential near the edges at $x = \pm(W/2 - \lambda^2/2b)$, where λ is the superconducting penetration depth of aluminum. Enforcing that the current density has continuous slope, we obtain the following function for the current density along the width of the loop

$$K(\bar{x}) = \begin{cases} K_0 \frac{1}{\sqrt{1-(2\bar{x})^2}} & |\bar{x}| \leq (1-\epsilon)/2 \\ K_0 \sqrt{\frac{e}{2\epsilon}} \exp\left[\left(|\bar{x}| - \frac{1}{2}\right)/\epsilon\right] & (1-\epsilon)/2 < |\bar{x}| \leq 1/2 \end{cases} \tag{3.10}$$

where $\bar{x} \equiv x/W$ and $\epsilon \equiv \lambda^2/bW$. Since $\epsilon \ll 1$, we keep only leading order terms in ϵ. Evaluating Eq. (3.9) with this particular $B(x)$ and using the definition $I = \int K(x)\,dx$, we obtain

$$\langle \Phi^2 \rangle = \frac{1}{3}\sigma m^2 P \left(\frac{\mu_0}{2}\right)^2 \frac{\int x K(x)^2\,dx}{(\int x K(x)\,dx)^2} \tag{3.11}$$

$$= \frac{\mu_0^2}{3\pi} m^2 \sigma \frac{P}{W} \left(\frac{\ln(2bW/\lambda^2)}{2\pi} + \frac{e-1}{2\pi}\right). \tag{3.12}$$

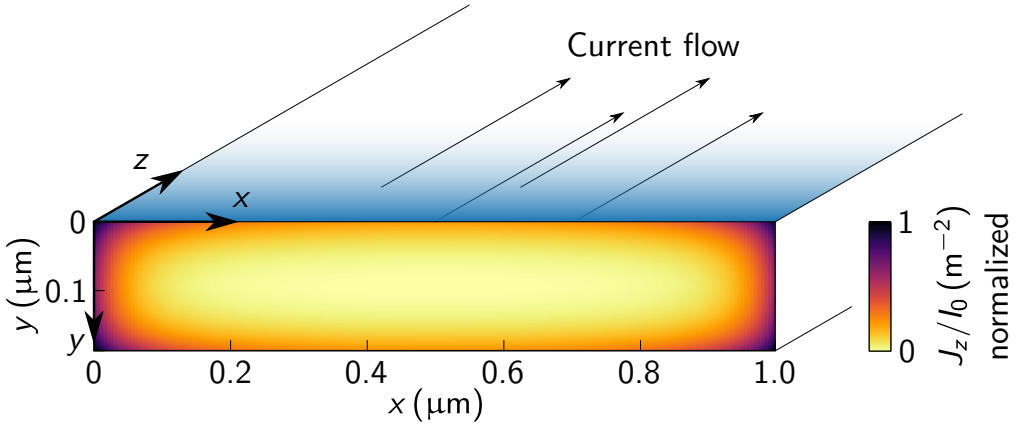

Figure 3-2: **Schematic drawing of a section of the junction loop in our experiment.** Current is flowing along the z-direction and we plot the numerically simulated current distribution J_z/I_0 at its cross-section, normalized to a reference current I_0. Simulation parameters are a standard design with wire width $W = 1\,\mu\text{m}$ and film thickness $b = 190\,\text{nm}$. In order to compute the magnetic field on the surface of the strip (blue) that enters in the flux noise model Eq. (3.9), we use Biot-Savart's law.

The important trends are that the flux variance, and therefore the flux noise power, increases linearly with the average perimeter P of the loop and decreases roughly inversely with its width W.

3.1.2 Numerical computation of the current distribution in a superconducting strip of finite thickness

We numerically compute the current distribution in a superconducting strip following the approach presented in Weeks et al. [101] and its extension by Sheen et al. [88]. It is based on the two-fluid model of superconductivity [96], where a complex conductivity accounts for both the resistive loss channel at non-zero frequencies (real part) as well as the kinetic energy of the supercurrent (imaginary part). The normal current is described by Ohm's law while the kinetic contribution is added through London's equation. The superconducting penetration depth λ enters via the complex conductivity.

We apply this method to calculate the current distribution in a single superconducting strip that is extended in the z-direction and discretized into an appropriate

number of parallel patches in the xy plane [see Fig. 3-2]. We extract the current distribution from the transmission line equation

$$\vec{I}(\omega) \propto -i\omega \mathbf{Y} \vec{V}, \tag{3.13}$$

where all voltages are set to an identical value (unity). The admittance matrix $\mathbf{Y}$ is comprised of a resistive part and an inductive part, which in turn depend on the complex conductivity and partial inductances that reflect the model geometry [101]. By dividing the currents I penetrating each patch by their cross-sectional area, we readily find the volume current density $J(x, y)$ in the xy-plane.

Subsequently, we find the magnetic field $\vec{B}(x)$ on the surface of the strip (blue region in Fig. 3-2) with Biot-Savart's formula by integrating the current density $J(x, y)$ over the volume of the junction loop,

$$\vec{B}(\vec{r}) = \frac{\mu_0}{4\pi} \iiint_V \frac{J(x,y)\hat{z} \times \vec{r}'}{|\vec{r}'|^3} \, dV, \tag{3.14}$$

where $\hat{z}$ denotes the unit vector along z and $\vec{r}'$ is the vector from any point in the integration volume to the point where the field is being computed. The norm of this magnetic field, which is mainly directed along x except for some contribution along y close to the edges, enters our flux noise model Eq. (3.9), where it is integrated again along the x-dimension. The integrations are numerically approximated by Riemann sums. We chose different numerical discretizations in the successive integrations along x in order to exclude a systematic error and verified our numerical procedure by observing its convergence.

In Fig. 3-3, we show the results of the numerical simulations for different thickness regimes of the superconducting film forming the loop. For each thickness b, we plot the numerically obtained factor $\int B^2(x)/I^2 \, dx$, a measure for the normalized magnetic field variance, versus the inverse wire width $1/W$. We show simulation results accounting for defect spins located only in the top surface of the loop (purple), and we also plot the numerical results taking into account all relevant interfaces (red), which are the top and bottom surfaces of the loop arms, their side faces, and the silicon-

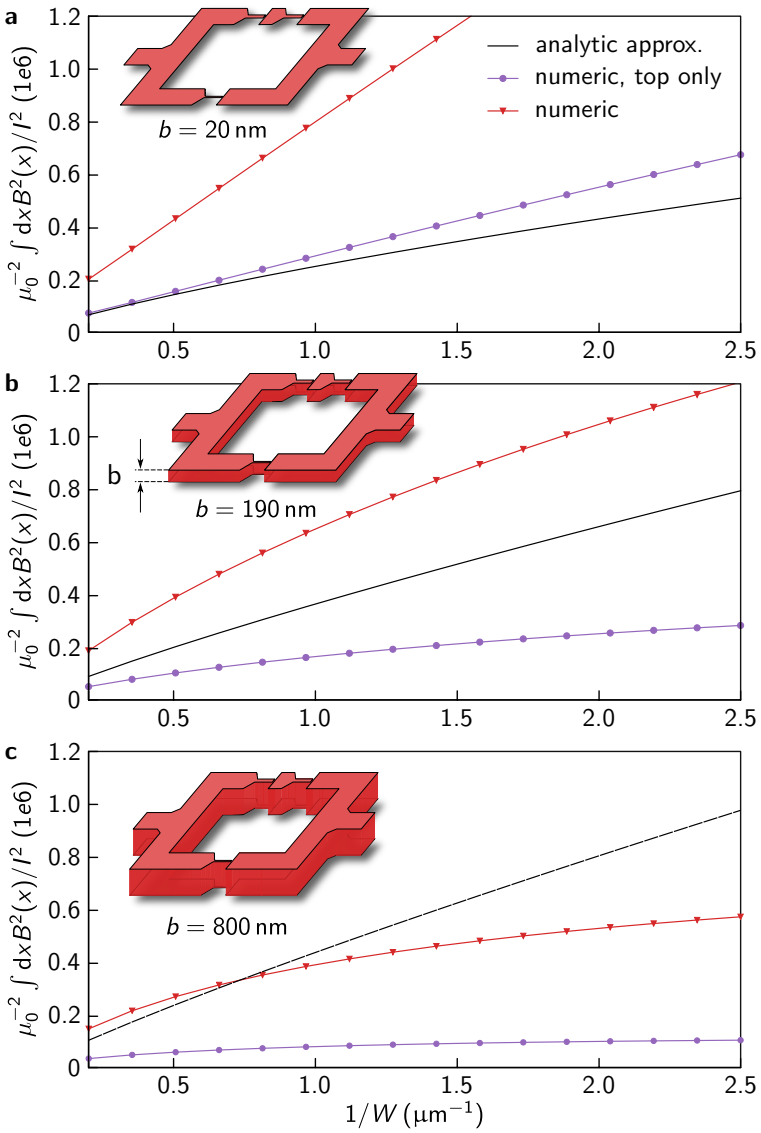

Figure 3-3: **Numerical simulation results for various film thicknesses b.** We plot the numerical value $\mu_0^{-2} \int B^2(x)/I^2\, dx$ which enters the model for magnetic flux noise in Eq. (3.9), replacing the analytic approximation. The purple lines and circles show the results for only considering the top surface of the loop and the red lines with triangles show the result for both the top surface and the side faces summed. The analytic approximation is given as a black line. **(a)** Results for a very thin aluminum thickness $b = 20\,\mathrm{nm}$, where the numerical simulation agrees with the analytic formula for $W \gg b, \lambda$. **(b)** Results for the thickness $b = 190\,\mathrm{nm}$ as used in our experiment. **(c)** The analytic expression breaks down entirely for a thick film with $b = 800\,\mathrm{nm}$, while the numerical result indicates a reduced noise sensitivity as compared to smaller wire thicknesses.

vacuum interfaces in the vicinity of the loop assuming an equal spin density across interfaces. The numerical simulation of the top surface can be directly compared to the analytic approximation, which we've computed previously to be

$$\int B^2(x)/I^2\,dx = \frac{\mu_0^2}{\pi W}\left(\frac{\ln(2bW/\lambda^2)}{2\pi} + \frac{e-1}{2\pi}\right). \tag{3.15}$$

We first verify our numerical approach by comparing simulation results for a thin strip with $b = 20\,\text{nm}$ to the result obtained with the approximate formula [see Fig. 3-3(a)]. For large wire widths $W \gg b, \lambda$ in particular, the approximation of the analytic formula is valid and it matches the numerical result for considering defect spins only in the top surface. For thin films, the numerical result recovers the expected linear dependence of $\int B^2(x)/I^2\,dx$ on $1/W$ to first order. Small deviations for smaller W reveal the limitation of the approximate formula [80]. For the film thickness $b = 190\,\text{nm}$ used in our experiment [see Fig. 3-3(b)], the numerical result and the analytic approximation diverge even for large W since the condition $b \sim \lambda$ is violated. For an even larger thickness of $b = 800\,\text{nm}$, the analytic approximation breaks down completely [see Fig. 3-3(c)]. Remarkably, we find that increasing the film thickness b reduces the noise amplitude considerably, an effect analogous to the reduction in noise with increasing wire width W. We want to point out that the contribution from the side faces of the junction loop vanishes in the limit of $b \to 0$ [see Fig. 3-3(a)].

3.2 Experimental Setup

Our experiment incorporates results from six different samples each comprising ten uncoupled, capacitively-shunted flux qubits [106] [see Fig. 3-4]. Qubit control and dispersive state readout are performed through individual capacitively coupled $\lambda/4$ waveguide resonators, which are in turn inductively coupled to a common $50\,\Omega$ transmission line. The samples are cooled down to approximately 10 mK in a Leiden dilution refrigerator. Microwave transmission through the transmission line is used to projectively measure the qubit state with a heterodyne detection scheme at room

temperature.

The samples are fabricated on a silicon substrate by dry etching an MBE grown, 250 nm thick aluminum film in an optical lithography process and then diced in $5 \times 5\,\mathrm{mm}^2$ chips. The junction loops, colored in red in Fig. 3-4(c), are fabricated with an electron beam lithography process and a double angle shadow evaporation technique [27] to form the Josephson junctions. Across the entire area of the junction loops, we evaporate 40 nm and 150 nm thick aluminum films, separated by an oxide layer created with a controlled in-situ oxidation. In addition to the desired Josephson junctions, this step also creates a large parasitic oxide layer between the aluminum films, which has been shown to host electric dipole two-level system defects that lead to qubit relaxation [50].

The Hamiltonian parameters of each flux qubit are nominally identical, with a shunt capacitance of 56 fF, a Josephson energy of the large junctions of $E_J/h = 36\,\mathrm{GHz}$, a capacitance across each large junction of 5 fF, and a large to small junction area ratio of 0.42. We observed a mean qubit frequency of 4.6 GHz and anharmonicity of 480 MHz at the half-flux sweet spot. These parameters are meant to match qubit A in Yan et. al. [106]. Across all flux qubits, we only vary the geometric parameters of their junction loops as illustrated in Fig. 3-4(d). While the thickness $b = 190\,\mathrm{nm}$ of the bilayer aluminum film is fixed, the side lengths, X, and Y, referenced to the inner circumference, and the wire width W are varied. Every sample varies either the inner loop perimeter $2X + 2Y$, the aspect ratio X/Y, or the width W. In order to reduce systematic errors, each qubit variant is represented twice within a chip, resulting in five distinct loop geometries per chip. The ranges of the parameter variations are centered around state-of-the-art values used in high-coherence c-shunt flux qubits, $X = 9\,\mu\mathrm{m}$, $Y = 8\,\mu\mathrm{m}$, and $W = 1\,\mu\mathrm{m}$ [106]. Figure 3-4(e) shows the effective circuit schematic for the one qubit-resonator pair coupled to the common transmission line, and a global coil located in the package lid is used to tune the flux threading the junction loops.

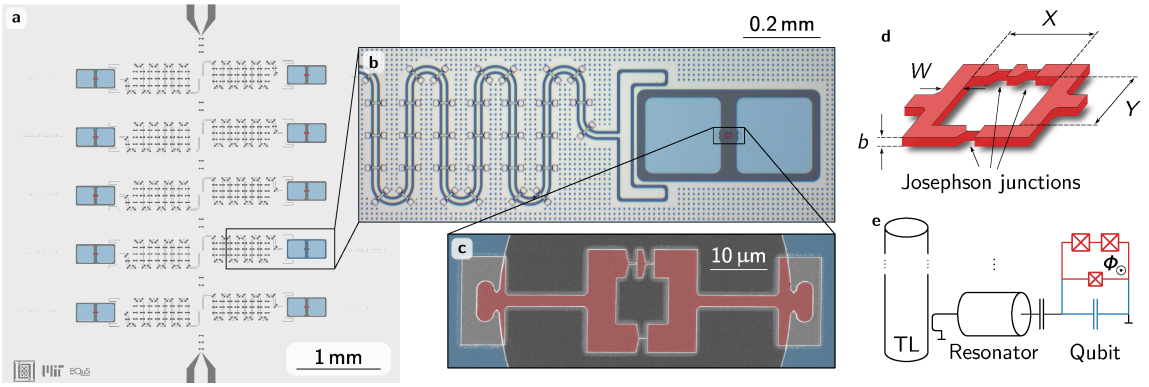

Figure 3-4: **Noise spectroscopy device.** **(a)** Each chip holds ten uncoupled capacitively shunted flux qubits with individual readout resonators, featuring five different junction loop geometries at a two-fold redundancy. **(b)** Optical micrograph of one of the qubits and part of its readout resonator. The capacitive shunt is colored in blue. **(c)** Electron microscope image of a fabricated C-shunt junction loop. **(d)** Schematic representation of the loop parameters varied across different designs. The loop dimensions X, Y are measured along the inner edge of the SQUID, W is the width of the superconducting leads, and b is the film thickness. **(e)** Effective schematic for one qubit-resonator pair coupled to the common transmission line (TL).

3.3 Experimental Protocol

We perform noise spectroscopy for every qubit using a sequence of measurements first demonstrated in [107]. We first extract the qubit spectrum around the sweet spot, $\Phi_{\text{ext}} = \Phi_0/2$ [see Fig. 3-5(a)]. Subsequently, we perform a spin-echo experiment, where a π-pulse in the middle of a Ramsey sequence inverts the sign of the phase accrual rate, mitigating quasi-static or low-frequency noise. As shown in Fig. 3-5(b), we observe an exponential decay function at the sweet spot, where decoherence is relaxation limited. Further away from the sweet spot, the decay function is predominantly Gaussian, indicative of pure dephasing due to $1/f$ noise [55, 107]. The Gaussian pure dephasing rate takes the form

$$\Gamma_\phi^{\text{E}} = \sqrt{A_\Phi \ln 2}\,|\partial\omega/\partial\Phi| \tag{3.16}$$

for the echo experiment, assuming Gaussian statistics of the qubit phase accumulation [55, 14] and a noise PSD $S_\Phi(\omega) = A_\Phi/|\omega|$ with noise amplitude $\sqrt{A_\Phi}$. To find

the exponential decay rate Γ_{exp} and Gaussian dephasing rate Γ_ϕ^{E}, we perform a fit to the decay function

$$p(t) \propto \exp[-\Gamma_{\mathrm{exp}} t - (\Gamma_\phi^{\mathrm{E}} t)^2] \tag{3.17}$$

[107] for each flux bias point. For the individual fits, Γ_{exp} is kept a free parameter with an initial guess of $(2T_1)^{-1}$, as extracted in a preceding relaxation measurement. In order to numerically extract the slope of the spectrum, we fit the hyperbola $\hbar\omega(\Phi) = \sqrt{\Delta^2 + \epsilon(\Phi)^2}$ to the data in Fig. 3-5(a), which is a good approximation over the measured range close to the sweet spot [105].

Figure 3-5(c) shows the pure dephasing rate Γ_ϕ^{E} as a function of the slope of the spectrum for one of the measured qubits. We perform two separate linear fits (for positive and negative slope) and extract the noise amplitude $\sqrt{A_\Phi}$ and its uncertainty from an error-weighted average. Since pure dephasing in the Gaussian approximation vanishes at the sweet spot, we enforce an intercept with the origin. About 20% of the qubits show a bending of data points to a finite (positive) dephasing rate near the sweet spot. We attribute these deviations to other higher-frequency dephasing processes, which do not significantly compromise the extracted noise amplitudes. The validity Eq. (3.16) is limited to a noise PSD $S(\omega) \propto \omega^{-\alpha}$ with $\alpha = 1$. While $1/f$ noise has been observed with a scaling where $\alpha \leq 1$ [16, 40, 28, 72], this assumption is compatible with previous experiments extrapolated to $\sim 10\,\mathrm{mK}$ [3] and is supported by the Gaussian decay function we observe in our experiment.

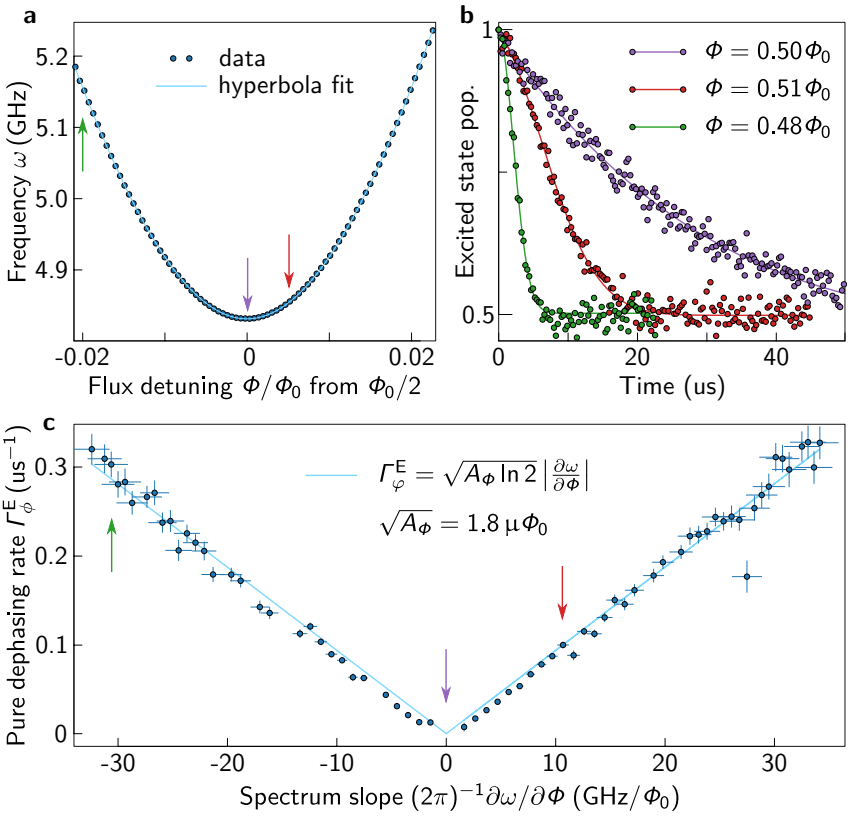

Figure 3-5: **Experimental technique used for noise spectroscopy.** **(a)** Qubit spectrum around its flux sweet spot at $\Phi = \Phi_0/2$. A hyperbolic fit enables us to numerically extract the slope $(2\pi)^{-1}\partial\omega/\partial\Phi$ of the spectrum. **(b)** Spin echo dephasing traces at three illustrative locations of the spectrum (indicated by the arrows). **(c)** By plotting the extracted pure dephasing rates Γ_ϕ^{E} as a function of the spectrum slope, we can extract the $1/f$ flux noise amplitude $\sqrt{A_\Phi}$ from a linear fit.

3.4 Geometric Trends

Figure 3-6 shows the measured flux noise amplitudes $\sqrt{A_\Phi}$ as a function of the loop geometry. We categorize the design variations into two groups. Qubits in the first group have loops with a constant wire width $W = 1\,\mu\text{m}$ but varying perimeters $21\,\mu\text{m} \leq P \leq 101\,\mu\text{m}$ [see Fig. 3-6(a)]. We define the perimeter $P = 2X + 2Y + 4W$, measured along the center-line of the wire. The second group of measured qubits have loops with a fixed inner perimeter $2X + 2Y = 34\,\mu\text{m}$ and varying wire width $0.4\,\mu\text{m} \leq W \leq 5\,\mu\text{m}$ [see Fig. 3-6(b)]. These sub-categories can be understood as line-cuts in the two dimensional parameter space $\sqrt{A_\Phi(P, W)}$, given in Fig. 3-7(a). Measured data show an approximately linear dependence of the noise power A_Φ on perimeter P [see Fig. 3-6(a)] and on the inverse wire width W [see Fig. 3-6(b)]. By investigating loops of varying aspect ratio X/Y, we are able to confirm the linear scaling of A_Φ with loop perimeter rather than its area.

Finally, we compare our experimental data with the previously derived model of $1/f$ flux noise arising from magnetic defects on the loop interfaces, reproduced here for convenience.

$$\langle \Phi^2 \rangle = \frac{\mu_0^2}{3\pi} m^2 \sigma \frac{P}{W} \left(\frac{\ln(2bW/\lambda^2)}{2\pi} + \frac{e-1}{2\pi} \right), \tag{3.18}$$

The scaling of flux noise with loop perimeter P can be intuitively understood, since the total number of magnetic defects increases proportionally. The inverse scaling with wire width W is less intuitive, given the increased number of participating defects for wider wires. It can be motivated by the following picture: for a constant persistent current in the loop, the magnetic field is diluted across more defect spins residing in the interfaces when increasing the wire width. Since the defects are uncorrelated, their contribution to the total flux noise partially cancels, resulting in an effective decrease of the total flux noise. Independent of the geometry, a uniform current density across the width of the loop arms minimizes the flux noise amplitude. The current distribution across the width of the junction loop only enters the flux noise

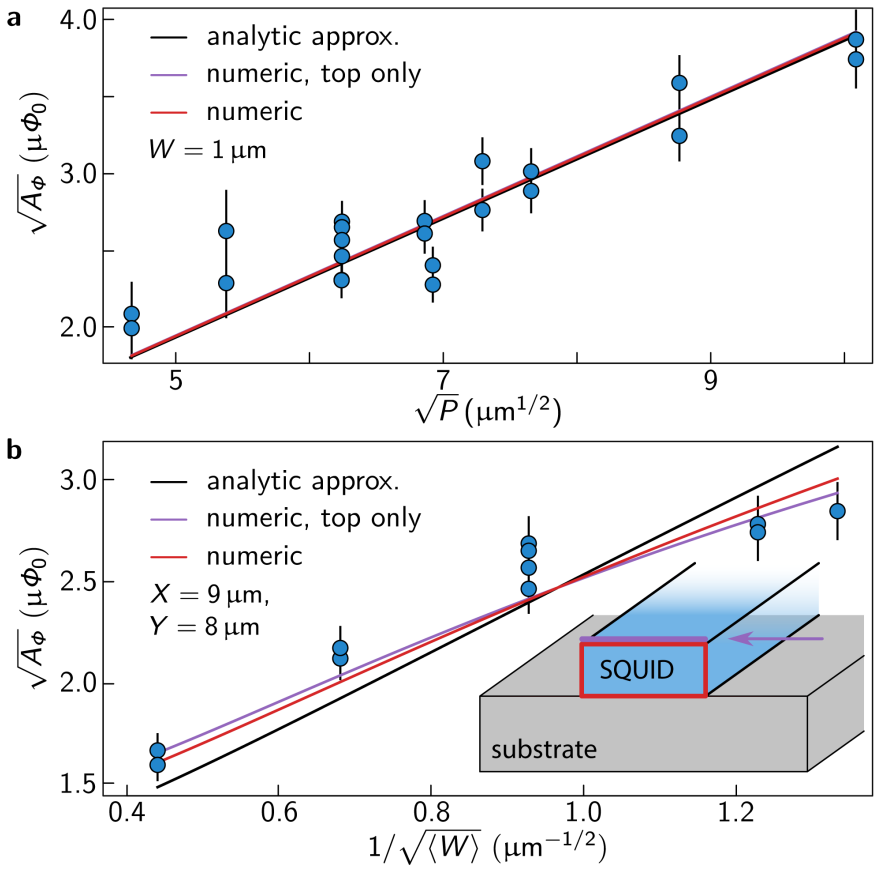

Figure 3-6: **1D plots of flux noise against perimeter and width.** Flux noise amplitudes $\sqrt{A_\Phi}$ as a function of SQUID geometry parameters for **(a)** constant wire width W and **(b)** constant inner perimeter $2X + 2Y$. Each line corresponds to an independent fit in this two-dimensional parameter space to the analytic approximation (black) and numeric variations (purple and red) of the model (see inset).

amplitude through the factor

$$\frac{\int K(x)^2\,dx}{\left(\int K(x)\,dx\right)^2}. \tag{3.19}$$

Minimizing this expression yields that a uniform current distribution $K(x) = \text{const.}$ minimizes flux noise. This provides an explanation for the previous observation that the presence of a superconducting ground plane reduces flux noise [49, 97].

In order to connect the noise amplitude $\sqrt{A_\Phi}$ extracted from measured data with the above model, we use

$$\langle \Phi^2 \rangle = \int_{-\infty}^{\infty} S_\Phi(\omega) g_\mathrm{E}(\omega)\,d\omega = 2A_\Phi \ln 2 \tag{3.20}$$

To account only for frequencies our echo experiment is sensitive to, the integration is weighted by its filter function [40, 72, 55, 14]

$$g_{\mathrm{E}} = \left(\frac{\sin^2(\omega t/4)}{\omega t/4} \right)^2 . \tag{3.21}$$

Both black lines in Fig. 3-6 belong to the same two-dimensional fit to the analytic approximation Eq. (3.12) using only a single fit parameter $m^2\sigma$. Rather than relying on a defect density reported in previous calculations or experiments, we are therefore able to extract its value from our experimental data. Assuming a penetration depth of $\lambda = 40\,\mathrm{nm}$ [74] and that the magnetic moment corresponds to a Bohr magneton, $m = \mu_{\mathrm{B}}$, we recover a surface spin density $\sigma = 1.2 \times 10^{17}\,\mathrm{m}^{-2}$, a factor of four off the previously predicted [46] and observed [83] value of $5 \times 10^{17}\,\mathrm{m}^{-2}$. With an effective spin magnetic moment of $1.8\mu_{\mathrm{B}}$, as suggested for defects formed by oxygen adsorbates on the SQUID surface [99], we extract $\sigma = 3.7 \times 10^{16}\,\mathrm{m}^{-2}$.

Due to an offset between the bottom and top metallizations in the shadow evaporation process, the width along the vertical arms of the junction loop is increased. This effect is most pronounced in qubits with small aspect ratios ($X \ll Y$) and thin wires. In order to account for this changing width in the junction loops loops, we plot an average width $\langle W \rangle$ in Fig. 3-6 and Fig. 3-7.

The analytic approximation of the model Eq. (3.12) is only valid in the regime where $b \sim \lambda$ and $W \gg \lambda$, but in our experiment, $b/\lambda \approx 5$. We attribute the deviations of data points in Fig. 3-6(b) from the linear scaling for thin wires (largest $1/\langle W \rangle$) to a partial breakdown of this analytic model. We thus use the numerical model developed in Section 3.1.2 to extend the original analytic model to treat more realistic loop geometries. With the magnetic field numerically computed with Biot-Savart's formula, the total flux noise as computed from the numeric model is found by replacing the integral in Eq. (3.9) with a numeric integration.

Fits to the model with our numerical extension are shown by the purple and red lines in Fig. 3-6. We find quantitative agreement with experimental data, including loops with small wire widths, where the numeric model is consistent with

deviations from the linear behavior as observed in experiment. For direct comparison with the analytic approximation, we show the numerical model only including the aluminum-vacuum surface on top of the loop (red). We validate our theoretical model by observing good agreement with the analytic approximation for a small film thickness $b \sim \lambda$ and we confirm that the analytic approximation is inaccurate for our film thickness of $b = 190\,\mathrm{nm}$ and breaks down completely for even higher film thicknesses. Based on our numerical results, we find that increasing the film thickness b decreases the flux noise amplitude, which is analogous to the effect we observe for increasing the wire width W.

In addition, we perform a fit to the numeric model including defect spins residing in all relevant interfaces comprising the junction loop, see regions colored in red in the inset schematic in Fig. 3-6(b), i.e., the top and side aluminum-vacuum interfaces, the bottom silicon-aluminum interface, and the silicon-vacuum interfaces beside the loop arms, where the magnetic field decays with a power law. Assuming $m = \mu_\mathrm{B}$, we obtain $\sigma = 2.6 \times 10^{17}\,\mathrm{m}^{-2}$ when considering only the top surface of the loop and $\sigma = 6.7 \times 10^{16}\,\mathrm{m}^{-2}$ when including all relevant interfaces with equal defect densities. We performed an alternative fit to measured data assuming different defect densities for the aluminum-vacuum, silicon-vacuum, and silicon-aluminum interfaces based on their extracted loss tangents [102], yielding a defect density in the aluminum-vacuum interface of $1 \times 10^{17}\,\mathrm{m}^{-2}$.

The two-dimensional fit to our numerical model including all relevant interfaces is depicted in Fig. 3-7(a), with measured data points shown in Fig. 3-7(b) and relative deviations from the model color-coded. While we measure time-averaged T_1 times in our qubits between 5 µs and 65 µs, with most data points around 20 µs, the extracted values of the noise amplitudes $\sqrt{A_\Phi}$ are in excellent agreement across all measured samples, demonstrating the robustness of our analysis. Dephasing times T_2 are limited by $2T_1$ at the sweet spot and are reduced to $\sim 1\,\mu\mathrm{s}$ for the largest frequency detuning from the sweet spot, while T_1 times are not limited by flux noise in these samples. Based on the spin echo filter function, our experiment is sensitive to noise frequencies in the range of 10 kHz to 1 MHz. The flux bias line used in our experiment is low-pass

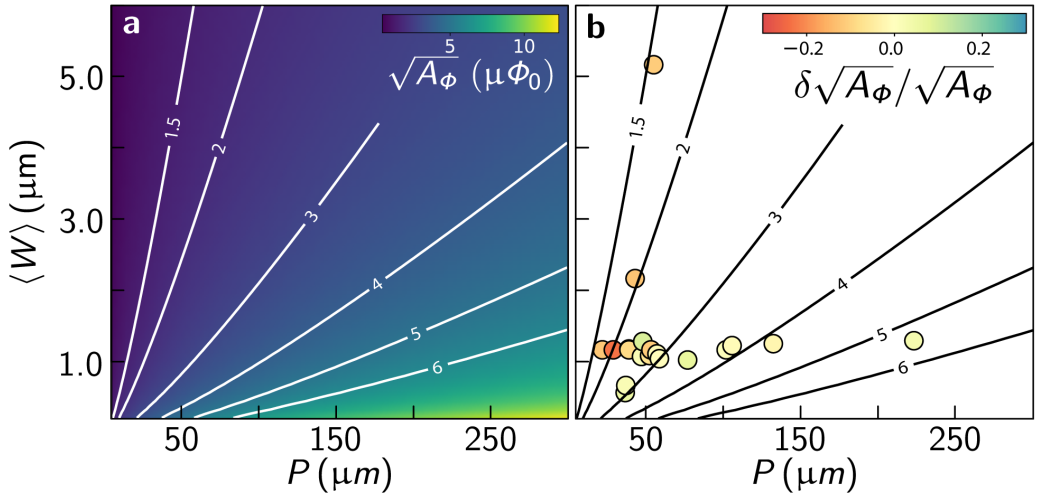

Figure 3-7: **2D plots of flux noise against perimeter and width.** **(a)** $\sqrt{A_\Phi}$ as a function of the effective width $\langle W\rangle$ and perimeter P based on a fit to the numeric model taking into account all relevant interfaces (red lines in Fig. 3-6). **(b)** Data points show experimentally investigated parameter combinations with relative deviations from the same numerical model color-coded.

filtered with a second-order RC-filter located at the 3 K stage of the cryostat. In the frequency range relevant to our experiment, we estimate the added flux noise by our setup to be at least two orders of magnitude lower than measured flux noise values, and therefore negligible. Additionally, flux noise that is caused by fluctuations in the bias voltage scales the noise amplitude as $\sqrt{A_\Phi} \propto \sqrt{\langle\Phi^2\rangle} \propto B \cdot X \cdot Y \propto P^2$, where B is the induced magnetic field in the junction loop. Since this is a different scaling than experimentally observed, we conclude that noise from the current source is insignificant for our experiment.

The noise amplitudes extracted in our experiment are similar to previous observations in phase qubits and flux qubits sensitive to noise frequencies below 1 Hz [9, 49]. Since our experiment combines the results of a large number of junction loops loops with geometry parameters distributed in a two-dimensional parameter space, the product of interface defect density and their coupling strength is a single fit parameter in our analysis. The quantitative agreement we observe between experimental data and the microscopic model therefore does not rely on a literature value for the defect density, but rather we are able to extract it from our data set. Given the good

agreement with the recently reported value [83], our experiment provides additional evidence for its accuracy.

Finally, we measure flux noise amplitudes of nine identical qubits with geometry parameters in the optimal limit according to our previous findings. The qubits have small loop perimeters $P = 32\,\mu\text{m}$ and increased wire widths $W = 2\,\mu\text{m}$. These parameters ensure that the three Josephson junctions can be integrated into the junction loop without compromising the fabrication quality, although even smaller P/W may be feasible. For the optimized samples, we find consistently low noise amplitudes with a mean of $1.64\,\mu\Phi_0$ and a standard deviation of $0.11\,\mu\Phi_0$. This verifies the model over a large parameter range and confirms that significant improvements in flux noise levels can be achieved by optimizing the loop geometry. A summary of the data underlying the results in this section is provided in Table 3.1.

The results of this experiment are not limited to the specific variant of flux qubit used, but are general to any qubit used in the framework of superconducting circuits with a closed loop. We substantiate this by measurements of $1/f$ flux noise in capacitively-shunted flux qubits where the capacitor is formed by a single floating pad that couples to ground, similar to the "Xmon" layout [7] (see Table 3.2). Both qubit architectures yield consistent flux noise amplitudes for identical junction loop geometries.

Table 3.1: **Complete dataset for all qubits measured in this experiment.** For each qubit, we list the junction loop geometry parameters X, Y, and W, the qubit transition frequency $\omega/2\pi$ at the optimal bias point, the average relaxation time $\bar{T}_1$ in the measured region of the spectrum, and the extracted noise amplitudes $\sqrt{A_\Phi}$ left and right of the optimal bias point. Missing values are due to a faulty qubit, electric two-level system modes cutting through the qubit spectrum, or have not been measured.

Sample	Qubit #	X (µm)	Y (µm)	W (µm)	$\omega/2\pi$ (GHz)	$\bar{T}_1$ (µs)	$\sqrt{A_\Phi}$ (µΦ_0) (left)	$\sqrt{A_\Phi}$ (µΦ_0) (right)
Varied Width	1	9.16	8	2	5.03	9	2.16	2.17
	2	9.16	8	0.5	4.29	26	2.78	2.78
	3	9.16	8	5	5.04	22	1.58	1.59
	4	9.16	8	0.4	4.08	38	2.81	2.87
	5	9.16	8	1	4.8	15	2.44	2.48
	6	9.16	8	5	5.61	16	-	1.66
	7	9.16	8	2	5.03	14	-	2.12
	8	9.16	8	1	4.62	8	2.58	2.54
	9	9.16	8	0.5	4.37	23	-	2.74
	10	9.16	8	0.4	-	-	-	-
Varied Area	1	12.95	11.31	1	4.73	7	3.08	3.07
	2	6.48	5.66	1	4.85	9	2.63	2.62
	3	25.91	22.63	1	4.61	13	3.65	3.83
	4	4.58	4	1	4.79	10	1.97	2.01
	5	9.16	8	1	4.66	13	2.67	2.69
	6	25.91	22.63	1	5.02	10	3.86	3.88
	7	12.95	11.31	1	4.38	17	2.75	2.77
	8	9.16	8	1	4.95	14	2.66	2.64
	9	6.48	5.66	1	4.51	16	2.29	2.28
	10	4.58	4	1	4.76	12	2.09	2.08
Varied Aspect Ratio	1	24.21	3.03	1	4.56	18	3.00	3.02
	2	8.56	8.56	1	4.23	15	-	2.30
	3	34.24	2.14	1	4.72	11	3.24	3.24
	4	4.28	17.12	1	4.32	17	2.29	2.26
	5	17.12	4.28	1	4.26	14	2.61	2.60
	6	34.24	2.14	1	4.57	15	3.57	3.60
	7	24.21	3.03	1	4.48	16	2.88	2.88
	8	17.12	4.28	1	4.57	16	2.64	2.73
	9	8.56	8.56	1	4.10	16	2.29	2.31
	10	4.28	17.12	1	4.07	17	2.41	2.39
Varied Y	1	18.32	45.25	1	-	-	-	-
	2	18.32	8	1	4.61	17	2.55	2.56
	3	18.32	90.51	1	4.55	9	4.62	4.57
	4	18.32	5.66	1	4.64	16	2.89	2.82
	5	18.32	32	1	4.77	13	3.54	3.65
	6	18.32	90.51	1	4.66	8	5.19	5.18
	7	18.32	45.25	1	4.43	10	4.26	4.29
	8	18.32	32	1	4.21	16	3.82	3.79
	9	18.32	8	1	4.63	15	2.90	2.94
	10	18.32	5.66	1	4.57	16	3.00	3.01
Identical	1	6.41	5.6	2	5.15	17	1.46	1.45
	2	6.41	5.6	2	5.07	17	1.55	1.50
	3	6.41	5.6	2	4.92	17	1.67	1.63
	4	6.41	5.6	2	4.57	18	1.69	1.70
	5	6.41	5.6	2	4.80	17	1.49	1.54
	6	6.41	5.6	2	3.00	45	1.93	1.83
	7	6.41	5.6	2	4.83	18	1.79	1.79
	8	6.41	5.6	2	4.84	15	1.69	1.70
	9	6.41	5.6	2	4.92	14	1.72	1.74
	10	6.41	5.6	2	4.87	17	1.71	1.68

Table 3.2: **Measured data of six qubits on one sample with either a floating or grounded shunt capacitor.** All other parameters were otherwise kept identical. The data show no trend in the noise amplitudes extracted for the different layouts, indicating that the noise amplitude values are not dependent on qubit architecture but only on the junction loop geometry. For each measured qubit, we list the loop geometry parameters X, Y, and W, the qubit transition frequency $\omega/2\pi$ at the optimal bias point, the average relaxation time $\bar{T}_1$ in the measured region of the spectrum, and the extracted noise amplitudes $\sqrt{A_\Phi}$ left and right of the optimal bias point. Missing values have not been measured.

sample	X (µm)	Y (µm)	W (µm)	$\omega/2\pi$ (GHz)	$\bar{T}_1$ (µs)	$\sqrt{A_\Phi}$ (µΦ_0) (left)	$\sqrt{A_\Phi}$ (µΦ_0) (right)	capacitor shape
Varied Pads	9.16	8	1	4.62	15	2.31	-	floating
	9.16	8	1	4.54	12	2.39	-	floating
	9.16	8	1	5.16	5	2.07	-	floating
	9.16	8	1	4.04	17	-	2.18	grounded
	9.16	8	1	4.67	14	2.31	2.33	grounded
	9.16	8	1	4.45	17	2.25	2.31	grounded

3.5 Discussion

We have experimentally demonstrated an approximately linear dependence of the flux noise power on junction loop perimeter and inverse wire width. We observed quantitative agreement of our data with an extension of a previously proposed model for magnetic defects residing in material interfaces. This extension is based on simulating the current distribution in the junction loops, resolving the limited applicability and accuracy of the analytic approximation considered previously. This is an important contribution towards solving the long-standing puzzle surrounding the origin of $1/f$ flux noise in conductors. The obtained results are expected to be universal for any superconducting circuit with a closed flux-biased loop. The observations – namely that wide wires, small perimeter loops, and large thickness films are favorable to suppress flux noise – can therefore serve as a guide to reduce the noise susceptibility of superconducting circuits. In the context of quantum information, this has a direct relevance for improving operational fidelities in both gate-model and quantum annealing approaches to quantum computing.

Chapter 4

Getting Started with Fluxonium

Starting from this Chapter, I shift focus toward my favorite superconducting qubit, the fluxonium. This qubit has largely defined my PhD in the EQuS group, and being able to experience all the new physics and additional challenges associated with an unfamiliar qubit has been a great blessing. This Chapter is organized in the order one would go about performing actual experiments, starting with the readout and initialization of fluxonium in Section 4.1, time-domain measurements for calibrating gates and characterizing qubits in Section 4.2, and finally the calibration and benchmarking of high-fidelity single-qubit fluxonium gates in Section 4.3. The information in this Chapter is meant to be generally applicable to any fluxonium experiment and will hopefully be of use to younger graduate students or those beginning their own experiments with fluxonium.

4.1 Readout and Initialization

4.1.1 Dispersive Readout

A prerequisite for any experiment using fluxonium qubits is to perform qubit state readout, without which one is not able to measure anything about the qubit. To briefly recap the discussion in Section 2.4.1, we define the fluxonium-resonator Hamil-

tonian to be

$$\hat{H} = 4E_C\hat{n}^2 + \frac{1}{2}E_L\hat{\phi}^2 - E_J\cos(\hat{\phi} - \phi_{\text{ext}}) + \hbar\omega\hat{a}^\dagger\hat{a} - i\hbar g\hat{n}(\hat{a} - \hat{a}^\dagger) \tag{4.1}$$

$$= \hat{H}_{\text{fluxonium}} + \hat{H}_{\text{resonator}} - i\hbar g\hat{n}(\hat{a} - \hat{a}^\dagger). \tag{4.2}$$

For standard qubit designs, we assume the **dispersive coupling regime** between the qubit and the resonator. That is, the coupling strength should be small compared to the detuning. Since many transitions contribute to the dispersive shift for fluxonium

$$\chi_j \equiv g^2 \sum_{k \neq j} \frac{2\omega_{j,k}}{\omega_{j,k}^2 - \omega_r^2} |\langle k|\,\hat{n}\,|j\rangle|^2 \tag{4.3}$$

(reproduced from Section 2.4.1, plotted and measured in Fig. 4-1), this condition must hold for all of these transitions. For distinguishing qubit states $|a\rangle$ and $|b\rangle$ (typically $|0\rangle$ and $|1\rangle$), the formal condition for the dispersive coupling regime is

$$\left| \frac{g\,\langle j|\,\hat{n}\,|k\rangle}{\omega_{jk} - \omega_r} \right| \ll 1 \tag{4.4}$$

for all states $k \neq j$ and for both $j = a$ and $j = b$. Here ω_{jk} is the transition frequency between states $|j\rangle$ and $|k\rangle$ of the fluxonium, and ω_r is the transition frequency of the resonator. For the regime of fluxonium qubits used in this thesis, the dispersive shift can be accurately calculated considering only the transitions $|0\rangle \leftrightarrow |3\rangle$, $|1\rangle \leftrightarrow |2\rangle$, and $|1\rangle \leftrightarrow |4\rangle$ at $\Phi_{\text{ext}} = 0.5\,\Phi_0$. While the dispersive regime is not necessary to achieve a resonator frequency that is dependent on the qubit state (and vice versa), it is necessary for a QND measurement; if the dispersive condition is violated, driving resonator transitions will induce qubit transitions in addition to just measuring its state.

In order to reliably distinguish the resonator between its different state dependent frequencies, this frequency difference must be large enough compared to the linewidth of the resonator (see Fig. 4-2). The regime $2\chi_{01} \equiv \chi_1 - \chi_0 \gg \kappa$ is traditionally known as the **strong coupling regime**; however, a ratio of $\chi_{01}/\kappa = 0.5$ can be shown to

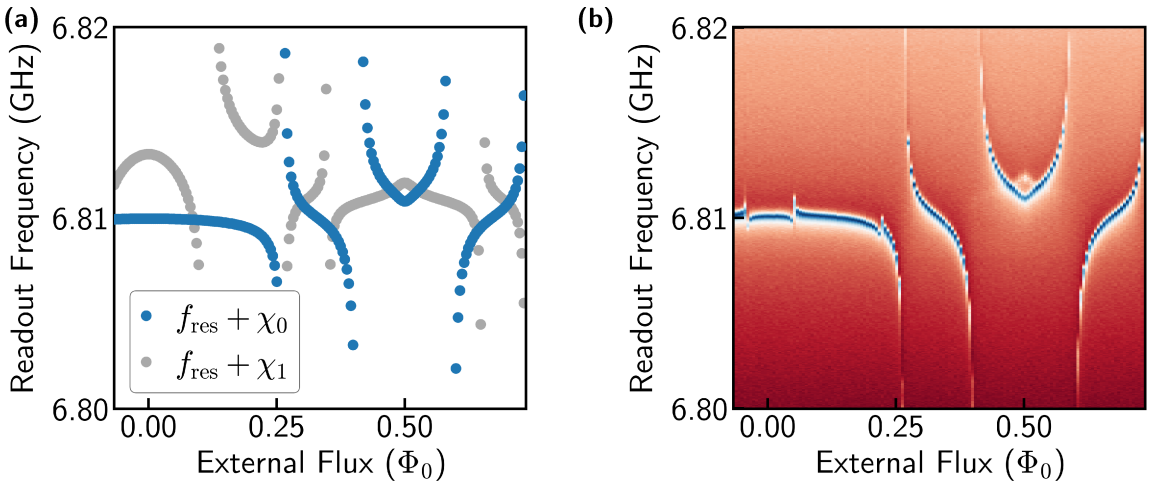

Figure 4-1: **Resonator shift from a fluxonium. (a)** Simulation of the resonator frequency with the fluxonium in $|0\rangle$ (blue) and $|1\rangle$ (gray). **(b)** Experimental spectroscopy of the resonator capacitively coupled to a fluxonium. Colors indicate the magnitude of transmission through the resonator.

be optimal for the readout signal-to-noise ratio [21].

By probing the measurement signal at the readout frequency, we obtain a signal that is now dependent on the qubit state. For example, by probing the resonator frequency corresponding to the qubit being in $|0\rangle$, we obtain a baseline signal level, and another (hopefully different) signal level when the qubit is in $|1\rangle$. To obtain the spectrum of the qubit, one then scans the frequency of qubit excitation pulse which is played right before the readout pulse. This technique is known as **two-tone spectroscopy**, and an illustration of it as a function of the qubit external flux is shown in Fig. 4-3.

4.1.2 Measurements at Low Qubit Frequency

At low qubit frequencies relative to the fridge temperature ($\hbar\omega \ll k_B T$), the thermal excitation of the qubit presents an additional challenge for two-tone spectroscopy. If there is an equal distribution of ground and excited state population at the start of the excitation pulse, population will swap symmetrically between $|0\rangle$ and $|1\rangle$, leaving the total population in $|0\rangle$ and $|1\rangle$ unchanged. Assuming a Boltzmann distribution of populations in a two-level system, a qubit with frequency ω will have a thermal

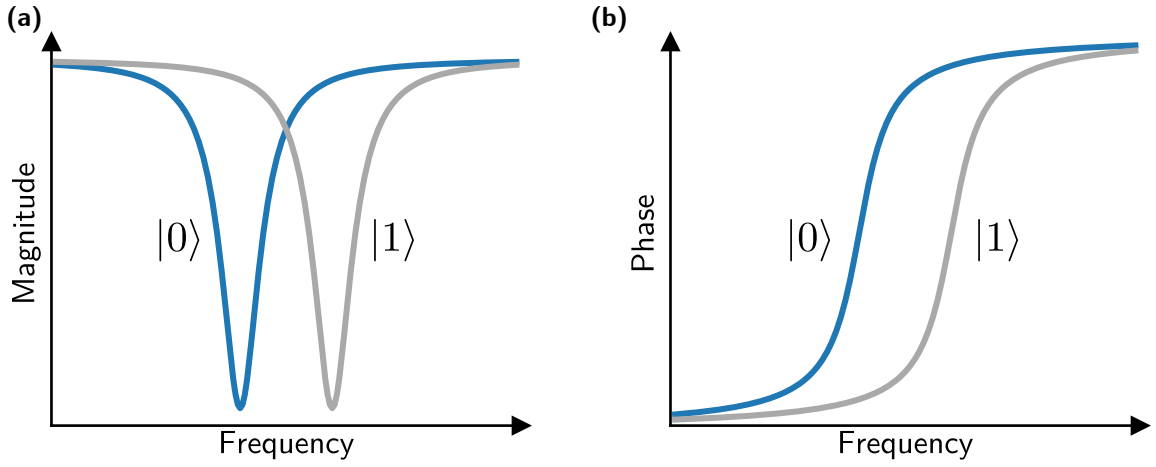

Figure 4-2: **Resonator shift dependent on qubit state. (a)** Illustration of the magnitude response of a resonator dependent on the qubit state. **(b)** Illustration of the phase response of a resonator dependent on the qubit state. We note that these illustrations are specific to a hanging resonator geometry.

excited state population of

$$p_1 = \frac{e^{-\hbar\omega/k_B T}}{1 + e^{-\hbar\omega/k_B T}}. \tag{4.5}$$

For reference, a 200 MHz qubit with an effective qubit temperature of $T = 30\,\mathrm{mK}$ has a thermal excited state population of 42%. If the qubit spectroscopy tone is long enough so that it completely mixes the qubit, the total signal will be proportional to 8% of the maximum possible signal. The same procedure without having an thermal excitation would result in 50% of the maximum possible signal. Making the standard assumption that noise decreases with the square root of the number of averages, having an equivalent signal-to-noise ratio with the 200 MHz qubit would require 40× more averages, a prohibitively large factor. In order to productively measure low frequency qubits, a state initialization protocol must be employed.

4.1.3 Readout Heralding

In our standard readout pulse sequence [Fig. 4-4(a)], the qubit and readout pulses are repeated according to a periodic trigger, with a fixed wait time τ_1 between the start of the trigger and the start of the readout pulses. The trigger period and τ_1

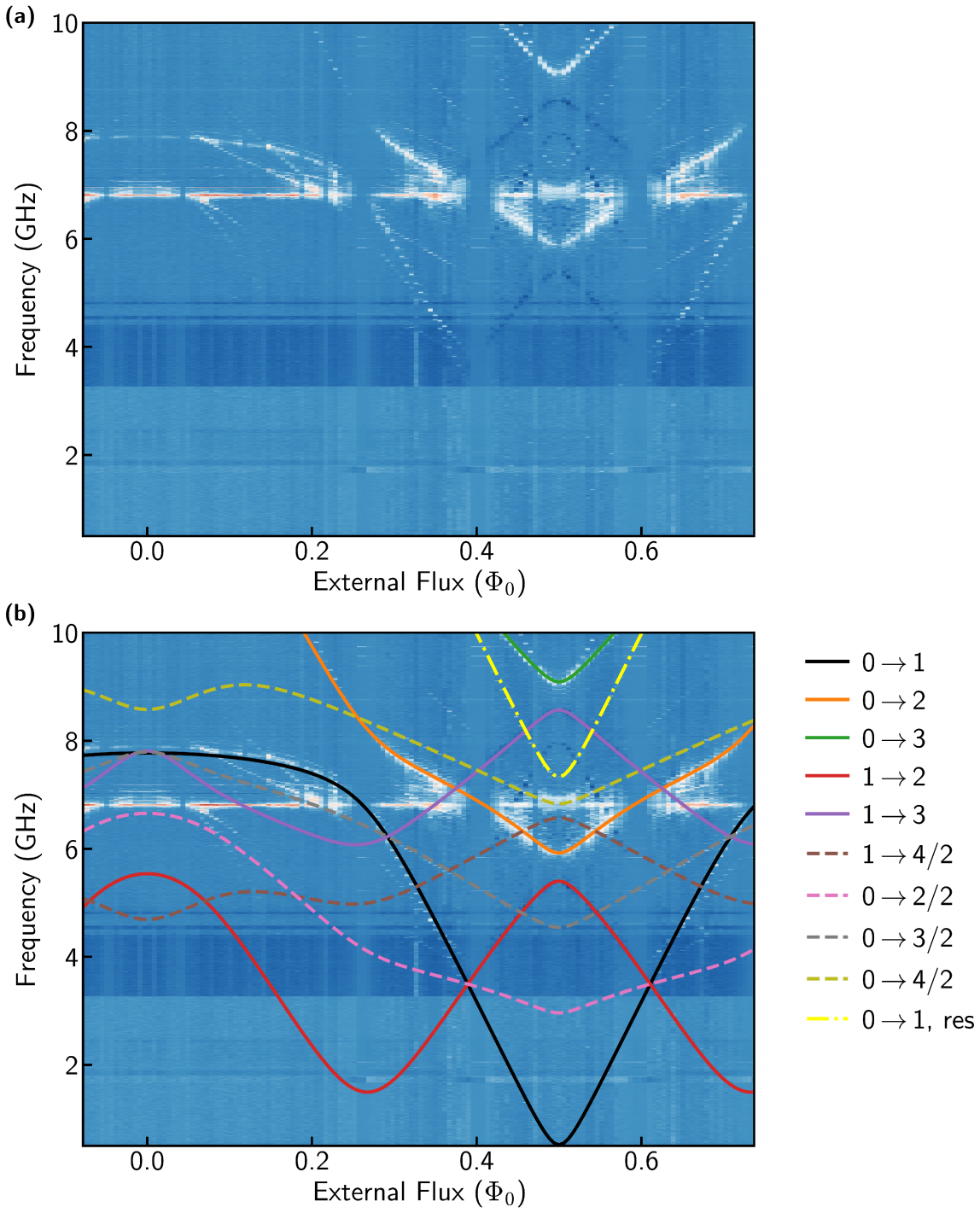

Figure 4-3: **Two-tone spectroscopy of a fluxonium qubit. (a)** Two-tone spectroscopy of fluxonium qubit as a function of the external flux. **(b)** Same data with fits overlaid. Qubit has extracted Hamiltonian parameters $E_C = 1.51\,\text{GHz}$, $E_L = 1.05\,\text{GHz}$, $E_J = 6.09\,\text{GHz}$. Legend indicates transitions between the correspond qubit states. The notation "/2" indicates a two-photon transition, and the text "res" indicates that a photon is additionally added to the resonator.

are chosen such the qubit sufficiently decays to its thermal equilibrium state between measurements.

To initialize our fluxonium qubits in either $|0\rangle$ or $|1\rangle$, we rely on a mostly QND single-shot readout. Then, we post-select the data for any choice of initial state: $\{|0\rangle, |1\rangle\}$ in order to herald that state [41]. In our simplest form of post-selection [Fig. 4-4(b)], the qubit pulses and readout are played back-to-back with only a short buffer time τ_2 to allow for photons to depopulate the readout resonator prior to the qubit pulses — ideally τ_2 is much longer than the resonator decay time and much shorter than the qubit decay time. It is important that this buffer time τ_2 is kept constant so that the initialization fidelity is constant throughout an experiment. Each readout serves a dual purpose of measuring the qubit state for the previous pulse sequence as well as projecting the state onto $|0\rangle$ or $|1\rangle$ for the next pulse sequence. Then, to post-select the data assuming an initial state of $|0\rangle$ ($|1\rangle$), one only accepts the measurements results when the previous readout result was $|0\rangle$ ($|1\rangle$).

We show a basic illustration of this technique in Fig. 4-5. Qubit state measurements were repeated with a 3 µs readout time and 2 µs wait time. The histogram of digitized single-shot measurements is shown in Fig. 4-5(a), with the first 2000 readout iterations plotted in Fig. 4-5(b) as a time series. Since the T_1 of the qubit is long compared to the duration of each iteration, a strong correlation exists between the result of one readout and the result of the next readout.

Despite losing a fraction of our data ($1/2^{\text{number of qubits}}$) due to this post-selection process, we gain an enormous speedup by not having to wait for the qubits to decay between measurements. In order for population to decay 99% (a typical value of a good readout fidelity) of the way back to thermal equilibrium, one must in general wait a time of $5T_1$. Assuming a T_1 of 1 ms (not atypical for fluxonium qubits measured in this thesis), this would amount to a 5 ms repetition rate between measurements. In contrast, many measurements such as spectroscopy, Rabi, and Ramsey, only last on order of 1-10 µs. For small numbers of qubits, this heralding process even has some advantages over active reset (applying a pi-pulse after the readout only if the measured state is $|1\rangle$). Since the readout discrimination is in general much less sensitive

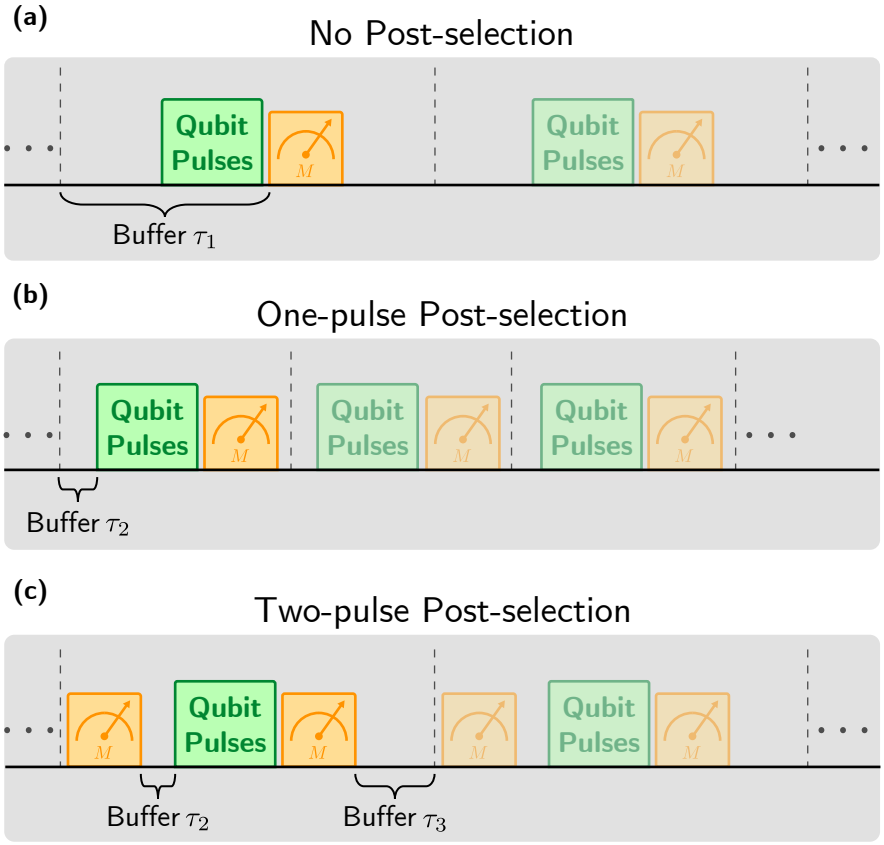

Figure 4-4: **Pulse diagram for different readout configurations. (a)** Standard measurement and readout sequence. Pulses are played on a repeated trigger so that the time between the trigger's start and the readout's start is kept constant. **(b)** Single-readout post-selection sequence, also known as heralding. Each readout pulse simultaneously sets the initial state for the subsequent qubit pulses and records the measurement outcome of the previous qubit pulses. To herald the fluxonium ground (excited) state $|0\rangle$ ($|1\rangle$), we only accept measurement results for which the previous readout result was $|0\rangle$ ($|1\rangle$). **(c)** Two-pulse post-selection (heralding) technique. The first readout is used to initialize the qubit state, and the second is used to measure the result of the qubit pulses. This extra readout pulse allows for an additional buffer time τ_3 without impacting the fidelity of the state preparation.

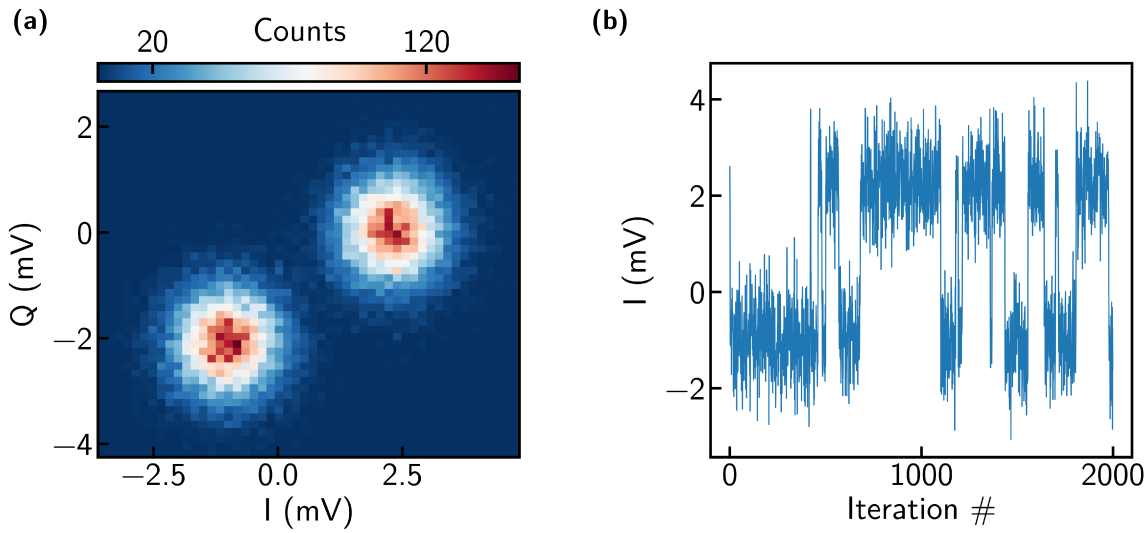

Figure 4-5: **Repeated single-shot readouts at the fluxonium sweet spot. (a)** Histogram of 30,000 digitized single-shot readouts. **(b)** Time series of the in-phase component (I), showing the first 2,000 single-shot readouts. The plot resembles a telegraph signal associated with the qubit switching states.

than a pi-pulse calibration, heralding is much more robust when relying on the same calibration over long periods of time or the same calibration over a small range of external fluxes. Several types of experiments in-fact do not require discarding any data, provided the dynamics of the system when starting in $|0\rangle$ mirror the dynamics of the system when starting in $|1\rangle$. For example, traces for measurements such as Rabi, Ramsey, and Echo are ideally symmetric about the population = 0.5 line. Put in another way, the relative (to the initial state) state population fully describes the decay rate and oscillation frequency of these measurements. If assuming $|0\rangle$ as the desired initial state, for all measurements starting in $|1\rangle$, the final measurement outcome can be flipped $(1 - \text{result})$ and then averaged into the rest of the data. It is without a doubt, however, that as the number of qubits increases, active reset is more advantageous than post-selection and is further required for quantum error correction.

Issues with Higher-Level State Discrimination

In principle, the above method of heralding works when driving to higher states of the fluxonium, but in practice we could not distinguish the $|1\rangle$ and $|2\rangle$ (and likely higher) states in single-shot. To work around this issue, we use a separate two-pulse heralding technique [Fig. 4-4(c)]. The first readout initializes the qubit in either $|0\rangle$ or $|1\rangle$, and the second readout records the result of the measurement. We use the same buffer time τ_2 to avoid measurement-induced dephasing of our qubit, and introduce an additional wait time $\tau_3 \sim 50\,\mu s$ to let any population in the higher states of the fluxonium to fall down to the computational states. Many of our measurements specifically involve driving from $|1\rangle$ to $|2\rangle$, and in these cases we can greatly enhance the readout contrast between these two states by performing a π-pulse on the fluxonium prior to the second readout. Any population measured in $|0\rangle$ is assumed to be $|1\rangle$ and any population measured in $|1\rangle$ is assumed to be $|2\rangle$. To accurately separate out populations in all three states ($|0\rangle$, $|1\rangle$, $|2\rangle$), we perform two-separate measurements; one with the extra π-pulse and one without.

On a more experimental note, it is essential to make sure that the phase of the readout demodulation is fixed relative to the phase of the readout pulses. If the readout phase is instead fixed relative to the start of the pulse sequence, then a variable length of the qubit pulses will cause a variable phase offset in the demodulated data and the "I-Q blobs" will be observed to rotate according to this phase offset.

4.1.4 Microwave Cooling

A separate initialization protocol developed in this thesis work follows the all-microwave reset protocol initially performed by Magnard et al. in a transmon architecture [53]. The basis for this protocol is to drive all excited fluxonium population into the readout resonator, which then decays on the timescale of the resonator linewidth κ. More precisely, we simultaneously drive the $|1\rangle_{qb}|0\rangle_{res} \leftrightarrow |2\rangle_{qb}|0\rangle_{res}$ transition and the $|2\rangle_{qb}|0\rangle_{res} \leftrightarrow |0\rangle_{qb}|1\rangle_{res}$ by applying a drive to the qubit [see Fig. 4-6(a)]. This process transfers any population in either the fluxonium $|1\rangle$ or $|2\rangle$ state into the excited

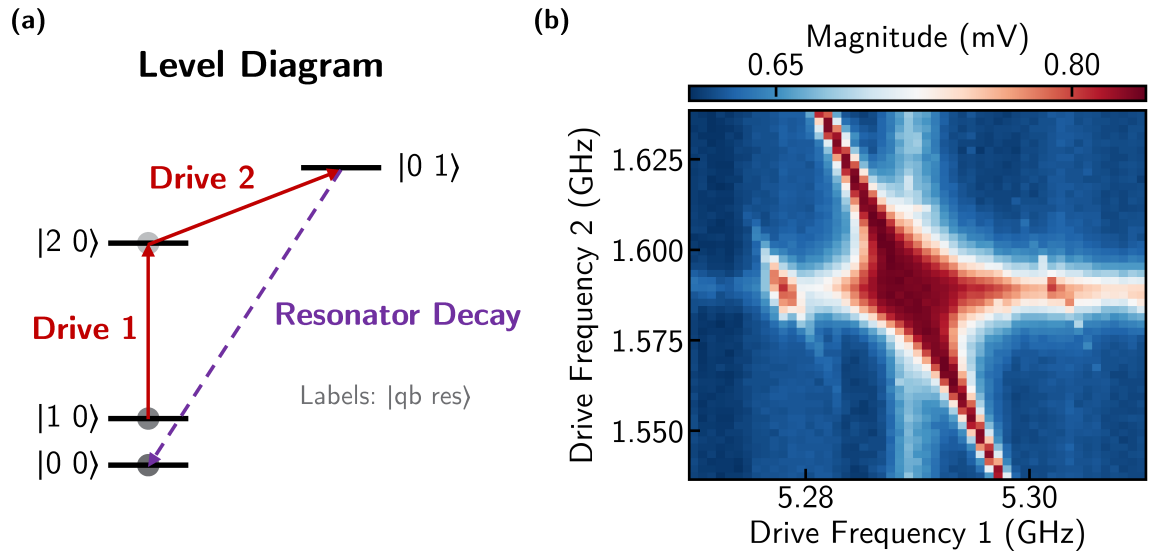

Figure 4-6: **Microwave Cooling. (a)** Level diagram of the microwave cooling protocol. Two simultaneous drives transfer population from the qubit $|1\rangle$ and $|2\rangle$ states into $|0\rangle$ by using the resonator decay. **(b)** Experimental scan of each of the two drives frequencies. The diagonally sloped resonance corresponds to the two-photon transition $|1\rangle_{\text{qb}}|0\rangle_{\text{res}} \rightarrow |0\rangle_{\text{qb}}|1\rangle_{\text{res}}$, and the horizontal resonance corresponds to the one-photon transition $|1\rangle_{\text{qb}}|0\rangle_{\text{res}} \leftrightarrow |2\rangle_{\text{qb}}|0\rangle_{\text{res}}$. Red correlates with larger population in the qubit ground state after application of the microwave drives.

state of the resonator, which then decays into the ground state of the system. Normally, a charge drive on the $|2\rangle_{\text{qb}}|0\rangle_{\text{res}} \leftrightarrow |0\rangle_{\text{qb}}|1\rangle_{\text{res}}$ transition would have zero matrix element, however it is only through the slight hybridization of the $|2\rangle_{\text{qb}}|0\rangle_{\text{res}}$ state with the $|1\rangle_{\text{qb}}|1\rangle_{\text{res}}$ that this transition is drivable. Nevertheless, the relative amplitude for this drive naturally needs to be much larger than that of Drive 1. To calibrate this cooling procedure, the frequencies of both drives are swept as in Fig. 4-6(b). The horizontal resonance corresponds to the $|1\rangle_{\text{qb}}|0\rangle_{\text{res}} \leftrightarrow |2\rangle_{\text{qb}}|0\rangle_{\text{res}}$ resonance and the diagonal resonance corresponds to the two-photon transition where both frequencies sum to the frequency difference between $|1\rangle_{\text{qb}}|0\rangle_{\text{res}}$ and $|0\rangle_{\text{qb}}|1\rangle_{\text{res}}$. By driving near the intersection of these two features for a duration corresponding to several multiples of $1/\kappa$, we are able to transfer population to the ground state as illustrated in the single-shots in Fig. 4-7(a-b).

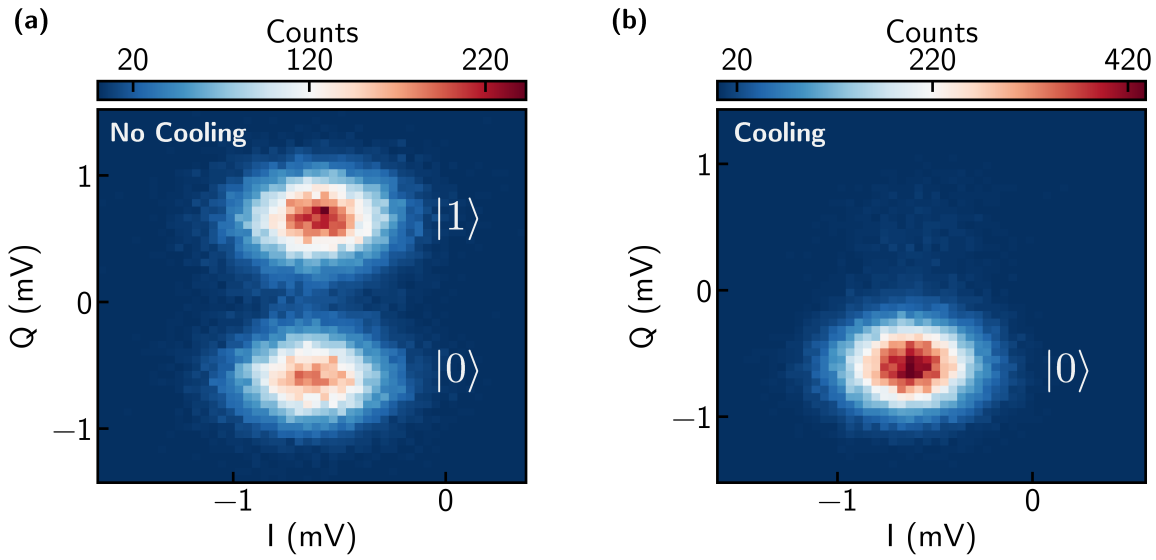

Figure 4-7: **Fluxonium single-shot readout histograms with and without microwave cooling. (a)** Single-shots without microwave cooling. There is a large distribution of both $|0\rangle$ and $|1\rangle$ states due to the thermal population. **(b)** Single-shots with microwave cooling prior to each readout, which transfers population into ground state.

4.1.5 Overview of Initialization Options

In addition to the initialization protocols demonstrated in this work, there is active-reset which relies on FPGA logic [32], several other microwave-based techniques which all relying on shoveling population into a resonator that then rapidly decays [109, 26, 6], and a technique relying on pure fast-flux control, in which the qubit frequency is tuned to several GHz in order the thermalize, before being brought back to the "sweet spot" [61]. The requirement to perform one of these (oftentimes complicated) reset protocols in order to work with such a low frequency qubit is often brought up as a reason for which low frequency qubits are more difficult or even more problematic than higher frequency qubits. While this may be a overhead cost in setting up initial measurements, this does not hold true in a future quantum processor. In order for any quantum computer to work (even those using other qubit platforms), quantum error-correction will be a necessary requirement, which itself requires fast-feedback to perform different qubit controls dependent on the results of readout measurements. In the long term, the ability to perform single-shot readout and some reset protocol

will be a requirement for all qubits. Due to not requiring any additional resources beyond single-shot readout and being both effective and efficient, we readout using post-selection for all further fluxonium experiments in this thesis.

4.2 Time-domain Measurements

In this Section, we briefly review the most common time-domain measurements performed on superconducting qubits, emphasizing any differences with fluxonium qubits. These measurements are generally useful for qubit calibration and characterization, with a more thorough overview available in Refs [47, 68, 16].

4.2.1 Rabi

We perform single-qubit rotations by resonantly driving with a microwave signal sent down either a charge line or a flux line coupled to the qubit. A drive with the functional form $A(t)$ results in an effective Hamiltonian drive term $\propto A(t)\hat{n}$ for the charge drive and $\propto A(t)\hat{\phi}$ for the flux drive [15]. We observe that driving the qubit through the readout resonator as is commonly done for higher-frequency qubits results in excess resonator photons, which dephase the qubit. If Ω is the Rabi frequency and δ is the detuning between the drive frequency and the qubit frequency, the population in the excited state should follow Eq. (1.39). We show the experimental pulse sequence and fitted data in Fig. 4-8(a) for the case with $\delta = 0$.

4.2.2 Lifetime T_1

In general, the T_1 describes the decay time constant for the population to return back to thermal equilibrium from any initial state.

$$p_e(t) = \left(p_e(0) - p_e^{\text{th}}\right) e^{-t/T_1} + p_e^{\text{th}} \tag{4.6}$$

$$p_g(t) = \left(p_g(0) - p_g^{\text{th}}\right) e^{-t/T_1} + p_g^{\text{th}} \tag{4.7}$$

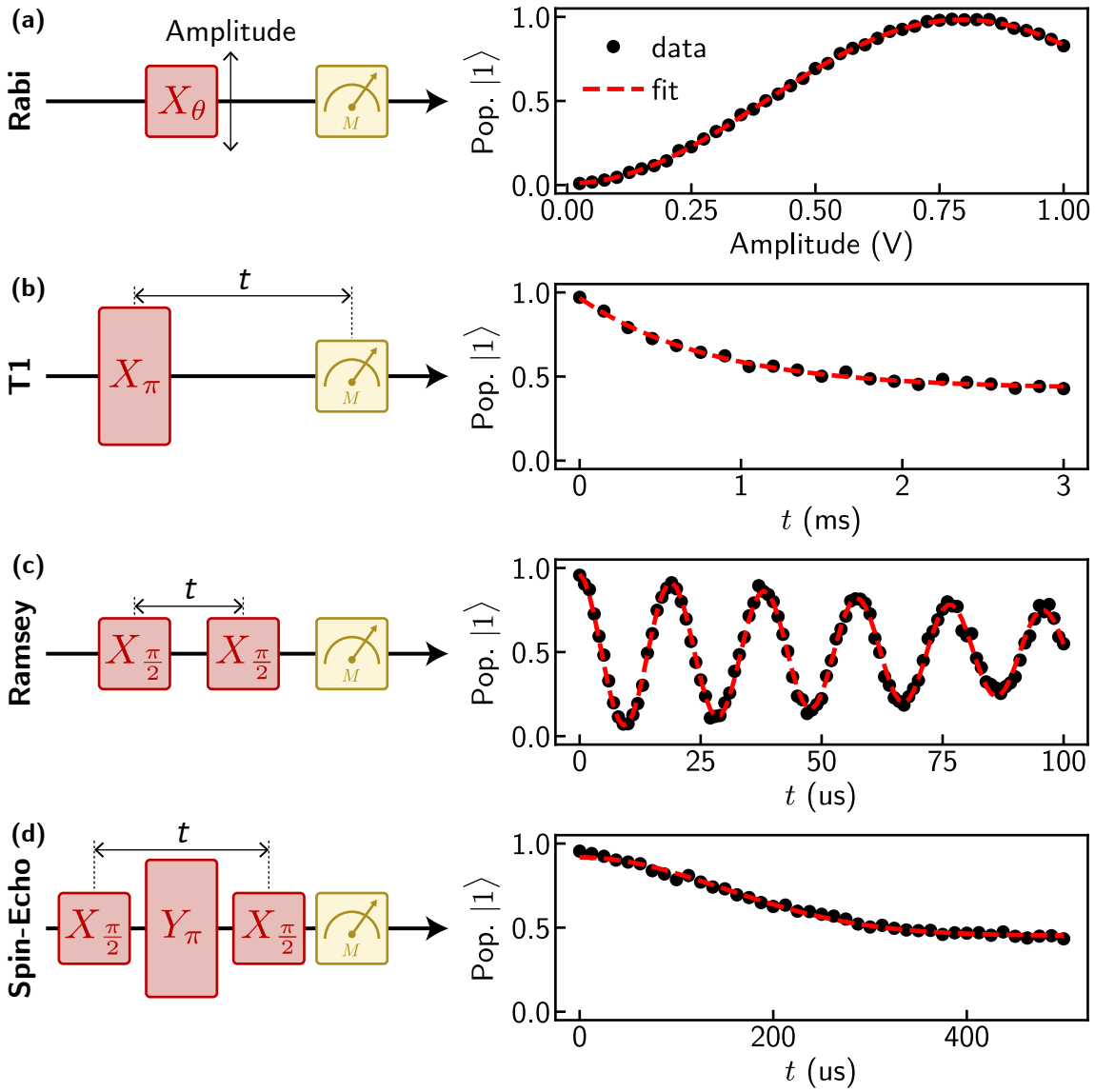

Figure 4-8: **Illustration of time-domain measurements.** Prior to each pulse sequence, the qubit is initialized in $|0\rangle$. **(a)** Rabi oscillations measured as a function of amplitude. Alternatively, these oscillations can be measured as a function of pulse duration. **(b)** T_1 measurement by initializing the state into $|1\rangle$ with a pi-pulse. Since low-frequency fluxonium qubits have considerable thermal population, a T_1 measurement can also be performed without a pi-pulse. In that case, there will be a decay from $|0\rangle$ to the thermal equilibrium state. **(c)** Ramsey oscillations as a function of time to measure T_2^R. **(d)** Spin-echo decay measured as a function of time.

For high-frequency qubits with low thermal population, this rule becomes synonymous with T_1 being the decay time constant from $|1\rangle$ to $|0\rangle$, which is likely more familiar. For those types of qubits, a microwave pulse is also necessary in order to measure T_1,

to pi-pulse the qubit state from $|0\rangle$ to $|1\rangle$ at the start of the measurements. With the heralding technique applied to fluxonium qubits, the qubit state can be prepared in either $|0\rangle$ or $|1\rangle$ without the need of a microwave pulse, and T_1 can be fit from a decay to the equilibrium mixed state in either case. This can be a useful technique to perform initial characterizations of a fluxonium qubit before the qubit frequency is known and without the need of a pi-pulse.

4.2.3 Ramsey

The Ramsey technique involves performing two pi-half pulses with a wait time t between them, then readout out right after. The Ramsey experiment serves two useful functions: the first is to characterize the decoherence time of the system (T_2), and the second is as a precise measure of the qubit frequency. Assuming the same detuning δ between the drive frequency and the qubit frequency and a completely Markovian dephasing process (with time constant T_ϕ), the excited state population as a function of time is

$$p_e(t) = e^{-t/T_2}\cos(\delta t) \tag{4.8}$$

where

$$\frac{1}{T_2} = \frac{1}{2T_1} + \frac{1}{T_\phi}. \tag{4.9}$$

By monitoring the time dependence of the fitted value of δ via repeated Ramsey measurements, one can extract the associated noise power spectral density of the qubit's frequency to measure the frequency stability of the qubit.

4.2.4 Spin-Echo

An alternative technique for measuring the T_2 time of a qubit is the spin-echo pulse sequence. This involves performing the same two pi-half pulses as in a Ramsey sequence, except a pi-pulse is inserted halfway in between the pi-half pulses (with wait time $t/2$ between the pi-pulse and each pi-half pulse). This additional pi-pulse serves to mitigate the effects of lower frequency (compared to $1/t$) noise in the qubit frequency

relative to the Ramsey experiment. Assuming a model of Markovian dephasing and $1/f$ flux noise, the decay function is partially exponential and partially Gaussian

$$p_e(t) = e^{-t/T_{\text{exp}}} e^{-(t/T_\phi)^2}. \tag{4.10}$$

Both the relative time constants between the exponential and Gaussian component as well as the the difference between Ramsey and spin-echo decay times gives useful information on the amount of colored noise vs. white noise. Additionally, comparing the T_2 times obtained via these techniques with $2T_1$ gives a measure of the amount of pure dephasing present in the system.

4.3 Single-Qubit Gate Calibration

In this section, we describe the Clifford randomized benchmarking techniques used to characterize our gates and analyze how different calibration errors translate into gate errors. This is useful to provide bounds on how accurate calibrations need to be, so as not to waste unnecessary measurement time. Finally, we detail our entire protocol for single-qubit gate calibration.

4.3.1 Single-Qubit Clifford Benchmarking

Clifford Randomized Benchmarking is a commonly used technique to benchmark the fidelity of gates [8]. For single-qubit gates, we decompose each element of the single-qubit Clifford group (C_1) into a convenient physical gate set. Following the decomposition done by Barends et al. and Sung et al, each element of C_1 is decomposed into the microwave gate set $\{I, \pm X/2, \pm Y/2, \pm X, \pm Y\}$, resulting in an average of 1.875 physical gates per Clifford [8, 94]. For our decompositions, we choose to make each gate the same physical length for benchmarking convenience: an I gate will physically idle for the specified gate duration, and pi-half pulses are created by halving the amplitude of the corresponding pi-pulse as opposed to being a separate calibrated pulse with roughly half the duration.

The following procedure is used to perform the benchmarking sequence:

1. Create a sequence of m random Clifford gates
2. Choose the $m+1$th Clifford such that it inverts the product of the previous m
3. Measure the survival rate after this full sequence (if initially in $|0\rangle$, measure $p_{|0\rangle}$).
4. Repeat the above steps varying m
5. Repeat the above steps varying the random number seed (we typically use 20 random seeds)
6. Fit the survival probability to the function

$$F(m) = A_0 p^m + B_0 \tag{4.11}$$

In this formula, A_0 and B_0 are meant to encapsulate all the SPAM errors of the system. The average error per Clifford is given by $r_{C_1} = (1-p)(1-1/d)$ where d is the dimension of the Hilbert space, $d = 2^n$ (n is the number of qubits). Using our previously noted gate decomposition, we calculate our average single-qubit gate error as

$$r_{1QB} = r_{C_1}/1.875. \tag{4.12}$$

Clifford Interleaved Randomized Benchmarking

While the above procedure gives us the average gate fidelity assuming some Clifford decomposition, it notably does not allow us to benchmark the fidelity of a single particular gate of interest. For this task, it is customary to employ **Clifford interleaved randomized benchmarking**. For this procedure, we do two separate randomized benchmarking experiments. The first is just standard randomized benchmarking, exactly the same as above, and for the second experiment we make the slight modification that in between each Clifford gate in the standard RB sequence, we insert a

gate G that we wish to benchmark [8, 51]. If p_{ref} is the fitted value of p for the standard RB experiment, and p_{int} is the fitted p value for the interleaved RB experiment, then the error per gate G is extracted as

$$r_G = (1 - 1/d)(1 - p_{\text{int}}/p_{\text{ref}}). \tag{4.13}$$

If σ denotes the one standard deviation uncertainty assuming gaussian error statistics,

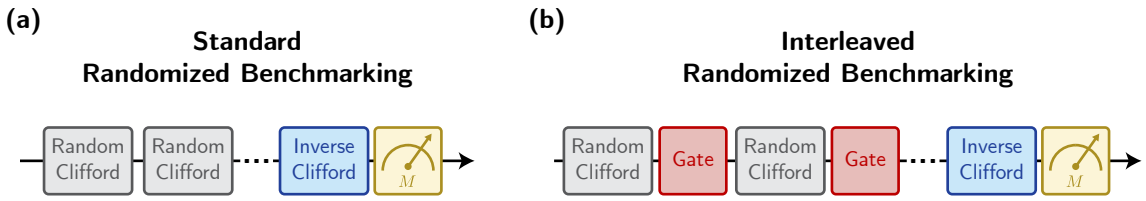

Figure 4-9: **Illustrative diagrams for randomized benchmarking (a)** Block diagram for standard randomized benchmarking. **(b)** Block diagram for interleaved randomized benchmarking, with the interleaved gate denoted 'Gate'.

then the uncertainty for the error per Clifford and the error per gate G are obtained via standard uncertainty propagation

$$\sigma_{r_{C_1}} = \left(1 - \frac{1}{d}\right) \sigma_{p_{\text{ref}}} \tag{4.14}$$

$$\sigma_{r_G} = \left(1 - \frac{1}{d}\right) \frac{\sqrt{p_{\text{ref}}^2 \sigma_{p_{\text{int}}}^2 + p_{\text{int}}^2 \sigma_{p_{\text{ref}}}^2}}{p_{\text{ref}}^2} \tag{4.15}$$

4.3.2 Calibration Algorithm

Due to the sufficiently large charge matrix elements of our fluxonium qubits, we perform all single-qubit gates using standard Rabi oscillations with a charge drive line. The pulses shaped by a pure cosine envelope with no flat top. We specifically calibrate the X_π pulse, and derive other pulses from it. Y pulses are created by adjusting the phase of the X pulses, pulses differing from π rotation are derived by linearly scaling the pulse amplitude, and Z gates are implemented through virtual-Z gates. While we could perform a more careful calibration by individually calibrating

all other gates in our microwave gate set for the RB decomposition , we find our single-qubit gates derived from this process more than sufficient to achieve state-of-the-art fidelities.

We detail the entire calibration sequence for an X_π gate in Fig. 4-10, with a flowchart illustrated provided in Fig. 4-10(m). Following an initial rough calibration of the qubit readout, sweet-spot voltage, frequency, and pi-pulse amplitude, the following procedure can be used to more precisely calibrate the qubit.

1. **Precise sweet-spot calibration** [Fig. 4-10(a, d)]. With fixed drive frequency (slightly negatively detuned from the qubit frequency) and fixed drive amplitude, Ramsey oscillations are obtained as a function of flux around the sweet spot. The oscillation frequencies are fit to a parabola, and the center of the parabola fit is used as the bias voltage corresponding to $\Phi_{\text{ext}} = 0.5\,\Phi_0$, termed the "sweet spot".

2. **Single-shot readout calibration** [Fig. 4-10(b, e)]. Although optimizing the readout does not impact the gate fidelity, we re-measure the locations of the single-shot blobs corresponding to $|0\rangle$ and $|1\rangle$ here to correct for flux-related changes in the readout signal.

3. **Precise qubit frequency calibration** [Fig. 4-10(c, f)]. To accurately obtain the qubit frequency, we perform qubit spectroscopy with a low enough power such that little power broadening is observed. This typically gives kHz-level precision, a sufficient starting point for DRAG. It is more common to extract the qubit frequency via Ramsey, but low power spectroscopy was found to be faster and more robust in our implementation. Furthermore, neither method correctly accounts for AC-stark shifts, meaning spending extra time for higher precision is not productive at this step.

4. **Derivative Removal by Adiabatic Gate (DRAG) calibration** [Fig. 4-10(g-h, j-k)]. The DRAG procedure seeks to reduce leakage and AC-stark shifts by modifying the original pulse by applying a compensation pulse in the out-of-phase quadrature proportional equal to the derivative of the original pulse

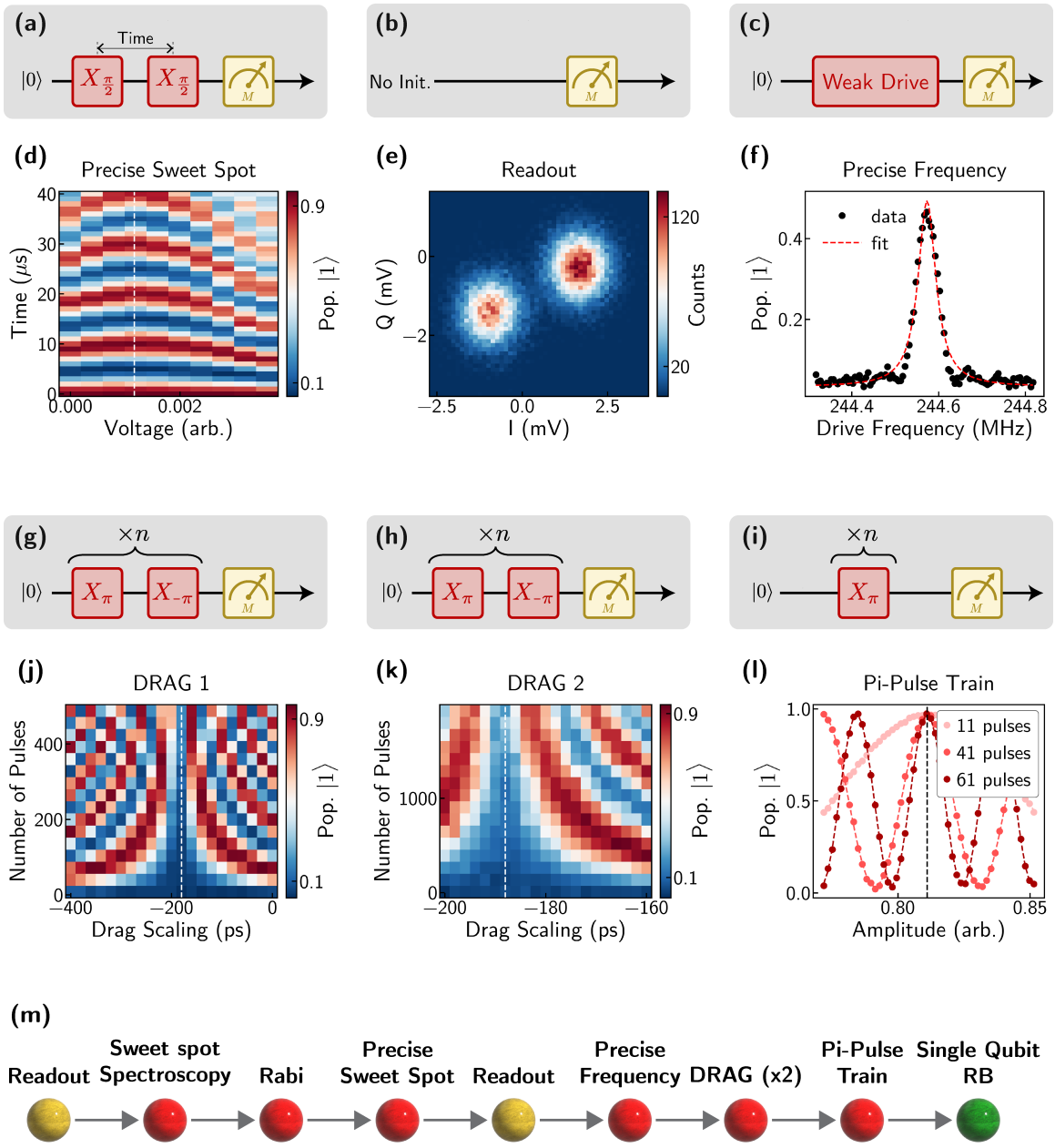

Figure 4-10: **Single-qubit X_π calibration procedure.** **(a-c, g-i)** Measurement pulse sequences for panels **(d-f, j-l)** respectively. **(d)** Ramsey vs. bias voltage measurement in order to precisely determine the voltage corresponding to $\Phi_{\text{ext}} = 0.5\,\Phi_0$ (termed the "sweet spot"). **(e)** Calibrating the readout I and Q coordinates for the fluxonium $|0\rangle$ and $|1\rangle$ states. **(f)** Low-power spectroscopy of the qubit to precisely determine the qubit frequency. **(j)** DRAG calibration of the qubit. We play a varying even number of X_π pulses with alternating amplitude while also varying the DRAG scaling. **(k)** A more precise DRAG calibration. **(l)** A pulse train consisting of an odd number of X_π pulses to precisely calibrate the amplitude of the pulse. **(m)** Calibration flowchart for single-qubit gates. Panels are shown for all calibrations starting from the precise sweet spot calibration.

multiplied by a to-be-calibrated DRAG parameter [62]. While scanning the DRAG parameter, we perform a train of π-pulses with alternating positive and negative amplitudes. This train of alternating pulses will result in the identity for perfectly calibrated pulses, but amplify the rotation error of off-resonant drives. The DRAG parameter which minimizes the observed oscillation between the $|0\rangle$ and $|1\rangle$ state is chosen. This measurement may be repeated with a larger number of pulses to increase the resolution of the DRAG parameter. Contrary to other fluxonium experiments [6, 93], we find DRAG calibration necessary to avoid coherent additional errors. We measure the optimal DRAG parameter to vary depending on the room temperature filtering scheme and not with the anharmonicity of the qubit, which leads us to suspect the calibration is correcting for small distortions in the drive line [37].

5. **Precise drive amplitude calibration** [Fig. 4-10(i, l)]. To improve the precision of a single Rabi oscillation, we utilize a pulse train with an odd number of pulses while varying the pulse amplitude. This serves to multiply the oscillation frequency by the number of pulses used, allowing for increased precision on the calibrated π-pulse amplitude.

4.3.3 Error Analysis

In this subsection we build up an analytic error model to estimate the impact of various types of coherent and incoherent errors on gate fidelities. We model our gates as completely positive trace-preserving (in some subspace) map $\mathcal{G}$ acting on an input state ρ. The Kraus representation theorem then allows us to express all such processes as

$$\mathcal{G}(\rho) = \sum_k G_k \rho G_k^\dagger \tag{4.16}$$

for some set of Kraus operators G_k obeying the normalization condition

$$\sum_k G_k^\dagger G_k = I. \tag{4.17}$$

The average state fidelity of such a process $\mathcal{G}$ is then given by

$$F = \frac{1}{n(n+1)} \left[\mathrm{Tr}\left(\sum_k M_k^\dagger M_k \right) + \sum_k |\mathrm{Tr}(M_k)|^2 \right]. \tag{4.18}$$

where $M_k = PU_0^\dagger G_k P$ and n is the dimension of the computational subspace [73]. In this expression, P is the projection operator onto the computational subspace, and U_0 is the ideal unitary operation of the process. For the special case that $\mathcal{G}$ is a unitary map, there is only one Kraus operator, which is the unitary matrix U describing $\mathcal{G}$. In this case, Eq. (4.18) simplifies to

$$F = \frac{1}{n(n+1)} \left[\mathrm{Tr}(MM^\dagger) + |\mathrm{Tr}(M)|^2 \right], \tag{4.19}$$

where $M = U_0^\dagger U$. In what follows, we model various processes to obtain the error that they contribute to gate fidelities.

T_1 Decay

For a qubit with lifetime T_1, we traditionally think of the relaxation of the qubit to be modeled as so on a density matrix

$$\mathcal{G}(\rho) = \begin{pmatrix} \rho_{00} + \rho_{11}(1 - e^{-t/T_1}) & \rho_{01} e^{-t/2T_1} \\ \rho_{10} e^{-t/2T_1} & \rho_{11} e^{-t/T_1} \end{pmatrix}, \tag{4.20}$$

where ρ_{ij} is the density matrix element at $t = 0$. With some trial and error, one can identify the Kraus operators as

$$G_0 = \begin{pmatrix} 1 & 0 \\ 0 & e^{-t/2T_1} \end{pmatrix}, \quad G_1 = \begin{pmatrix} 0 & \sqrt{1 - e^{-t/T_1}} \\ 0 & 0 \end{pmatrix}. \tag{4.21}$$

Note that these indeed satisfy the normalization condition $\sum_k G_k^\dagger G_k = I$. There are two different interpretations of this set of Kraus operators. 1) In computing $G_0 \rho G_0^\dagger$, it is evident that G_0 is responsible for the decay of the excited state and the resultant

dephasing due to this decay. Similarly, one can see that G_1 is responsible for bringing population back into the ground state. 2) In a Monte-Carlo formalism of qubit decay, G_0 corresponds to the normalized no-jump state evolution under an effective unitary, and G_1 corresponds to the jump evolution. Regardless of interpretation, the important point is that these two operators give the process $\mathcal{G}(\rho)$ written above, and plugging these into Eq. (4.18) (with $U_0 = I$) results in

$$F = \frac{1}{6}\left(3 + e^{-t/T_1} + 2e^{-t/2T_1}\right). \tag{4.22}$$

Assuming a small time t_g relative to T_1, we can Taylor expand this to recover the more familiar formula

$$F = 1 - \frac{1}{3}\frac{t_g}{T_1}. \tag{4.23}$$

While we calculated this as the fidelity of the identity operation on a single qubit with some duration t_g, it also serves as the coherence limited fidelity of single-qubit gates in general. This can be reasoned by noting that any non-identity single-qubit gate can be mapped onto some unitary transformation of the operators G_k, and equation Eq. (4.18) is invariant under unitary transformation of the Kraus operators. We should sure hope so given that the Kraus operators are only unique up to a unitary transformation in the first place.

Pure Dephasing

For a pure memoryless dephasing process with time constant T_ϕ, the associated Kraus operators are

$$G_0 = \begin{pmatrix} e^{-t/2T_\phi} & 0 \\ 0 & e^{-t/2T_\phi} \end{pmatrix}, \quad G_1 = \begin{pmatrix} \sqrt{1-e^{-t/T_\phi}} & 0 \\ 0 & 0 \end{pmatrix}, \quad G_2 = \begin{pmatrix} 0 & 0 \\ 0 & \sqrt{1-e^{-t/T_\phi}} \end{pmatrix} \tag{4.24}$$

Once again, I unfortunately do not offer the insight on how to generate Kraus operators for arbitrary quantum processes, but the validity of the Kraus operators presented

can be verified by computing

$$\sum_k G_k^\dagger \rho G_k = \begin{pmatrix} \rho_{00} & e^{-t/T_\phi}\rho_{01} \\ e^{-t/T_\phi}\rho_{10} & \rho_{11} \end{pmatrix}, \tag{4.25}$$

which shows that the this process places an exponential decay on the off-diagonal elements of the single-qubit density matrix, exactly what we assume decoherence is. Using Eq. (4.18), we can see that the fidelity of this dephasing process has the same expression as the fidelity of a T_1 channel

$$F = 1 - \frac{1}{3}\frac{t_g}{T_\phi}. \tag{4.26}$$

Rabi Calibration Error

We assume a purely coherent error arising from an over- or under-rotation of a Rabi oscillation when calibrating for a pi-pulse. In this case, the ideal unitary corresponding to a pi-pulse U_0 and the unitary modeling the Rabi oscillation at time t with Rabi frequency Ω is

$$U_0 = \begin{pmatrix} 0 & i \\ i & 0 \end{pmatrix}, \quad U = \begin{pmatrix} \cos(\Omega t/2) & i\sin(\Omega t/2) \\ i\sin(\Omega t/2) & \cos(\Omega t/2) \end{pmatrix}. \tag{4.27}$$

Insertion into Eq. (4.19) results in a fidelity of

$$F = \frac{1}{6}(2 + 4\sin^2(\Omega t/2)) \approx 1 - \frac{1}{6}\theta_{\text{err}}, \tag{4.28}$$

where $\theta_{\text{err}} = \Omega t - \pi$ is the rotation error for the pi-pulse. In our typical calibrations, the pi-pulse is calibrated using an approximately 1 V output on the AWGs. The rotation angle error can then be converted into a voltage error V_{err}

$$F = 1 - \frac{1}{6}(\pi V_{\text{err}})^2. \tag{4.29}$$

For a fidelity of $F = 99.999\%$, we can tolerate a voltage error of $V_{\text{err}} = 2.5\,\text{mV}$, which is well within the specs of typical hardware noise.

Drive Frequency Error

In addition to the drive amplitude, the drive frequency is the other control knob governing the pi-pulse calibration. The full unitary corresponding to off-resonant Rabi oscillations is

$$U(t) = e^{i\delta t/2}\begin{pmatrix} \cos(\tilde{\Omega}t/2) - i\frac{\delta}{\tilde{\Omega}}\sin(\tilde{\Omega}t/2) & i\frac{\Omega}{\tilde{\Omega}}\sin(\tilde{\Omega}t/2) \\ i\frac{\Omega}{\tilde{\Omega}}\sin(\tilde{\Omega}t/2) & \cos(\tilde{\Omega}t/2) + i\frac{\delta}{\tilde{\Omega}}\sin(\tilde{\Omega}t/2) \end{pmatrix}, \tag{4.30}$$

where δ is the drive detuning ($\delta = \omega_{\text{drive}} - \omega_{\text{qubit}}$), Ω is the Rabi frequency, and $\tilde{\Omega} = \sqrt{\Omega^2 + \delta^2}$ is the generalized Rabi frequency. Assuming that the pi-pulses are correctly calibrated for a full rotation ($\tilde{\Omega} = \pi$), the ideal and experimental unitaries become

$$U_0 = \begin{pmatrix} 0 & i \\ i & 0 \end{pmatrix}, \quad U = e^{i\delta t/2}\frac{i}{\tilde{\Omega}}\begin{pmatrix} -\delta & \Omega \\ \Omega & \delta \end{pmatrix}, \tag{4.31}$$

with the fidelity calculated using Eq. (4.19) to be

$$F = \frac{1}{6}\left(2 + 4\frac{\Omega^2}{\Omega^2 + \delta^2}\right) \approx 1 - \frac{2}{3}\frac{\delta^2}{\Omega^2}. \tag{4.32}$$

In order to realize a 99.999% fidelity gate, we require $\delta/\Omega \leq 0.0039$, which will typically necessitate DRAG calibration or some other pulse correction techniques to compensate for AC-stark shifts.

Chapter 5

FTF Architecture for Quantum Computing

The fluxonium qubit [56, 29, 67] is a promising alternative to the transmon for gate-based quantum information processing [66], offering increased lifetimes [92] and larger anharmonicities. Namely, energy relaxation times exceeding 1 ms [75, 93] have been observed, alongside anharmonicities of several GHz when operated at an external bias of a half-flux quantum, termed the "sweet spot".

With these advantages, fluxonium qubits have already achieved single-qubit gate fidelities above 99.99% [93]. Two-qubit gates relying on capacitive coupling [6, 26, 61, 30, 103], however, are more challenging because the same small transition matrix elements which improve T_1 concomitantly reduce the interaction strength between qubits. Moreover, direct capacitive coupling results in an undesired, always-on entangling rate (ZZ). In previous works, a variety of strategies were employed to reduce the ZZ, such as keeping coupling strengths small or using AC-Stark drives, all of which have their own individual drawbacks. Finally, two-qubit gates must also reliably contend with frequency collisions with spectator qubits if they are to be scaled to larger arrays of qubits without sacrificing fidelity.

In this Chapter, we introduce the fluxonium-transmon-fluxonium circuit (FTF) as a novel architecture for coupling fluxonium qubits via a transmon coupler. FTF suppresses the static ZZ rate down to kHz levels in a manner nearly insensitive to

design parameter variations while simultaneously providing strong couplings for two-qubit gates via non-computational states. Using FTF, we propose and demonstrate a microwave-activated CZ gate between two fluxonium qubits in a 2D-planar geometry. This gate takes advantage of strong capacitive couplings which create a manifold of highly hybridized states that mix the first higher transition ($|1\rangle \leftrightarrow |2\rangle$) of both fluxonium qubits with the transmon's lowest transition ($|0\rangle \leftrightarrow |1\rangle$). Despite these strong couplings, the computational states remain relatively unhybridized due to the large qubit-coupler detuning, allowing for high-quality single-qubit gates in addition to the two-qubit gate. We applied microwave pulses to drive a full oscillation to and from this manifold contingent on both fluxonium qubits starting in their excited states and benchmarked CZ gate fidelities of up to 99.992 ± 0.009 % in 50 ns via Clifford-interleaved randomized benchmarking.

The flux tunability of the transmon coupler also allows for the operation of the CZ gate at a wide range of microwave drive frequencies, providing a convenient way to avoid frequency collisions *in situ* in larger-scale devices. Such *in situ* tunability is critical for microwave-activated gates, as dependence on a particular frequency layout places an exponentially difficult demand on fabrication precision [89, 39] as the number of qubits increases. Our devices also exhibit up to millisecond T_1 in a multi-qubit planar geometry, placing them among the highest coherence superconducting qubits to date and priming them for use in larger systems.

5.1 The FTF Architecture

Our device configuration consists of two differential fluxonium qubits capacitively coupled to a grounded transmon coupler (see [Fig. 5-1(a)] for a simplified circuit schematic), with a much weaker direct capacitive coupling between the two fluxonium qubits [Fig. 5-1(b)]. The two lowest-lying states of each fluxonium form the computational basis ($|00\rangle, |01\rangle, |10\rangle, |11\rangle$), and the first excited state of the coupler, in addition to the second excited states of the fluxonium qubits, serve as useful non-computational states. Modeling only the qubits and their pairwise capacitive

couplings, our system Hamiltonian is

$$\begin{aligned}\hat{H}/h &= \sum_{i=1,2} 4E_{C,i}\hat{n}_i^2 + \frac{1}{2}E_{L,i}\hat{\phi}_i^2 - E_{J,i}\cos(\hat{\phi}_i - \phi_{\text{ext},i}) \\ &+ 4E_{C,c}\hat{n}_c^2 - E_{J1,c}\cos(\hat{\phi}_c) - E_{J2,c}\cos(\hat{\phi}_c - \phi_{\text{ext},c}) \\ &+ J_{1c}\hat{n}_1\hat{n}_c + J_{2c}\hat{n}_2\hat{n}_c + J_{12}\hat{n}_1\hat{n}_2, \end{aligned} \tag{5.1}$$

where E_C, E_J, and E_L represent the charging, Josephson, and inductive energies, respectively. Subscripts $i = 1, 2$ index the two fluxonium nodes, and subscript c labels the coupler node. Here we also introduced the external phase ϕ_{ext}, which is related to the external flux Φ_{ext} through the expression $\Phi_{\text{ext}}/\Phi_0 = \phi_{\text{ext}}/2\pi$ for each qubit. For both our main device (Device A) and a secondary device (Device B), the experimentally obtained Hamiltonian parameters are listed in Table 5.1, along with the measured coherence times. All fluxonium resonators had approximately $\chi_{01} = 0.3\,\text{MHz}$ and $\kappa = 1.5\,\text{MHz}$.

Table 5.1: **Characterization of FTF devices.** Hamiltonian parameters for both Device **A** and Device **B** were obtained by fitting two-tone spectroscopy data and the static ZZ rate vs. coupler flux. Coherence times were measured by biasing each fluxonium at $\Phi_{\text{ext}} = 0.5\,\Phi_0$ using only the global flux bias. Unless otherwise stated, all data corresponds to Device A.

		E_C (GHz)	E_L (GHz)	E_J (GHz)	N_{JJ}	$\omega_{01}/2\pi$ (GHz)	$\omega_r/2\pi$ (GHz)	T_1 (µs)	T_2^R (µs)	T_2^E (µs)
A	Fluxonium 1	1.41	0.80	6.27	102	0.333	7.19	560	160	200
A	Fluxonium 2	1.30	0.59	5.71	102	0.242	7.08	1090	70	190
A	Transmon c	0.32		3.4, 13	–	–	7.30	–	–	–
B	Fluxonium 1	1.41	0.88	5.7	102	0.426	7.20	450	230	240
B	Fluxonium 2	1.33	0.60	5.4	102	0.281	7.09	1200	135	310
B	Transmon c	0.30		3.0, 13	–	–	7.31	–	–	–

		J_{1c} (MHz)	J_{2c} (MHz)	J_{12} (MHz)
A	Coupling Strengths	570	560	125
B	Coupling Strengths	550	550	120

5.1.1 Gate Operation

The operating principles of FTF are fundamentally different than those of all-transmon circuits [106]. Due to its relatively high frequency, the coupler interacts negligibly

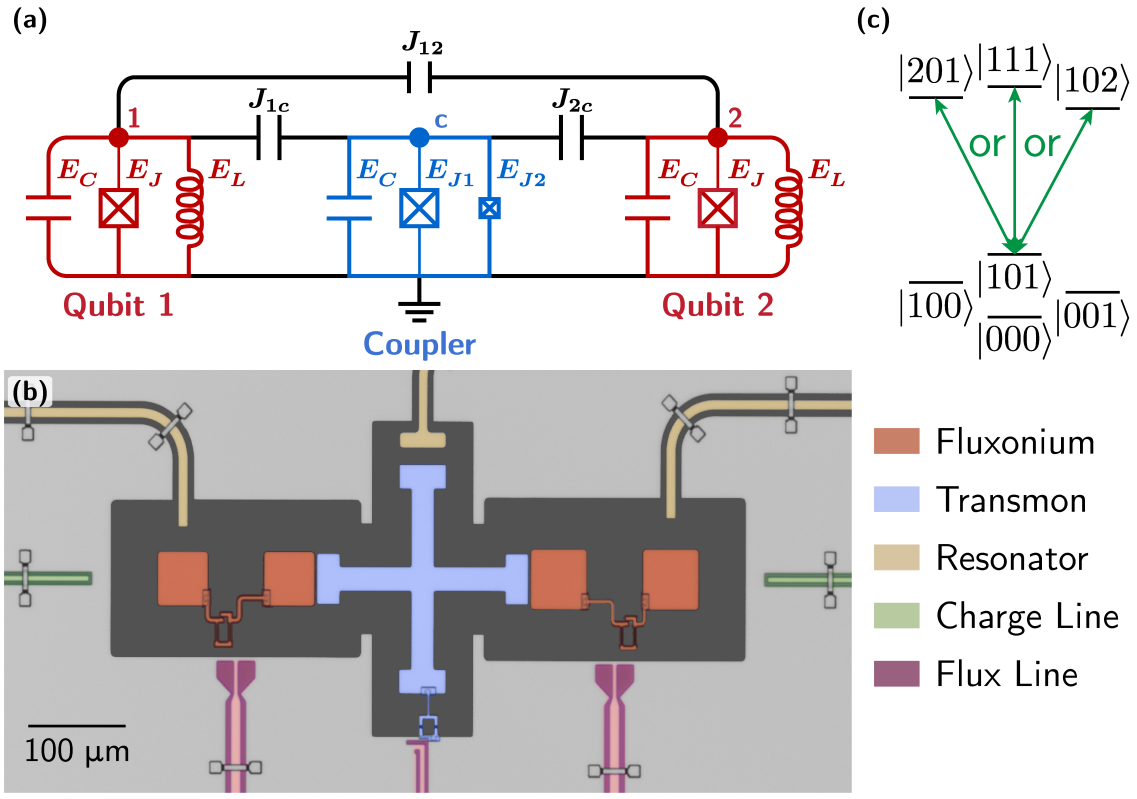

Figure 5-1: **Device overview and gate principle.** **(a)** Simplified circuit schematic of two fluxonium qubits (red) capacitively coupled to a tunable-transmon coupler (blue). **(b)** False-colored optical micrograph of the two fluxonium qubits and the transmon along with their readout resonators, charge lines, and local flux lines. Arrays of 102 Josephson junctions in series form the fluxonium inductances. **(c)** Energy level diagram illustrating the principle of the CZ gate. In practice, levels $|201\rangle$, $|102\rangle$, and $|111\rangle$ are highly hybridized, and selectively driving any of these transitions results in a CZ gate.

with the computational states of the qubits. Instead, the coupler predominantly interacts with the higher levels of the qubits, acting as a resource for two-qubit gates without adversely affecting single-qubit gates.

We describe the quantum state of the system using the notation $|jkl\rangle$, where j, k, and l denote the energy eigenstates in the uncoupled basis of fluxonium 1, the coupler, and fluxonium 2, respectively. While coupler-based gates are often activated by baseband flux pulses, here we generate the required entangling interaction via a microwave pulse from $|101\rangle$ to a non-computational state of the joint system. As illustrated in Fig. 5-1(c), a single-period Rabi oscillation from $|101\rangle$ to either $|201\rangle$,

$|111\rangle$, or $|102\rangle$ gives the 180° conditional phase shift necessary for a CZ gate, provided no other transitions are being driven. We note that, throughout this Chapter, we label the eigenstates according to their maximum overlap with the uncoupled qubit/coupler states at $\Phi_{\text{ext,c}} = 0$ (equivalently $\Phi_{\text{ext,c}} = 1\,\Phi_0$). We perform this labeling at $\Phi_{\text{ext,c}} = 0$ because tuning the coupler flux results in avoided crossings among the higher levels of the system.

In general, stronger coupling strengths result in larger detunings from parasitic transitions in two-qubit gate schemes, yet doing so often results in unintended consequences. Two common drawbacks of larger coupling strengths are remedied using the FTF architecture: (1) crosstalk due to non-nearest-neighbor couplings, and (2) unwanted static ZZ interactions. In all transmon-based architectures, the same level repulsion that enables the two-qubit gate also creates level repulsions within the computational subspace. This is because all transition frequencies and charge matrix elements of adjacent levels in a transmon have similar values. As this hybridization among the computational states increases, charge drives will produce non-local microwave crosstalk to unwanted qubit transitions. In FTF, the large ratio of transition matrix elements $|\langle 2|\,\hat{n}\,|1\rangle|/|\langle 1|\,\hat{n}\,|0\rangle|$ for fluxonium qubits, the large fluxonium anharmonicity, and the large detunings between the transmon and each fluxonium all serve to mitigate these negative side-effects.

5.1.2 *ZZ* Reduction

Formally, the ZZ interaction rate is defined as

$$\zeta = (E_{11} - E_{10} - E_{01} + E_{00})/h \tag{5.2}$$

(for two qubits) or

$$\zeta = (E_{101} - E_{100} - E_{001} + E_{000})/h \tag{5.3}$$

(for two qubits and a coupler). It describes an unwanted, constant, controlled-phase-type entangling rate caused by the collective level repulsions from the many non-

computational states of superconducting qubits acting on the computational states, which must be minimized.

A key feature of the FTF architecture is its ability to suppress ζ, despite the strong coupling strengths that would typically amplify it. This low ζ can be understood by considering the couplings J_{ij} perturbatively up to fourth order. At each order m, the perturbative correction can be considered an mth-order virtual transition between the states of the uncoupled qubits; the strength of a particular transition is proportional to the product of the corresponding couplings J_{ij}. In Fig. 5-2(a), we illustrate the dominant virtual transitions up to fourth order: the first-order correction is zero; at second order, only direct transitions between the two fluxonium qubits contribute to ζ; at third order, the only allowed transitions form three-cycles between the three qubits; and at fourth order, we find that transmon-mediated transitions between the two fluxonium qubits dominantly contribute to ζ (further details can be found in the appendix of Ref. [24]). As such, we can write ζ to fourth order as

$$\zeta \approx J_{12}^2 \zeta^{(2)} + J_{12} J_c^2 \zeta^{(3)} + J_c^4 \zeta^{(4)}, \tag{5.4}$$

where $\zeta^{(i)}$ depend only on the uncoupled states, and we assume $J_{1c} = J_{2c} = J_c$. Specifically, we find our device to be well-described by $\zeta^{(2)} = -2.1 \times 10^{-3}\,\mathrm{GHz}^{-1}$, $\zeta^{(3)} = 1.4 \times 10^{-3}\,\mathrm{GHz}^{-2}$, and $\zeta^{(4)} = -2.6 \times 10^{-4}\,\mathrm{GHz}^{-3}$ at $\Phi_{\mathrm{ext,c}} = 0.5\,\Phi_0$, obtaining by a numerical computation of the perturbation theory. Critically, both the second- and fourth-order terms are negative, while the third-order term is positive. This is a direct consequence of the perturbation theory: for virtual transitions to excited states above the computational subspace, even-order terms describe level repulsions, while odd-order terms describe level attractions. The relatively low ZZ in the FTF system stems from this cancellation between even and odd terms.

To understand this quantitatively, we numerically calculate ζ by diagonalizing Eq. (5.1) as a function of J_c and J_{12} [Fig. 5-2(b)]. We find that ζ can be almost perfectly canceled by appropriate choices of the couplings, as traced by the darker

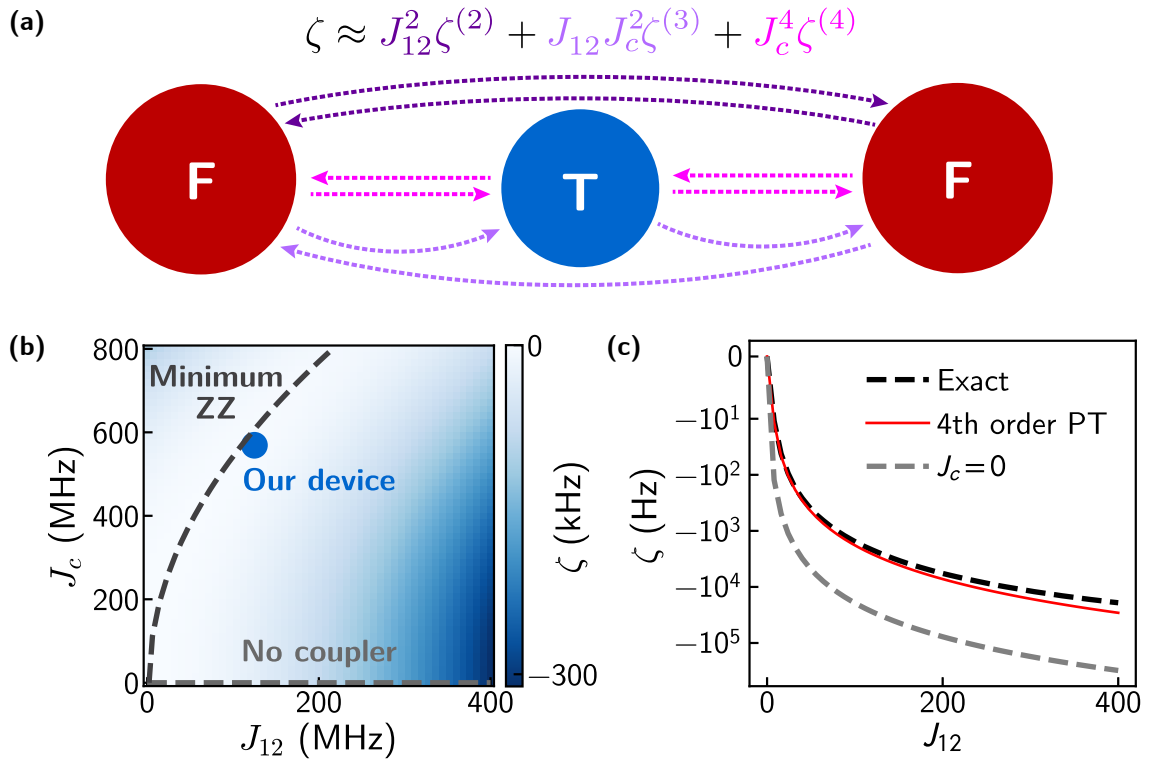

Figure 5-2: ***ZZ*-reduction in the FTF architecture. (a)** A perturbative treatment of the couplings J_{ij} shows energy shifts in FTF to be dominated by virtual transitions (dashed arrows) of second (dark purple), third (light purple), and fourth (pink) order between the fluxonium qubits (maroon circles) and the coupler (blue circle). **(b)** Numerical simulation of ζ as a function of $J_c = J_{1c} = J_{2c}$ and J_{12} with the experimentally extracted qubit parameters. With the coupler, a ratio of coupling strengths always exists that minimizes ζ (dark gray). **(c)** Plot of ζ along the "Minimum ZZ" parabola in (a), as a function of J_{12}. The black curve shows a numerical diagonalization of the Hamiltonian, which is accurately described by 4th order perturbation theory (red). Without the coupler (gray), $|\zeta|$ is roughly an order of magnitude larger for this range of coupling strengths.

dashed line. Within perturbation theory, this curve of minimum ζ is a parabola:

$$d\zeta/dJ_{12} = 0 \tag{5.5}$$

$$\implies J_{12} = -J_c^2\zeta^{(3)}/2\zeta^{(2)}. \tag{5.6}$$

By inserting this expression into Eq. (5.4), we obtain the dependence of ζ *along* the

parabola

$$\zeta_{\min} = J_c^4(-\zeta^{(3)}\zeta^{(3)}/4\zeta^{(2)} + \zeta^{(4)}). \tag{5.7}$$

For our device parameters, the two terms in parentheses almost cancel, summing to -2×10^{-6} GHz^{-3}.

Importantly, $|\zeta|$ remains below 10 kHz for J_c values of up to 1 GHz, while maintaining the optimal coupling ratio. To take full advantage of this phenomenon, we designed the coupling strengths to be as large as reasonable for our geometry. Despite the large coupling strengths, ζ is only weakly dependent on J_c, and J_{12}: independent errors in J_c and J_{12} by up to 20% would increase ζ in our device by a maximum of 11 kHz (modeling the worst case scenario in which J_{12} increases and J_c decreases). Such robustness will be critical in larger-scale devices, as capacitive coupling strengths cannot be changed after device fabrication and are subject to fabrication variations. In Fig. 5-2(c), we compute ζ as a function of J_{12} (assuming the optimal corresponding value of J_c) with an exact numerical diagonalization (black) and perturbation theory (red), illustrating that perturbation theory up to 4th order is a sufficient description of the total ZZ rate in the FTF system.

The value of ζ is also insensitive to the coupler frequency, allowing us to safely bias the system at any $\Phi_{\text{ext,c}}$. This is unsurprising, as the coupler energy levels are far from any resonances with the computational states. In other words, any change in the coupler frequency must compete with the large detuning between the coupler and fluxonium $|0\rangle \leftrightarrow |1\rangle$ transitions. To validate our models, we experimentally determined ζ by measuring the frequency of fluxonium 1 using a Ramsey experiment while preparing fluxonium 2 in the ground or excited state. Taking the difference in fitted frequencies associated with the two initial state preparations yields the experimental value of ζ, which we find to closely follow our numerical simulations as a function of the coupler flux [see Fig. 5-3(a)]. An alternative approach to ZZ reduction with fluxonium qubits is to apply always-on AC-Stark drives [103, 26]. While this is an effective means to reduce ZZ in few-qubit devices, the requirement of an additional calibrated drive per qubit becomes increasingly prohibitive as system sizes grow.

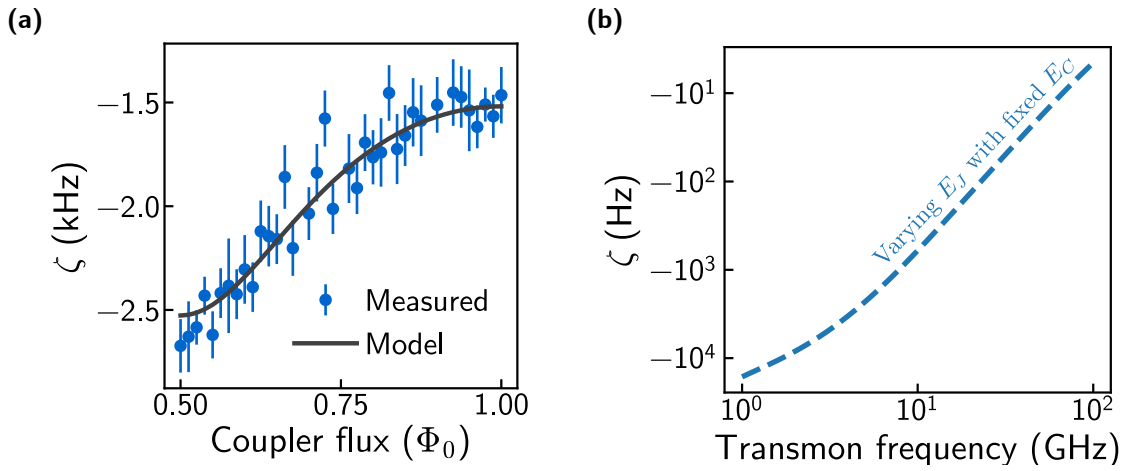

Figure 5-3: **Numerical simulations of ζ in the FTF system. (a)** Measured and simulated ζ as a function of the coupler flux for the experimental device parameters. The ZZ rate remains nearly constant between -1.5 and $-2.7\,\mathrm{kHz}$. **(b)** Numerical simulation of ζ as a function of the coupler frequency. The Device A parameters from Table 5.1 are used, except the effective transmon E_J is changed to vary the transmon frequency. As this frequency increases, $|\zeta|$ decreases asymptotically to below $10\,\mathrm{Hz}$ for this set of device parameters.

Another interesting feature of FTF is that if the transmon frequency is tuned toward infinity, ζ does not return to its value with only the two fluxonium qubits and can in fact decrease even further. In Fig. 5-3(b), we numerically simulate ζ as a function of the coupler frequency using the Device A parameters and find that ζ asymptotes to less than $10\,\mathrm{Hz}$ as the transmon frequency increases. When the transmon frequency is tuned, not only do the energy level detunings increase, but the charge matrix element also increases through the effective E_J. This increase in the charge matrix elements prevents the level repulsions involving the coupler from vanishing even when the coupler frequency becomes infinitely large. This feature makes FTF useful even in fluxonium gate schemes that do not involve the non-computational states. By coupling a fixed frequency transmon (or resonator) with a high frequency (arising from a high E_J) to each fluxonium with the appropriate coupling strengths, ζ can be reduced to near 0 in a robust manner without needing any measurement or calibration of the extra transmon element.

5.1.3 Grounded vs. Differential Qubits

In this section, we elucidate our conscious decision to use a grounded transmon with differential fluxonium qubits. While identical qubits can be designed with both differential and grounded designs, this choice can still have important consequences in multi-qubit circuits. By using a differential fluxonium, we reduce the amount of capacitance that coupling appendages contribute to the total effective qubit capacitance. A differential qubit also allows for a larger total area of capacitor pads for the same qubit charging energy E_C. This is important to allow for enough physical room to couple other circuit elements such as resonators, charge lines, flux lines, and other qubits to each fluxonium. We will now show that the choice of a grounded transmon has the critical feature of maintaining a near-optimal ratio of J_c^2/J_{12} while freely varying the fluxonium-transmon coupling capacitance, allowing for leading-order insensitivity to common parameter variations.

Grounded Transmon

To minimize the ZZ interaction ζ, we need $J_c^2/J_{12} = -2\zeta^{(2)}/\zeta^{(3)} \approx 2.97\,\text{GHz}$ using the parameters for Device A. We claim that by using a grounded transmon, we can target this value of J_c/J_{12} with first-order insensitivity to the coupling capacitance (between the transmon and the adjacent fluxonium pad) C_c. Consequently, C_c becomes a free parameter in the device design, and uncertainty in its value will, to first order, have no effect on ζ. To understand this theoretically, we assume the simplified circuit schematic represented in Fig. 5-4(a). All capacitances not explicitly labeled are small and qualitatively unimportant in this analysis.

We can write down the capacitance matrix of this circuit as

$$\mathbf{C} = \begin{pmatrix} C_F & -C_{f2} & 0 & 0 & 0 \\ -C_{f2} & C_F + C_c & -C_c & 0 & 0 \\ 0 & -C_c & C_t + 2C_c & 0 & -C_c \\ 0 & 0 & 0 & C_F & -C_{f2} \\ 0 & 0 & -C_c & -C_{f2} & C_F + C_c \end{pmatrix}, \tag{5.8}$$

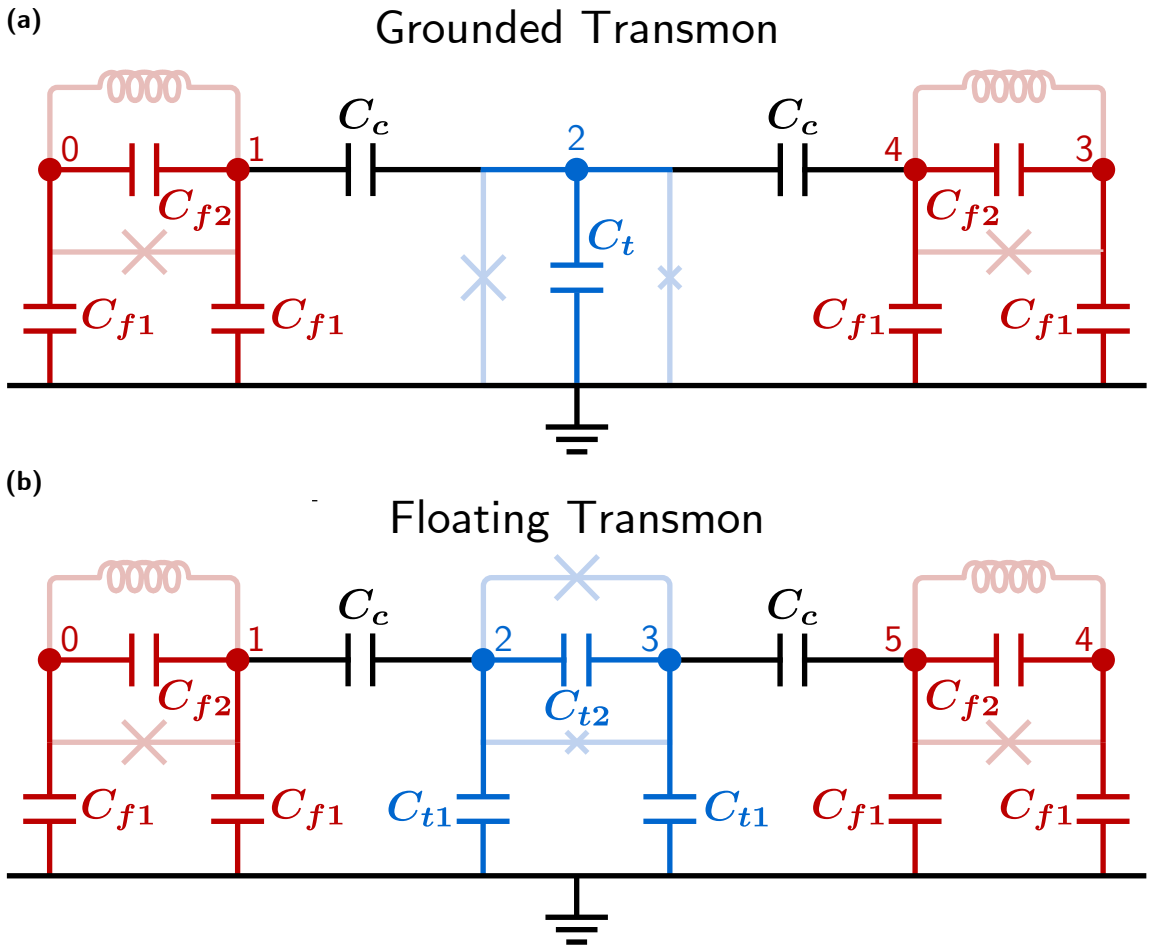

Figure 5-4: **Simplified circuit model of FTF circuits.** **(a)** FTF circuit with a grounded transmon. The capacitance network is simplified for the purpose of a theoretical analysis, with no direct fluxonium-fluxonium capacitance. **(b)** Same circuit except with a differential transmon coupler.

where we defined $C_F = C_{f1}+C_{f2}$ for convenience. In order to isolate the relevant mode of each differential qubit, we perform a standard variable transformation into sum and difference coordinates which modifies the capacitance matrix as $\tilde{\mathbf{C}} = (\mathbf{M}^T)^{-1}\mathbf{C}\mathbf{M}^{-1}$ with

$$\mathbf{M} = \begin{pmatrix} 1 & 1 & 0 & 0 & 0 \\ 1 & -1 & 0 & 0 & 0 \\ 0 & 0 & 1 & 0 & 0 \\ 0 & 0 & 0 & 1 & 1 \\ 0 & 0 & 0 & 1 & -1 \end{pmatrix}, \tag{5.9}$$

The qubit modes for each differential qubit are then solely determined by the difference coordinates, with the resultant three-qubit nodes on indices 1, 2, and 4. We can straightforwardly discard the modes corresponding to summed coordinates in the Hamiltonian and compute coupling strengths between nodes as $J_{ij} = 4e^2\tilde{\mathbf{C}}^{-1}[i,j]$. Thus,

$$J_c^2/J_{12} = 4e^2\frac{\tilde{\mathbf{C}}^{-1}[1,2]^2}{\tilde{\mathbf{C}}^{-1}[1,4]} \tag{5.10}$$

$$\approx 4e^2\frac{1}{C_t} + \mathcal{O}(C_t^{-2}), \tag{5.11}$$

where we performed a Taylor expansion assuming C_c, C_{f1}, and C_{f2} are small compared to C_t in the final step. We see that to leading order, the value of J_c^2/J_{12} is solely determined by C_t^{-1}, with any dependence on C_c scaling with $\mathcal{O}(C_t^{-2})$. By inserting the designed values of $C_t = 45\,\text{fF}$ $C_{f1} = 11\,\text{fF}$, and $C_{f2} = 2.8\,\text{fF}$, Eq. (5.10) gives 2.8 GHz and Eq. (5.11) gives 3.4 GHz. We emphasize that Eq. (5.11) illustrates a concept in our architecture and that exact design simulations of our coupling strengths were performed with full 5×5 capacitance matrices with no mathematical approximations.

Differential Transmon

To investigate how these relationships would compare when substituting for a differential transmon, we model the hypothetical circuit with the capacitance network in Fig. 5-4(b). The capacitance matrix, in this case, is

$$\mathbf{C} = \begin{pmatrix} C_F & -C_{f2} & 0 & 0 & 0 & 0 \\ -C_{f2} & C_F + C_c & -C_c & 0 & 0 & 0 \\ 0 & -C_c & C_T + C_c & -C_{t2} & 0 & 0 \\ 0 & 0 & -C_{t2} & C_T + C_c & 0 & -C_c \\ 0 & 0 & 0 & 0 & C_F & -C_{f2} \\ 0 & 0 & 0 & -C_c & -C_{f2} & C_F + C_c \end{pmatrix} \tag{5.12}$$

where we have likewise defined $C_T = C_{t1} + C_{t2}$. The transformation matrix in this case is

$$\mathbf{M} = \begin{pmatrix} 1 & 1 & 0 & 0 & 0 & 0 \\ 1 & -1 & 0 & 0 & 0 & 0 \\ 0 & 0 & 1 & 1 & 0 & 0 \\ 0 & 0 & 1 & -1 & 0 & 0 \\ 0 & 0 & 0 & 0 & 1 & 1 \\ 0 & 0 & 0 & 0 & 1 & -1 \end{pmatrix} \tag{5.13}$$

and our coupling ratio is

$$J_c^2/J_{12} = 4e^2 \frac{\tilde{\mathbf{C}}^{-1}[1,3]^2}{\tilde{\mathbf{C}}^{-1}[1,5]} \tag{5.14}$$

$$\approx 4e^2 \frac{1}{C_{t2}} + \mathcal{O}(C_{t1}^{-1}). \tag{5.15}$$

While still independent of C_c to leading order, the value of $4e^2/C_{t2}$ is far too large compared to the optimal value of $-2\zeta^{(2)}/\zeta^{(3)} \approx 2.97\,\text{GHz}$. Furthermore, FTF benefits from as high of coupling strengths as possible, and a differential transmon reduces the values of J_c and J_{12} for a fixed value of C_c.

5.2 Experimental Setup

In this Section we describe the experimental setup including the wiring, readout, and flux biasing used in the subsequent calibrations.

5.2.1 Wiring

This experiment was conducted in a Bluefors XLD600 dilution refrigerator operated at around 20 mK, with the full wiring setup shown in Fig. 5-5. At the mixing chamber (MXC), the device was magnetically shielded with a superconducting can, surrounded by a Cryoperm-10 can. To reduce thermal noise from higher temperature stages, we typically used in total 23 dB attenuation for the coupler flux lines, 30 dB attenuation for the fluxonium flux lines, 50 dB total attenuation on charge lines, and 70 dB

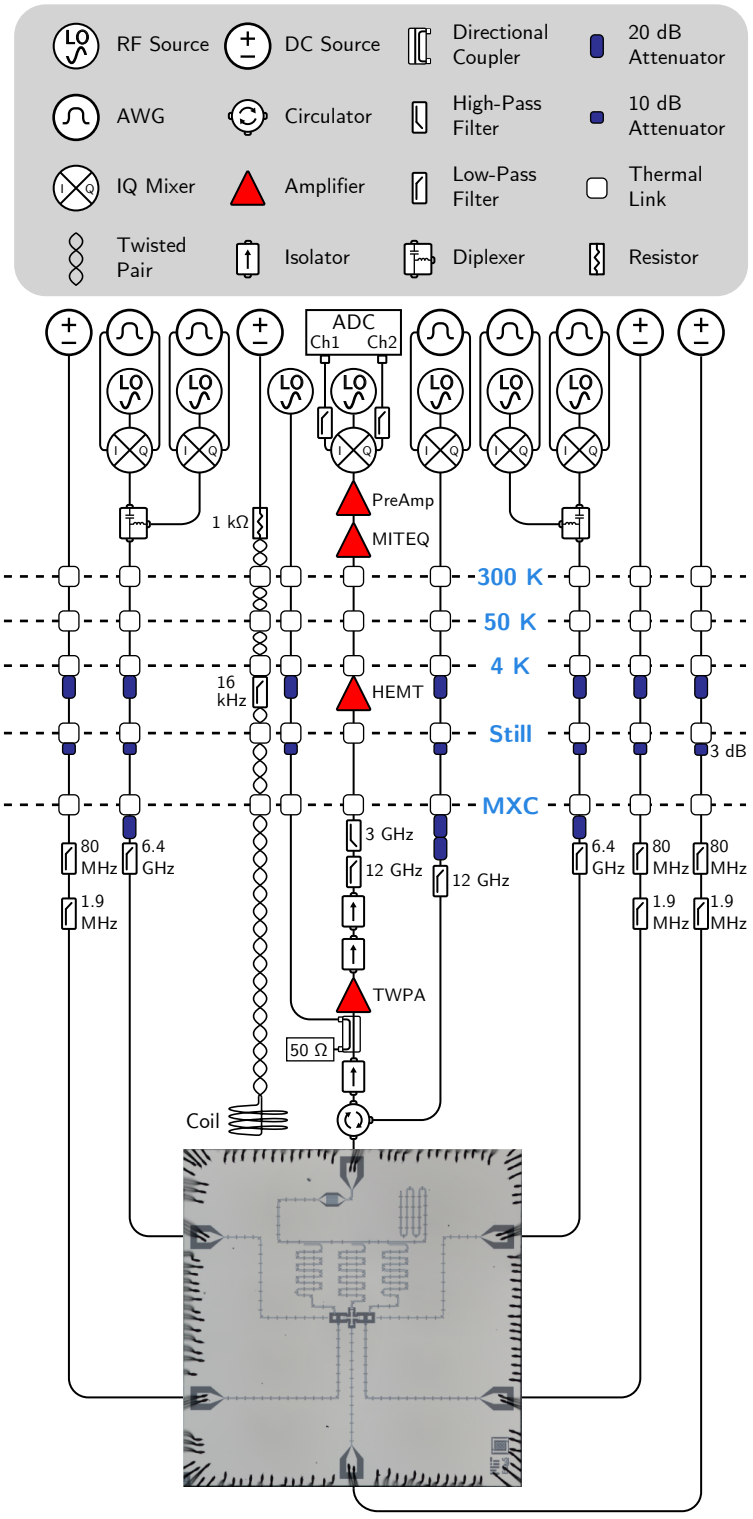

Figure 5-5: **A detailed wiring schematic of the experimental setup.**

total attenuation on the readout input – the exact value of the attenuation at Still varied between 3 dB and 10 dB across the flux lines of both devices, though this difference was not critical for any experiment. The readout output was first amplified by a Josephson traveling-wave parametric amplified (JTWPA), pumped by a Holzworth RF synthesizer, then amplified further with a high-electron-mobility transistor (HEMT) amplifier at the 4 K stage, another HEMT at room temperature, and a final Stanford Research SR445A amplifier, before being digitized by a Keysight M3102A digitizer.

All AC signals – readout, single- and two-qubit gate pulses – were generated by single sideband mixing of Keysight M3202A 1GSa/s arbitrary waveform generators with Rohde and Schwarz SGS100A SGMA RF sources. For each qubit, the single- and two-qubit gate pulses were combined at room temperature via a diplexer from Marki Microwave (DPXN-2 for Qubit 1 and DPXN-0R5 for Qubit 2). For these diplexers, the single-qubit gate frequencies occur at low enough frequencies to fall in the pass band of the DC port. All these control electronics were synchronized through a common SRS 10 MHz rubidium clock.

The DC voltage bias for each qubit flux line as well as the global bobbin was supplied by a QDevil QDAC. The flux lines by design support RF flux, but in this experiment were filtered by 80 MHz and 1.9 MHz low-pass filters at the MXC. The current for the global coil was carried through a twisted pair, with a homemade 16 kHz cutoff RC filter at the 4 K stage.

Table 5.2: **Summary of control equipment.** The manufacturers and model numbers of the control equipment used for this experiment.

Component	Manufacturer	Model
Dilution Fridge	Bluefors	XLD600
RF Source	Rohde and Schwarz	SGS100A
DC Source	QDevil	QDAC I
Control Chassis	Keysight	M9019A
AWG	Keysight	M3202A
ADC	Keysight	M3102A

5.2.2 Readout and Initialization

In thermal equilibrium, our fluxonium qubits have nearly equal populations in the ground and excited states ($k_{\mathrm{B}}T > \hbar\omega_{01}$). To address this, we initialized each qubit in either the ground or excited state at the beginning of each experiment using the one-pulse and two-pulse post-selection techniques detailed in Section 4.1.3. To realize independent qubit initialization in our system, each qubit was capacitively coupled to a separate readout resonator, allowing us to perform high-fidelity, single-shot readout within the full computational basis. We note that all three resonators were further coupled to a common Purcell filter [84].

5.2.3 DC Biasing

We used a global biasing coil to tune the flux across the entire device and additional local flux lines biased through coaxial cables for independent control of each qubit. This allowed us to freely change the coupler flux while holding each fluxonium at $\Phi_{\mathrm{ext}} = 0.5\Phi_0$. Although only DC flux was required in our experiment, our device is fully compatible with fast-flux pulses. As such, FTF presents an opportunity to investigate iSWAP, Landau-Zener, or other flux-modulated gates in a system with low static ZZ rates [6, 17, 109, 86, 85, 63].

Unfortunately, we found that our qubit coherence times were sensitive to bias-induced heating from the coaxial flux lines. We have found that both qubit T_1 and T_2 (both Ramsey and spin-echo) drop with increasing current. To minimize this effect when performing two-qubit experiments, the global coil was used to simultaneously bias the two fluxonium qubits as close as possible to their operation points $\Phi_{\mathrm{ext},1} = \Phi_{\mathrm{ext},2} = 0.5\,\Phi_0$. The local flux lines were then used to more precisely tune $\Phi_{\mathrm{ext},1}$ and $\Phi_{\mathrm{ext},2}$ and bias the coupler flux. Curiously, no bias-induced heating was observed from the global coil, which was biased using twisted pairs, as opposed to coaxial cables. When DC biasing the local flux lines with twisted pairs though, we observe a sharp drop in T_2 times. We emphasize that this nonideality is not fundamental nor unique to the FTF architecture and can be improved in future experiments

by optimized construction and filtering of our flux-bias lines.

5.3 Gates

5.3.1 Single-Qubit Gates

To deconvolve the aforementioned heating effects from the measurement results, we biased the qubits solely with the global coil when characterizing individual qubit coherences (see Table 5.1). Notably, fluxonium 2 in our device achieves a lifetime of over a millisecond, with similar performance reproduced in Device B (see Section 5.5). In accordance with the higher qubit frequency, fluxonium 1 has a shorter lifetime, and the T_2^E of all characterized qubits peaks between 200-300 µs, likely limited by photon-shot noise from occupation of the resonator or filtering of the flux lines.

We realized single-qubit gates by calibrating Rabi oscillations generated by a resonant charge drive using a cosine pulse envelope. To quantify the fidelities of these gates, we performed individual as well as simultaneous Clifford randomized benchmarking (RB) using a microwave-only gate set, $\{I, \pm X, \pm Y, \pm X_{\pi/2}, \pm Y_{\pi/2}\}$, to generate the Clifford group, resulting in an average of 1.875 gates per Clifford [51, 8]. In our decomposition, all gates had an equal time duration and were derived from a single calibrated X_π pulse by halving the amplitude and/or shifting its phase (see Section 4.3 for the full calibration sequence). Here, both qubits were biased at $\Phi_{\text{ext}} = 0.5\,\Phi_0$ with minimal current through the coupler flux line.

In Fig. 5-6(a), we varied the pulse width from 10 ns to 42 ns and found average single-qubit gate fidelities consistently near or above 99.99% and show the explicit randomized benchmarking traces in Figs. 5-6(b-c) for a gate duration of 18 ns. In this range, the incoherent error begins to trade off with the coherent error (from violating the rotating wave approximation), with qubit 1 able to tolerate a shorter gate time than qubit 2 due to its higher frequency. This coherent error is manifest in the randomized benchmarking traces as an increase in the standard deviation of the data across different randomization seeds. We note gates were additionally calibrated

at 6 ns with significantly lower fidelities on both qubits due to large coherent errors. Overall, our fidelities from simultaneously applied gates are $<5\times10^{-5}$ lower than the individually applied ones, a testament to the low ZZ rate measured in our system. We suspect the small difference in fidelity is caused by microwave crosstalk between charge lines and qubits.

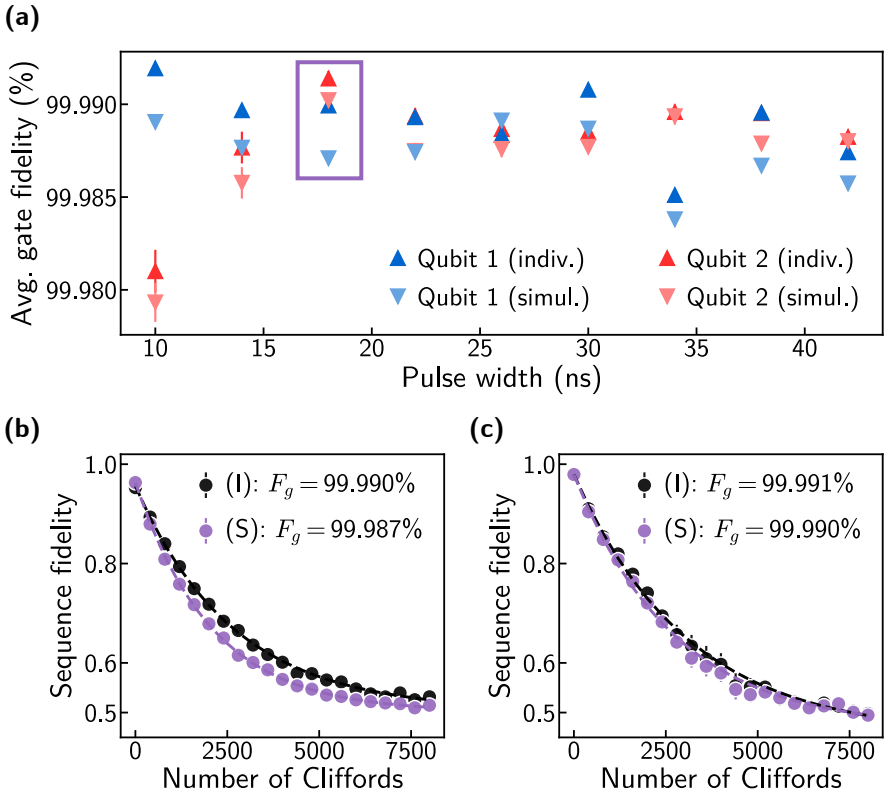

Figure 5-6: **Single-qubit benchmarking on our multi-qubit device. (a)** Average single-qubit gate fidelities obtained by individual and simultaneous Clifford randomized benchmarking as a function of pulse width. **(b-c)** Individual (I) and simultaneous (S) RB traces of a 18 ns gate (purple box in (a)) for qubit 1 and qubit 2, respectively. Individual and simultaneous average gate fidelities have a standard error of about 3×10^{-6} for qubit 1 and 4×10^{-6} for qubit 2. The larger error bars in the qubit 2 data arise from coherent errors, which begin to overtake the incoherent errors for gates shorter than 18 ns (red points in (a)).

In the gates presented in this section, only the X_π gate was calibrated and all other gates were derived from it by scaling the pulse amplitude or adjusting the pulse phase. It is likely slightly better gates could be achieved by individually calibrating each gate, especially in the regime of significant coherent error, or by numerically

optimizing over the pulse envelope.

5.3.2 Two-Qubit Gate Calibration

We began our investigation of the two-qubit CZ gate by performing spectroscopy of the relevant non-computational state transitions. With the system post-selected for all computational states $|000\rangle$, $|100\rangle$, $|001\rangle$, and $|101\rangle$, we swept the coupler flux $\Phi_{\text{ext,c}}$ to map out the transition frequencies to all relevant non-computational states [see Fig. 5-7]. Most importantly, this includes the transition frequency from $|101\rangle$ to the three dressed states $|201\rangle$, $|111\rangle$, and $|102\rangle$ [see Fig. 5-7(c)]. We found that $|111\rangle$ crosses both $|201\rangle$ and $|102\rangle$ (at $\Phi_{\text{ext,c}} \approx 0.65\,\Phi_0$), with an avoided crossing strength of nearly 1 GHz. With such strong hybridization, a high-performance gate could be realized by driving any of the three energy levels over a wide coupler flux range. Nevertheless, the transitions yielded varying performance depending on their coherence times and the proximity of undesired transitions.

We activated the gate interaction associated with each transition by simultaneously applying a phase-locked charge drive to each fluxonium near the transition frequency [Fig. 5-8(a)]. These drives were chosen to have equal amplitude, with a relative phase between them to maximize constructive interference at the intended transition. We found that using two constructive drives was a convenient method for reducing the total applied power for a given Rabi rate, resulting in a reduced AC-Stark shift from off-resonant transitions. In severe cases, a large AC-Stark shift could prevent the realization of a 180° conditional phase and increase leakage into non-computational states. While theoretically we expect the relative phase and amplitude to be important for reducing leakage, we found that as long as a 180° conditional phase was attainable, the CZ gate fidelity was relatively insensitive to these two parameters. Figure 5-7(b) shows the familiar Rabi chevrons when the transition is driven as a function of frequency; in experimental practice, our two-qubit gate is quite similar to driving single-qubit Rabi oscillations. The faint chevron near 4.52 GHz is the result of the oscillation from the $|001\rangle$ state, which was visible due to imperfect state initialization.

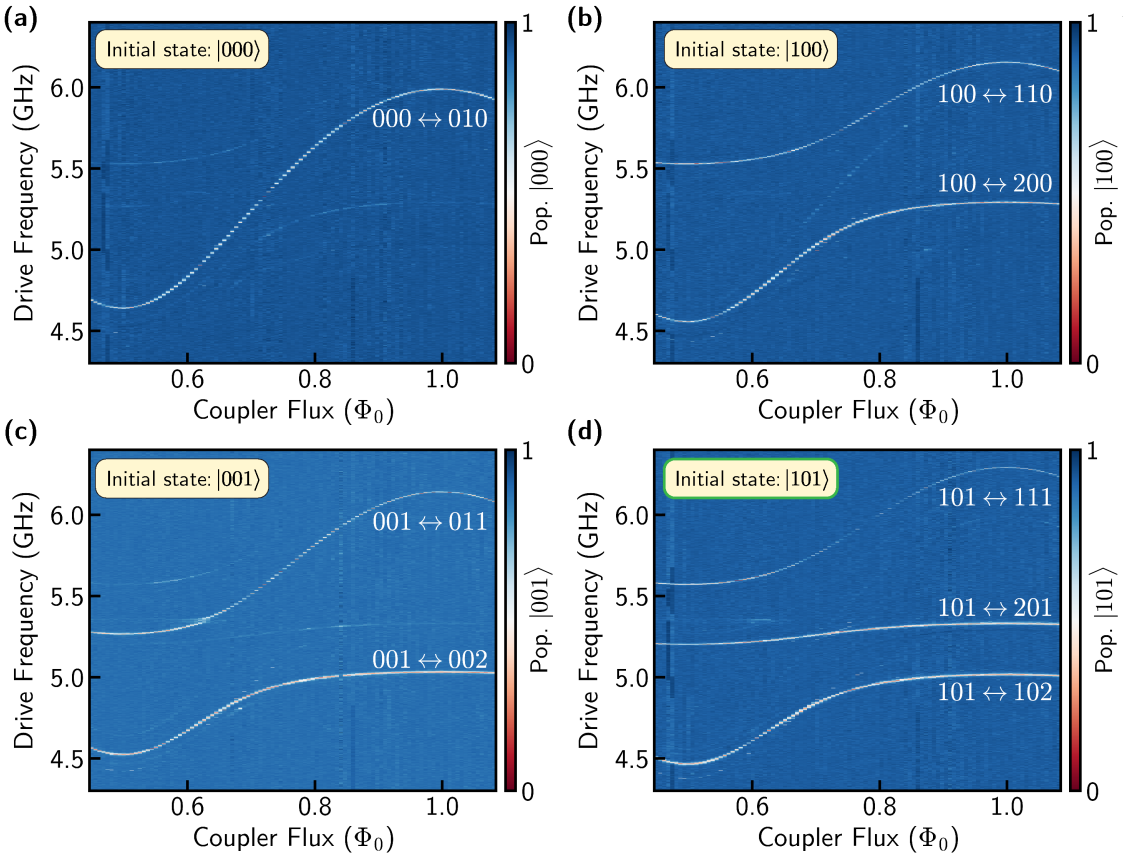

Figure 5-7: **Two-tone spectroscopy of the higher energy levels of the FTF system.** Panels **(a-d)** consist of the same spectroscopy run post-selecting for $|000\rangle$, $|100\rangle$, $|001\rangle$, or $|101\rangle$ respectively. **(d)** Shows the relevant transitions for driving the CZ gate in our experiment.

When performing a fine calibration of our CZ gate, we increased the pulse width of the single-qubit gates to 50 ns, trading off single-qubit gate fidelities so that coherent errors would not skew our tomography pulses. We also increased the idle padding between pulses from 4 ns to 10 ns because computational state lifetimes have only a secondary effect on our CZ gate fidelities. For a given transition and pulse duration, there were four critical parameters associated with the CZ gate to calibrate:

1. **Overall drive amplitude** Fig. 5-9(a, d). The overall drive amplitude of the two drives is calibrated to minimize the leakage into the driven state. This is done on the basis of a single Rabi oscillation with variable drive amplitude.

2. **Drive frequency** Fig. 5-9(b, e). The drive frequency was calibrated by per-

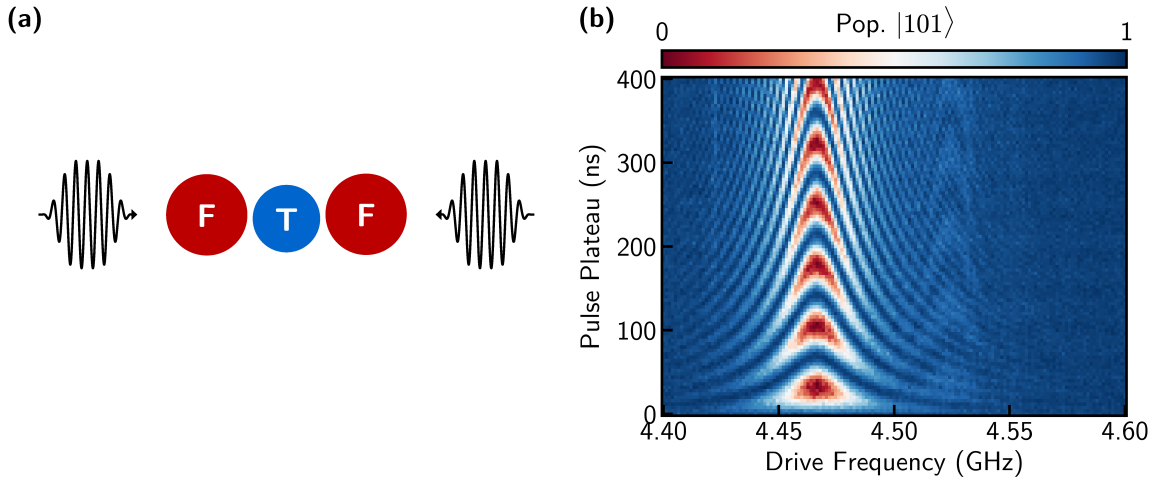

Figure 5-8: **Driven dynamics of CZ gate (a)** Illustration of how gates were driven in this experiment. Simultaneous frequency-locked pulses were applied to the charge lines of each fluxonium. **(b)** Time-domain Rabi oscillations of the $|101\rangle \leftrightarrow |102\rangle$ transition as a function of the drive frequency. The faint chevron pattern at 4.52 GHz arises from the $|001\rangle \leftrightarrow |002\rangle$ transition and is visible due to imperfect state initialization.

forming a Ramsey-like measurement on qubit 1 to measure its phase accrual after a pulse-train of CZ gates, depending on whether or not qubit 2 started in $|0\rangle$ or $|1\rangle$. We choose the drive frequency which results in the closest intersection of the three resultant lines, which should in principle tune the conditional phase to 180°, though we note that controlled-phase gates of variable angles could also be achieved. In the absence of AC-stark shifts and to a first-order approximation, the drive frequency should be exactly resonant with the driven transition to obtain 180°.

3. **Single-qubit phases** Fig. 5-9(c, f). Once the CZ interaction was properly tuned, we measured the single-qubit phase accumulation (Z rotation) during the CZ interaction using the same Ramsey like measurement. These Z-rotations were corrected for in software through virtual-Z gates [57].

Since adjusting the drive frequency slightly changes the amplitude corresponding to a single period and vice-versa, we alternately performed these two calibrations three times in total. In practice, this iterative process was sufficiently accurate and much

faster than performing a two-dimensional calibration for both parameters simultaneously. We illustrate the complete flowchart of this calibration in Fig. 5-9(g)

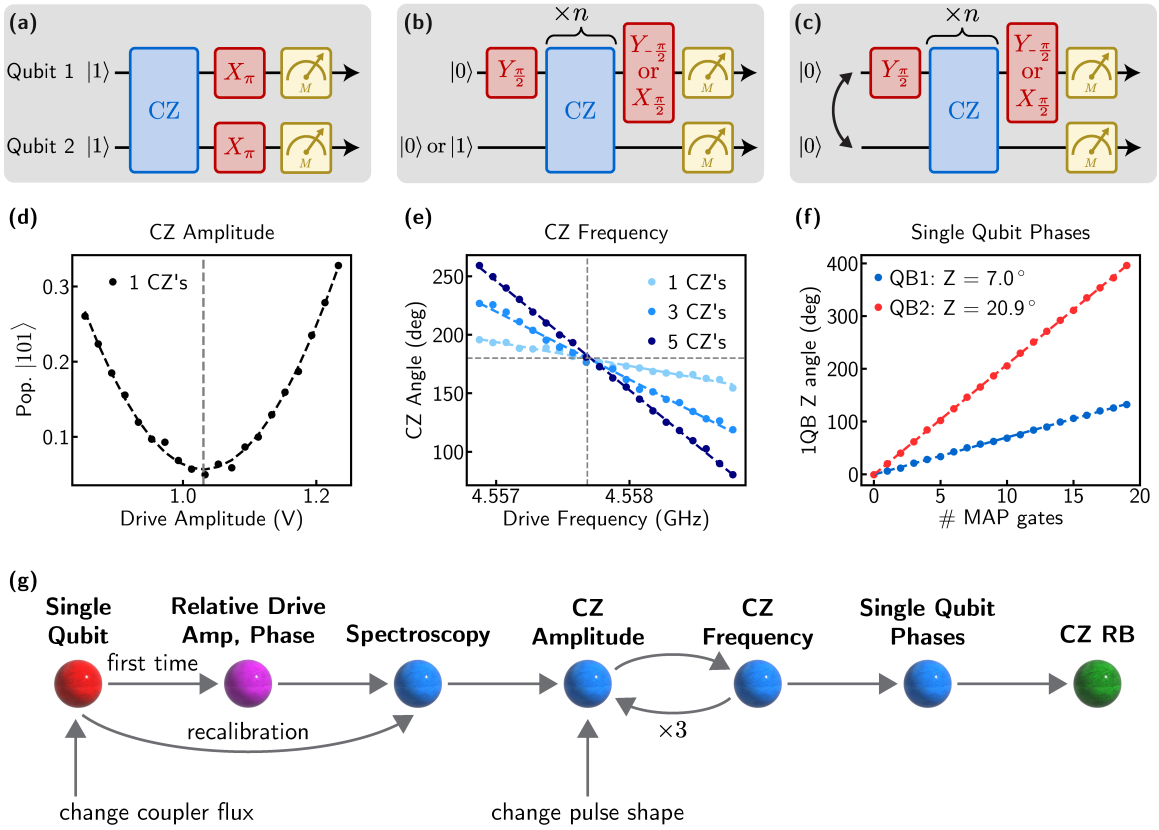

Figure 5-9: **CZ Gate calibration procedure.** **(a-c)** Pulse sequences for **(d-f)** respectively. The double arrow in (c) indicates that the same pulse sequence was performed twice, with qubits 1 and 2 exchanged. **(d)** Calibrating the global amplitude of the CZ drive by minimizing the leakage. **(e)** Calibrating the frequency of the CZ drive by measuring a conditional phase accumulation via Ramsey-like measurements. Each gate should contribute a 180° conditional phase shift. **(f)** Measuring the single-qubit phase accumulations per CZ gate using the same Ramsey-like measurements. **(g)** Graphical illustration of the full two-qubit calibration routine. When recalibrating the system for small flux drifts or periodic check-ins, we found it unnecessary to recalibrate the relative drive amplitude or phase.

After calibration, we extract the gate fidelity by performing Clifford interleaved randomized benchmarking, averaging over 20 different random seeds [20, 52, 8]. Similar to our single-qubit Clifford decomposition, we generated the two-qubit Clifford group with the gate set $\{I, \pm X, \pm Y, \pm X_{\pi/2}, \pm Y_{\pi/2}, \text{CZ}\}$, yielding an average of 8.25 single-qubit gates and 1.5 CZ gates per Clifford.

5.3.3 CZ Gate vs. Flux

The FTF approach offers a potential solution to frequency-crowding by allowing for an adjustable gate operation frequency. To demonstrate this frequency-flexibility in our device, we linearly sampled the coupler flux $\Phi_{\text{ext,c}}$ at 21 values between $0.5\,\Phi_0$ and $1\,\Phi_0$ and calibrated a CZ gate across all three transitions in Fig. 5-7(d) while maintaining a constant 100 ns pulse length [Fig. 5-10]. Each data point in Fig. 5-10 represents a fully automated re-calibration of all single- and two-qubit gate parameters without manual fine-tuning. We further emphasize this robustness by including fidelities from Device B, a second fully characterized device with similar performance. While designed to be nominally identical, the non-computational states in Device B differ by up to 300 MHz from Device A with no significant detriment to the gate fidelities (see Section 5.5 for additional characterization of Device B). While these fidelities remain unoptimized over the pulse width, they indicate the ease and robustness of the tuneup, as well as the accessibility of state-of-the-art gate fidelities at a variety of drive frequencies.

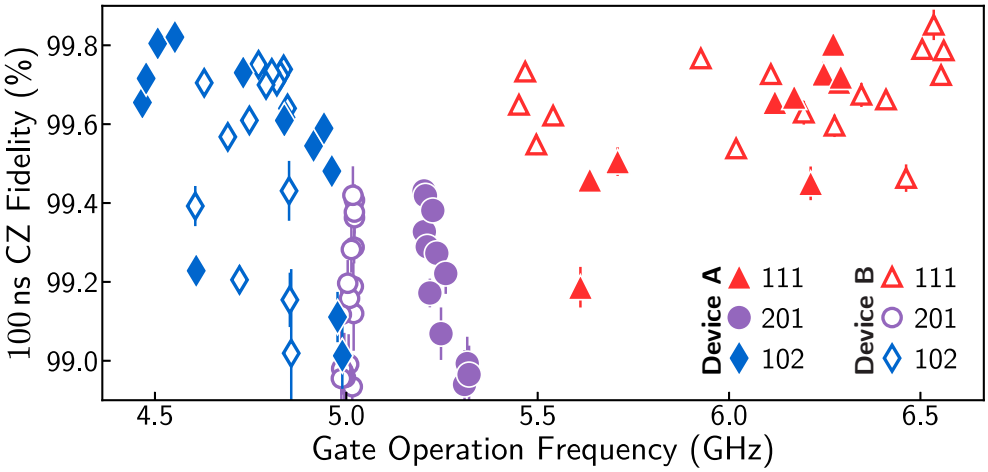

Figure 5-10: **CZ gate fidelities versus operation frequency.** All gate fidelities were obtained from interleaved randomized benchmarking, averaging over 20 random seeds. CZ gates used a fixed 100 ns cosine pulse envelope, driving each transition in Fig. 5-7(d) across the entire $0.5 - 1\,\Phi_0$ range, linearly sampled over 21 points. A secondary device (Device B) with slightly different Hamiltonian parameters shows the reliability of our architecture. Points with fidelity below 98.9% correspond to failures in the automated calibration and are therefore excluded from the plot. All gate fidelities were obtained from interleaved randomized benchmarking averaged over different 20 randomizations, with error bars corresponding to the standard error.

Figure 5-11 shows an alternate plotting of the data in Fig. 5-10, illustrating more explicitly what frequencies each calibrated gate corresponds to. Each subplot features the fidelity of the CZ gate as a function of the coupler flux, with the spectrum of the associated transition in gray in the background. While many calibrated points have low fidelity, the most important aspect of this architecture is that there exist multiple transitions for which high fidelity is achievable, allowing flexibility in the operation frequency. Nevertheless, we discuss the most common failure mechanisms and reasons for low fidelity to shed additional insights on the limits of our automated calibration versus the inherent limit of the transition being driven.

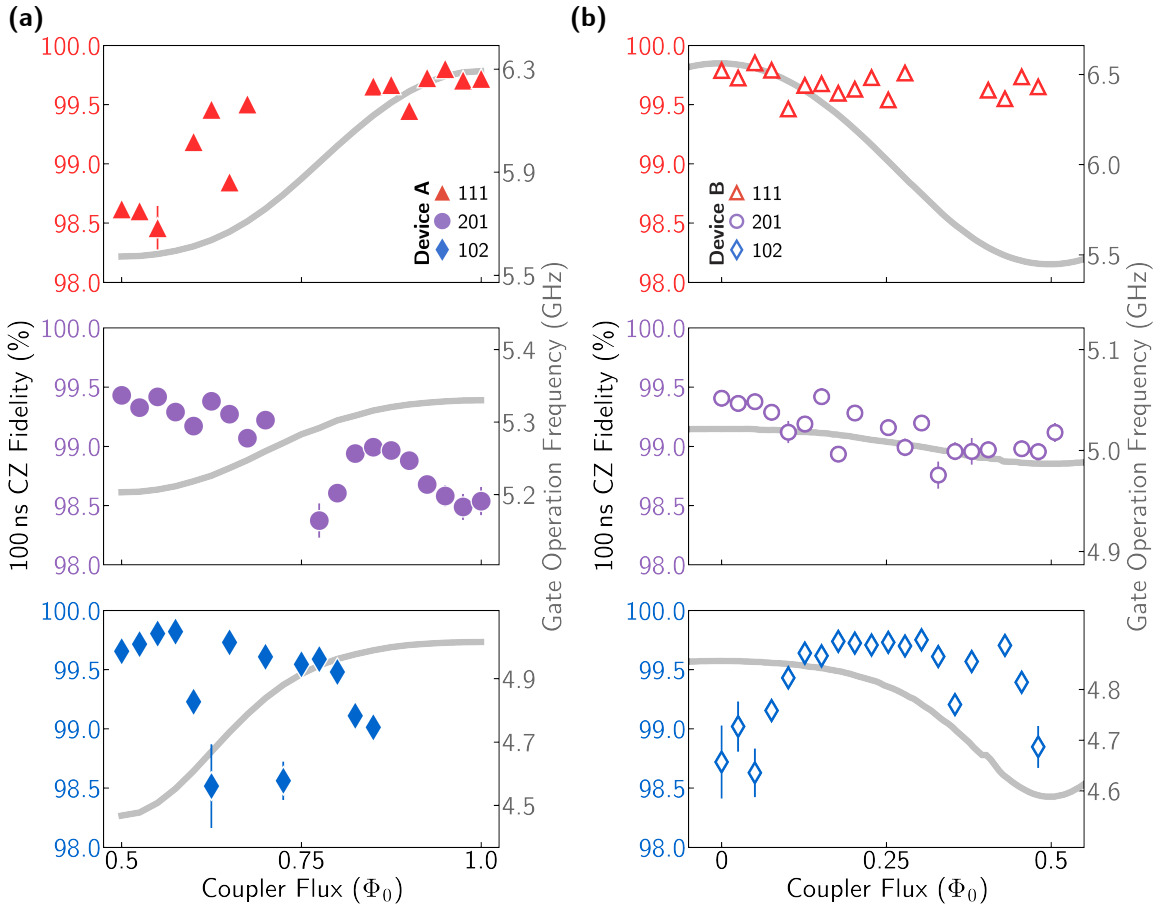

Figure 5-11: **Alternate plotting of RB vs. Flux data.** Gate fidelities with a fixed 100 ns pulse width as a function of the coupler flux for Device A **(a)** and **(b)**. The drive frequency is plotted in gray, represented on the right axis. All points missing from the full set of 21 correspond to more severe calibration failures.

The most common reason for low-performance operation points was nearby un-

wanted transitions, leading to a high amount of leakage. This is most evident in Device A, in which the $|101\rangle \leftrightarrow |111\rangle$ transition at $\Phi_{\text{ext,c}} = 1.0\,\Phi_0$, and the $|101\rangle \leftrightarrow |102\rangle$ transition at $\Phi_{\text{ext,c}} = 0.5\,\Phi_0$ are furthest detuned from their nearest unwanted transition, resulting in higher fidelities in these regions. Where these unwanted transitions have a much smaller detuning, we expect to obtain higher fidelities by increasing the drive pulse beyond 100 ns.

A second common mechanism for failed calibration was the inability to find a drive frequency corresponding to a 180° conditional phase shift. Due to the large hybridization, we occasionally measured AC-Stark shifts large enough to counter-balance the natural change in the conditional-phase angle as a function of drive detuning. The calibration could be recovered by either using a slower gate or by adjusting the relative drive amplitudes to tweak the total AC-stark shift. Other less common mechanisms for a failed calibration include TLSs or accidental resonances with undesired transitions, including higher-photon transitions.

Figure 5-12 shows the individual qubit coherence times as a function of the local coupler flux. Each coherence time was simultaneously measured on each qubit, with both qubits precisely re-tuned to $\Phi_{\text{ext}} = 0.5\,\Phi_0$ for each value of the coupler flux. Notably, these coherence times are slightly shorter than those listed in Table 5.1 due to bias-induced heating of the local flux lines. However, these coherence times are a more accurate representation of the quality of the qubits when performing two-qubit gates and simultaneous single-qubit gates. When performing simultaneous single-qubit gates, we biased the coupler at roughly $\Phi_{\text{ext,c}} = 0.77\,\Phi_0$, corresponding to no current being sent through the coupler flux line. We suspect the low Ramsey time of qubit 2 to be caused by Aharonov-Casher dephasing from coherent quantum phase slips [23, 59], based on its Hamiltonian parameters.

To investigate the trade-off between coherent and incoherent error, we characterized the gate fidelity as a function of the pulse width. In general, all fidelities in Fig. 5-10 may be improved by optimizing over this pulse width, with our highest fidelity gates using the $|101\rangle \leftrightarrow |102\rangle$ transition at $\Phi_{\text{ext,c}} = 0.575\Phi_0$ [Fig. 5-13(a)]. At the observed optimal gate time of 85 ns for this transition, we benchmarked a

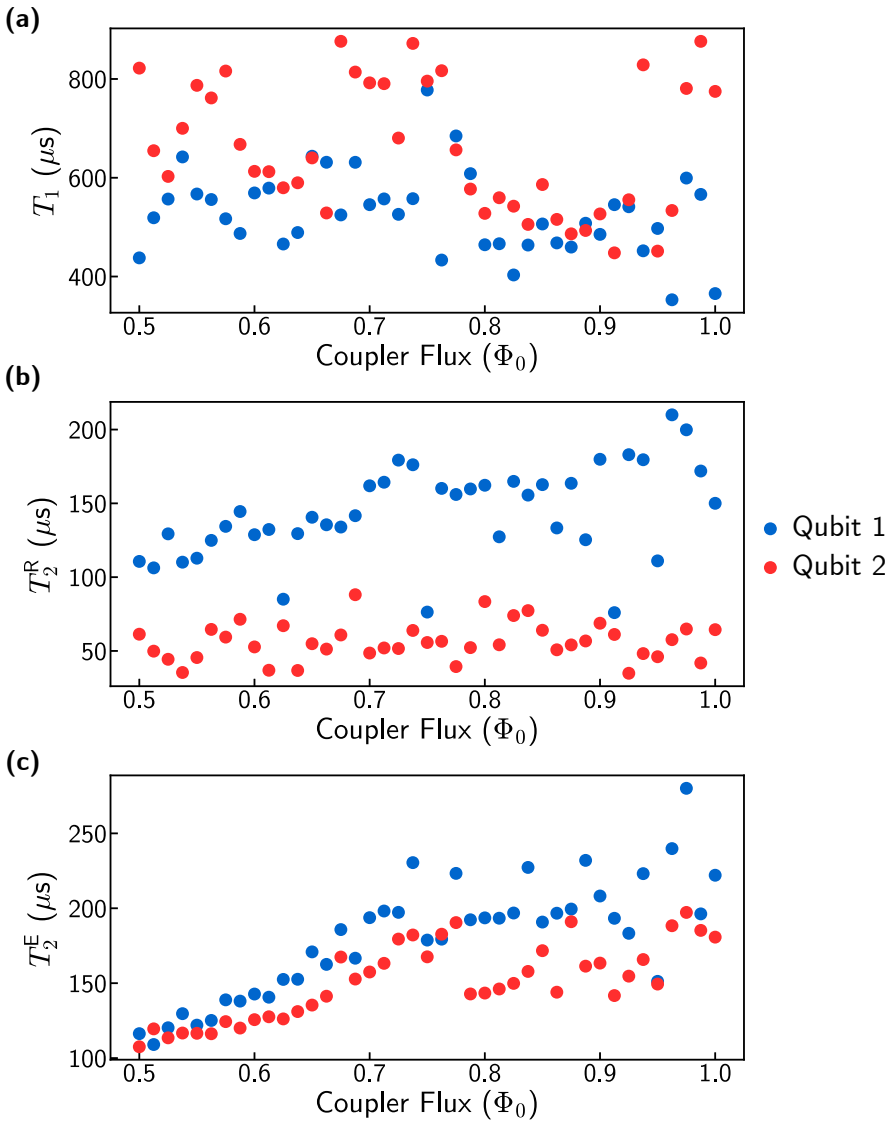

Figure 5-12: **Qubit coherences in Device A with both qubits biased at half-flux-quantum**. Panels **(a)**, **(b)**, **(c)** show the T_1, Ramsey, and echo decay times respectively as a function of the coupler flux. All decays were fit to an exponential and measurements were performed over a 12 hour period.

CZ fidelity of $99.89\% \pm 0.02\%$ [Fig. 5-13(a)]. For longer gate durations, the gate error is dominated by the lifetime of the driven non-computational state, measured to be around 10 µs at this transition and, in general, varied from $5 - 20$ µs across all transitions in Fig. 5-7(d). The coherence times of the computational states also reduce the fidelity, but for our devices this error is negligible compared to the T_1 of the non-computational state. At shorter gate lengths, coherent leakage into non-

computational levels dominates the error, but due to the extreme degree of hybridization of the non-computational states and their subpar readout, we were not able to experimentally measure the location of the leaked population. Furthermore, the application of established pulse shaping techniques [62] did not improve the fidelity. Master equation simulations of the Hamiltonian [Eq. (5.1)] under the CZ drive using the experimentally extracted parameters suggest gates down to 30 ns could be realized with less than 10^{-4} coherent error, suggesting that further improvements may be possible with our current devices.

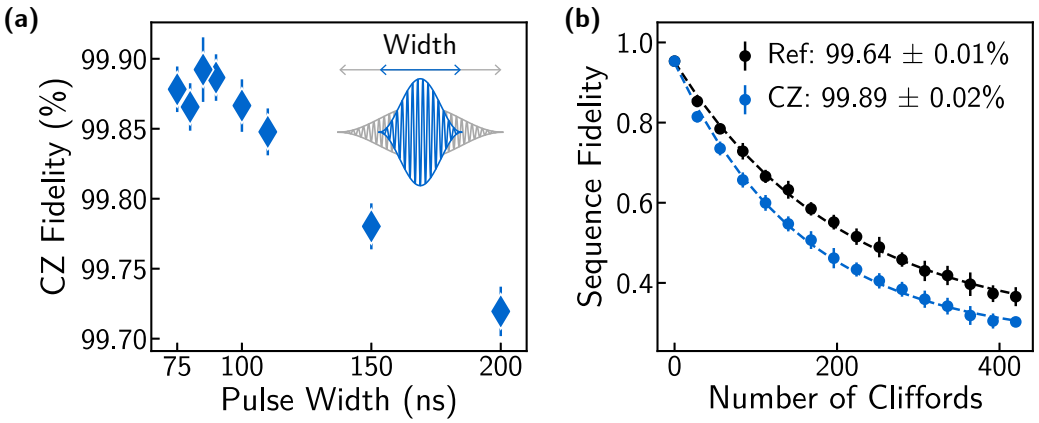

Figure 5-13: **CZ gate optimization. (a)** Gate fidelities as a function of the width of the cosine pulse envelope. The $|101\rangle \leftrightarrow |102\rangle$ transition was used at $\Phi_{\text{ext,c}} = 0.575\,\Phi_0$. Benchmarking traces are averaged over 20 randomizations. **(b)** Standard and interleaved randomized benchmarking trace corresponding to the 85 ns data point.

5.3.4 Reinforcement Learning for CZ Gates

To further improve the gate fidelity, we deployed a model-free reinforcement learning agent [82, 2, 70, 100, 79], closely following the protocol described by Sivak *et al.* [91]. While reinforcement learning could not mitigate the incoherent errors dominating the gate at longer pulse widths, at shorter gate times (<70 ns) we found that it did offer an improvement via fine adjustments of the pulse parameters. To train the agent, we first seeded it with a physics-based pulse calibration with a pulse width of 60 ns; our physics-based calibration failed at gate times less than this. Then, with a fixed CZ pulse width of 50 ns, the agent was trained to maximize the sequence fidelity of

interleaved randomized benchmarking at 28 Cliffords with a fixed random seed by optimizing the pulse shape and virtual-Z gates [Fig. 5-14].

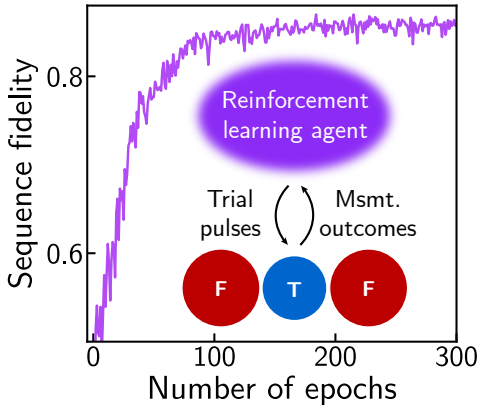

Figure 5-14: **Reinforcement learning process.** Fidelity of an interleaved randomized benchmarking sequence with 28 Cliffords using trial CZ gates sampled from the policy of a model-free reinforcement learning agent. After each epoch, the measurement results were used to update the agent's policy according to the PPO algorithm.

After each round of training, the optimized pulse was repeatedly evaluated by performing interleaved randomized benchmarking over 70 total Clifford sequences [Fig. 5-15]. Training was then repeated using the optimized pulse shape from the previous training round as the seed for the next. For the training run shown in Fig. 5-15, the fidelity peaked after the second round of training (orange points), with a time-averaged value of $99.922 \pm 0.009\%$. A Wilcoxon signed-rank test gives 97% confidence that this mean is above 99.90%. As the run progressed, the average fidelity was observed to degrade. We hypothesize that this was due to system drifts beyond what the agent was able to mitigate.

In the data shown in Fig. 5-15, the agent was given full control of the I and Q quadratures of the pulse envelope as well as the single-qubit virtual-Z rotation angles. $I(t)$ and $Q(t)$ were discretized into six points equally spaced in time [Fig. 5-16(a)] with a cubic interpolation determining the remaining points. Perhaps the most distinctive feature of the learned pulse is the shape of $Q(t)$: while the agent was seeded with $Q(t) = 0$, the learned pulse shape displays a distinct oscillation in $Q(t)$. Although we do not fully understand the origin of this oscillation, some intuition may

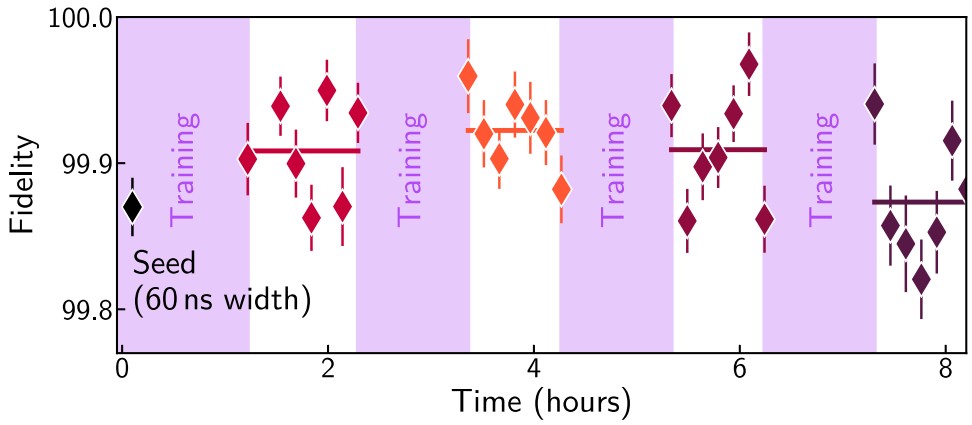

Figure 5-15: **Reinforcement training and testing run.** In a full training run, the agent was first seeded with a 50 ns cosine pulse, with an amplitude determined by a physics-calibrated 60 ns gate (black diamond) but scaled by 60/50. Then, the agent was trained to optimize the sequence fidelity of the 50 ns pulse. The learned gate was then repeatedly evaluated using interleaved randomized benchmarking averaged over 10 randomizations. The next round of training was seeded with the optimized pulse from the previous round. Horizontal bars indicate the averaged fidelity after each round of training. All uncertainties correspond to the standard error of the mean.

be gained by examining the Fourier transform of the pulse shape [Fig. 5-16(a) inset]. In the frequency domain, the oscillation in $Q(t)$ results in a distinct asymmetry of the pulse shape: at positive detunings from the carrier frequency, the spectral weight is suppressed, and vice versa for negative detunings. We hypothesize that this learned pulse asymmetry mitigates the effects of the nearest undesired transition, which is detuned by $\sim$+65 MHz at this bias point. However, we also note that attempts to mitigate the effects of this undesired transition using more established pulse shaping techniques did not improve the gate fidelity [62].

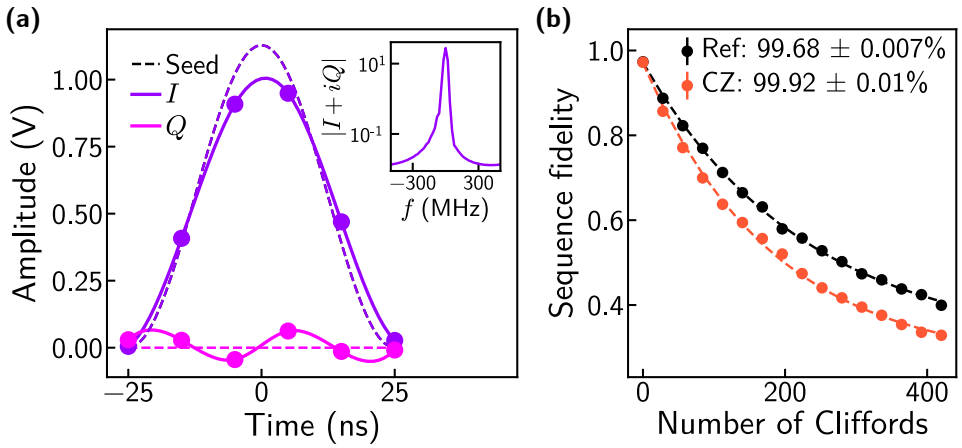

Figure 5-16: **Optimized gate results.** **(a)** Optimized pulse shape as learned by the agent. The agent was given control over six evenly-spaced $I(t)$ and $Q(t)$ voltage points (colored circles), with the pulse in between points determined by a cubic interpolation. Inset shows the Fourier transform of $I(t) + iQ(t)$. **(b)** Reference and interleaved randomized benchmarking curves averaged over all 70 randomizations after the second round of training (orange points in Fig. 5-15).

5.3.5 Relative Drive Amplitude and Phase Calibration

In this Section, we describe a leakage cancellation protocol utilizing destructive interference of the two drives; however, we note that a difference in gate fidelity could not be observed using this method. As a result, for the data in Fig. 5-10, a simpler procedure was implemented to save calibration time: the relative drive phase was tuned to constructively interfere at the desired transition, and the relative amplitudes were kept equal. Despite this fact, we include the information here for transparency on what was attempted to improve gate fidelities.

In driving our desired transition, off-resonant parasitic transitions always contribute to leakage. With two separate charge drive lines in our device, we can tune each drive line's relative phase and amplitudes for complete destructive interference on a parasitic transition of our choosing while retaining a nonzero drive on our gate transition. Without loss of generality, we take $|101\rangle \leftrightarrow |111\rangle$ to be our CZ gate transition and $|100\rangle \leftrightarrow |200\rangle$ to be the closest parasitic transition that we'd like to eliminate. We model the pulse seen by the qubits $i \in \{1, 2\}$ as

$$\text{Pulse}_i(t) = A_i \cos(\omega t + k x_i + \phi_i), \tag{5.16}$$

where $A_i > 0$ is the pulse amplitude, ω is the angular frequency, k is the wavenumber of the pulse, x_i is the effective distance from each pulse's origin to its destination, and ϕ_i is an additional constant phase offset of each pulse, specified in software.

The Rabi frequency of the undesired transition can then be written as

$$\langle 200| \hat{H} |100\rangle \propto \sum_i A_i \cos(\omega t + k x_i + \phi_i) \langle 200| \hat{n}_i |100\rangle \tag{5.17}$$

For this matrix element to be zero for all times, we require the two pulses to be 180° out of phase with each other with equal effective amplitudes. Mathematically, these two conditions are satisfied by specifying the relative phase and amplitude of the two drives:

$$\phi_2 - \phi_1 = \pi - k(x_2 - x_1) \tag{5.18}$$

$$\frac{A_2}{A_1} = \frac{\langle 200| \hat{n}_1 |100\rangle}{\langle 200| \hat{n}_2 |100\rangle}, \tag{5.19}$$

We note that since

$$\langle 200| \hat{N}_1 |100\rangle \,/\, \langle 200| \hat{N}_2 |100\rangle \neq \langle 111| \hat{N}_1 |101\rangle \,/\, \langle 111| \hat{N}_2 |101\rangle$$

generally, these conditions are not expected to provide complete destructive interference on our main transition of interest.

Experimentally, our procedures for calibrating A_2/A_1 and $\phi_2 - \phi_1$ are illustrated in Fig. 5-17. In all measurements for this calibration, we π-pulsed both fluxonium qubits before readout as discussed in Section 4.1.3 to increase signal contrast. We initially started with two arbitrarily amplitudes A_1, A_2, and then scanned the phase difference $\phi_2 - \phi_1$ (varying ϕ_2 with ϕ_1 fixed) while measuring the $|100\rangle \leftrightarrow |200\rangle$ Rabi oscillation (on resonance) [Figs. 5-17(a, c)]. With the value of $\phi_2 - \phi_1$ set to minimize the oscillation rate (dashed line), A_2/A_1 was scanned (varying A_2 with A_1 fixed) while

measuring the same Rabi oscillation [Figs. 5-17(b, d)]. The slowest Rabi oscillation (dashed line) was then used to choose the optimal value of A_2/A_1. Furthermore, as motivated by Eq. (5.19), this ratio would be independent of frequency and thus didn't require further calibration. On the other hand, we were interested in the phase which caused destructive interference when driving at our two-qubit gate frequency, not at the $|100\rangle \leftrightarrow |200\rangle$ resonance. This required calibrating for the phase dispersion caused by cable length differences. By repeating the relative phase calibration in a frequency bandwidth in which the $|100\rangle \leftrightarrow |200\rangle$ Rabi oscillation was still visible, we uncovered the expected linear dispersion [Fig. 5-17(e)], which we extrapolated as a function of drive frequency.

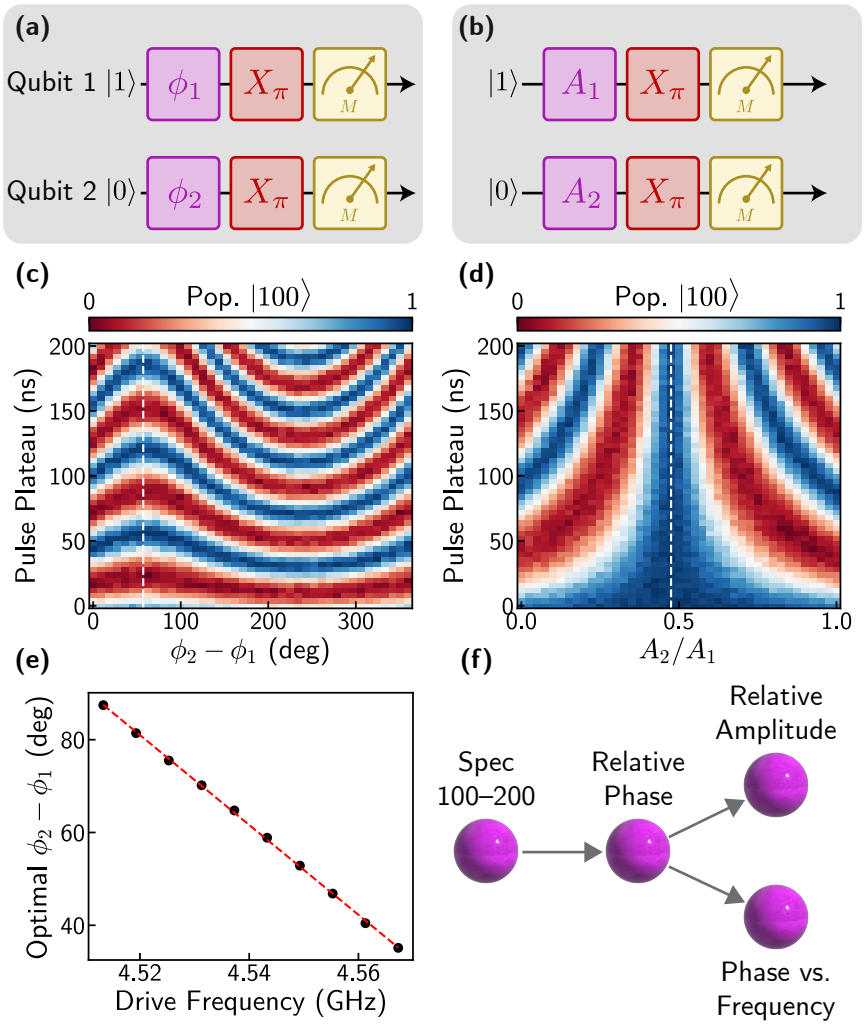

Figure 5-17: **Relative drive amplitude and phase calibration. (a, b)** Pulse sequences for (d-f) respectively. π-pulses before measurement are purely for increasing signal contrast. **(c)** Rabi oscillation of the unwanted transition with a frequency-locked drive on each charge line. The phase difference was scanned to show destructive (white dashed line) and constructive interference. **(d)** With $\phi_2 - \phi_1$ specified to give destructive interference, the relative amplitudes of the two drives were scanned for *complete* destructive interference (white dashed line). **(e)** The value of $\phi_2 - \phi_1$ that gave destructive interference was extracted as a function of drive frequency. The linear fit is motivated by a cable length difference. **(f)** Calibration flowchart for the illustrated procedure.

5.4 Error Analysis

In this section, we build up an analytic error budget to estimate the impact of various types of coherent and incoherent errors on gate fidelities. We model our gates as a

completely positive trace-preserving (in some subspace) map $\mathcal{G}$ acting on an input state ρ. The Kraus representation theorem then allows us to express all such processes as

$$\mathcal{G}(\rho) = \sum_k G_k \rho G_k^\dagger \tag{5.20}$$

for some set of Kraus operators G_k obeying the normalization condition

$$\sum_k G_k^\dagger G_k = I. \tag{5.21}$$

The average state fidelity of such a process $\mathcal{G}$ is then given by

$$F = \frac{1}{n(n+1)} \left[\mathrm{Tr}\left(\sum_k M_k^\dagger M_k \right) + \sum_k |\mathrm{Tr}(M_k)|^2 \right], \tag{5.22}$$

where $M_k = P U_0^\dagger G_k P$, and n is the dimension of the computational subspace [73]. Correspondingly, P is the projection operator onto the computational subspace, and U_0 is the ideal unitary operation of the process. We reproduce here the error corresponding to relaxation (T_1) and pure (Markovian) dephasing (T_ϕ) corresponding to a gate of length t_g.

$$F_{1 \text{ qubit}} = 1 - \frac{t_g}{3}\left(\frac{1}{T_1} + \frac{1}{T_\phi}\right) \tag{5.23}$$

$$F_{2 \text{ qubits}} = 1 - \frac{4t_g}{5}\left(\frac{1}{T_1} + \frac{1}{T_\phi}\right) \tag{5.24}$$

One critical assumption in these well-known formulas is that the gate operation stays within the computational subspace, an invalid assumption for our two-qubit gate.

5.4.1 Relaxation of Higher Energy Levels

In our two-qubit gate, there are five relevant states: the computational states $|00\rangle$, $|01\rangle$, $|10\rangle$, $|11\rangle$ and the non-computational state we drive to $|\alpha\rangle$. For mathematical simplicity, we imagine modeling an identity gate composed of two CZ gates. The error per unit time will not change, and this allows us to use $U_0 = I$ as well as simplifies

phases in our Kraus operators. We model the incoherent decay under driven evolution as if $|11\rangle$ and $|\alpha\rangle$ decay into each other at equivalent rates (a valid assumption when the gate time t_g is small compared to the relaxation rate $T_{1,\alpha}$). Assuming no other decay channels, the full set of Kraus operators for this process is

$$G_0 = \frac{1}{\sqrt{2}} \begin{pmatrix} 1 & 0 & 0 & 0 & 0 \\ 0 & 1 & 0 & 0 & 0 \\ 0 & 0 & 1 & 0 & 0 \\ 0 & 0 & 0 & 1 & 0 \\ 0 & 0 & 0 & 0 & e^{-t/2T_1} \end{pmatrix} \tag{5.25}$$

$$G_1 = \frac{1}{\sqrt{2}} \begin{pmatrix} 0 & 0 & 0 & 0 & 0 \\ 0 & 0 & 0 & 0 & 0 \\ 0 & 0 & 0 & 0 & 0 \\ 0 & 0 & 0 & 0 & \sqrt{1-e^{-t/T_1}} \\ 0 & 0 & 0 & 0 & 0 \end{pmatrix} \tag{5.26}$$

$$G_2 = \frac{1}{\sqrt{2}} \begin{pmatrix} 1 & 0 & 0 & 0 & 0 \\ 0 & 1 & 0 & 0 & 0 \\ 0 & 0 & 1 & 0 & 0 \\ 0 & 0 & 0 & e^{-t/2T_1} & 0 \\ 0 & 0 & 0 & 0 & 1 \end{pmatrix} \tag{5.27}$$

$$G_3 = \frac{1}{\sqrt{2}} \begin{pmatrix} 0 & 0 & 0 & 0 & 0 \\ 0 & 0 & 0 & 0 & 0 \\ 0 & 0 & 0 & 0 & 0 \\ 0 & 0 & 0 & 0 & 0 \\ 0 & 0 & 0 & \sqrt{1-e^{-t/T_1}} & 0 \end{pmatrix} \tag{5.28}$$

One can verify the behavior of these operators by computing that

$$\langle 11| \mathcal{G}(\rho) |11\rangle = \frac{\rho_{11} + \rho_\alpha}{2} + \frac{\rho_{11} - \rho_\alpha}{2} e^{-t/T_{1,\alpha}}. \tag{5.29}$$

Finally, we take the projection operator to be

$$P = |00\rangle\langle 00| + |01\rangle\langle 01| + |10\rangle\langle 10| + |11\rangle\langle 11|. \tag{5.30}$$

Inserting these operators into Eq. (5.22) and Taylor expanding in $t_g/T_{1,\alpha} < 1$, we obtain

$$F \approx 1 - \frac{1}{8}\frac{t_g}{T_{1,\alpha}}. \tag{5.31}$$

5.4.2 CZ Phase Error

We consider an error in phase calibration, in which we successfully return all population back to the computational subspace, but with a $|11\rangle$ state phase of $\pi + d\phi$. In the unitary special case of Eq. (5.22) ($\mathcal{G}(\rho) = U\rho U^\dagger$), we need only compute

$$M = U_0^\dagger U \tag{5.32}$$

$$= \begin{bmatrix} 1 & 0 & 0 & 0 \\ 0 & 1 & 0 & 0 \\ 0 & 0 & 1 & 0 \\ 0 & 0 & 0 & -1 \end{bmatrix} \begin{bmatrix} 1 & 0 & 0 & 0 \\ 0 & 1 & 0 & 0 \\ 0 & 0 & 1 & 0 \\ 0 & 0 & 0 & e^{-i\pi - id\phi} \end{bmatrix} \tag{5.33}$$

$$= \begin{bmatrix} 1 & 0 & 0 & 0 \\ 0 & 1 & 0 & 0 \\ 0 & 0 & 1 & 0 \\ 0 & 0 & 0 & e^{-id\phi} \end{bmatrix}. \tag{5.34}$$

Inserting this into Eq. (5.22), we obtain

$$F = \frac{7 + 3\cos(d\phi)}{10} \approx 1 - \frac{3}{20}d\phi^2. \tag{5.35}$$

Values of note, are that for a fidelity of 99.9%, we can tolerate a phase error of 4.7° and for a fidelity of 99.99%, we can tolerate a phase error of 1.5°. We can similarly convert this into an error on drive frequency, assuming the drive frequency is the sole degree

of freedom in tuning the aforementioned phase. The geometric phase accumulation associated with some frequency change δ of a full-period driven oscillation is $\delta t_g/2$. The angle errors above then translate into 0.5 MHz error for 99.9% fidelity and 160 kHz for 99.99% fidelity.

5.4.3 Amplitude Error

In calibrating the Rabi oscillation corresponding to our CZ gate, chose a fixed gate time and calibrated the amplitude of the pulse to obtain a single-period oscillation. The unitary corresponding to this Rabi rotation in our five-state Hilbert space $\{|00\rangle, |01\rangle, |10\rangle, |11\rangle |\alpha\rangle\}$ is

$$U = \begin{pmatrix} 1 & 0 & 0 & 0 & 0 \\ 0 & 1 & 0 & 0 & 0 \\ 0 & 0 & 1 & 0 & 0 \\ 0 & 0 & 0 & \cos(\Omega t/2) & -i\sin(\Omega t/2) \\ 0 & 0 & 0 & -i\sin(\Omega t/2) & \cos(\Omega t/2) \end{pmatrix} \tag{5.36}$$

where Ω is the Rabi oscillation of the CZ pulse. Projecting onto the computational subspace (P) and assuming an ideal CZ unitary

$$U_0 = |00\rangle\langle 00| + |01\rangle\langle 01| + |10\rangle\langle 10| - |11\rangle\langle 11|, \tag{5.37}$$

we insert $M = PU_0^\dagger UP$ into Eq. (5.22) to obtain

$$F = \frac{1}{10}(6 - 3\cos(\Omega t/2) + \cos^2(\Omega t/2)) \approx 1 - \frac{1}{16}d\theta^2. \tag{5.38}$$

Converting this amplitude error into a phase error $d\theta = \Omega t - 2\pi$, 99.9% fidelity corresponds to a 7.25° error and 99.99% fidelity corresponds to a 2.29° error. To relate this more directly to our experimental apparatus, assuming that the pulse is calibrated to a roughly 1 V amplitude, these phases correspond to voltage errors of 20 mV and 6.4 mV respectively.

We conclude this section by emphasizing that at the error levels discussed, calibration precision is quite lenient and that errors will be dominated by decoherence and other unmodeled behavior such as leakage through neighboring transitions. Furthermore, all calculations performed are meant to model the fidelity of a single-qubit, which may not necessarily be equal to the fidelity extracted from interleaved randomized benchmarking due to the nature of coherent errors.

5.5 Secondary Device

In this section, we show data corresponding to Device B, a secondary device. Device B is an identically designed device, with extracted Hamiltonian parameters varying by up to 10% as compared to Device A, typical of fabrication variations and differences in device aging. The coherence times and single-qubit gate fidelities remain consistently high across both devices, and in particular, fluxonium 2 on Device B exhibited a median T_1 of 1.26 ms averaged over 8 hours [see Fig. 5-18(a)]. This, along with the measured lifetimes of fluxonium 2 on Device A, indicates a reliable process and design for achieving high lifetime qubits in a planar geometry. Curiously, the single-qubit gate fidelities in Fig. 5-18(b) were found to be optimized near a pulse width of 50 ns, a significant difference between the optimal pulse width of 18 ns for Device A. We currently do not have an explanation for this discrepancy.

We measured a nearly identical value (within 1 kHz) of the ZZ interaction rate in this device [Fig. 5-18(c)], supporting our claim that the ZZ reduction does not rely on any precise parameter matching and is a reliable method to achieve (absolute) values below 10 kHz. Most importantly, despite changes of up to 300 MHz in the $|1\rangle \leftrightarrow |2\rangle$ transition frequencies of the fluxonium qubits, we could still demonstrate high-fidelity CZ gates across a large frequency range [Fig. 5-10] with peak fidelities above 99.8% [see Figs. 5-18(d-f)].

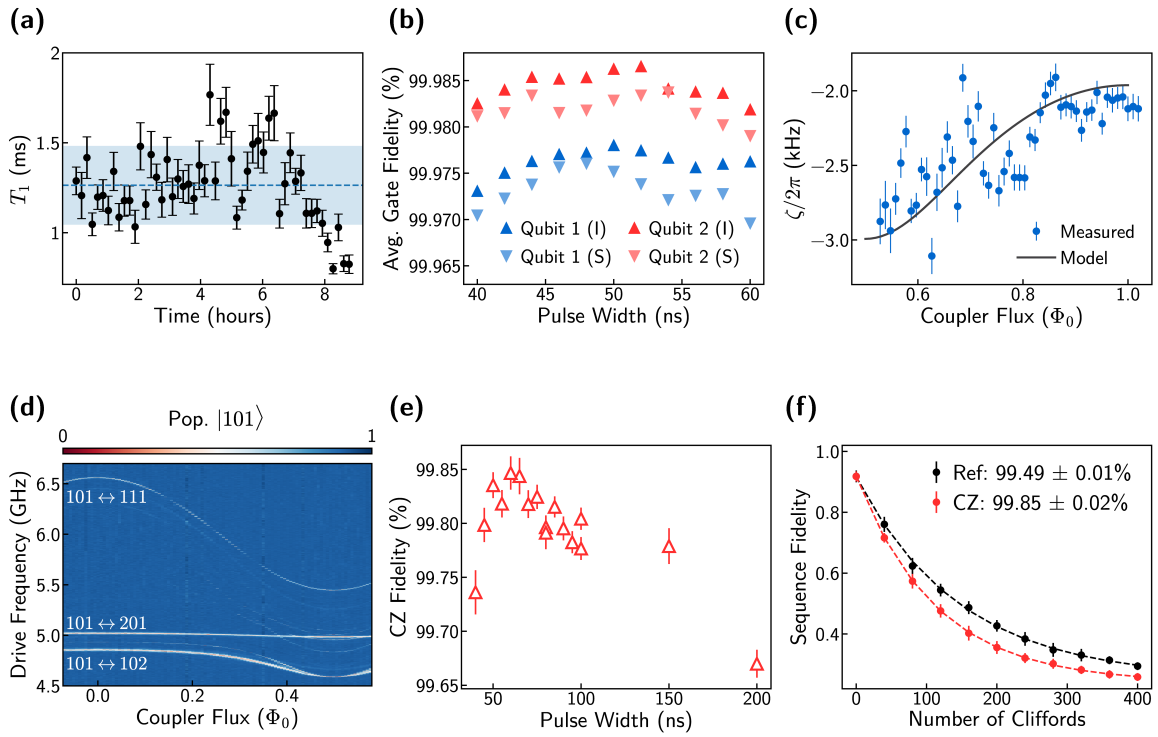

Figure 5-18: **Selected data from Device B. (a)** Repeated T_1 measurements of fluxonium 2 over a roughly nine-hour time span. The dashed blue line indicates the median T_1 of 1.26 ms, and the blue shaded region encompasses ±1 standard deviations. **(b)** Individual (I) and simultaneous (S) randomized benchmarking for both qubits, varying the width of a cosine pulse envelope. **(c)** Measured ZZ-interaction strength as a function of the coupler flux. **(d)** Spectroscopy of the non-computational states which activate the two-qubit gate. **(e)** CZ fidelities with varying pulse width, driving the $|101\rangle \leftrightarrow |111\rangle$ transition at $\Phi_{\text{ext,c}} = 0.063$. **(f)** Reference and interleaved randomized benchmarking trace averaged over 20 random seeds for a pulse width of 60 ns.

5.6 Discussion

Our work demonstrates an architecture in which high-fidelity, robustness against parameter variations, and extensibility are simultaneously realized. We observed millisecond fluxonium lifetimes despite couplings to neighboring qubits, resonators, flux lines, and charge lines, all within a 2D-planar architecture. Both the single- and two-qubit gates performed here are also simple – operating on the basis of a Rabi oscillation. The relative simplicity of this two-qubit gate was afforded by the FTF Hamiltonian and yielded a high fidelity operation across a large frequency-tunable

range, reproduced across multiple devices.

One of the most notable features of the FTF scheme is the capacity for large coupling strengths while simultaneously reducing the ZZ interaction strength to kHz levels. This is all done without strict parameter matching or additional drives. In fact, even computational state gates such as iSWAP or cross-resonance can benefit from FTF by utilizing this ZZ reduction without worrying about additional complications for single- and two-qubit gates. A fixed-frequency transmon (or simply a resonator) would suffice for this use case.

Despite already high gate fidelities, many avenues exist for improvement. First and foremost, the device heating when DC biasing qubits to their simultaneous sweet spot and tuning the coupler flux reduces the coherence times of our qubits. By optimizing the mutual inductance between the flux lines and the qubits and improving the thermalization and filtering of the flux lines, we anticipate improvements in future experiments. Even in the absence of local heating, we estimate a photon-shot-noise limit of $T_2 \sim 400\,\mu\text{s}$ assuming an effective resonator temperature of $T_{\text{eff}} = 55\,\text{mK}$ [104]. Simply decreasing χ and κ should increase this T_2 limit at the expense of readout speed, which could be a worthwhile exchange in the high T_1, low T_2 limit.

As is typical of fluxonium gates involving the non-computational states, the largest contribution to gate infidelity is the coherence of the $|201\rangle$, $|111\rangle$, $|102\rangle$ manifold; however, the lifetimes of these states are much lower than expected given coherence times measured on transmons with similar frequencies. By optimizing regions of high electric field density that exist in our current design (notably the small fluxonium-transmon capacitor gap), we expect to improve these coherence times as well.

While fluxonium has long exhibited impressive individual qubit performance, our work demonstrates a viable path forward for fluxonium-based large-scale processors capable of pushing the boundaries of noisy intermediate-scale quantum computing.

Chapter 6

Conclusions

The results of the work presented in this thesis constitute the latest technological advancement in the development of fluxonium qubits for quantum computing. Over the course of my PhD, I've had the privilege to see the fluxonium qubit go the distance from an academically niche qubit to a serious contender for the best superconducting qubit to build a quantum computer with. In the first year of my graduate career, the fluxonium qubit had just demonstrated competitive coherence times [67], and the first theoretical proposal for a fluxonium two-qubit gate was put forth [65]. In the following two years, these would eventually lead to record-breaking single-qubit gate fidelities [93] and a very respectable first demonstration of a fluxonium two-qubit gate [30]. In the fourth year of my PhD, a flurry of additional two-qubit gates [6, 26, 61] by different groups around the world would be demonstrated, marking an era of quantum computing with fluxonium qubits. Finally, the main work of this thesis demonstrates the highest published two-qubit gate fidelities out of all superconducting qubits as well as the highest simultaneous single-qubit gate fidelities of all superconducting qubits.

Additionally, the FTF scheme introduced has potential application to any fluxonium two-qubit gate, not just the specific one demonstrated here. Any fluxonium two-qubit gate that uses the higher-levels can take advantage of the level repulsions supplied by the transmon, and any two-qubit gate that only uses the fluxonium computational states can utilize the transmon as a passive element which suppresses the

static ZZ rate. The FTF scheme also requires only capacitive couplings in a 2D planar geometry, the same circuit layout architecture currently used to build quantum processors with over 100 coupled transmons [5, 1]. Furthermore, the experimental device used had local charge lines, flux lines, and readout for each qubit, while still retaining up to 1 ms qubit lifetimes, priming the FTF architecture for use in coupled fluxonium qubit lattices.

A demonstration of high-fidelity fluxonium single- and two-qubit gates in a lattice of qubits is undoubtedly the next big step forward for FTF and the fluxonium qubit as a whole. Although a variety of two-qubit gates exist for one to pick from in an attempt to scale up, many additional challenges exist that remain unaddressed. The first obstacle is that most current two-qubit gate works do not address the impact of spectator qubits in a multi-qubit circuit. For example, the iSWAP gate [6] cannot be performed in a grid of qubits without frequency collisions, the CR gate [26] relies on a precise frequency layout of all qubits and must contend with microwave crosstalk between single- and two-qubit gates, and microwave-activated CZ gates [30] (including this work) must come up with strategies to perform isolated two-qubit gates when more than two qubits are coupled.

A second challenge is to retain high coherences in circuits comprising a lattice of fluxoniums. The $\langle 0|\,\hat{n}\,|1\rangle$ matrix element is often increased along with the qubit frequency in order for fast gates to be performed [61, 6, 26], resulting in a sacrifice in T_1. The smaller inherent qubit capacitance also poses challenges for creating grids of capacitively coupled qubits. Whereas in transmon architectures, the summed coupling capacitance is only a fraction of the total qubit capacitance, it can easily account for a large fraction of the total qubit capacitance in fluxonium architectures. This can result in conflicting requirements for the qubit capacitance, coupling strengths, and the physical area required to couple several other qubits and control lines.

Despite the obstacles presented, active research is being conducted to find solutions, with the work presented in this thesis a major stepping-stone toward a fluxonium-based quantum processor.

Appendix A

Designing the FTF Device

This Chapter details the calculations and design considerations made in designing the FTF circuit. This primarily includes the general design of fluxonium and transmon qubits and the coupling between qubits to various other circuit elements in a planar geometry.

A.1 Junction Parameters

This Section contains information for calculating E_J, E_L, and the contribution to various circuit capacitances from the Josephson junctions.

A.1.1 Josephson Energy

The Josephson energy of a Josephson junction is directly defined through the critical current I_c of the junction. This critical current can in turn be defined as a product of the critical current areal density j_c (a fabrication constant) and the cross-sectional area of the junction A_{J} (a geometrical design parameter).

$$E_J \text{ (SI)} = \frac{I_c \Phi_0}{2\pi} = \frac{A_{\mathrm{JJ}} j_c \Phi_0}{2\pi} \tag{A.1}$$

$$E_J \text{ (GHz)} = \frac{I_c \Phi_0}{2\pi} = \frac{A_{\mathrm{JJ}} j_c}{4\pi e \times 10^9} \tag{A.2}$$

Optimizing j_c

For a given value of E_J, the junction area A_{JJ} can be freely traded off with j_c, while retaining a fixed value. The qubit T_1 is observed to degrade due to electric-field coupling to two-level system defects which reside in the small junction. It is thus favorable to minimize A_{JJ} by compensating with j_c.

A.1.2 Inductive Energy

The inductive energy of the Josephson junction array can be calculated by dividing the Josephson energy of one junction by the total number of junctions N_{JJ}. This can be understood as the inductance of each junction adding in series, with E_L proportional to the inverse inductance.

$$E_L = \frac{1}{N_{\mathrm{JJ}}} E_{J,\text{large junction}} \tag{A.3}$$

Optimizing N_{JJ}

For a given value of E_L, the number of array junctions N_{JJ} can be freely traded off with the area of each array junction while retaining a fixed value. The charge dispersion arising from Aharonov-Casher dephasing, however, is not invariant to this trade-off, with a smaller dephasing rate corresponding to larger values of N_{JJ} and A_{JJ} (with fixed E_L) [23]. Since an arbitrarily large N_{JJ} can introduce additional problems such as increased flux noise or lower frequency chain modes, I recommended to only increase N_{JJ} large enough so that T_2 times are not limited by Aharonov-Casher dephasing.

A.1.3 Capacitance Across Junction

The two separate conductors surrounding the insulating barrier of the Josephson junction also forms a capacitance. With an empirically determined capacitance per unit area c_{J}, this junction capacitance is computed as

$$C_{\mathrm{J}} = c_{\mathrm{J}} A_{\mathrm{JJ}} \tag{A.4}$$

A.1.4 Junction Chain Capacitance

The capacitance to ground of a single junction C_g may be estimated by direct electromagnetic simulations; however, of particular interest for fluxonium qubits is the effective capacitance to ground of a series array of junctions. Mathematically, this involves resolving the capacitance network of a near infinite chain of islands with a capacitance between each island and a capacitance between each island and ground. The full circuit schematic of this simplified array model of the junction chain is shown in Fig. A-1(a).

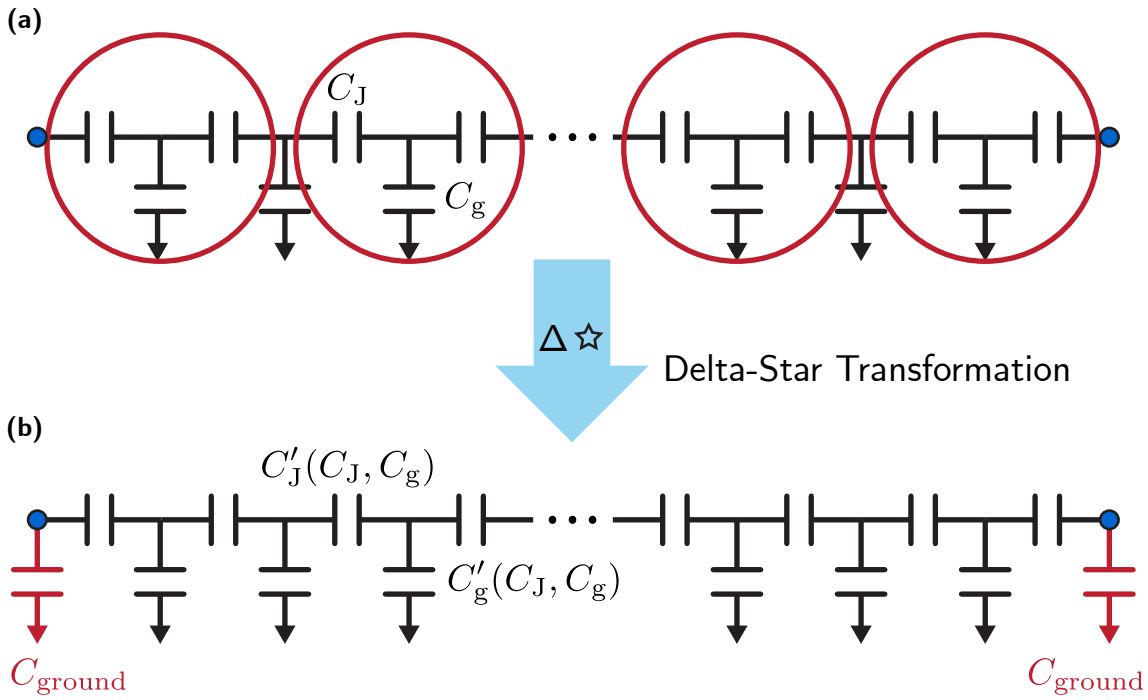

Figure A-1: **Capacitance network model of a junction array. (a)** Model of a junction array with capacitance C_J between junctions and C_g between each junction to ground **(b)** Capacitance network after application of the delta-star transformation to the circuit subsections circled in red. The new capacitance network has the exact same form except with different capacitance values C'_J, C'_g and an accumulating capacitance to ground at the end nodes of the junction chain.

After simplifying the circuit between the two end nodes (blue nodes), the total capacitance to ground can then be read off from the capacitance to ground of the end nodes (red capacitances in Fig. A-1(b)). The simplification starts by performing a delta-star transformation [95] (specifically, going from a 'star' circuit to a 'delta'

circuit) on every 'star' circuit in the capacitance network (red circles in A-1(a)), then simplifying any parallel summed capacitances. Done in this way, the resultant circuit after this first round of transformations has the exact same structure as the original circuit but with different capacitance values $C_{\mathrm{J}} \to C'_{\mathrm{J}}$, $C_{\mathrm{g}} \to C'_{\mathrm{g}}$ and a direct capacitance to ground from the two end nodes. This transformation can be repeatedly applied with the following recurrence relations governing all capacitances

$$C_{\mathrm{J},n+1} = \frac{C_{\mathrm{J},n}^2}{C_{\mathrm{g},n} + 2C_{\mathrm{J},n}} \tag{A.5}$$

$$C_{\mathrm{g},n+1} = \frac{2C_{\mathrm{J},n}C_{\mathrm{g},n}}{C_{\mathrm{g},n} + 2C_{\mathrm{J},n}} + C_{\mathrm{g},n} \tag{A.6}$$

$$C_{\mathrm{ground},n+1} = \frac{C_{\mathrm{J},n}C_{\mathrm{g},n}}{C_{\mathrm{g},n} + 2C_{\mathrm{J},n}} + C_{\mathrm{ground},n} \tag{A.7}$$

$$\tag{A.8}$$

where n is number of transformations, corresponding to $N_{\mathrm{JJ}} \sim 2^n$ total junctions. In general, these recurrence relations must be computed numerically, but simple analytic solutions exist for two important limits.

When $N_{\mathrm{JJ}} \ll \sqrt{C_{\mathrm{J}}/C_{\mathrm{g}}}$, the total capacitance to ground for each end node is given by

$$C_{\mathrm{ground}} \approx \frac{N_{\mathrm{JJ}} - 1}{2} C_{\mathrm{g}} \approx \frac{N_{\mathrm{JJ}}}{2} C_{\mathrm{g}}. \tag{A.9}$$

This can be understood as the total summed parallel capacitance split up across the two end nodes, which can then be added together in parallel to obtain NC_{g} as the total chain capacitance to ground.

Interestingly, in the limit $N_{\mathrm{JJ}} \gg \sqrt{C_{\mathrm{J}}/C_{\mathrm{g}}}$, or equivalently in the limit of infinite junctions, the total ground capacitance does not diverge to infinity. Instead, a non-

trivial fixed point (denoted by *) of the recurrence relation exists:

$$C_{\mathrm{J}}^{*} = 0 \tag{A.10}$$

$$C_{\mathrm{g}}^{*} = \sqrt{4C_{\mathrm{J}}C_{\mathrm{g}} + C_{\mathrm{g}}^{2}} \tag{A.11}$$

$$\boxed{C_{\mathrm{ground}}^{*} = \frac{1}{2}\left(\sqrt{4C_{\mathrm{J}}C_{\mathrm{g}} + C_{\mathrm{g}}^{2}} - C_{\mathrm{g}}\right) \approx \sqrt{C_{\mathrm{J}}C_{\mathrm{g}}},} \tag{A.12}$$

where the final approximation is made in the regime where $C_{\mathrm{J}} \gg C_{\mathrm{g}}$. Intuitively, the finite steady-state behavior of the total ground capacitance can be thought of as a compromise between the resultant series capacitance across the two nodes tending to zero and the resultant parallel capacitance to ground summing to infinity. Full numerical evaluations of the recurrence relations are plotted as a function of N_{JJ} for a variety of $C_{\mathrm{J}}/C_{\mathrm{g}}$ ratios and compared against the analytic limits in Fig. A-2. Typical fluxonium qubits used in this thesis have a simulated value of $C_{\mathrm{J}}/C_{\mathrm{g}} \approx 30$.

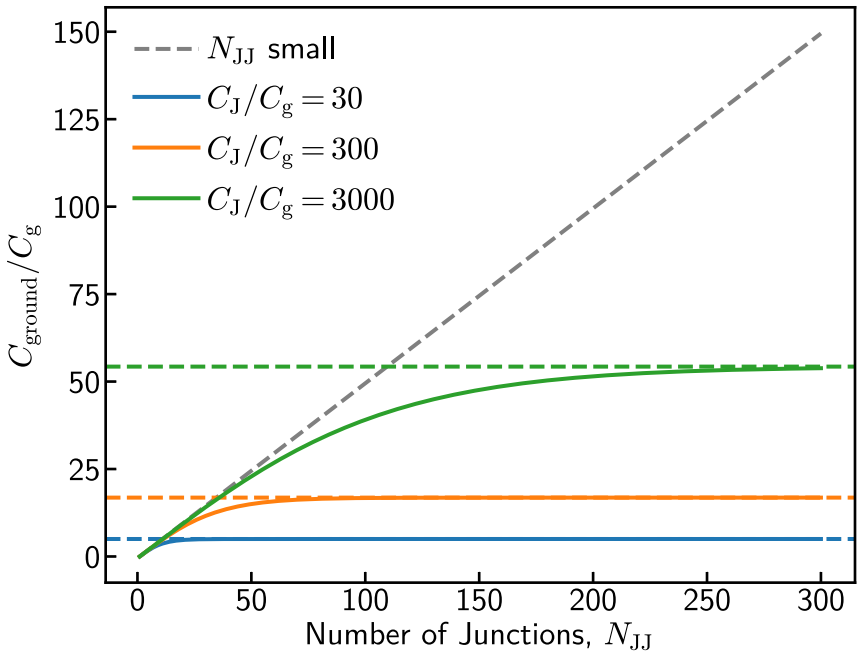

Figure A-2: **Numerical computational of ground capacitance.** The exact recurrence relation is numerically evaluated as a function of N_{JJ} for three different values of $C_{\mathrm{J}}/C_{\mathrm{g}}$. The gray dashed line corresponds to the small junction limit, and the colored dashed lines represent to the corresponding infinite junction limit.

A.2 DC Electromagnetic Simulations

DC electromagnetic simulations provide a method to simulate the capacitance matrix of a designed circuit. The familiar kinetic component of the circuit QED Hamiltonian is completely governed by the capacitance matrix

$$\hat{T} = 2e^2 \hat{\vec{n}} \mathbf{C}^{-1} \hat{\vec{n}}, \tag{A.13}$$

as derived in Section 2.1.3. It is important to understand that this kinetic energy term contains all the capacitive coupling information, and parameters just need to be extracted one by one and converted to their more conventional definitions in literature. In this section, we use Maxwell to numerically simulate this capacitance matrix [Fig. A-3(a)] and outline a procedure for extracting various quantities of interest, such as qubit E_C's, qubit-qubit coupling strengths, qubit-resonator coupling strengths, and qubit-charge line coupline strengths. Figure A-3(b) shows the capacitance matrix directly displayed from the Maxwell software. In order to convert this matrix into the circuit QED capacitance matrix, a few modifications must be made. First, junction capacitances must be manually added in. Individual junctions will add their capacitance value between its two nodes, and junction arrays will contribute to a direct capacitance to ground. Second, the resonators in our simulation were cropped, thus their capacitance to ground is inaccurate. We replace each total resonator capacitance with its theoretical value assuming a desired resonator frequency and a $50\,\Omega$ impedance. This value will factor into the charge matrix element of the resonator mode. Finally, we delete the original indices 5, 6, and 10 to remove the charge lines and ground plane from the capacitance matrix [Fig. A-3(b)]: the ground plane is not treated as a separate node in the circuit QED formalism, and we will use a classical treatment of the charge control lines.

(a)

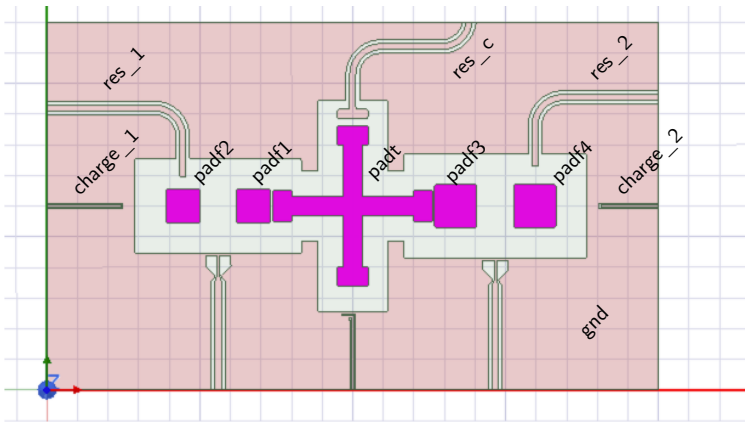

(b)

Index:	0	1	2	3	4	N/A	N/A	5	6	7	N/A
	padf1	padf2	padt	padf3	padf4	charge_1	charge_2	res_1	res_c	res_2	gnd
padf1	21.595	-1.4274	-8.2702	-0.063898	-0.039248	-0.01302	-0.0015637	-0.25948	-0.071687	-0.015285	-11.433
padf2	-1.4274	18.089	-0.54791	-0.041906	-0.029265	-0.061828	-0.0012287	-1.5796	-0.04435	-0.011794	-14.343
padt	-8.2702	-0.54791	81.548	-10.986	-0.6149	-0.021233	-0.016096	-0.22794	-4.0189	-0.17844	-56.666
padf3	-0.063898	-0.041906	-10.986	28.85	-2.1416	-0.0027954	-0.013861	-0.024474	-0.13072	-0.2388	-15.206
padf4	-0.039248	-0.029265	-0.6149	-2.1416	23.087	-0.0020886	-0.075141	-0.017802	-0.086088	-1.2576	-18.823
charge_1	-0.01302	-0.061828	-0.021233	-0.0027954	-0.0020886	23.617	-9.0424E-05	-0.028603	-0.0028077	-0.00085876	-23.484
charge_2	-0.0015637	-0.0012287	-0.016096	-0.013861	-0.075141	-9.0424E-05	18.62	-0.00076097	-0.003339	-0.018805	-18.489
res_1	-0.25948	-1.5796	-0.22794	-0.024474	-0.017802	-0.028603	-0.00076097	57.365	-0.032766	-0.0076802	-55.186
res_c	-0.071687	-0.04435	-4.0189	-0.13072	-0.086088	-0.0028077	-0.003339	-0.032766	61.736	-0.057447	-57.288
res_2	-0.015285	-0.011794	-0.17844	-0.2388	-1.2576	-0.00085876	-0.018805	-0.0076802	-0.057447	54.495	-52.708
gnd	-11.433	-14.343	-56.666	-15.206	-18.823	-23.484	-18.489	-55.186	-57.288	-52.708	323.63

Figure A-3: **Maxwell DC electromagnetic simulation of FTF device. (a)** Imported .gds file corresponding to the capacitance network of the FTF design. **(b)** Simulated capacitance matrix in units of fF. Diagonal entries are total summed capacitances touching the node, and off-diagonal entries are the negative of the capacitance between the two corresponding nodes.

A.2.1 Qubit Parameters

Due to the presence of differential qubits, we perform the standard variable transformation into difference and sum coordinates

$$\mathbf{M} = \begin{pmatrix} 1 & 1 & 0 & 0 & 0 & 0 & 0 & 0 \\ 1 & -1 & 0 & 0 & 0 & 0 & 0 & 0 \\ 0 & 0 & 1 & 0 & 0 & 0 & 0 & 0 \\ 0 & 0 & 0 & 1 & 1 & 0 & 0 & 0 \\ 0 & 0 & 0 & 1 & -1 & 0 & 0 & 0 \\ 0 & 0 & 0 & 0 & 0 & 1 & 0 & 0 \\ 0 & 0 & 0 & 0 & 0 & 0 & 1 & 0 \\ 0 & 0 & 0 & 0 & 0 & 0 & 0 & 1 \end{pmatrix}, \tag{A.14}$$

with the new effective capacitance matrix defined as $\tilde{\mathbf{C}} = \mathbf{M}^{-1}\mathbf{C}\mathbf{M}^{-1}$. The qubit charging energies and coupling strengths are then straightforwardly read off as

$$\begin{aligned} E_{C_1} &= \frac{e^2}{2}\tilde{\mathbf{C}}^{-1}[1,1] & J_{1c} &= 4e^2\tilde{\mathbf{C}}^{-1}[1,2] \\ E_{C_c} &= \frac{e^2}{2}\tilde{\mathbf{C}}^{-1}[2,2] & J_{2c} &= 4e^2\tilde{\mathbf{C}}^{-1}[2,4] \\ E_{C_2} &= \frac{e^2}{2}\tilde{\mathbf{C}}^{-1}[4,4] & J_{12} &= 4e^2\tilde{\mathbf{C}}^{-1}[1,4], \end{aligned} \tag{A.15}$$

with the Hamiltonian (truncated to only qubit degrees of freedom) as defined in Eq. (5.1).

A.2.2 Qubit - Resonator Couplings

The coupling strength between a qubit and a resonator can be computed through the corresponding matrix element of the inverse capacitance matrix. As an example, the coupling Hamiltonian term between qubit 1 and resonator 1 is

$$4e^2\tilde{\mathbf{C}}^{-1}[1,5]\hat{n}_1\hat{n}_{r1}. \tag{A.16}$$

For a fluxonium qubit, the coupling strength g is conventionally defined with the resonator matrix element included and qubit matrix element excluded.

$$-i\hbar g\hat{n}_1(\hat{a}_{r1} - \hat{a}_{r1}^\dagger) = 4e^2\tilde{\mathbf{C}}^{-1}[1,5]\hat{n}_1\hat{n}_{r1} \tag{A.17}$$

$$\boxed{\hbar g = e\sqrt{\frac{\pi\hbar}{2Z_0}}\tilde{\mathbf{C}}^{-1}[1,5].} \tag{A.18}$$

The impedance Z_0 in this expression uses the special case of a $\lambda/4$-resonator

$$Z_0 = \frac{\pi}{4}\sqrt{\frac{L}{C}} = 50\,\Omega, \tag{A.19}$$

where L and C are the inductance and capacitance of the resonator [76]. This expression can be used with any qubit; however, transmon literature typically features a slightly different convention for the definition of g. In that case, the qubit charge matrix element is often included inside the coupling strength

$$-\hbar g(\hat{a}_1 - \hat{a}_1^\dagger)(\hat{a}_{r1} - \hat{a}_{r1}^\dagger) = 4e^2\tilde{\mathbf{C}}^{-1}[1,5]\hat{n}_1\hat{n}_{r1} \tag{A.20}$$

$$\hbar g = e\sqrt{\frac{\pi\hbar}{2Z_0}}\left(\frac{32E_C}{E_J}\right)^{1/4}\tilde{\mathbf{C}}^{-1}[1,5]. \tag{A.21}$$

For a typical transmon with $E_J/E_C \approx 50$, this correction amounts to multiplying the original expression by ~ 0.9, a small factor compared to typical design uncertainties.

A.2.3 Qubit - Charge Line Couplings

As derived in Fig. 2.4.3, an arbitrary collection of voltage sources capacitively coupled to the nodes of the circuit results in the Hamiltonian

$$H = 2e^2\vec{n}^T(\mathbf{C} + \mathbf{N}_{\text{xy}})^{-1}\vec{n} + 2e\vec{V}^T\mathbf{C}_{\text{xy}}\mathbf{C}^{-1}\vec{n} + \frac{1}{2}\vec{\Phi}^T L_{\text{inv}}\vec{\Phi} + V_{\text{JJ}}(\vec{\Phi}). \tag{A.22}$$

To determine the coupling of each charge line to each qubit, this equation can be used after computing the new effective capacitance matrices according to the variable

transformation $\mathbf{M}$

$$\mathbf{C} \rightarrow (\mathbf{M}^{-1})^T \mathbf{C} \mathbf{M}^{-1} \tag{A.23}$$

$$\mathbf{N}_{\text{xy}} \rightarrow (\mathbf{M}^{-1})^T \mathbf{N}_{\text{xy}} \mathbf{M}^{-1} \tag{A.24}$$

$$\mathbf{C}_{\text{xy}} \rightarrow \mathbf{C}_{\text{xy}} \mathbf{M}^{-1}. \tag{A.25}$$

A.2.4 Capacitive Quantum Crosstalk

In addition to each resonator coupling to the intended qubit, there is also unwanted coupling to other qubits due to the renormalization of capacitances which occurs when computing the matrix inverse. This crosstalk exists even if the direct capacitance (we would denote this classical crosstalk) between the two components is zero. Using the same capacitance matrix from previous examples, the quantity

$$\frac{\tilde{\mathbf{C}}^{-1}[2,5]}{\tilde{\mathbf{C}}^{-1}[1,5]} \tag{A.26}$$

describes the coupling strength ratio between resonator 1 to the coupler and resonator 1 to qubit 1. Likewise, $\tilde{\mathbf{C}}^{-1}[4,5]/\tilde{\mathbf{C}}^{-1}[1,5]$ would describe the crosstalk ratio between resonator 1 to qubit 2 and resonator 1 to qubit 1. In the designed FTF circuit, we observe significant crosstalk between the coupler resonator and the fluxonium qubits (up to $\sim 30\%$ of the coupler resonator - coupler coupling strength) and lower crosstalk between the fluxonium resonators and the coupler qubit (up to $\sim 15\%$ of the fluxonium resonator - fluxonium qubit coupling strength). This asymmetry is due to the transmon qubit having a larger qubit capacitance than the fluxonium qubits; a fixed amount of coupling capacitance will produce a larger coupling strength to the fluxonium than the transmon. In the discussion thus far, we've considered only the crosstalk ratios for the readout resonators, but since the charge lines couple to the qubits in the same capacitive manner, the same crosstalk ratios computed here also apply to the charge line crosstalk.

A.3 RF Electromagnetic Simulations

In this Section we use Sonnet to perform planar RF electromagnetic simulations to extract relevant circuit parameters. We use Sonnet to obtain the resonator frequencies, resonator linewidths, Purcell filter parameters, mutual inductance of flux lines, and T_1 loss of charge and flux lines. Sonnet also provides a way to double check the qubit capacitances, qubit-resonator coupling strengths, and qubit-qubit coupling strengths, though we note that Maxwell is much more time efficient for quantities that both simulation techniques are able to extract.

A.3.1 Resonator Simulations

We consider quarter wavelength hanging resonators inductively coupled to a reflection feed line [Fig. A-4(a)]. Assuming a loss rate of κ from the resonator into the feed line and no other loss channels, the S_{11} reflection coefficient probed at the input of the feed line is [12]

$$S_{11}(\omega) = -\frac{\kappa/2 - i(\omega - \omega_r)}{\kappa/2 + i(\omega - \omega_r)}. \tag{A.27}$$

For convenience, we fit to the derivative of the phase of $S_{11}(\omega)$ [see Fig. A-4(b)], which becomes a familiar Lorentzian with full-width half-max κ and center frequency ω_r

$$\frac{d}{d\omega}\angle S_{11}(\omega) = \frac{d}{d\omega}\arctan\left(-\frac{\kappa(\omega - \omega_r)}{\left(\frac{\kappa}{2}\right)^2 - (\omega - \omega_r)^2}\right) \tag{A.28}$$

$$\boxed{\frac{d}{d\omega}\angle S_{11}(\omega) = -\frac{\kappa}{\left(\frac{\kappa}{2}\right)^2 + (\omega - \omega_r)^2}}. \tag{A.29}$$

Since the signal passing through the resonator is coherently reflected at the end of the feed line, the full structure of the feed line is important in capturing the coupling strength between the resonator and the feed line. Simulations involving transmission feed lines, in contrast, do not need to contain the full feed line.

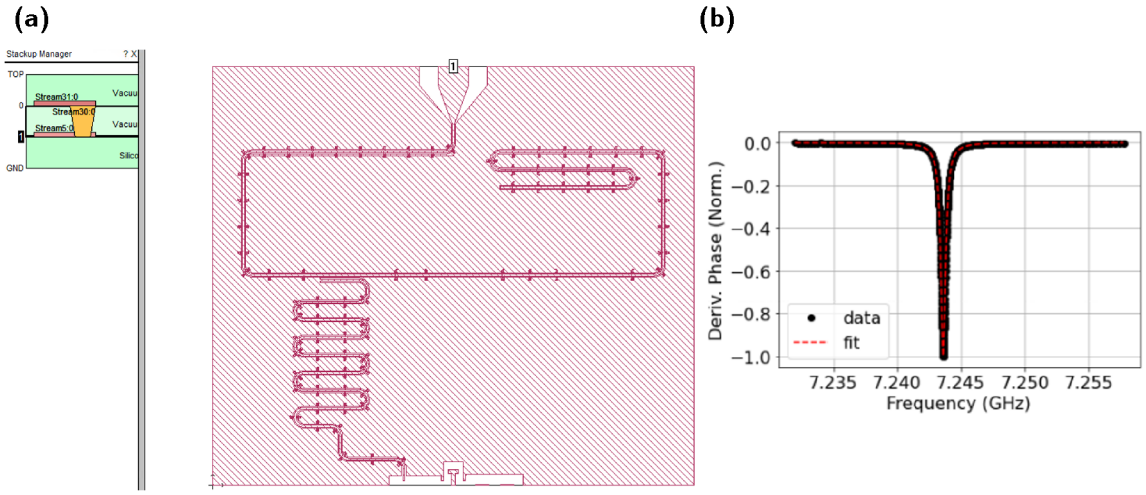

Figure A-4: **Sonnet resonator simulations.** **(a)** Sonnet screenshot setting up scattering matrix simulations of the resonator probed at the input of the feed line. **(b)** The normalized derivative of the phase of $S_{11}(\omega)$ fitted to a Lorentzian.

A.3.2 Purcell Filter Simulation

For the main devices used in the FTF experiment, the resonators were instead coupled to a Purcell filter, which was in turn coupled to the feed line [Fig. A-5(a)]. Assuming a loss rate of κ_f for the Purcell filter resonator to the feed line, γ_f for the internal loss of the Purcell filter, γ_r for the internal loss of the readout resonator, and $\mathcal{G}$ the coupling strength between the Purcell filter resonator and the readout resonator, the S_{11} scattering matrix element is given by [84, 13]

$$S_{11}(\omega) = -\frac{i(\omega_f - \omega) - \kappa_f/2 + \gamma_f/2 + \frac{\mathcal{G}^2}{i(\omega_r - \omega) + \gamma_r/2}}{i(\omega_f - \omega) + \kappa_f/2 + \gamma_f/2 + \frac{\mathcal{G}^2}{i(\omega_r - \omega) + \gamma_r/2}}. \tag{A.30}$$

Since $|S_{11}(\omega)| = 1$, we retain full information by fitting $\angle S_{11}(\omega)$, as shown in [Fig. A-5(b)]. The effective decay rate as a function of frequency caused by the Purcell filter is then given by [84]

$$\kappa(\omega) = \frac{4\mathcal{G}^2}{\kappa_f} \frac{1}{1 + [2(\omega - \omega_f)/\kappa_f]^2}. \tag{A.31}$$

The Purcell filter used in the experiment was designed with a $\sim 7.25\,\text{GHz}$ resonance frequency with a loss rate of $\sim 375\,\text{MHz}$ into the feed line and a coupling strength of $\mathcal{G} = 11\text{–}14\,\text{MHz}$. These parameters result in effective readout linewidths of $1 - 2\,\text{MHz}$

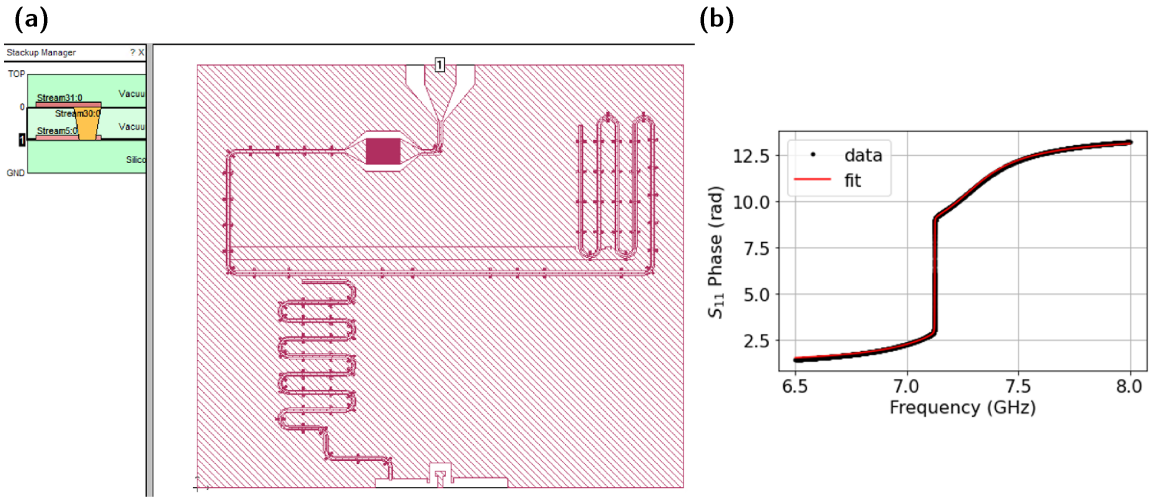

Figure A-5: **Sonnet Purcell filter simulations. (a)** Screen shot of simulation setup for one resonator. **(b)** Fitting to $\angle S_{11}(\omega)$ to extract all relevant parameters.

for each qubit, and the Purcell filter safely covers the frequency range of all resonators. More importantly for the FTF experiment, the Purcell filter reduces the relaxation due to the Purcell effect for the $|1\rangle_{\text{transmon}} \rightarrow |0\rangle_{\text{transmon}}$ and $|2\rangle_{\text{fluxonium}} \rightarrow |1\rangle_{\text{fluxonium}}$ transitions.

A.3.3 Flux Lines

The mutual inductance between a flux line and a qubit is simulated by importing the junctions in a closed loop and placing one port at the input of the flux line and another port in the middle of the qubit loop [Fig. A-6]. The impedance matrix is simulated at a single arbitrary frequency ω and the mutual inductance follows as

$$M = \frac{\text{Im}[Z_{12}]}{\omega}. \tag{A.32}$$

The designed values in the experimental device were $\sim 0.16\,\text{pH}$.

A.3.4 Decay Rate into Control Lines

The loss rate of each qubit to an input line (flux or charge) can be simulated by probing the line in reflection while creating a harmonic mode with the qubit capac-

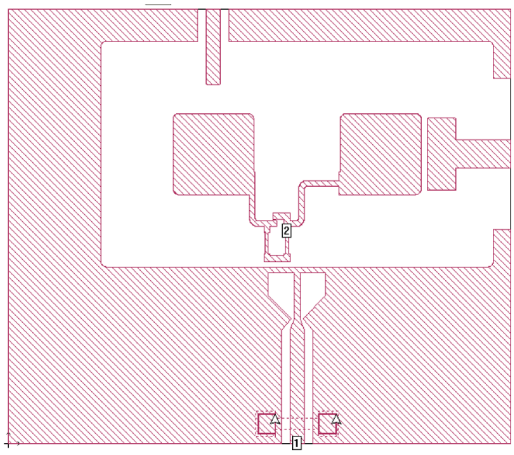

Figure A-6: **Sonnet mutual inductance simulations.** Screenshot of simulation setup for one flux line - qubit pair.

itor pads and a lumped element inductor [Fig. A-7(a)]. For this simulation and all following simulations, lumped element capacitors are also added to each qubit to compensate for the missing junction capacitances. As in other reflection measurements,

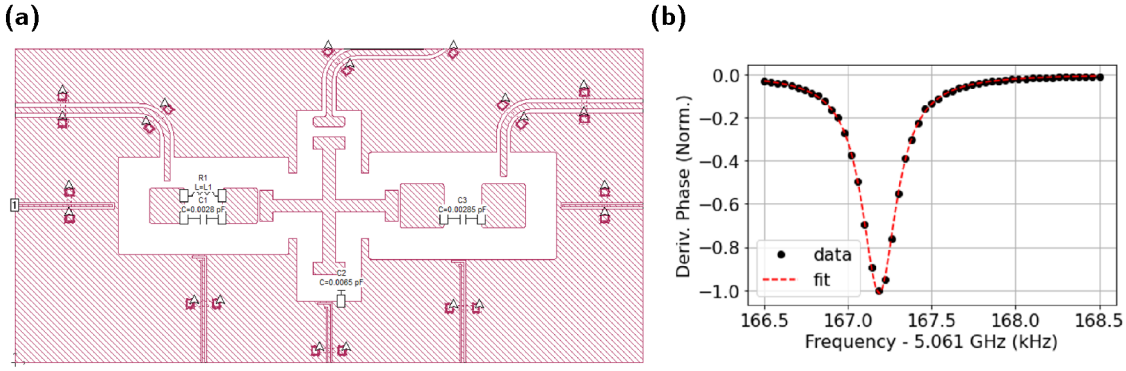

Figure A-7: **Sonnet simulation for loss into local lines (a)** Simulation setup for the loss into the qubit 1 charge line by qubit 1. The qubit is modeled as a harmonic oscillator with the correct capacitance and resonance frequency. **(b)** Lorentzian fit to the derivative of the phase of $S_{11}(\omega)$.

the microwave reflection coefficient, assuming a loss rate of κ (due to the qubit), is given by Eq. (A.27), which can be fit to a Lorentzian by taking a derivative of the phase Eq. (A.29) [Fig. A-7(b)]. In the case of qubit loss, this κ is governed by Fermi's golden rule

$$\kappa(\omega) = 2\pi \sum_i |g_i|^2 \delta(\omega - \omega_i). \tag{A.33}$$

When extracting this κ in our Sonnet simulation, the qubit becomes a harmonic oscillator, which has the same charge matrix elements as a transmon (for fixed capacitance and qubit frequency), but not a fluxonium. To convert this loss rate to that of a fluxonium qubit, the loss rate needs to be re-scaled according to the matrix element ratio between a fluxonium and a harmonic oscillator

$$\frac{g_{\text{qubit}}}{g_{\text{HO}}} = \frac{\langle 0_{\text{qubit}}| \hat{n} |1_{\text{qubit}}\rangle}{\langle 0_{\text{HO}}| \hat{n} |1_{\text{HO}}\rangle} \tag{A.34}$$

$$= \left(\frac{E_{L,\text{qubit}}}{E_{L,\text{HO}}}\right)^{1/4} \langle 0_{\text{qubit}}| \hat{a} - \hat{a}^\dagger |1_{\text{qubit}}\rangle . \tag{A.35}$$

We note that since the qubit frequency and qubit capacitance are accurately represented in the Sonnet simulation, the ratio between charge matrix elements is equal to the ratio between phase matrix elements [see Eq. (2.104)]. If κ_{HO} is the loss rate extracted from the fit in Fig. A-7(b), then the loss rate of the qubit is

$$\boxed{\kappa_{\text{qubit}} = \kappa_{\text{HO}} \sqrt{\frac{E_{L,\text{qubit}}}{E_{L,\text{HO}}}} |\langle 0_{\text{qubit}}| \hat{a} - \hat{a}^\dagger |1_{\text{qubit}}\rangle|^2}. \tag{A.36}$$

A.3.5 Qubit Capacitance

All parameters extracted from this point onward can also be simulated through DC electromagnetic simulations (Maxwell). As such, these techniques mainly serve to double-check the extracted parameters. We found that the RF and DC simulation techniques agreed to within 15% for all matching simulations.

To extract the qubit capacitance, a lumped element inductor is inserted in place of the qubit loop [Fig. A-8]. The qubit once again is modeled as a harmonic oscillator, and the total qubit capacitance is

$$C = \frac{1}{L\omega_{\text{HO}}^2} + C_{\text{JJ}}, \tag{A.37}$$

where C_{JJ} is the additional capacitance from Josephson junctions.

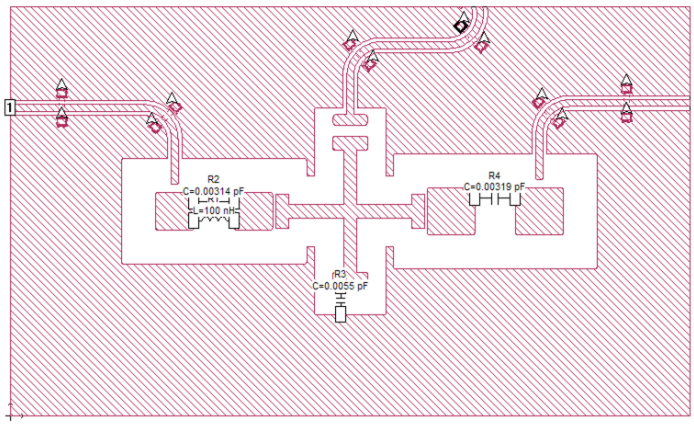

Figure A-8: **Sonnet simulation to extract the qubit capacitances.** Simulation setup probing the resonance of qubit 1 by placing a lumped element inductor between the qubit 1 capacitor pads and measuring the reflection at the qubit 1 resonator port.

A.3.6 Qubit - Qubit Coupling

To extract the qubit-qubit coupling strength between a desired pair of qubits, lumped element inductors are used to create harmonic oscillators in place of the two qubits [Fig. A-9(a)]. The inductance of one of the qubits is swept so that the two qubit frequencies tune through each other [Fig. A-9(b)], and the difference between the dressed qubit frequencies is fit to the hyperbola [Fig. A-9(c)]

$$\text{Difference Frequency} = \sqrt{\Delta^2 + 4J_{\text{sonnet}}^2}, \tag{A.38}$$

where Δ is the bare frequency difference between the two qubits and $2J_{\text{sonnet}}$ is the avoided crossing size as measured in the Sonnet simulation. This expression can be derived by taking the difference between the two eigenvalues of the familiar two-level system Hamiltonian

$$H = \begin{pmatrix} 0 & J_{\text{sonnet}} \\ J_{\text{sonnet}} & \Delta \end{pmatrix}. \tag{A.39}$$

At this point, we once again need to account for matrix elements to convert away from the harmonic oscillator coupling strength. As usual, we define the coupling

strength J between two qubits (1 and 2 without loss of generality) to be

$$\hat{H}_{\text{qubit-qubit}}/\hbar = J\hat{n}_1\hat{n}_2. \tag{A.40}$$

To equate this with the avoided crossing extracted in the Sonnet simulation, we insert harmonic oscillator matrix elements in Eq. (A.40), which is valid because J defined in this way is a geometric quantity depending on the capacitance network, independent of the qubit matrix elements:

$$H_{\text{qubit-qubit}}/\hbar = -\frac{J}{2}\left(\frac{E_{L_1}}{8E_{C_1}}\right)^{1/4}\left(\frac{E_{L_2}}{8E_{C_2}}\right)^{1/4}(\hat{a}_1 - \hat{a}_1^\dagger)(\hat{a}_2 - \hat{a}_2^\dagger) \tag{A.41}$$

$$= -\frac{J}{16}\frac{\hbar\omega}{\sqrt{E_{C_1}E_{C_2}}}(\hat{a}_1 - \hat{a}_1^\dagger)(\hat{a}_2 - \hat{a}_2^\dagger) \tag{A.42}$$

$$\implies J_{\text{sonnet}} = \frac{J}{16}\frac{\hbar\omega}{\sqrt{E_{C_1}E_{C_2}}} \tag{A.43}$$

$$\boxed{J = 16J_{\text{sonnet}}\frac{\sqrt{E_{C_1}E_{C_2}}}{\hbar\omega}}. \tag{A.44}$$

In this derivation, we defined $\omega = \omega_1 = \omega_2$ as the common frequency when the two qubits are on resonance, extracted as the mean resonance frequency at the avoided crossing [Fig. A-9(d)].

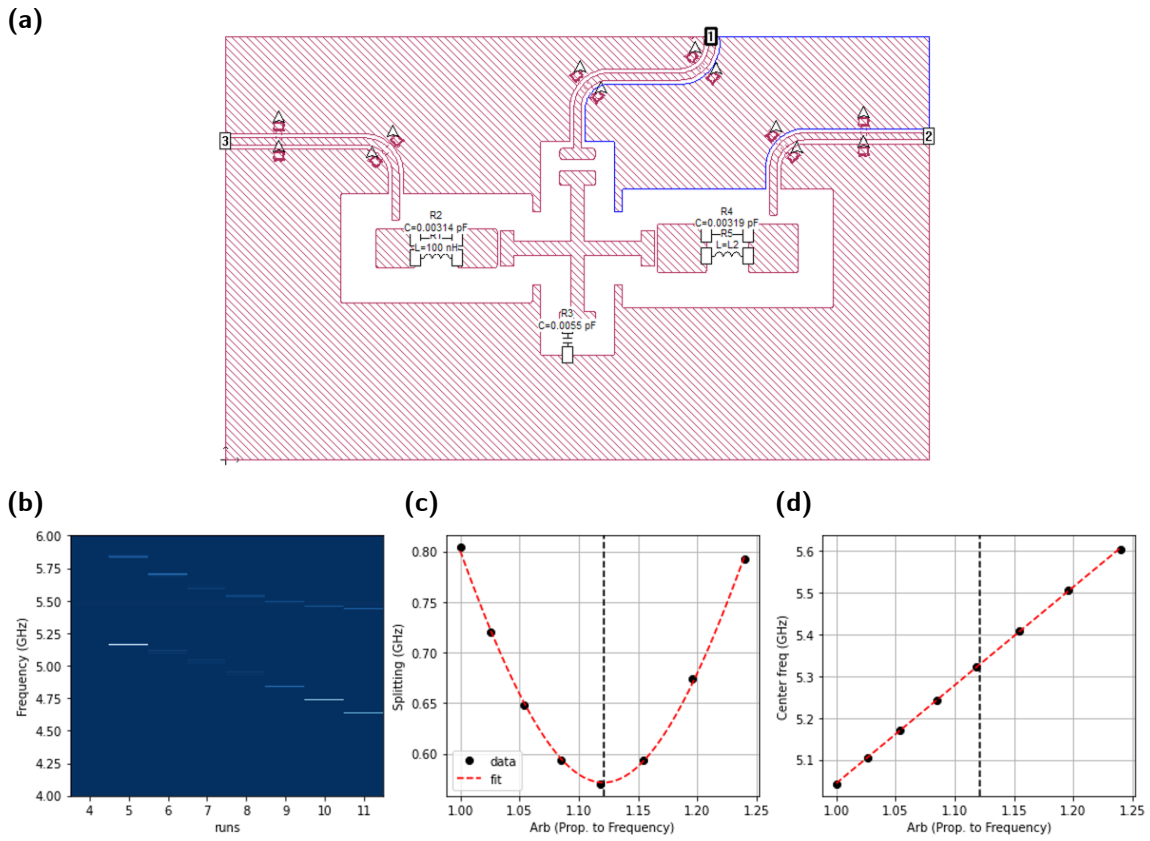

Figure A-9: **Sonnet simulation to extract qubit-qubit coupling strengths.** **(a)** Simulation setup with qubits 1 and 2 modeled as harmonic oscillators using lumped element inductors. The microwave reflection coefficient can be measured through either port 2 or port 3. **(b)** Avoided crossing between the two qubits as one of the qubit inductances is scanned. **(c)** The difference between the two dressed harmonic oscillator frequencies as the inductance of one of them is scanned. The points are fit to a hyperbola to extract the avoided crossing size. **(d)** The mean frequency as a function of the inductance to extract the bare frequency on resonance.

A.3.7 Qubit - Resonator Coupling

Similar to the procedure for extracting the qubit-qubit coupling strength, the qubit-resonator couplings strengths are extracted by representing a qubit as a harmonic oscillator and then tuning it through resonance with a resonator by scanning the inductance [Fig. A-10(a-b)]. By fitting the difference frequency to the hyperbola

$$\text{Difference Frequency} = \sqrt{\Delta^2 + 4g_{\text{sonnet}}^2}, \tag{A.45}$$

we extract the avoided crossing size $2g_{\text{sonnet}}$, where Δ is the bare frequency difference between the qubit and the resonator [Fig. A-10(c)].

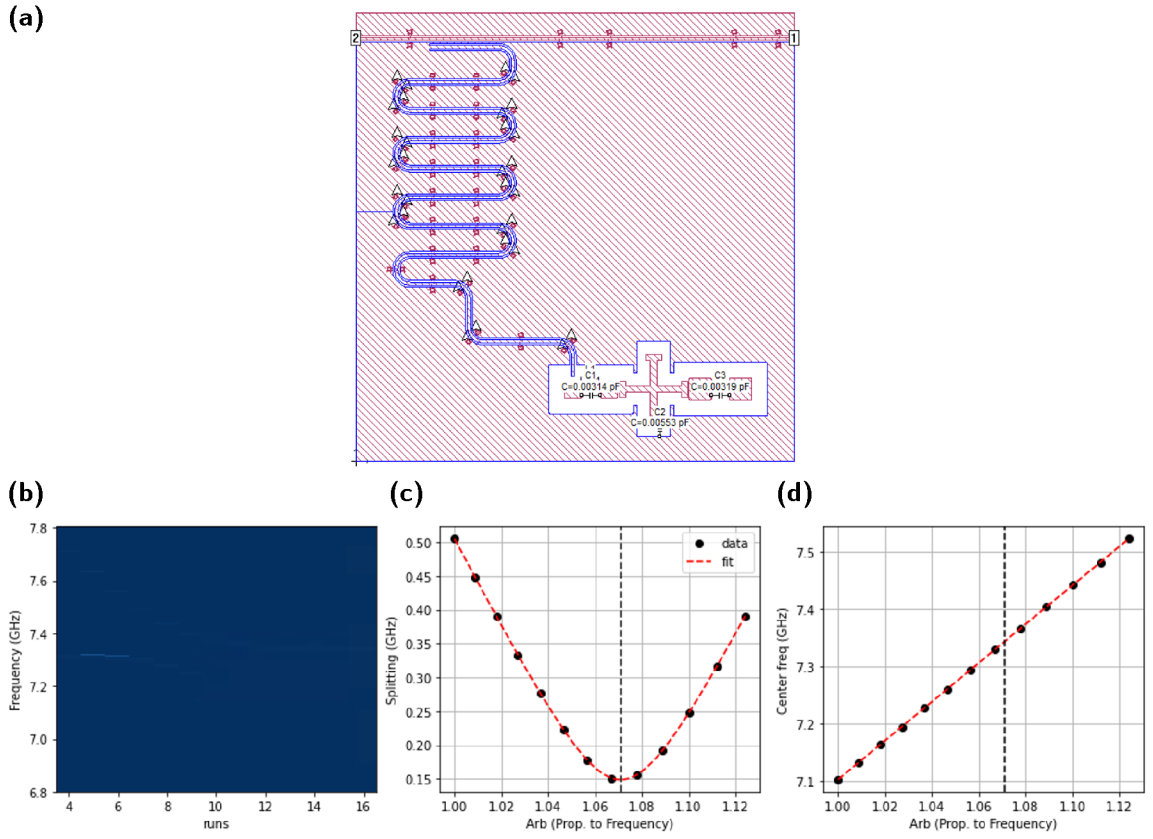

Figure A-10: **Sonnet simulation to extract qubit-resonator coupling strengths.** **(a)** Simulation setup with resonator 1 coupled to qubit 1. The qubit 1 inductance is scanned until qubit 1 goes through resonance with resonator 1. **(b)** Avoided crossing between the qubit and resonator as the inductance is scanned. **(c)** The difference between the two dressed frequencies as the inductance is scanned. **(d)** The mean frequency of the two resonances as the inductance is scanned to extract the bare frequency on resonance.

Since the qubit frequency is altered (with fixed E_C) when measuring the avoided crossing, the qubit matrix element artificially changes. Furthermore, due to the transmon and fluxonium literature often using different conventions for the qubit-resonator coupling strength g, it behooves one to be very careful when designing for these quantities. To aid in our conversion between different definitions of the coupling strength, we introduce another definition of this coupling strength g_{geo}, defined as the coefficient

of the two charge operators in the coupling Hamiltonian

$$\hat{H}_{\text{qubit-res}}/\hbar = g_{\text{geo}}\hat{n}_{\text{qubit}}\hat{n}_{\text{res}}. \tag{A.46}$$

As in the case of the qubit-qubit coupling strength, g_{geo} is completely determined by the capacitance network fo the circuit. Our approach will be to convert between g_{geo} and all other conventions for the coupling strength. We first derive a relation between g_{geo} and g_{sonnet} by approximating the qubit as the harmonic oscillator used in Sonnet

$$\hat{H}_{\text{qubit-res}}/\hbar = -g_{\text{geo}}\sqrt{\frac{\hbar\omega_{\text{qubit}}}{16E_{C_{\text{qubit}}}}}\sqrt{\frac{\hbar\omega_{\text{res}}}{16E_{C_{\text{res}}}}}(\hat{a}_{\text{qubit}} - \hat{a}^{\dagger}_{\text{qubit}})(\hat{a}_{\text{res}} - \hat{a}^{\dagger}_{\text{res}}). \tag{A.47}$$

Thus, for our first relation, we have

$$g_{\text{sonnet}} = g_{\text{geo}}\frac{\hbar\omega_{\text{res}}}{16\sqrt{E_{C_{\text{qubit}}}E_{C_{\text{res}}}}}, \tag{A.48}$$

where we have set ω_{qubit} equal to ω_{res} because the size of the avoided crossing is measured in Sonnet when the qubit is resonant with resonator. We more formally arrive at this expression by noting that the size of the avoided crossing $2g_{\text{sonnet}}$ should be equal to $2|\langle 01|\hat{H}_{\text{qubit-res}}|10\rangle|$ when the qubit and resonator are resonant. The exact value of ω_{res} is once again extracted as the mean frequency at the avoided crossing [Fig. A-10(c-d)].

Transmon Convention

In the transmon convention, g_{transmon} is defined as the coefficient of the raising and lowering operators

$$\hat{H}_{\text{qubit-res}}/\hbar = -g_{\text{transmon}}(\hat{a}_{\text{qubit}} - \hat{a}^{\dagger}_{\text{qubit}})(\hat{a}_{\text{res}} - \hat{a}^{\dagger}_{\text{res}}). \tag{A.49}$$

Notably, since the qubit matrix element is included in g_{transmon}, it depends on the qubit frequency and is not constant. By comparing this with Eq. (A.46) and then substituting g_{geo} with g_{sonnet} using Eq. (A.48), we arrive between the desired conver-

sion between the simulated g_{sonnet} and the desired g_{transmon}

$$g_{\text{transmon}} = g_{\text{geo}} \frac{\hbar}{16} \sqrt{\frac{\omega_{\text{qubit}} \omega_{\text{res}}}{E_{C_{\text{qubit}}} E_{C_{\text{res}}}}} \tag{A.50}$$

$$\boxed{g_{\text{transmon}} = g_{\text{sonnet}} \sqrt{\frac{\omega_{\text{qubit}}}{\omega_{\text{res}}}}}. \tag{A.51}$$

To summarize, in order to convert between the Sonnet simulation and the traditional transmon definition, the qubit frequency needs to be scaled back from its altered value to its real value. Since matrix elements are proportional to $E_J^{1/4}$, they are equivalently proportional to $\sqrt{\omega}$ (using $\hbar\omega = \sqrt{8E_C E_J}$).

Fluxonium Convention

In the fluxonium convention that we use, $g_{\text{fluxonium}}$ excludes the qubit matrix element and contains the resonator matrix element

$$\hat{H}_{\text{qubit-res}}/\hbar = -i g_{\text{fluxonium}} \hat{n}_{\text{qubit}} (\hat{a}_{\text{res}} - \hat{a}_{\text{res}}^\dagger). \tag{A.52}$$

Once again, we compare this with Eq. (A.46) then substitute g_{geo} with g_{HO} using Eq. (A.48) obtain

$$g_{\text{fluxonium}} = g_{\text{geo}} \sqrt{\frac{\hbar\omega_{\text{res}}}{16 E_{C_{\text{res}}}}} \tag{A.53}$$

$$\boxed{g_{\text{fluxonium}} = 4 g_{\text{sonnet}} \sqrt{\frac{E_{C_{\text{qubit}}}}{\hbar\omega_{\text{res}}}}} \tag{A.54}$$

Bibliography

[1] Rajeev Acharya, Igor Aleiner, Richard Allen, Trond I Andersen, Markus Ansmann, Frank Arute, Kunal Arya, Abraham Asfaw, Juan Atalaya, Ryan Babbush, et al. Suppressing quantum errors by scaling a surface code logical qubit. *arXiv preprint arXiv:2207.06431*, 2022.

[2] Zheng An and DL Zhou. Deep reinforcement learning for quantum gate control. *Europhysics Letters*, 126(6):60002, 2019.

[3] SM Anton, JS Birenbaum, SR O'Kelley, Vladimir Bolkhovsky, Danielle A Braje, George Fitch, Matthew Neeley, GC Hilton, H-M Cho, KD Irwin, et al. Magnetic flux noise in dc squids: temperature and geometry dependence. *Physical review letters*, 110(14):147002, 2013.

[4] Frank Arute, Kunal Arya, Ryan Babbush, Dave Bacon, Joseph C Bardin, Rami Barends, Rupak Biswas, Sergio Boixo, Fernando GSL Brandao, David A Buell, et al. Quantum supremacy using a programmable superconducting processor. *Nature*, 574(7779):505–510, 2019.

[5] Philip Ball. First 100-qubit quantum computer enters crowded race. *Nature*, 599:542, 2021.

[6] Feng Bao, Hao Deng, Dawei Ding, Ran Gao, Xun Gao, Cupjin Huang, Xun Jiang, Hsiang-Sheng Ku, Zhisheng Li, Xizheng Ma, et al. Fluxonium: an alternative qubit platform for high-fidelity operations. *Physical Review Letters*, 129(1):010502, 2022.

[7] Rami Barends, Julian Kelly, Anthony Megrant, Daniel Sank, Evan Jeffrey, Yu Chen, Yi Yin, Ben Chiaro, Josh Mutus, Charles Neill, et al. Coherent josephson qubit suitable for scalable quantum integrated circuits. *Physical review letters*, 111(8):080502, 2013.

[8] Rami Barends, Julian Kelly, Anthony Megrant, Andrzej Veitia, Daniel Sank, Evan Jeffrey, Ted C White, Josh Mutus, Austin G Fowler, Brooks Campbell, et al. Superconducting quantum circuits at the surface code threshold for fault tolerance. *Nature*, 508(7497):500–503, 2014.

[9] Radoslaw C Bialczak, R McDermott, M Ansmann, M Hofheinz, N Katz, Erik Lucero, Matthew Neeley, AD O'Connell, H Wang, AN Cleland, et al. 1/f flux noise in josephson phase qubits. *Physical review letters*, 99(18):187006, 2007.

[10] Vincent Bouchiat, D Vion, Ph Joyez, D Esteve, and MH Devoret. Quantum coherence with a single cooper pair. *Physica Scripta*, 1998(T76):165, 1998.

[11] Ronald Newbold Bracewell and Ronald N Bracewell. *The Fourier transform and its applications*, volume 31999. McGraw-Hill New York, 1986.

[12] Jochen Braumüller. *Quantum simulation experiments with superconducting circuits*, volume 20. KIT Scientific Publishing, 2018.

[13] Jochen Braumüller. Notes on input-output formalism applied for designing purcell filters. Unpublished, 2019.

[14] Jochen Braumüller, Leon Ding, Antti P Vepsäläinen, Youngkyu Sung, Morten Kjaergaard, Tim Menke, Roni Winik, David Kim, Bethany M Niedzielski, Alexander Melville, et al. Characterizing and optimizing qubit coherence based on squid geometry. *Physical Review Applied*, 13(5):054079, 2020.

[15] Jacob Bryon, DK Weiss, Xinyuan You, Sara Sussman, Xanthe Croot, Ziwen Huang, Jens Koch, and Andrew Houck. Experimental verification of the treatment of time-dependent flux in circuit quantization. *arXiv preprint arXiv:2208.03738*, 2022.

[16] Jonas Bylander, Simon Gustavsson, Fei Yan, Fumiki Yoshihara, Khalil Harrabi, George Fitch, David G Cory, Yasunobu Nakamura, Jaw-Shen Tsai, and William D Oliver. Noise spectroscopy through dynamical decoupling with a superconducting flux qubit. *Nature Physics*, 7(7):565–570, 2011.

[17] Daniel L. Campbell, Yun-Pil Shim, Bharath Kannan, Roni Winik, David K. Kim, Alexander Melville, Bethany M. Niedzielski, Jonilyn L. Yoder, Charles Tahan, Simon Gustavsson, and William D. Oliver. Universal nonadiabatic control of small-gap superconducting qubits. *Phys. Rev. X*, 10:041051, Dec 2020.

[18] Jerry M Chow, Jay M Gambetta, Andrew W Cross, Seth T Merkel, Chad Rigetti, and M Steffen. Microwave-activated conditional-phase gate for superconducting qubits. *New Journal of Physics*, 15(11):115012, 2013.

[19] Claude Cohen-Tannoudji, Jacques Dupont-Roc, and Gilbert Grynberg. *Atom-photon interactions: basic processes and applications*. John Wiley & Sons, 1998.

[20] Antonio D Córcoles, Jay M Gambetta, Jerry M Chow, John A Smolin, Matthew Ware, Joel Strand, Britton LT Plourde, and Matthias Steffen. Process verification of two-qubit quantum gates by randomized benchmarking. *Physical Review A*, 87(3):030301, 2013.

[21] T Daniel. *Sank. Fast, Accurate State Measurement in Superconducting Qubits*. PhD thesis, PhD thesis, University of California, Santa Barbara, ProQuest Dissertations . . . , 2014.

[22] Michel H Devoret et al. Quantum fluctuations in electrical circuits. *Les Houches, Session LXIII*, 7(8), 1995.

[23] Agustin Di Paolo, Thomas E Baker, Alexandre Foley, David Sénéchal, and Alexandre Blais. Efficient modeling of superconducting quantum circuits with tensor networks. *npj Quantum Information*, 7(1):11, 2021.

[24] Leon Ding, Max Hays, Youngkyu Sung, Bharath Kannan, Junyoung An, Agustin Di Paolo, Amir H Karamlou, Thomas M Hazard, Kate Azar, David K Kim, et al. High-fidelity, frequency-flexible two-qubit fluxonium gates with a transmon coupler. *arXiv preprint arXiv:2304.06087*, 2023.

[25] Paul Adrien Maurice Dirac. *The principles of quantum mechanics*. Oxford university press, 1981.

[26] Ebru Dogan, Dario Rosenstock, Loïck Le Guevel, Haonan Xiong, Raymond A Mencia, Aaron Somoroff, Konstantin N Nesterov, Maxim G Vavilov, Vladimir E Manucharyan, and Chen Wang. Demonstration of the two-fluxonium cross-resonance gate. *arXiv preprint arXiv:2204.11829*, 2022.

[27] GJ Dolan. Offset masks for lift-off photoprocessing. *Applied Physics Letters*, 31(5):337–339, 1977.

[28] Pulak Dutta and PM Horn. Low-frequency fluctuations in solids: 1 f noise. *Reviews of Modern physics*, 53(3):497, 1981.

[29] N. Earnest, S. Chakram, Y. Lu, N. Irons, R. K. Naik, N. Leung, L. Ocola, D. A. Czaplewski, B. Baker, Jay Lawrence, Jens Koch, and D. I. Schuster. Realization of a Λ system with metastable states of a capacitively shunted fluxonium. *Phys. Rev. Lett.*, 120:150504, Apr 2018.

[30] Quentin Ficheux, Long B Nguyen, Aaron Somoroff, Haonan Xiong, Konstantin N Nesterov, Maxim G Vavilov, and Vladimir E Manucharyan. Fast logic with slow qubits: microwave-activated controlled-z gate on low-frequency fluxoniums. *Physical Review X*, 11(2):021026, 2021.

[31] Christopher J Foot. *Atomic physics*, volume 7. OUP Oxford, 2004.

[32] Richard Gebauer, Nick Karcher, Daria Gusenkova, Martin Spiecker, Lukas Grünhaupt, Ivan Takmakov, Patrick Winkel, Luca Planat, Nicolas Roch, Wolfgang Wernsdorfer, et al. State preparation of a fluxonium qubit with feedback from a custom fpga-based platform. In *AIP Conference Proceedings*, volume 2241, page 020015. AIP Publishing LLC, 2020.

[33] David J Griffiths and Darrell F Schroeter. *Introduction to quantum mechanics*. Cambridge university press, 2018.

[34] Peter Groszkowski, A Di Paolo, AL Grimsmo, A Blais, DI Schuster, Andrew Addison Houck, and Jens Koch. Coherence properties of the 0-π qubit. *New Journal of Physics*, 20(4):043053, 2018.

[35] Lukas Grünhaupt, Martin Spiecker, Daria Gusenkova, Nataliya Maleeva, Sebastian T Skacel, Ivan Takmakov, Francesco Valenti, Patrick Winkel, Hannes Rotzinger, Wolfgang Wernsdorfer, et al. Granular aluminium as a superconducting material for high-impedance quantum circuits. *Nature materials*, 18(8):816–819, 2019.

[36] Simon Gustavsson, Jonas Bylander, Fei Yan, William D Oliver, Fumiki Yoshihara, and Yasunobu Nakamura. Noise correlations in a flux qubit with tunable tunnel coupling. *Physical Review B*, 84(1):014525, 2011.

[37] Simon Gustavsson, Olger Zwier, Jonas Bylander, Fei Yan, Fumiki Yoshihara, Yasunobu Nakamura, Terry P Orlando, and William D Oliver. Improving quantum gate fidelities by using a qubit to measure microwave pulse distortions. *Physical review letters*, 110(4):040502, 2013.

[38] TM Hazard, ADPA Gyenis, Agustin Di Paolo, AT Asfaw, SA Lyon, AAHA Blais, and AA Houck. Nanowire superinductance fluxonium qubit. *Physical review letters*, 122(1):010504, 2019.

[39] Jared B Hertzberg, Eric J Zhang, Sami Rosenblatt, Easwar Magesan, John A Smolin, Jeng-Bang Yau, Vivekananda P Adiga, Martin Sandberg, Markus Brink, Jerry M Chow, et al. Laser-annealing josephson junctions for yielding scaled-up superconducting quantum processors. *npj Quantum Information*, 7(1):1–8, 2021.

[40] G Ithier, E Collin, P Joyez, PJ Meeson, Denis Vion, Daniel Esteve, F Chiarello, A Shnirman, Yu Makhlin, Josef Schriefl, et al. Decoherence in a superconducting quantum bit circuit. *Physical Review B*, 72(13):134519, 2005.

[41] JE Johnson, Christopher Macklin, DH Slichter, R Vijay, EB Weingarten, John Clarke, and Irfan Siddiqi. Heralded state preparation in a superconducting qubit. *Physical review letters*, 109(5):050506, 2012.

[42] Kosuke Kakuyanagi, Takayoshi Meno, Shiro Saito, Hayato Nakano, Kouichi Semba, Hideaki Takayanagi, Frank Deppe, and Alexander Shnirman. Dephasing of a superconducting flux qubit. *Physical review letters*, 98(4):047004, 2007.

[43] Andrew J Kerman. Flux–charge duality and topological quantum phase fluctuations in quasi-one-dimensional superconductors. *New Journal of Physics*, 15(10):105017, 2013.

[44] Jens Koch, M Yu Terri, Jay Gambetta, Andrew A Houck, DI Schuster, J Majer, Alexandre Blais, Michel H Devoret, Steven M Girvin, and Robert J Schoelkopf. Charge-insensitive qubit design derived from the cooper pair box. *Physical Review A*, 76(4):042319, 2007.

[45] Roger H Koch, John Clarke, WM Goubau, John M Martinis, CM Pegrum, and Dale J Van Harlingen. Flicker (1/f) noise in tunnel junction dc squids. *Journal of low temperature physics*, 51(1-2):207–224, 1983.

[46] Roger H Koch, David P DiVincenzo, and John Clarke. Model for 1/f flux noise in squids and qubits. *Physical review letters*, 98(26):267003, 2007.

[47] Philip Krantz, Morten Kjaergaard, Fei Yan, Terry P Orlando, Simon Gustavsson, and William D Oliver. A quantum engineer's guide to superconducting qubits. *Applied physics reviews*, 6(2):021318, 2019.

[48] P Kumar, S Sendelbach, MA Beck, JW Freeland, Zhe Wang, Hui Wang, C Yu Clare, RQ Wu, DP Pappas, and R McDermott. Origin and reduction of 1/f magnetic flux noise in superconducting devices. *Physical Review Applied*, 6(4):041001, 2016.

[49] T Lanting, AJ Berkley, B Bumble, P Bunyk, A Fung, J Johansson, Anupama Kaul, A Kleinsasser, E Ladizinsky, F Maibaum, et al. Geometrical dependence of the low-frequency noise in superconducting flux qubits. *Physical Review B*, 79(6):060509, 2009.

[50] Jürgen Lisenfeld, Alexander Bilmes, Anthony Megrant, Rami Barends, Julian Kelly, Paul Klimov, Georg Weiss, John M Martinis, and Alexey V Ustinov. Electric field spectroscopy of material defects in transmon qubits. *npj Quantum Information*, 5(1):105, 2019.

[51] Easwar Magesan, Jay M Gambetta, and Joseph Emerson. Scalable and robust randomized benchmarking of quantum processes. *Physical review letters*, 106(18):180504, 2011.

[52] Easwar Magesan, Jay M Gambetta, Blake R Johnson, Colm A Ryan, Jerry M Chow, Seth T Merkel, Marcus P Da Silva, George A Keefe, Mary B Rothwell, Thomas A Ohki, et al. Efficient measurement of quantum gate error by interleaved randomized benchmarking. *Physical review letters*, 109(8):080505, 2012.

[53] Paul Magnard, Philipp Kurpiers, Baptiste Royer, Theo Walter, J-C Besse, Simone Gasparinetti, Marek Pechal, Johannes Heinsoo, Simon Storz, Alexandre Blais, et al. Fast and unconditional all-microwave reset of a superconducting qubit. *Physical review letters*, 121(6):060502, 2018.

[54] Johannes Majer, JM Chow, JM Gambetta, Jens Koch, BR Johnson, JA Schreier, L Frunzio, DI Schuster, Andrew Addison Houck, Andreas Wallraff, et al. Coupling superconducting qubits via a cavity bus. *Nature*, 449(7161):443–447, 2007.

[55] Yuriy Makhlin and Alexander Shnirman. Dephasing of solid-state qubits at optimal points. *Physical review letters*, 92(17):178301, 2004.

[56] Vladimir E Manucharyan, Jens Koch, Leonid I Glazman, and Michel H Devoret. Fluxonium: Single cooper-pair circuit free of charge offsets. *Science*, 326(5949):113–116, 2009.

[57] David C McKay, Christopher J Wood, Sarah Sheldon, Jerry M Chow, and Jay M Gambetta. Efficient z gates for quantum computing. *Physical Review A*, 96(2):022330, 2017.

[58] Ray Mencia, Ivan Pechenezhskiy, Long Nguyen, Yen-Hsiang Lin, and Vladimir Manucharyan. Blochnium: A flux-tunable qubit with flux-insensitive coherence times. *Bulletin of the American Physical Society*, 65, 2020.

[59] Ari Mizel and Yariv Yanay. Right-sizing fluxonium against charge noise. *Physical Review B*, 102(1):014512, 2020.

[60] JE Mooij, TP Orlando, L Levitov, Lin Tian, Caspar H Van der Wal, and Seth Lloyd. Josephson persistent-current qubit. *Science*, 285(5430):1036–1039, 1999.

[61] Ilya N Moskalenko, Ilya A Simakov, Nikolay N Abramov, Dmitry O Moskalev, Anastasiya A Pishchimova, Nikita S Smirnov, Evgeniy V Zikiy, Ilya A Rodionov, and Ilya S Besedin. High fidelity two-qubit gates on fluxoniums using a tunable coupler. *npj Quantum Information*, 8(1), 2022.

[62] F. Motzoi, J. M. Gambetta, P. Rebentrost, and F. K. Wilhelm. Simple pulses for elimination of leakage in weakly nonlinear qubits. *Phys. Rev. Lett.*, 103:110501, Sep 2009.

[63] Pranav S. Mundada, András Gyenis, Ziwen Huang, Jens Koch, and Andrew A. Houck. Floquet-engineered enhancement of coherence times in a driven fluxonium qubit. *Phys. Rev. Applied*, 14:054033, Nov 2020.

[64] Yu Nakamura, Yu A Pashkin, and Jaw Shen Tsai. Coherent control of macroscopic quantum states in a single-cooper-pair box. *nature*, 398(6730):786–788, 1999.

[65] Konstantin N Nesterov, Ivan V Pechenezhskiy, Chen Wang, Vladimir E Manucharyan, and Maxim G Vavilov. Microwave-activated controlled-z gate for fixed-frequency fluxonium qubits. *Physical Review A*, 98(3):030301, 2018.

[66] Long B Nguyen, Gerwin Koolstra, Yosep Kim, Alexis Morvan, Trevor Chistolini, Shraddha Singh, Konstantin N Nesterov, Christian Jünger, Larry Chen, Zahra Pedramrazi, et al. Scalable high-performance fluxonium quantum processor. *arXiv preprint arXiv:2201.09374*, 2022.

[67] Long B Nguyen, Yen-Hsiang Lin, Aaron Somoroff, Raymond Mencia, Nicholas Grabon, and Vladimir E Manucharyan. High-coherence fluxonium qubit. *Physical Review X*, 9(4):041041, 2019.

[68] Long Bao Nguyen. *Toward the Fluxonium Quantum Processor*. PhD thesis, University of Maryland, College Park, 2020.

[69] Michael A Nielsen and Isaac Chuang. Quantum computation and quantum information, 2002.

[70] Murphy Yuezhen Niu, Sergio Boixo, Vadim N Smelyanskiy, and Hartmut Neven. Universal quantum control through deep reinforcement learning. *npj Quantum Information*, 5(1):33, 2019.

[71] TP Orlando, JE Mooij, Lin Tian, Caspar H Van Der Wal, LS Levitov, Seth Lloyd, and JJ Mazo. Superconducting persistent-current qubit. *Physical Review B*, 60(22):15398, 1999.

[72] E Paladino, YM Galperin, G Falci, and BL Altshuler. 1/f noise: Implications for solid-state quantum information. *Reviews of Modern Physics*, 86(2):361, 2014.

[73] Line Hjortshøj Pedersen, Niels Martin Møller, and Klaus Mølmer. Fidelity of quantum operations. *Physics Letters A*, 367(1-2):47–51, 2007.

[74] Charles P Poole, Horacio A Farach, and Richard J Creswick. *Superconductivity*. Academic press, 2013.

[75] Ioan M Pop, Kurtis Geerlings, Gianluigi Catelani, Robert J Schoelkopf, Leonid I Glazman, and Michel H Devoret. Coherent suppression of electromagnetic dissipation due to superconducting quasiparticles. *Nature*, 508(7496):369–72, 2014.

[76] David M Pozar. *Microwave engineering*. John wiley & sons, 2011.

[77] CM Quintana, Yu Chen, Daniel Sank, AG Petukhov, TC White, Dvir Kafri, Ben Chiaro, Anthony Megrant, Rami Barends, Brooks Campbell, et al. Observation of classical-quantum crossover of 1/f flux noise and its paramagnetic temperature dependence. *Physical review letters*, 118(5):057702, 2017.

[78] Matthew Reagor, Christopher B Osborn, Nikolas Tezak, Alexa Staley, Guenevere Prawiroatmodjo, Michael Scheer, Nasser Alidoust, Eyob A Sete, Nicolas Didier, Marcus P da Silva, et al. Demonstration of universal parametric entangling gates on a multi-qubit lattice. *Science advances*, 4(2):eaao3603, 2018.

[79] Kevin Reuer, Jonas Landgraf, Thomas Fösel, James O'Sullivan, Liberto Beltrán, Abdulkadir Akin, Graham J Norris, Ants Remm, Michael Kerschbaum, Jean-Claude Besse, et al. Realizing a deep reinforcement learning agent discovering real-time feedback control strategies for a quantum system. *arXiv preprint arXiv:2210.16715*, 2022.

[80] EH Rhoderick and EM Wilson. Current distribution in thin superconducting films. *Nature*, 194:1167–1168, 1962.

[81] Chad Rigetti and Michel Devoret. Fully microwave-tunable universal gates in superconducting qubits with linear couplings and fixed transition frequencies. *Phys. Rev. B*, 81:134507, Apr 2010.

[82] John Schulman, Filip Wolski, Prafulla Dhariwal, Alec Radford, and Oleg Klimov. Proximal policy optimization algorithms. *CoRR*, abs/1707.06347, 2017.

[83] S Sendelbach, D Hover, A Kittel, M Mück, John M Martinis, and R McDermott. Magnetism in squids at millikelvin temperatures. *Physical review letters*, 100(22):227006, 2008.

[84] Eyob A Sete, John M Martinis, and Alexander N Korotkov. Quantum theory of a bandpass purcell filter for qubit readout. *Physical Review A*, 92(1):012325, 2015.

[85] F Setiawan, Peter Groszkowski, and Aashish A Clerk. Fast and robust geometric two-qubit gates for superconducting qubits and beyond. *arXiv preprint arXiv:2208.04249*, 2022.

[86] F. Setiawan, Peter Groszkowski, Hugo Ribeiro, and Aashish A. Clerk. Analytic design of accelerated adiabatic gates in realistic qubits: General theory and applications to superconducting circuits. *PRX Quantum*, 2:030306, Jul 2021.

[87] Ramamurti Shankar. *Principles of quantum mechanics*. Springer Science & Business Media, 2012.

[88] David M Sheen, Sami M Ali, Daniel E Oates, Richard S Withers, and JA Kong. Current distribution, resistance, and inductance for superconducting strip transmission lines. *IEEE Transactions on Applied Superconductivity*, 1(2):108–115, 1991.

[89] Sarah Sheldon, Easwar Magesan, Jerry M. Chow, and Jay M. Gambetta. Procedure for systematically tuning up cross-talk in the cross-resonance gate. *Phys. Rev. A*, 93:060302, Jun 2016.

[90] Peter W Shor. Polynomial-time algorithms for prime factorization and discrete logarithms on a quantum computer. *SIAM review*, 41(2):303–332, 1999.

[91] V. V. Sivak, A. Eickbusch, H. Liu, B. Royer, I. Tsioutsios, and M. H. Devoret. Model-free quantum control with reinforcement learning. *Phys. Rev. X*, 12:011059, Mar 2022.

[92] WC Smith, A Kou, X Xiao, U Vool, and MH Devoret. Superconducting circuit protected by two-cooper-pair tunneling. *npj Quantum Information*, 6(1):8, 2020.

[93] Aaron Somoroff, Quentin Ficheux, Raymond A Mencia, Haonan Xiong, Roman V Kuzmin, and Vladimir E Manucharyan. Millisecond coherence in a superconducting qubit. *arXiv preprint arXiv:2103.08578*, 2021.

[94] Youngkyu Sung, Leon Ding, Jochen Braumüller, Antti Vepsäläinen, Bharath Kannan, Morten Kjaergaard, Ami Greene, Gabriel O Samach, Chris McNally, David Kim, et al. Realization of high-fidelity cz and zz-free iswap gates with a tunable coupler. *Physical Review X*, 11(2):021058, 2021.

[95] Jeremy Tatum. Libretexts physics, 5.7: Delta-star transform, 2022. Accessed on April 10, 2023.

[96] Michael Tinkham. *Introduction to superconductivity*. Courier Corporation, 2004.

[97] Theodore Van Duzer and Charles William Turner. *Principles of superconductive devices and circuits*. Pearson, 1981.

[98] Uri Vool and Michel Devoret. Introduction to quantum electromagnetic circuits. *International Journal of Circuit Theory and Applications*, 45(7):897–934, 2017.

[99] Hui Wang, Chuntai Shi, Jun Hu, Sungho Han, C Yu Clare, and RQ Wu. Candidate source of flux noise in squids: adsorbed oxygen molecules. *Physical review letters*, 115(7):077002, 2015.

[100] Zhikang T. Wang, Yuto Ashida, and Masahito Ueda. Deep reinforcement learning control of quantum cartpoles. *Phys. Rev. Lett.*, 125:100401, Sep 2020.

[101] WT Weeks, LL-H Wu, MF McAllister, and A Singh. Resistive and inductive skin effect in rectangular conductors. *IBM Journal of Research and Development*, 23(6):652–660, 1979.

[102] Wayne Woods, Greg Calusine, Alexander Melville, Arjan Sevi, Evan Golden, David K Kim, Danna Rosenberg, Jonilyn L Yoder, and William D Oliver. Determining interface dielectric losses in superconducting coplanar-waveguide resonators. *Physical Review Applied*, 12(1):014012, 2019.

[103] Haonan Xiong, Quentin Ficheux, Aaron Somoroff, Long B. Nguyen, Ebru Dogan, Dario Rosenstock, Chen Wang, Konstantin N. Nesterov, Maxim G. Vavilov, and Vladimir E. Manucharyan. Arbitrary controlled-phase gate on fluxonium qubits using differential ac stark shifts. *Phys. Rev. Research*, 4:023040, Apr 2022.

[104] Fei Yan, Dan Campbell, Philip Krantz, Morten Kjaergaard, David Kim, Jonilyn L Yoder, David Hover, Adam Sears, Andrew J Kerman, Terry P Orlando, et al. Distinguishing coherent and thermal photon noise in a circuit quantum electrodynamical system. *Physical Review Letters*, 120(26):260504, 2018.

[105] Fei Yan, Simon Gustavsson, Archana Kamal, Jeffrey Birenbaum, Adam P Sears, David Hover, Ted J Gudmundsen, Danna Rosenberg, Gabriel Samach, Steven Weber, et al. The flux qubit revisited to enhance coherence and reproducibility. *Nature communications*, 7(1):1–9, 2016.

[106] Fei Yan, Philip Krantz, Youngkyu Sung, Morten Kjaergaard, Daniel L Campbell, Terry P Orlando, Simon Gustavsson, and William D Oliver. Tunable coupling scheme for implementing high-fidelity two-qubit gates. *Physical Review Applied*, 10(5):054062, 2018.

[107] F Yoshihara, K Harrabi, AO Niskanen, Y Nakamura, and Jaw Shen Tsai. Decoherence of flux qubits due to 1/f flux noise. *Physical review letters*, 97(16):167001, 2006.

[108] Xinyuan You, James A Sauls, and Jens Koch. Circuit quantization in the presence of time-dependent external flux. *Physical Review B*, 99(17):174512, 2019.

[109] Helin Zhang, Srivatsan Chakram, Tanay Roy, Nathan Earnest, Yao Lu, Ziwen Huang, DK Weiss, Jens Koch, and David I Schuster. Universal fast-flux control of a coherent, low-frequency qubit. *Physical Review X*, 11(1):011010, 2021.